Coating and Hybridization Approaches of Inorganic Materials Using Polymeric Materials to Enhance the Li- and Na-Ion Battery Performance of Alternative Electrode Materials

Dissertation zur Erlangung des Grades
„Doktor der Naturwissenschaften“

im Promotionsfach Chemie
am Fachbereich Chemie, Pharmazie und Geowissenschaften
der Johannes Gutenberg-Universität Mainz

vorgelegt von
Bernd Oschmann
geboren in Pfaffenhofen a.d. Ilm

Mainz, Juni 2015

Die vorliegende Arbeit wurde in der Zeit von Oktober 2012 bis Juni 2015 am Institut für Organische Chemie der Johannes Gutenberg-Universität Mainz unter der Betreuung von Herrn XXX angefertigt. Teile der Arbeit wurden darüber hinaus an der Seoul National University (XXX, März und April 2014), sowie am Helmholtz Institut für elektrochemische Energiespeicherung Ulm (XXX, insbesondere Februar bis Juni 2015) angefertigt.

Dekan: XXX
1. Berichtserstatter: XXX
2. Berichtserstatter: XXX
Tag der mündlichen Prüfung: 03.08.2015

Contents

1 Abstract

1.1 Deutsche Zusammenfassung

Diese Arbeit beschäftigt sich mit Ansätzen, die elektronische Leitfähigkeit in alternativen, neuartigen Elektrodenmaterialien für Lithium-Ionen Batterien zu erhöhen. Alternativen Elektrodenmaterialien, wie z.Bsp. nanostrukturiertes Titandioxid oder Schwefel, die eine erhöhte Sicherheit oder eine höhere Kapazitäten im Vergleich zu derzeitigen Lithium-Ionen Batteriesystemen aufweisen, sind zunächst elektronisch schlecht leitend bzw. sogar elektronisch isolierend. Um die Elektronenperkolation innerhalb des Elektrodenmaterials zu gewährleisten, wurden hier vier Ansätze entwickelt. Ein Ansatz beruht auf der Herstellung von Blockcopolymeren über RAFT (reversible addition fragmentation chain transfer) Polymerisation, die einerseits einen graphitisierbaren Block enthalten und andererseits einen Block, der an die Oberfläche nanostrukturierter Übergangsmetalloxide anbindet. Nach Anbindung des Polymers konnte durch thermische Behandlung ein homogener Kohlenstofffilm auf der Oberfläche der Partikel erzeugt werden. Das somit hergestellte Material wurde als Elektrodenmaterial in Lithium-Ionen Batterien durch u.a. galvanostatisches Zyklisieren und Cyclovoltammetrie evaluiert und es konnte gezeigt werden, dass sich der Kohlenstofffilm im Hinblick auf Kapazität und Langzeitzyklisierbarkeit positiv auf die Batterieperformance der untersuchten Materialien auswirkte.

Als alternative zu diesem thermischen Ansatz wurden auch zwei nicht thermische Ansätze gewählt: Einerseits wurde funktionalisiertes Graphen, eine exfoliierte Monolage von Graphit, verwendet, um anorganische Nanopartikel leitfähig zu umhüllen. Mit Graphen umhüllte Partikel wurden ebenfalls Batterietests unterzogen, wobei wiederum die Umhüllung einen positiven Einfluss auf die Batterieergebnisse des Materials aufzeigte.

Andererseits wurde ein Blockcopolymer bzw. endgruppenfunktionalisiertes Polymer bestehend aus einem leitfähigen Polymer, das durch durch Grignard Metathese (GRIM) Polymerisation hergestellt wurde, und bestehend aus Ankerstruktur(en), die wiederum an die Oberfläche anorganischer Materialien anbinden kann, hergestellt. Das so hergestellte Ma-

terial wurde an ein anorganisches Kathodenmaterial angebunden und das Hybridmaterial in Lithium-Ionen Batterien als Kathodenmaterial untersucht. Hierbei konnte das Polymer jedoch die Batterieperformance des Materials nicht positiv beeinflusse.

Schließlich wurde in einem vierten Ansatz ein Copolymer bestehend aus Schwefel und leitfähigem Polymer hergestellt. Dies gelang durch die Umsetzung von geschmolzenem, radikalischem Schwefel mit einem durch GRIM Polymerisation hergestellten Polythiophen, welches in der Reaktion kovalent an den Schwefel eingebaut wird. Auch dieses Material wurde elektrochemisch als Kathodenmaterial charakterisiert und zeigte eine verbesserte Batterieperformance verglichen mit einem einfachen Gemisch aus Polythiophen und Schwefel, bei dem Schwefel und Polymer nicht kovalent verbunden sind.

1.2 English abstract

The focus of this work is the development of four approaches aiming an increased electronic conductivity within alternative, novel electrode materials for lithium-ion or lithium based batteries. Alternative electrode materials, such as nanostructured titanium dioxide or sulfur, which can enhance the safety or which can increase the specific capacity compared to current commercially available batteries, are electronically hardly conductive or even electronically isolating. Herein, four approaches were developed in order to increase the possibility for electrons to percolate within the electrode material. Therefore, the first approach deals with the synthesis of block copolymers by RAFT (reversible addition fragmentation chain transfer) polymerization. These polymers consist on the one hand of a graphitizable block and on the other hand of a block, that can bind onto the surface of nanostructured transition metal oxides. Once the polymers are coordinated on the particles surface, the polymer coating can be transformed into a carbonaceous coating on the particle surface by pyrolysis. The materials synthesized by this route were applied as electrode materials in lithium-ion batteries and were characterized by galvansotatic cycling as well as cyclic voltammetry. The results of these characterizations proved the positive influence of the carbon coating with respect to the specific capacity, long term cycling and C-rate capability. As a further approach, two non-thermal approaches were developed.

One approach is based on the use of functionlized graphene, which is an electronically conductive, exfoliated monolayer of graphite. This material can be used to wrap inorganic particles. Particles wrapped with graphene were applied as electrode materials and the battery performance of these materials was investigated. It could be shown that the graphene wrapping enhances the battery performance.

The other approach is based on the use of a conductive polymer, which is synthesized by Grignard metathesis (GRIM) polymerization and consists of either an anchoring block or anchoring end-group. This polymer could be coordinated onto the surface of an inorganic cathode material and the hybrid material was investigated as an cathode material in lithium-ion batteries. However, the polymer coating could not improve the battery performance of

the inorganic particles.

Finally, as a fourth approach a copolymer consisting of sulfur and a conductive polymer was synthesized. The copolymer synthesis was achieved by the reaction of a radicalic molten sulfur species with the polythiophene, which is incorporated covalently into the sulfur. This copolymer was applied as a cathode material in a lithium-sulfur battery and showed an enhanced battery performance compared to a simple physical mixture of polythiophene and sulfur (not covalently bond), as the elctric contact is expected to be enhanced by the covalent linkage of sulfur and polymer.

2 Introduction

The efficient storage of electric energy is one of the major challenges in this century. Energy storage is necessary in order to gain independence from limited fossil fuels and to be able to store energy obtained by renewable energy sources, such as wind power or solar power. Especially with respect to electric mobility, i.e. the production of electric vehicles, it is necessary to develop energy storage devices with a high specific and volumetric capacity. Particularly, lithium-ion batteries are promising energy storage devices, which might meet the needed requirements. However, currently the commercially available lithium-ion batteries suffer from several issues and thus cannot be reasonably used in these future application fields.

The research and development of new electrode materials is a promising approach to improve the state-of-the-art lithium-ion battery. Nevertheless, even the alternative electrode materials possess some limitation, as especially a low electric conductivity. Within this dissertation, several approaches are introduced to increase the electronic conductivity within different alternative inorganic electrode materials, whereby this is achieved by organic/inorganic hybridization. The focus of this work is on the one hand the variation of very different morphologies of the different inorganic materials and on the other hand the variation of the hybridization approaches. Herein, a thermal carbon coating approach and several non-thermal hybridization approaches are presented using a conductive polymer or graphene based material. The prepared hybrid systems are evaluated as anode and cathode materials, respectively, in lithium-ion batteries.

2.1 Fundamentals of Battery Technology

Batteries represent one possibility to store electric energy. In the case of batteries, the energy is stored in the form of chemical energy and is converted to electric energy by redox reactions. The set-up of such battery systems corresponds to the set-up of a galvanic cell. Figure 1 shows schematically the set-up of the Daniell element, an example for such a galvanic cell. These cells consist of two electrodes, which are located in an electrolyte solution. In the case

of the Daniell element, the electrodes consist of zinc and copper.

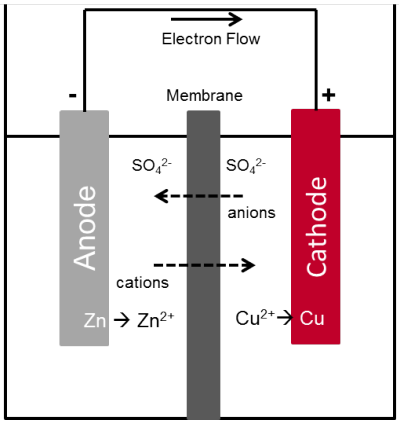

Figure 1: Schematic set-up of the Daniell element.

The electrodes are connected electrically conducting with a wire. Both half-cells are separated by a semipermeable membrane, the separator. As there is a difference between both electrode active materials with respect to the redox potential, a redox reaction starts. The oxidation takes place at the electrode with the more negative potential and the reduction at the electrode with the more positive potential. In the case of the Daniell element, zinc is oxidized to Zn^{2+} (reduction potential: -0.76 V vs. standard hydrogen cell) and Cu^{2+} is reduced to elemental copper (reduction potential: +0.52 V vs. standard hydrogen cell). As long as the redox reactions are reversible, the reactions can be driven in the inverse direction by the application of the opposite voltage. Cells, which are reversible, are called rechargeable batteries. In the environment of the electrochemical society, commonly simply ”“battery”” is used even for an rechargeable element. Cells, that are not reversible, are called primary cells.

Within the last 200 years, since the development of the ”“Voltaic pile”” by Allessandro Volta in the year 1800, many different battery systems were developed based on many different combinations of electrode materials, such as the lead-acid batter, (with Pb and PbO_2 as electrode material), the nickel-zinc battery (with NiOOH and Zn as electrodes) or the lithium-ion battery. During the last 20 years, lithium-ion batteries established themselves on the market, first of all in portable electronic devices. The attractiveness of lithium-ion batteries is based

on two electrochemical reasons: the anodes based on lithium-ion or metallic lithium material offer a very negative potential (-3.04 V vs Li/Li^+ vs. the standard hydrogen electrode), which enables high cell voltages. In addition, these electrode materials allow high specific and volumetric capacities.[1] Both features cause a high energy density (both with respect to the volume as well as with respect to the weight) compared to other battery systems, as shown in Figure 2.

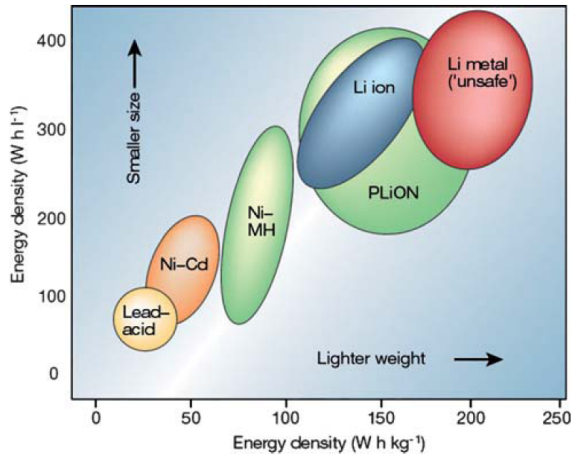

Figure 2: Comparison of different battery systems with respect to the gravimetric and volumetric energy density.[1]

Further advantages of lithium-ion batteries are the low self-discharge, long life time, a high efficiency and a quite low memory effect, which is the loss of capacity due to a partial (and not complete) discharge.[2,3,4,5]

Important physical quantities, which are used to characterize batteries, are the following:

- the specific capacity (amount of charge stored with respect to the mass of active material)
- the volumetric capacity (amount of charge stored with respect to the volume of the active material)
- the C-rate capability (development of specific capacity during the application of different specific current densities). High capacities at high C-rates are desirable causing

short charging times

- the cycling stability
- the potential profile during the redox reaction (influences the cell voltage and the energy density)
- the coulomb efficiency (quotient of the discharge and charge capacity)
- the energy efficiency (quotient of discharge and charge energy density)

These physical quantities will be discussed further in the discussion chapter for the evaluation of synthesized materials as electrode materials in lithium-ion batteries.

2.2 Commercial Lithium-Ion Batteries and Their Issues

The commercialization of lithium-ion batteries was achieved in 1991 by Sony.[6] Since then the electrode materials of commercialized lithium-ion batteries are based on intercalation compounds. Lithium-ions can be incorporated as a guest component into layered crystalline host structures. This insertion and deinsertion takes place at a certain insertion potential at the anode and cathode.

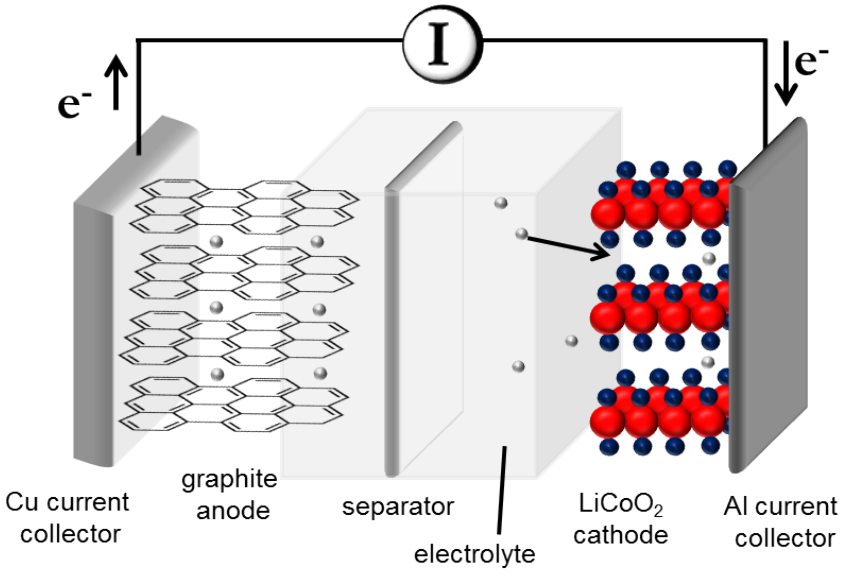

Figure 3: Schematic set-up of a commercial lithium-ion battery.

In commercial lithium-ion batteries graphite is used as anode material and lithiumcobaltoxide is used as cathode material,[7] as schematically shown in Figure 3. This set-up is also called "rocking chair battery", as the lithium ions diffuse back and forth between anode and cathode. Thus, the redox reaction occurring at the anode can be described with the following equation:

$$\mathrm{Li_xC_n} \underset{\text{charge}}{\overset{\text{discharge}}{\rightleftharpoons}} \mathrm{xLi^+ + xe^- + C_n} \tag{1}$$

The insertion of lithium into the host structure commonly causes a volume expansion of the host structure, in case of graphite the expansion is about 10.3 %.[8] Furthermore, lithium remains positively charge in the intercalation compound Li_xC_n, so that graphite as the host structure is reduced during the insertion. The maximum lithium content is LiC_6 corresponding to a theoretical capacity of 372 mAh g^{-1}.[9]

For the cathode the insertion reaction can be described as follows:

$$\mathrm{Li^+ + e^- + CoO_2} \underset{\text{charge}}{\overset{\text{discharge}}{\rightleftharpoons}} \mathrm{LiCoO_2} \tag{2}$$

The theoretical capacity is in this case 270 mAh g^{-1}.[10]

Aqueous electrolytes cannot be used in lithium-ion batteries due to the high reactivity of the lithium metal or lithium insertion compounds towards water.[11] Alternatively, organic electrolytes like ethylene carbonate or propylene carbonate with solved electrolyte salts such as $LiPF_6$ are used.[11] The cell voltage of common lithium-ion batteries is not within the stability window of these electrolytes causing a decomposition of the electrolytes and the formation of the so called "'solid electrolyte interphase"' (SEI) on the interphase between the anode and the electrolyte.[12 2 9] This SEI consists partially of organic compounds and partially of

organometallic lithium containing compounds as shown in Figure 4.

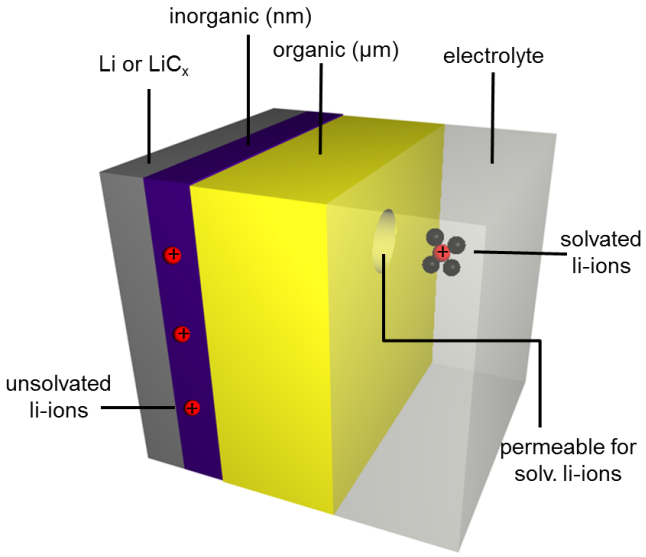

Figure 4: Scheme of the "'solid electrolyte interphase"'.

This formation of the SEI is disadvantageous due to the irreversible loss of lithium-ions. On the other hand, the formation of the SEI is limited to the first few charge and discharge cycles, since the SEI is permeable for lithium-ions only, but not for electrons,[13] which prevents a further decomposition of the electrolytes during the cycling.

The use of metallic lithium would be a great improvement towards current lithium-ion batteries with respect to the capacity (3860 mAh g^{-1} for metallic lithium and 372 mAh g^{-1} for graphite), but due to a safety risk related to the SEI formation this is not possible: The SEI is not homogeneously deposited onto the anode surface, so that the metallic lithium is deposited preferably at areas with a thin SEI layer (because of a lower resistance) resulting in an irregular, dendritic growth of the lithium during the charge process. These dendrites can grow even to the cathode causing a short cut. Thus, the use of metallic lithium is currently an inevitable safety risk and as a consequence impossible.[14]

The advantage of the use of graphite instead of metallic lithium is the avoidance of dendritic growth of lithium. The set-up of a commercial lithium-ion battery in Figure 3 implies the advantageous towards other battery systems discussed in chapter 2.1, but still some issues

remain and there is a lot of space for improvement: The use of graphite still induces the formation of the SEI implying an irreversible loss of lithium, i.e. the loss of active material and capacity fading during cycling. Furthermore, there is still a safety issue, as the decomposition of the electrolyte causes the formation of gaseous products such as CO_2.[15] If the pressure within the cell becomes too high, the cell might burst and burn.[16]

The theoretical capacity of graphite (372 mAh g^{-1}), which can be practically almost fully reached, is high compared to other battery systems. However, for the use in electric vehicles the capacity is too low, as the driving ranges are rather short. For instance, the driving range for a Nissan Leaf would be 160 km.[17] The short driving range in combination with long charging times (compared to the time required to refill a fuel car) makes the currently available electric vehicle not attractive.

Also $LiCoO_2$ has several disadvantages: The theoretical capacity is 270 mAh g^{-1}, but practically only 150 mAh g^{-1} can be achieved.[10,18] This again causes rather short driving ranges. Besides this electrochemical disadvantages of $LiCoO_2$, also ecological and economic disadvantages have to be stated: Due to the presence of cobalt, $LiCoO_2$ is a toxic compound. Moreover, the natural abundance of this material is quite low causing high costs.[19]

All these issues prove, that the current lithium-ion battery is not perfected yet.

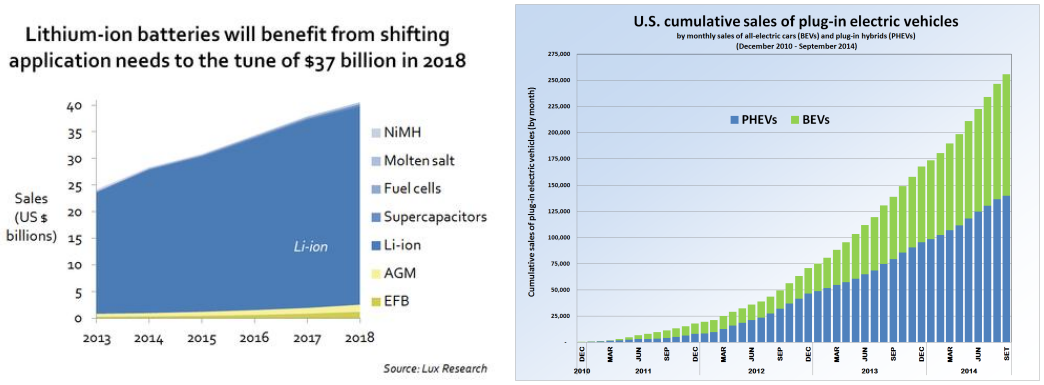

Figure 5: Development of the lithium-ion battery market (a)[20] and development of the electric and hybrid car market in USA (b).[21]

The increasing demand of lithium-ion batteries (as demonstrated in Figure 5), also caused

by the expected increase of electric and hybrid car sells (see Figure 5(b)), requires the improvement of lithium-ion batteries.

A highly promising approach to improve lithium-ion batteries is the development of new electrode materials, which exhibit higher capacities, lower costs or which solve the safety risks.

2.3 Alternative Anode and Cathode Materials and Their Challenges

There is a broad variety of alternative anode and cathode materials differing both in the compound class and in the way of reaction with lithium. Three different ways of reaction are possible:
First, there are the already introduced insertion and intercalation compounds. In this case, lithium-ions are incorporated as a guest into the host crystal structure. Second type are the "'conversion compounds"'. These materials are converted during the reaction with lithium and new compounds are formed as explained for some examples below. Finally, alloying compounds, basically metals, which can form alloys with lithium, are available. By the use of these materials, the creation of high energy and high power batteries might become possible, but the reduction of the safety risk is not always possible.
However, there are general issues and requirements for the use of these materials, which will be discussed in section 2.3.1.

2.3.1 General Issues of Alternative Electrode Materials

The internal electronic and ionic resistance within a battery is mainly limited by the active material, as the ionic resistance within the electrolyte and the electronic resistance through the current collector and conductive additives is by far lower compared to the the resistance within the active material.[22]
Therefore, the idea of using nanostructured active material particles came up, i.e. particles with dimensions in the nanometer range with a high surface-to-volume ratio, which indeed

was proven to be advantageous.[23 24 25 26] Nanostructured materials imply shorter diffusion distances for both electrons and lithium-ions within the active material due to the higher surface-to-volume ratio compared to microstructured materials. This enables an improved battery performance (higher capacity, shorter charging time) due to enhanced ionic diffusion kinetics. Finally, the use of nanomaterial causes also an increased electrode/electrolyte interphase,[27 24] while a complete lithiation of micrometer sized material is often not possible due to kinetic reasons.[28]

In addition, the size and the morphology of the active material has a large impact on the electrochemical performance as well. Thus, the use of tubes increases the surface compared to nanorods of the same dimension and shortens further the diffusion distances for electrons and lithium-ions. Alternatively, nanostructures with a high interconnectivity proved to improve the C-rate performance.[29 30 31]

However, the down-sizing from micrometer scale to nanometer scale causes further challenges: The downsizing causes shorter diffusion distances for electrons, but the increased surface of nanoparticles causes an increased interfacial resistance from the particle/particle boundaries,[22] so there is a need to create an electronic percolating network covering the particle/particle interfaces.[25] The increased surface of the active material can also cause further side reactions, for instance with the electrolyte.[25] Ways to enhance the electronic conductivity on the surface of the particles and ways to protect the active material surface need to be developed.

2.3.2 Alternative Anode Materials

Generally, nanostructured transition metal oxides (as well as some main group oxides) are attractive alternatives as anode material, whereby the different transition metal oxides have different advantages.

For titanium dioxide the theoretical capacity is 335 mAh g^{-1} (for the fully lithiated $LiTiO_2$).[32] This is comparable with the capacity of graphite (372 mAh g^{-1}). The use of TiO_2 offers an enhanced safety.[33 34] Since the insertion reaction of lithium into TiO_2 occurs at a voltage

within the stability window of the electrolytes (between 1.2 and 2.0 V vs. Li/Li^+) no SEI is formed and no gaseous side products are formed.[2,35] Especially the anatase crystal structure is suitable for the lithium insertion in TiO_2 (compared to rutile and brookite structures), as there are higher efficiencies for anatase.[36,37] In the case of anatase the use of nanomaterial is very desirable, and the formation of the fully lithiated $LiTiO_2$ is limited to a small thickness of 4 nm below the surface.[38] Hence, particles in the micrometer range can only form the $Li_{0,55}TiO_2$ phase with a lower lithium content.[39,32] Besides the increased safety further advantages for the use of TiO_2 are the low production costs and the environmental sustainability.

A further attractive transition metal oxide is zinc oxide with a theoretical capacity of 978 mAh g^{-1}, which is almost three times higher than the capacity of graphite. The lithiation of ZnO occurs in two steps: First, ZnO is decomposed according to the following equation:

$$ZnO + 2Li^+ + 2e^- \rightarrow Zn + Li_2O \tag{3}$$

The problem of this first step is the irreversible formation of Li_2O, which is an electronic isolator and does not participate in the redox reaction during the further cycling steps.[40] Anyway, the formed metallic zinc forms Li/Zn alloys in the voltage range between 0 and 0.8 V vs. Li/Li^+, whereby these alloy reactions are reversible:

$$Zn + Li^+ + e^- \rightleftharpoons LiZn \tag{4}$$

A further challenge is the volume change of the active material during the alloying process. The volume expansion during the reaction from Zn to LiZn is 71%. These volume changes may cause an electronic isolation of particles as well as separation of particles from the current collector. This causes a decay of capacity.[41] Due to high theoretical capacities also Fe_2O_3 (theoretical capacity: 1005 mAh g^{-1}, conversion compound)[42,43] and SnO_2(theoretical ca-

pacity: 718 mAh g^{-1}, conversion compound and alloying material)[44] are interesting. These materials will be discussed later in more detail.
Also silicon is a highly interesting material (theoretical capacity: 4200 mAh g^{-1}), but due to huge volume changes during the cycling (volume expansion during lithiation: 323 %) this material is highly challenging, and thus, will not be discussed within this dissertation.

For a reasonable application of the previously discussed materials, it is necessary to develop approaches to increase the electronic conductivity within the nanocomposite materials and to develop approaches to buffer the volume changes of the active material. Within this thesis, some approaches to achieve these goals, are presented in the following chapters.

2.3.3 Alternative Cathode materials

Cathode materials, which are close to commercialization are for example $LiNi_{0.5}Mn_{1.5}O_4$ or $LiNi_{0.33}Mn_{0.33}Co_{0.33}O_2$ (NMC). $LiNi_{0.5}Mn_{1.5}O_4$ is very attractive due to the high intercalation potential of almost 5 V with a specific capacity of 148 mAh g^{-1} resulting in a high power battery.[45,46] However, due to the high voltage, side reactions occur at the electrodes, which might be prevented by a suitable coating.
Similarly, the replacement of $LiCoO_2$ by NMC is attractive due to an increasing battery energy density by the use of NMC as well as due to the reduced Co-amount.[47] Again, in this case coatings are attractive that protect the electrode/electrolyte interface.[48,49]
Although these materials are close to commercialization, there are also several very attractive alternative electrode materials with very high theoretical capacities. But these are still far from commercialization due to several issues. Especially sulfide materials with a high sulfur content and even sulfur itself belong to this group of alternative cathode materials. For instance, FeS_2 (pyrite) offers a theoretical capacity of 890 mAh g^{-1} and the capacity of sulfur is 1675 mAh g^{-1}, thus, several times higher than the capacity of the currently used $LiCoO_2$ (theoretically 270 and practically 150 mAh g^{-1}).[50,51] Tarascon et al. predict an increase of the energy density for the use of sulfur in commercial lithium-ion batteries as shown in Figure 6:[52]

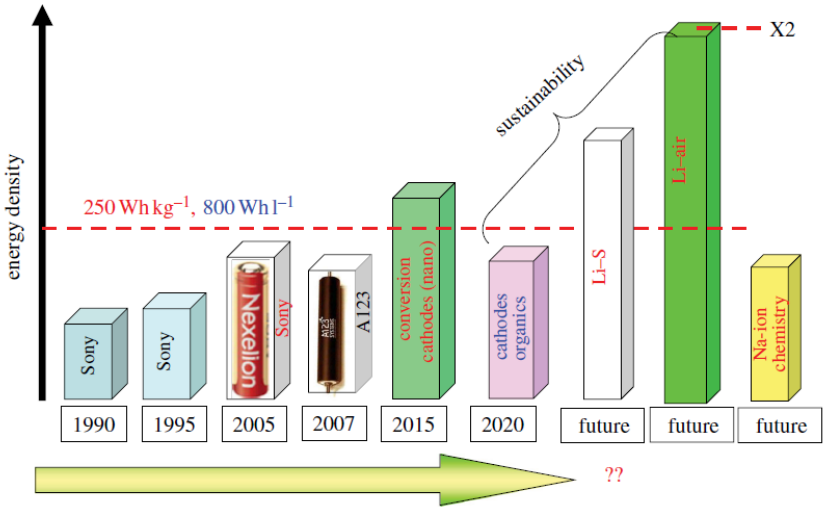

Figure 6: Predicted energy density of lithium-ion batteries.[52]

Further advantages for the sulfides towards $LiCoO_2$ are the low toxicity of the sulfides and the low costs due to the huge natural abundance: Sulfur is produced as a side product during the desulfurization of gas.[53]

However, these materials feature also several issues: Sulfur is an electronic isolator (electronic conductivity of sulfur: $5 \cdot 10{-}30$ S cm^{-1}),[54] which is a big problem for the electron diffusion within sulfur based electrodes.

Furthermore, sulfur is a conversion compound and it is reduced stepwise. Several kind of polysulfides are formed in the range of 2.50 V and 2.05 V vs. Li/Li^+ ($S_8 + 2\,e^- \rightarrow S_n{}^{2-}$ with $8 \geq n \geq 4$). These polysulfides are finally reduced to Li_2S in the range of 2.05 V and 1.5 V.[55] The intermediately formed polysulfides $S_n{}^{2-}$ with $8 \geq n \geq 3$ are soluble in commonly used electrolytes. Thus,dis during the charge and discharge process active material is dissolved into the electrolyte. The finally formed Li_2S is insoluble. The solubility of the polysulfides causes several problems: The dissolved polysulfides are lost for further cycling and cause a strong capacity fading during cycling within the first 100 cycles.[56 57 58 59] This is a big issue, as for the common applications a cycling stability for more than 1000 cycles is desired. Another problem of the solubility of the polyelectrolytes is the so called ”shuttle mechanism” shown in Figure 7 for the charging process. The solved polysulfides can diffuse from the

cathode to the anode and can be reduced during the charging process to polysulfides of lower order, or can be even reduced to insoluble Li_2S and are deposited irreversibly onto the anode surface.[60] The not fully reduced polysulfides can diffuse back from the anode to the cathode, where they are oxidized again, and can further shuttle between anode and cathode.[61 60 58] This results in a reduction in the coulombic efficiency, as energy is consumed by the redox processes of the dissolved and diffusing polysulfides.

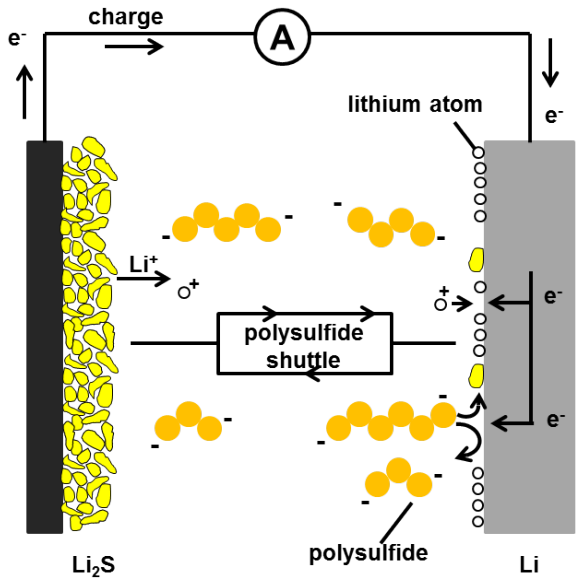

Figure 7: Schematic illustration of the ”shuttle mechanism”.

A further challenge of the sulfur is the volume expansion of 22% during the cycling to Li_2S. This can again cause a capacity fading as discussed in the previous chapter.[62]

Pyrite belongs to the ”conversion compounds” as well, whereby the following reactions occur during the discharge:[63 50]

$$FeS_2 + 2Li^+ + 2e^- \rightarrow Li_2FeS_2 \tag{5}$$

$$Li_2FeS_2 + 2Li^+ + 2e^- \rightarrow Fe^0 + Li_2S \quad (6)$$

Li_2S formed during the discharge forms the polysulfides during the charge process, so that there are the same issues as for sulfur (shuttle mechanism, capacity fading).[50]

In summary, sulfidic conversion compounds have two main issues: The low electronic conductivity as well as the formation of soluble polysulfides. Thus, strategies have to be developed that address these issues. Such strategies developed within this thesis involve the use of polymers as conducting materials oder precursor for conducting and encapsulating material, which were synthesized by polymerization techniques described in the following chapters.

2.4 Sodium-Ion Battery as a Potential Post-Lithium-Ion Battery Technology

As described in the previous chapters, lithium-ion batteries have a high potential to serve for the future demand of electrical energy storage. This is probably true for the next decades and maybe next century, but there are doubts that batteries based on lithium can supply energy storage on a long-term basis, as the lithium resources are limited.[64] Thus, research groups started evaluating so called post-lithium-ion battery technologies based on alternative elements such as magnesium, aluminium and sodium, as these materials are more abundant and cheaper.[65 66 67] So far, these technologies are far from commercialization and only fundamental work has been done.

Sodium-ion batteries are rather close to the lithium-ion battery technology, as both elements are alkali metals and thus share some similar chemical properties. Generally, for the sodium-ion battery a rocking chair set-up can be applied as already introduced in Figure 3 for the lithium-ion battery.

Voltages and specific capacities obtained by sodium-ion batteries are lower compared to lithium-ion batteries,[66] so sodium-ion batteries are rather highly interesting for stationary

energy storage devices, where cost is more important than weight and volume of the battery. However, sodium-ions are larger compared to lithium-ions and thus, intercalation and diffusion through electrode material becomes more difficult. Developing reasonable electrode materials, especially anode materials, for sodium-ion batteries is still a challenge. Furthermore, many of the potential electrode materials for sodium-ion batteries suffer from low electric conductivity as already described in the previous chapter for lithium-ion batteries. Some of the materials prepared within this thesis were applied as electrode materials in sodium-ion batteries, whereby the focus was to increase the conductivity by a coating strategy as described in the following chapters.

2.5 Controlled Radical polymerization

The application of radical polymerization enables the synthesis of macromolecules using a wide range of vinyl monomers. The polymerization is initiated with radical starters, for instance peroxide or diazo derivatives, which form radicals induced by heat or light. These radicals can react with the double bond of the vinylmonomer building up a polymeric structure. During the free-radical polymerization different reactions involving radicals can occur : 1) the initiation (radical generation), 2) the propagation, 3) chain transfer by atom transfer or atom abstraction reaction and 4) termination reactions by radical-radical recombination or by disproportionation reaction of radicals.[68] The chain transfer and termination reactions cause a broad polydispersities, i.e. a broad molecular weight distribution, and prevent a possible reinitiation of the terminated polymers. As a result, the synthesis of block copolymers is not possible by free-radical polymerization.

However, within the past decades, controlled or living radical polymerization techniques were developed enabling a control over the end-group and low polydispersities[69] (PDI $<$ 1.5). Furthermore, the synthesis of more complex polymer structures, such as well-defined block and graft copolymers, stars, combs and networks become possible.

The idea of the living radical polymerization techniques is based on three principles: First, the reduction of the undesired side or termination reactions by the reduction of the radical concentration and an enhanced life time of the growing polymer chain. From a kinetic point

of view the reduction of radical concentration reduces the reaction rate of the termination reaction, as the termination reaction is second order with respect to the radical concentration, whereas propagation is only first order.[70] The termination reactions cannot be completely avoided, but can be suppressed by the reduction of the radical concentration.

Secondly, the living radical polymerization is based on the following dynamic equilibrium reaction shown in Figure 8 involving an active species, that is a polymer chain including a free radical, and an inactive or dormant species containing no radical, which is kinetically favoured. This equilibrium suppresses side reactions, as there is a large number of growing polymer chains compared to the number of radicals required. This "persistent radical effect" is a key factor of the living radical polymerization techniques.[70]

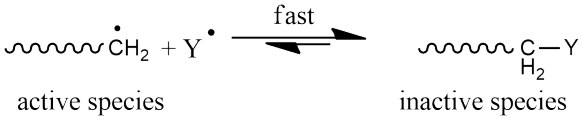

Figure 8: Equilibrium of active in inactive species during controlled radical polymerization.

Averaged over the time, all polymer chains exist for the same time in the form of the active species during the polymerization of this living radical polymerization process, so that the chains grow uniformly. Furthermore, the polymer chains contain finally defined end-groups. As the third key principle a fast initiation should be named, as this enables a constant concentration of growing chains.

Currently, three controlled radical polymerization techniques are applied in many laboratories. These techniques are named NMP (nitroxide-mediated polymerization)[71] first reported by Rizzardo et al. and further developed by Geroges et al. and Hawker et al.,[72,73] ATRP (atom transfer radical polymerization) developed by Matyjaszewski et al.[74] and the RAFT (reversible addition fragmentation chain transfer) polymerization, which was developed by Rizzardo and Moad.[75] They will be briefly described in the following.

Nitroxide-Mediated Polymerization (NMP)

The NMP is based on the use of alkoxyamines, typically alkoxyamines based on the (2,2,6,6-

Tetramethylpiperidin-1-yl)oxy (TEMPO) structure. This method is limited to only few monomers like styrene (TEMPO). By modification of the alkoxydes monomers like (Meth)acrylester and isoprene can be polymerized, too.[73,76] The mechanism of this polymerization technique is shown in Figure 9.

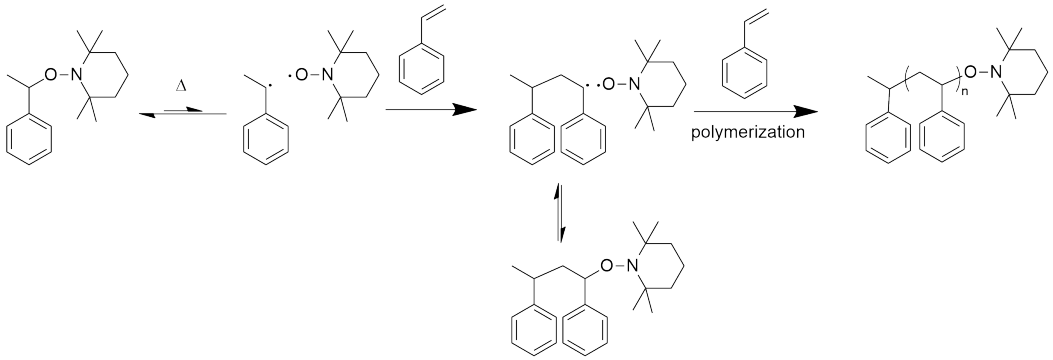

Figure 9: Mechanism of the NMP.

Atom Transfer Radical Polymerization (ATRP)

The ATRP is based on a reversible atom transfer of halogen atoms between a catalyst and the active polymer chain, whereas the polymer chain becomes dormant after the transfer of the halogen to the polymer chain. Typically, as transition metal catalyst, copper (Cu(I)), is used, which undergoes redox reactions during the transfer. Besides the catalyst, an alkyl haolgenide as an initiator, a ligand, which stabilizes and solubilizes the catalyst, and a monomer is added. The reaction is initiated by the redox reaction between the Cu(I), which forms a Cu(II) ion, and the initiator. The formed alkyl radical starts the polymerization reaction with the monomer. The dormant polymer species is formed by the reaction of the Cu(II) with the growing polymer chain as described in the following figure:

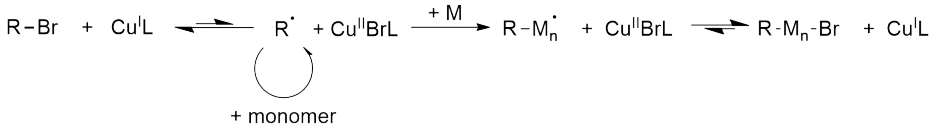

Figure 10: Mechanism of the ATRP.

As shown in Figure 10, the polymers are end-group functionalized with a halogen atom.

Thus, the polymer can be used as a macroinitiator for a block copolymerization reaction. This polymerization can be applied to numerous monomers, but it is not applicable to acidic monomers, since these monomers might protonate the typically nitrogen containing ligands. A further disadvantage of this polymerization is the difficulty to remove the catalyst.[77]

Reversible Addition Fragmentation Chain Transfer

In case of the RAFT polymerization a so-called chain transfer agent (CTA) besides the monomer and the initiator is used. Common structures of chain transfer agents are especially dithioesters or trithiocarbonates, but also other structures can be used as shown in Figure 11.[78,79]

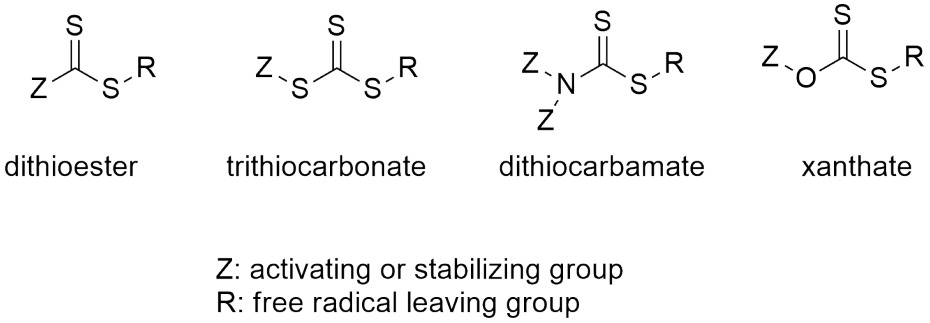

Figure 11: Typical CTA structures.

The use of the CTA enables a sequence of addition-fragmentation equilibria (see Figure 12), which is the key feature of this polymerization.

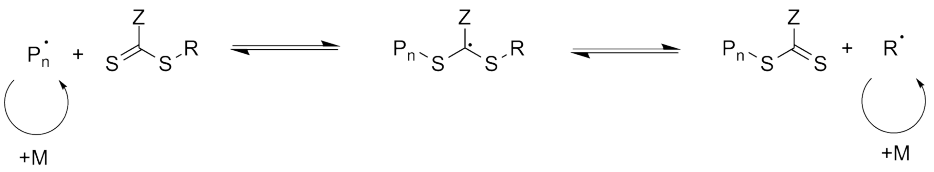

Figure 12: Addition-fragmentation equlilbria of the RAFT polymerization.

After the dissociation of the initiator and the addition of a few monomers to the initiator radical these addition-fragmentation reactions take place. The rapid equilibrium between the dormant polymer species (covalently bound to the CTA) and the active propagating

radical causes an equal probability for all chains to grow and is thus responsible for low polydispersities and control over molecular weight. Since the CTA/initiator ratio is chosen high (commonly around 10:1), the radical concentration is low and the polymers bear the corresponding CTA end groups. This enables a block copolymerization by the use of a the polymer as a macro-CTA in a second step.[80] Furthermore, the α and ω modification of the polymers by polymer analogous reactions is well established.[81 82 83]

The RAFT polymerization turned out to be a very versatile polymerization technique as a huge number of monomers can be polymerized by a proper choice of CTA. Several review articles report, which CTA is suitable for which monomer.[79 84 85]

The use of reactive ester monomers is also possible.[86 87] This is a very powerful tool, which plays an important role in this dissertation. The polymerization of reactive esters offers the possibility to introduce a huge variety of functional structures into the polymer, for example dyes, radioactive labeled structures or structures, that can bind to inorganic particles.[88 89 90]

2.6 Grignard Metathesis Polymerization for the Synthesis of Conducting Polymers

Fully conjugated polymers owe interesting properties, especially semiconducting properties, and are thus handled as candidates in several applications, such as in optoelectronic devices (organic photovoltaics or organic light emitting diodes) or in batteries.[91 92] For the discovery of conjugated (conductive) polymers in 1970, Alan J. Heeger, Alan G. MacDiarmid and Hideki Shirakawa received the Nobel prize in 2000.[93]

Polythiophenes are one example for this compound class. Especially, poly(3-hexylthiophene-2,5-diyl) (P3HT) shown in Figure 13 is a prominent example used in photovoltaic devices as a hole conducting material.[94]

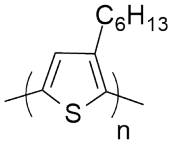

Figure 13: Structure of poly(3-hexylthiophene-2,5-diyl).

The synthesis of highly regioregular P3HT, which possesses higher electronic conductivity compared to regioirregular P3HT, is possible by the application of the so called Grignard metathesis (GRIM) polymerization developed by McCullough et al.[95 96] Therefore, 2,5-dibromo-3-hexylthiophene is first reacted with a sterically demanding Grignard compound such as *tert.*-butylmagnesium chloride (tBuMgCl).

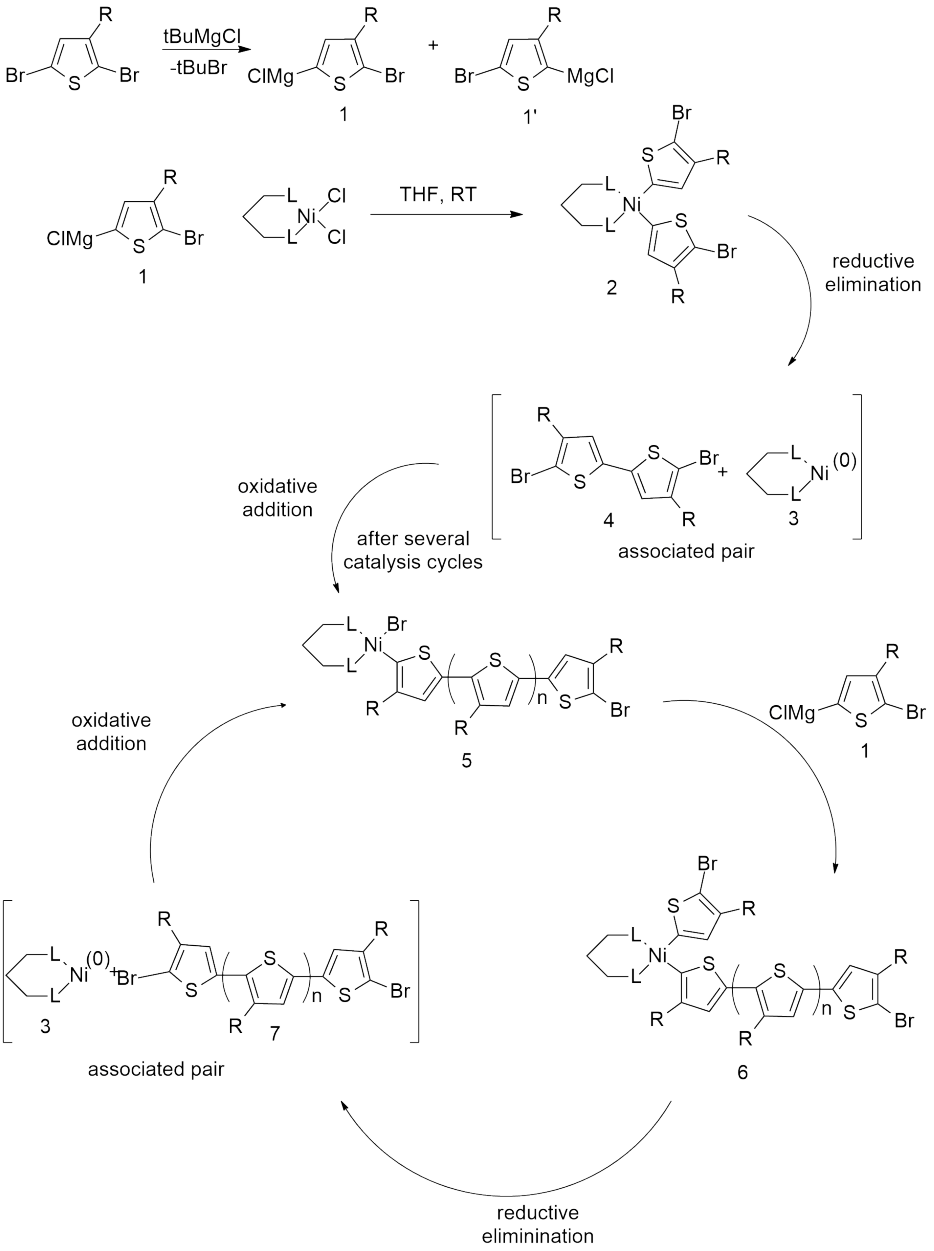

Figure 14: Mechanism of the GRIM polymerization.

The Grignard compound inserts preferably into the sterically less hindered 5-position (see Figure 14) to form the active monomer (**1**) by a bromine-magnesium exchange (also referred to as Grignard metathesis). The side product (**1'**) does not participate in the following polymerization step due to the sterical hindrance.[96]

The following polymerization is based on a nickel-catalyzed cross-coupling "quasi"-living polymerization using typically (Ni(dppp)Cl_2) (dichloro(1,3-bis(diphenylphosphino)propane)nickel) as a catalyst.[97] In the first step two 2-bromo-5-chloromagnesium-3-alkylthiophene monomers react with the nickel catalyst forming a bis(organyl)-nickel compound (**2**). After the reductive elimination a 5,5-dibromobithienyl (**4**) product and a Ni(0) (**3**) catalyst is formed, thus a tail-to-tail coupling is involved in the first step. This step is followed by an oxidative addition step of the monomer to the Ni(0) center forming compound (**5**). Another monomer coordinates to the nickel complex (**6**). After reductive elimination and oxidative addition of the Ni(0) complex the described steps are repeated.[97] The monomers, which are incorporated after the first step, insert via the sterically less hindered head-to-tail coupling.

Besides the ability to synthesize highly regioregular P3HT, the GRIM polymerization offers also the possibility to functionalize P3HT with certain end-groups, whereby the end-group modification can be achieved by three ways:[98] First, the use of a Ni-based functional initiator allows the introduction of an end-group as introduced by Bronstein et al. Second, the addition of another Grignard reagent at the end of the polymerization quenches the reaction and introduces the organic rest of the Grignard reagent as an end-group.[99,100,101,102] In this case, at the end of the polymerization a solution of the second Grignard R'MgBr reagent is added in excess to the polymerization reaction.

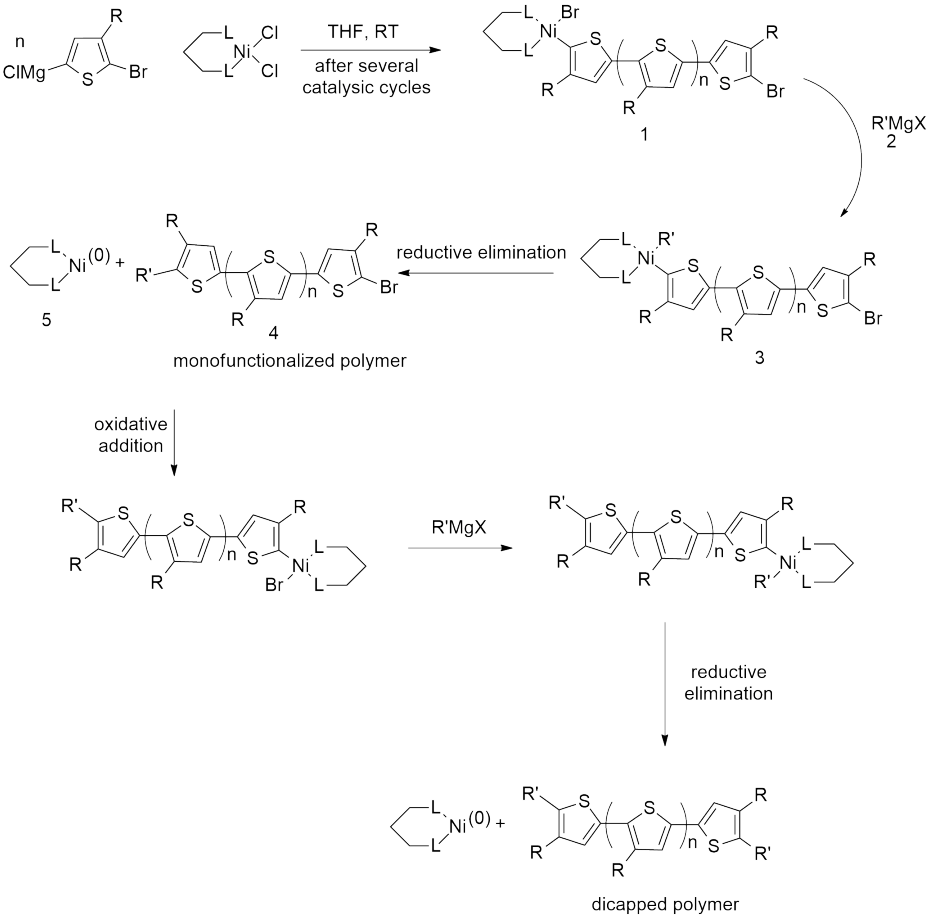

Figure 15: Mechanism of the end-group functionalization during the GRIM polymerization.

The organyl compound of the Grignard reagent coordinates to the nickel catalyst (**3**, see Figure 15) and finally inserts at the end of the polymer chain (**4**) to obtain monocapped polymer. Depending on the Grignard reagent it is in some cases also possible to form dicapped polymer, which is also described in Figure 15.[100]

As a third possibility to introduce end-groups in P3HT post-polymerization methods of end-functional P3HT were described.[103,104] For example, the exchange of an H-terminated aromatic end-group with an aldehyde is described by the application of the Vilsmeier reaction.[103] The synthesis of P3HT via GRIM polymerization with the selective introduction of end-groups is also conducted within this thesis as explained below.

2.7 Synthesis Methodes, Properties and The Application of Graphene in Batteries

Graphene is a single sheet of graphite. Thus, it consists of a monolayer of hexagonally ordered, sp^2 hybridized carbon atoms (also referred to as honeycomb crystal lattice, see Figure 16).

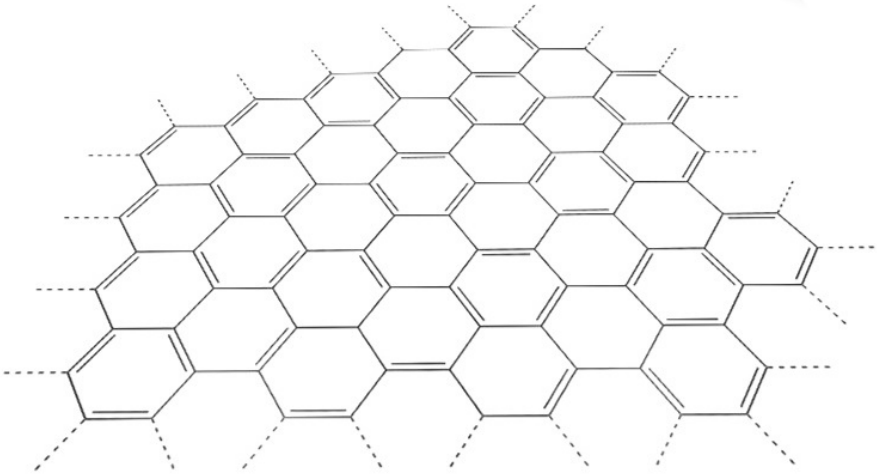

Figure 16: Excerpt of the graphene structure.

Due to its unique properties such as the high thermal conductivity,[105] the high mechanical strength,[106] high electronic conductivity and high charge carrier mobility,[107,108] graphene gained a huge interest within the last few year. Furthermore, Konstantin Novoselov and Andre Geim even received the Nobel prize for the discovery and investigation of the properties of graphene in 2010.

For this thesis, graphene is an interesting material due to its high electronic conductivity.

Graphene can be synthesized by several methods of which some are introduced here. Generally, both bottom-up and top-down approaches were developed. The method, which was used by Geim et al., is a simple top-down approach: adhesive tape can be deposited onto a graphite single crystal and pulled off, finally yielding in single graphene layers that can be

transferred to silicon wafer for further investigations.[109]

A second approach is a chemical vapor deposition method.[110] For example, a thin nickel film is used as a template. First, this nickel film is exposed to argon at around 1000 °C. Mixing methane to the argon gas leads to the formation of carbon atoms on the surface of the nickel film, finally forming the hexagonal structured carbon layer on top of the nickel film.[111]

A bottom-up approach developed by Müllen et al. is based on the chemical synthesis of graphene starting from small molecules forming first polyphenylene dendrimers and finally graphene-like well-defined molecules.[112]

The method used in the experiments described here for the preparation of graphene is based on a top-down approach. In a first step, graphite is oxidized, for instance using potassium permanganate, sulfuric acid and sodium nitrate as oxidizing reagents, applying a method developed by Hummer et al. in 1958 yielding in so called ”graphene oxide”.[113] The graphene oxide can be exfoliated in polar solvents to single sheets by ultrasonication. These single sheets bear functional groups, such as carboxylic acid groups, especially at the edges of the sheets, as well as epoxide or hydroxyl groups as shown in Figure 17.

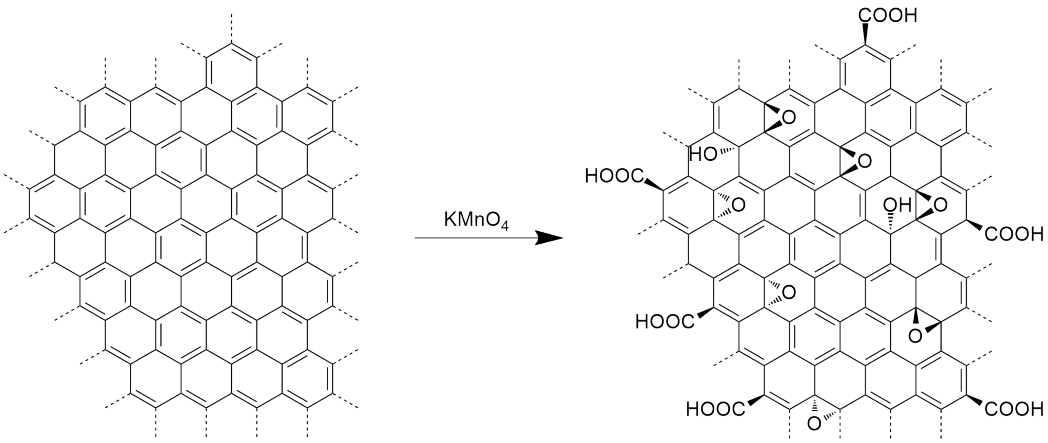

Figure 17: Synthesis of graphene oxide.

The graphene oxide can be reduced to the so called ”reduced graphene oxide” by chemical reduction, for instance with hydrazine, or by a thermal treatment.[114,115] Since not all functional groups can be removed by this methods, the resulting reduced graphene oxide is not a

perfect monolayer of sp^2-hybridized carbon atoms, thus owing defects within the hexagonal structure and causing less advanced properties compared to the perfectly reduced graphene oxide. However, this method enables the synthesis of quite conductive and still dispersible graphene-like structures in larger quantities.

References

[1] Liu, D.; Cao, G. *Energ. Environ. Sci.* **2010**, *3*, 1218–1237.

[2] Scrosati, B.; Garche, J. *J. Power Sources* **2010**, *195*, 2419–2430.

[3] Winter, M.; Brodd, R. J. *Chemical Reviews* **2004**, *104*, 4245–4270.

[4] Bradley A. Johnson, R. E. W. *Journal of Power Sources* **1998**, *70*, 48–54.

[5] Borchard-Tuch, C. *Chemie in unserer Zeit* **2003**, *37*, 436–437.

[6] Armand, M.; Tarascon, J.-M. *Nature* **2008**, *451*, 652–657.

[7] Nagura, J. *JEC Battery Newslett.* **1991**, 17–25.

[8] Song, X. Y. *J. Electrochem. Soc.* **1996**, *143*, 2419–2430.

[9] Winter, M.; Besenhard, J. O.; Spahr, M. E.; Novák, P. *Adv. Mater.* **1998**, *10*, 725–763.

[10] Mizushima, K.; Jones, P.; Wiseman, P.; Goodenough, J. *Mater. Res. Bull.* **1980**, *15*, 783–789.

[11] Xu, K. *Chem. Rev.* **2004**, *104*, 4303–4418.

[12] Peled, E. *Journal of The Electrochemical Society* **1979**, *126*, 2047.

[13] Zhang, S.; Xu, K.; Jow, T. *Electrochim. Acta* **2006**, *51*, 1636–1640.

[14] Vincent, C. A. *Solid State Ionics 134 (2000) 159–167* **2000**, 159–167.

[15] Yazami, R. *Electrochim. Acta* **1999**, *45*, 87–97.

[16] Yu, P.; Ritter, J. A.; White, R. E.; Popov, B. N. *Journal of The Electrochemical Society* **2000**, *147*, 1280.

[17] Bruce, P. G.; Freunberger, S. A.; Hardwick, L. J.; Tarascon, J.-M. *Nature Materials* **2011**, *11*, 19–29.

[18] Saavedra-Arias, J. J.; Thomas, R.; Karan, N.; Ishikawa, Y.; Katiyar, R. *ECS Transactions* **2009**, *16*, 9–18.

[19] Padhi, A. K. *J. Electrochem. Soc.* **1997**, *144*, 1188.

[20] lux source, 2013; http://www.designnews.com/document.asp?doc_id=265737.

[21] EDTA, 2014; http://electricdrive.org/index.php?ht=d%2Fsp%2Fi%2F20952%2Fpid%2F20952.

[22] Li, H.; Zhou, H. *Chemical Communications* **2012**, *48*, 1201.

[23] Aricò, A. S.; Bruce, P.; Scrosati, B.; Tarascon, J.-M.; van Schalkwijk, W. *Nat. Mater.* **2005**, *4*, 366–377.

[24] Bruce, P. G.; Scrosati, B.; Tarascon, J.-M. *Angewandte Chemie International Edition* **2008**, *47*, 2930–2946.

[25] Guo, Y.-G.; Hu, J.-S.; Wan, L.-J. *Advanced Materials* **2008**, *20*, 2878–2887.

[26] Wagemaker, M.; Mulder, F. M. *Accounts of Chemical Research* **2013**, *46*, 1206–1215.

[27] Scrosati, B.; Hassoun, J.; Sun, Y.-K. *Energy & Environmental Science* **2011**, *4*, 3287.

[28] Jiang, C.; Wei, M.; Qi, Z.; Kudo, T.; Honma, I.; Zhou, H. *J. Power Sources* **2007**, *166*, 239–243.

[29] Feckl, J. M.; Fominykh, K.; Döblinger, M.; Fattakhova-Rohlfing, D.; Bein, T. *Angewandte Chemie International Edition* **2012**, *51*, 7459–7463.

[30] Zhang, Y.; Tang, Y.; Yin, S.; Zeng, Z.; Zhang, H.; Li, C. M.; Dong, Z.; Chen, Z.; Chen, X. *Nanoscale* **2011**, *3*, 4074.

[31] Huang, G.; Zhang, F.; Zhang, L.; Du, X.; Wang, J.; Wang, L. *Journal of Materials Chemistry A* **2014**, 8048–8053.

[32] Yang, Z.; Choi, D.; Kerisit, S.; Rosso, K. M.; Wang, D.; Zhang, J.; Graff, G.; Liu, J. *J. Power Sources* **2009**, *192*, 588–598.

[33] Wagemaker, M.; Mulder, F. M. *Accounts of Chemical Research* **2012**, 120210133049004.

[34] Myung, S.-T.; Takahashi, N.; Komaba, S.; Yoon, C. S.; Sun, Y.-K.; Amine, K.; Yashiro, H. *Advanced Functional Materials* **2011**, *21*, 3231–3241.

[35] Fröschl, T.; Hörmann, U.; Kubiak, P.; Kučerová, G.; Pfanzelt, M.; Weiss, C. K.; Behm, R. J.; Hüsing, N.; Kaiser, U.; Landfester, K.; Wohlfahrt-Mehrens, M. *Chemical Society Reviews* **2012**, *41*, 5313.

[36] Natarajan, C.; Setoguchi, K.; Nogami, G. *Electrochimica Acta* **1998**, *43*, 3371–3374.

[37] Bresser, D.; Paillard, E.; Binetti, E.; Krueger, S.; Striccoli, M.; Winter, M.; Passerini, S. *J. Power Sources* **2012**, *206*, 301–309.

[38] van de Krol, R.; Goossens, A.; Schoonman, J. *The Journal of Physical Chemistry B* **1999**, *103*, 7151–7159.

[39] Zachau-Christiansen, B.; West, K.; Jacobsen, T.; Atlung, S. *Solid State Ionics* **1988**, *28-30*, 1176–1182.

[40] Li, H. *Solid State Ionics* **1999**, *123*, 189–197.

[41] Liu, J.; Li, Y.; Ding, R.; Jiang, J.; Hu, Y.; Ji, X.; Chi, Q.; Zhu, Z.; Huang, X. *The Journal of Physical Chemistry C* **2009**, *113*, 5336–5339.

[42] Larcher, D.; Masquelier, C.; Bonnin, D.; Chabre, Y.; Masson, V.; Leriche, J.-B.; Tarascon, J.-M. *Journal of The Electrochemical Society* **2003**, *150*, A133.

[43] Reddy, M. V.; Subba Rao, G. V.; Chowdari, B. V. R. *Chemical Reviews* **2013**, *113*, 5364–5457.

[44] Lou, X. W.; Li, C. M.; Archer, L. A. *Advanced Materials* **2009**, *21*, 2536–2539.

[45] Zhong, Q. *Journal of The Electrochemical Society* **1997**, *144*, 205.

[46] Arrebola, J. C.; Caballero, A.; Cruz, M.; Hernán, L.; Morales, J.; Castellón, E. R. *Advanced Functional Materials* **2006**, *16*, 1904–1912.

[47] Whittingham, M. S. *Chemical Reviews* **2004**, *104*, 4271–4302.

[48] Abouimrane, A.; Odom, S. A.; Tavassol, H.; Schulmerich, M. V.; Wu, H.; Bhargava, R.; Gewirth, A. A.; Moore, J. S.; Amine, K. *Journal of the Electrochemical Society* **2012**, *160*, A268–A271.

[49] Xu, K.; Cresce, A. v. *Journal of Materials Chemistry* **2011**, *21*, 9849.

[50] Montoro, L.; Rosolen, J.; Shin, J.; Passerini, S. *Electrochim. Acta* **2004**, *49*, 3419–3427.

[51] Cheon, S.-E.; Ko, K.-S.; Cho, J.-H.; Kim, S.-W.; Chin, E.-Y.; Kim, H.-T. *J. Electrochem. Soc.* **2003**, *150*, A796–A799.

[52] Tarascon, J.-M. *Philosophical Transactions of the Royal Society A: Mathematical, Physical and Engineering Sciences* **2010**, *368*, 3227–3241.

[53] Eow, J. S. *Environ. Prog.* **2002**, *21*, 143–162.

[54] Dean, J. A., Ed. *Lange's Handbook of Chemistry*, 3rd ed.; 1985.

[55] Yuan, L.; Qiu, X.; Chen, L.; Zhu, W. *J. Power Sources* **2009**, *189*, 127–132.

[56] Mikhaylik, Y. V.; Akridge, J. R. *Journal of The Electrochemical Society* **2004**, *151*, 1969–1976.

[57] Bresser, D.; Passerini, S.; Scrosati, B. *Chemical Communications* **2013**, *49*, 10545.

[58] Akridge, J. R. *Solid State Ionics* **2004**, *175*, 243–245.

[59] Evers, S.; Nazar, L. F. *Accounts of Chemical Research* **2013**, *46*, 1135–1143.

[60] Ji, X.; Nazar, L. F. *J. Mater. Chem.* **2010**, *20*, 9821–9826.

[61] Marmorstein, D.; Yu, T.; Striebel, K.; McLarnon, F.; Hou, J.; Cairns, E. *J. Power Sources* **2000**, *89*, 219–226.

[62] He, X.; Ren, J.; Wang, L.; Pu, W.; Jiang, C.; Wan, C. *J. Power Sources* **2009**, *190*, 154–156.

[63] Son, S.-B.; Yersak, T. A.; Piper, D. M.; Kim, S. C.; Kang, C. S.; Cho, J. S.; Suh, S.-S.; Kim, Y.-U.; Oh, K. H.; Lee, S.-H. *Advanced Energy Materials* **2014**, *4*, n/a.

[64] Gruber, P. W.; Medina, P. A.; Keoleian, G. A.; Kesler, S. E.; Everson, M. P.; Wallington, T. J. *Journal of Industrial Ecology* **2011**, *15*, 760–775.

[65] Aurbach, D.; Gofer, Y.; Lu, Z.; Schechter, A.; Chusid, O.; Gizbar, H.; Cohen, Y.; Ashkenazi, V.; Moshkovich, M.; Turgeman, R. *Journal of Power Sources* **2001**, *97-98*, 28–32.

[66] Kim, S.-W.; Seo, D.-H.; Ma, X.; Ceder, G.; Kang, K. *Advanced Energy Materials* **2012**, *2*, 710–721.

[67] Lin, M.-C.; Gong, M.; Lu, B.; Wu, Y.; Wang, D.-Y.; Guan, M.; Angell, M.; Chen, C.; Yang, J.; Hwang, B.-J.; Dai, H. *Nature* **2015**, *520*, 324–328.

[68] Matyjaszewski, K.; Davis, T. P. *Handbook of radical polymerization*; Wiley-Interscience: Hoboken and N.J, 2002.

[69] Colombani, D. *Progress in Polymer Science* **1997**, *22*, 1649–1720.

[70] Matyjaszewski, K. *Current Opinion in Solid State and Materials Science* **1996**, *1*, 769–776.

[71] Solomon, D. H.; Rizzardo, E.; Cacioli, P. (Rizzardo). 1985.

[72] Georges, M. K.; Veregin, R. P. N.; Kazmaier, P. M.; Hamer, G. K. *Macromolecules* **1993**, *26*, 2987–2988.

[73] Hawker, C. J.; Bosman, A. W.; Harth, E. *Chemical Reviews* **2001**, *101*, 3661–3688.

[74] Wang, J.-S.; Matyjaszewski, K. *Journal of the American Chemical Society* **1995**, *117*, 5614–5615.

[75] Chiefari, J.; Chong, Y. K.; Ercole, F.; Krstina, J.; Jeffery, J.; Le, T. P. T.; Mayadunne, R. T. A.; Meijs, G. F.; Moad, C. L.; Moad, G.; Rizzardo, E.; Thang, S. H. *Macromolecules* **1998**, *31*, 5559–5562.

[76] Benoit, D.; Grimaldi, S.; Robin, S.; Finet, J.-P.; Tordo, P.; Gnanou, Y. *Journal of the American Chemical Society* **2000**, *122*, 5929–5939.

[77] SHEN, Y.; TANG, H.; DING, S. *Progress in Polymer Science* **2004**, *29*, 1053–1078.

[78] Keddie, D. J.; Moad, G.; Rizzardo, E.; Thang, S. H. *Macromolecules* **2012**, *45*, 5321–5342.

[79] Moad, G.; Rizzardo, E.; Thang, S. H. *Australian Journal of Chemistry* **2005**, *58*, 379.

[80] Moad, G.; Rizzardo, E.; Thang, S. H. *Australian Journal of Chemistry* **2012**, *65*, 985.

[81] Roth, P. J.; Kessler, D.; Zentel, R.; Theato, P. *Journal of Polymer Science Part A: Polymer Chemistry* **2009**, *47*, 3118–3130.

[82] Roth, P. J.; Haase, M.; Basche, T.; Theato, P.; Zentel, R. *Macromolecules* **2010**, *43*, 895–902.

[83] Roth, P. J.; Kessler, D.; Zentel, R.; Theato, P. *Macromolecules* **2008**, *41*, 8316–8319.

[84] Moad, G.; Chong, Y.; Postma, A.; Rizzardo, E.; Thang, S. H. *Polymer* **2005**, *46*, 8458–8468.

[85] Moad, G.; Rizzardo, E.; Thang, S. H. *Australian Journal of Chemistry* **2009**, *62*, 1402.

[86] Eberhardt, M.; Théato, P. *Macromolecular Rapid Communications* **2005**, *26*, 1488–1493.

[87] Theato, P.; Klok, H.-A. *Functional polymers by post-polymerization modification: Concepts, guidelines, and applications*.

[88] Nuhn, L.; Hirsch, M.; Krieg, B.; Koynov, K.; Fischer, K.; Schmidt, M.; Helm, M.; Zentel, R. *ACS Nano* **2012**, *6*, 2198–2214.

[89] Allmeroth, M.; Moderegger, D.; Gündel, D.; Koynov, K.; Buchholz, H.-G.; Mohr, K.; Rösch, F.; Zentel, R.; Thews, O. *Biomacromolecules* **2013**, *14*, 3091–3101.

[90] Oschmann, B.; Bresser, D.; Tahir, M. N.; Fischer, K.; Tremel, W.; Passerini, S.; Zentel, R. *Macromolecular Rapid Communications* **2013**, *34*, 1693–1700.

[91] Coakley, K. M.; McGehee, M. D. *Chemistry of Materials* **2004**, *16*, 4533–4542.

[92] Novák, P.; Müller, K.; Santhanam, K. S. V.; Haas, O. *Chemical Reviews* **1997**, *97*, 207–282.

[93] Rehahn, M. *Chemie in unserer Zeit* **2003**, *37*, 18–30.

[94] Ma, W.; Yang, C.; Gong, X.; Lee, K.; Heeger, A. J. *Advanced Functional Materials* **2005**, *15*, 1617–1622.

[95] Loewe, R. S.; Khersonsky, S. M.; McCullough, R. D. *Advanced Materials* **1999**, *11*, 250–253.

[96] Loewe, R. S.; Ewbank, P. C.; Liu, J.; Zhai, L.; McCullough, R. D. *Macromolecules* **2001**, *34*, 4324–4333.

[97] Iovu, M. C.; Sheina, E. E.; Gil, R. R.; McCullough, R. D. *Macromolecules* **2005**, *38*, 8649–8656.

[98] Handa, N. V.; Serrano, A. V.; Robb, M. J.; Hawker, C. J. *Journal of Polymer Science Part A: Polymer Chemistry* **2015**, *53*, 831–841.

[99] Jeffries-EL, M.; Sauvé, G.; McCullough, R. D. *Advanced Materials* **2004**, *16*, 1017–1019.

[100] Jeffries-EL, M.; Sauvé, G.; McCullough, R. D. *Macromolecules* **2005**, *38*, 10346–10352.

[101] Kochemba, W. M.; Kilbey, S. M.; Pickel, D. L. *Journal of Polymer Science Part A: Polymer Chemistry* **2012**, *50*, 2762–2769.

[102] Lohwasser, R. H.; Thelakkat, M. *Macromolecules* **2011**, *44*, 3388–3397.

[103] Liu, J.; McCullough, R. D. *Macromolecules* **2002**, *35*, 9882–9889.

[104] Mougnier, S.-J.; Brochon, C.; Cloutet, E.; Fleury, G.; Cramail, H.; Hadziioannou, G. *Macromolecular Rapid Communications* **2012**, *33*, 703–709.

[105] Balandin, A. A.; Ghosh, S.; Bao, W.; Calizo, I.; Teweldebrhan, D.; Miao, F.; Lau, C. N. *Nano Letters* **2008**, *8*, 902–907.

[106] Lee, C.; Wei, X.; Kysar, J. W.; Hone, J. *Science* **2008**, *321*, 385–388.

[107] Stankovich, S.; Dikin, D. A.; Dommett, G. H. B.; Kohlhaas, K. M.; Zimney, E. J.; Stach, E. A.; Piner, R. D.; Nguyen, S. T.; Ruoff, R. S. *Nature* **2006**, *442*, 282–286.

[108] Bolotin, K.; Sikes, K.; Jiang, Z.; Klima, M.; Fudenberg, G.; Hone, J.; Kim, P.; Stormer, H. *Solid State Communications* **2008**, *146*, 351–355.

[109] Geim, A. K.; MacDonald, A. H. *Physics Today* **2007**, *60*, 35–41.

[110] Zhang, Y.; Zhang, L.; Zhou, C. *Accounts of Chemical Research* **2013**, *46*, 2329–2339.

[111] Kim, K. S.; Zhao, Y.; Jang, H.; Lee, S. Y.; Kim, J. M.; Kim, K. S.; Ahn, J.-H.; Kim, P.; Choi, J.-Y.; Hong, B. H. *Nature* **2009**, *457*, 706–710.

[112] Chen, L.; Hernandez, Y.; Feng, X.; Müllen, K. *Angewandte Chemie International Edition* **2012**, *51*, 7640–7654.

[113] Hummers, W. S.; Offeman, R. E. *Journal of the American Chemical Society* **1958**, *80*, 1339.

[114] Li, D.; Müller, M. B.; Gilje, S.; Kaner, R. B.; Wallace, G. G. *Nature Nanotechnology* **2008**, *3*, 101–105.

[115] Dreyer, D. R.; Park, S.; Bielawski, C. W.; Ruoff, R. S. *Chemical Society Reviews* **2009**, *39*, 228.

3 Objectives of This Thesis

As explained in the introduction, current lithium and sodium-ion batteries should be improved with respect to specific capacities and safety. Promising alternative electrode materials suffer from several issues, such as low electronic conductivity, low cycling stability and partial degradation of the active material. Thus, approaches have to be developed, which overcome these issues.

The aim of this thesis is the development of such approaches, that are supposed to increase the electronic conductivity by hybridization of organic and inorganic materials. This concept aims at the preparation of a conductive coating , which (i) encapsulates/protects the inorganic nanoparticles and (ii) acts simultaneously as a highway for electrons. From the inorganic side different kind of alternative electrode materials should be used ranging from insertion materials (TiO_2 nanorods and nanotubes), conversion-alloying compounds (ZnO, SnO_x) to pure conversion compounds (Fe_2O_3, FeS_2 and sulfur). These materials shall be applied as anode and cathode materials respectively. Besides the variation of the alternative electrode material itself, this work shall also focus on the use of materials with advanced morphology, whereby besides nanorods also advanced morphologies such as nanotubes or multipods, sponge-like structures and superparticles shall be used.

From the organic side different kind of hybridization steps should be developed in order to increase the electronic conductivity within the electrode material, whereby the variation of inorganic material requires the development of different kind of hybridization steps. Therefore, the organic counterpart for the hybridization needs to be adjusted to the used inorganic material.

The first approach is based on a thermal carbon coating approach. In this case, copolymers (both block and statistical copolymers) shall be synthesized, that consist of anchoring units, which can bind onto the inorganic particles, as well as of carbon precursor units, that can be transformed into a partially graphitic shell by pyrolysis (see Figure 18). The variation of inorganic particles requires the adjustment of the polymer. Thus, the variation of the anchoring unit is required, as different inorganic particles require different kind of coordination

chemistry.

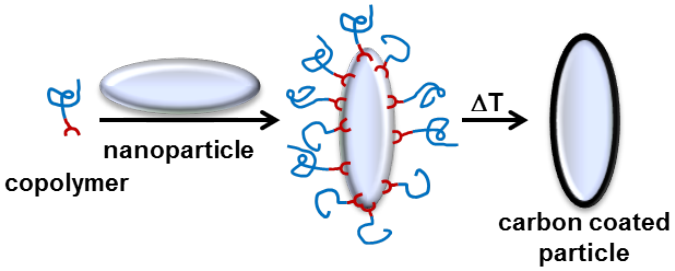

Figure 18: Thermal carbon coating approach using carbon precursor copolymers.

By this approach a thin and homogeneous carbon coating should be gained, which is advantageous towards currently applied carbon coating methods, where small carbon precursor molecules without anchoring structures, for instance glucose, are mixed in a slurry with the active material. For these typical carbon coating approaches, the carbon precursor is typically inhomogeneously distributed, thus yielding in an inhomogeneously distributed carbonaceous material after pyrolysis.

Besides this thermal carbon coating approach, which can be only applied to thermally stable inorganic materials, also a non-thermal approach should be developed. In this case, graphene should be used. In order to coat or wrap graphene around particles, it is necessary to introduce functional groups into the graphene structures, which can interact with the inorganic nanoparticle surface. This enables a post functionalization and wrapping of the nanoparticles as shown in Figure 19. Different kind of thermally unstable particles shall be coated by this approach. Besides this thermal carbon coating approach, which can be only applied to thermally stable inorganic materials, also a non-thermal approach should be developed. In this case, graphene should be used. In order to coat or wrap graphene around particles, it is necessary to introduce functional groups into the graphene structures, which can interact with the inorganic nanoparticle surface. This enables a post functionalization and wrapping of the nanoparticles as shown in Figure 19. Different kind of thermally unstable particles shall be coated by this approach.

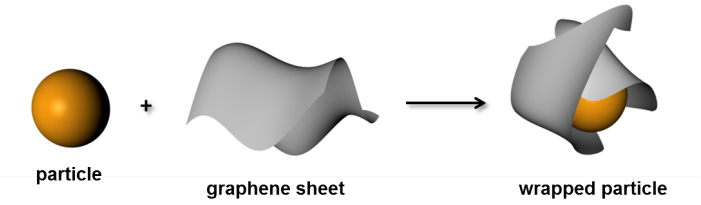

Figure 19: Non-thermal carbon coating approach using graphene sheets.

Another non-thermal coating approach using a conductive polymer should be developed. For this approach a conductive polymer should be synthesized, which contains anchoring units. This polymer should be used to coat inorganic particles to increase the electric conductivity.

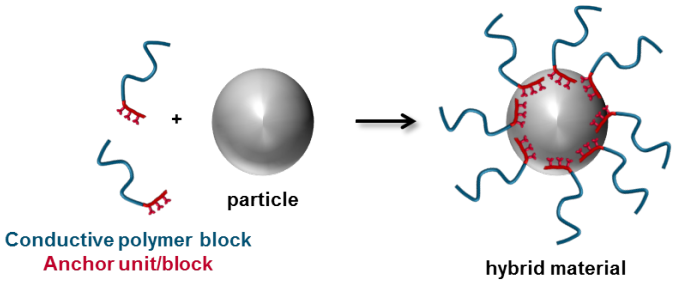

Figure 20: Non-thermal coating approach using conductive polymers.

Finally, as a very different kind of hybridization approach, a so called ”inverse vulcanization” approach with sulfur should be applied. Inverse vulcanization of sulfur using special small molecule dienes could improve the cycling stability of sulfur and reduce the problems of the formation of soluble polysulfides. However, in order to increase the conductivity within inverse vulcanized sulfur, the incorporation of conductive material is required. Thus, an approach should be developed using conductive polymer, which should be covalently incorporated into sulfur.

All prepared materials shall be evaluated as electrode materials in lithium-ion or sodium-ion batteries. Proper characterization methods should be applied in order to characterize the electrode materials, especially galvanostatic cycling and cyclic voltammetry, but also more

advanced techniques such as in-situ XRD were applied. In order to investigate the influence of the coatings or the hybridization, typically non-coated particles or non-hybridized materials should be compared with the coated or hybridized materials.

4 Results and Discussion

4.1 Thermal Carbon Coating Approach

Introducing a conductive carbon coating onto a nanoparticle surface is one approach to increase the conductivity within nanostructured electrode materials. An increased conductivity enables faster charging and increases at the same time the battery life time. Desired are coatings, that are homogeneously distributed, thin enough to allow the lithium diffusion through the coating, and conductive. Additionally, in some cases the stabilization of the nanoparticle surface with respect to side reactions with the electrolyte or with respect to the degradation of the nanoparticle itself is required.

Common carbon coating approaches in the lithium-ion battery research are based on the use of carbon precursor molecules (typically sugar molecules), which are dissolved in a solvent and mixed with the active material. After the removal of the solvent by reduced pressure, the composite is pyrolyzed. During the drying step the small molecules cannot form a homogeneous coating on the nanoparticle surface, so this approach results in an inhomogeneous distribution of carbonaceous material.

For a thermal carbon coating approach of inorganic nanoparticles, copolymers are synthesized, which consist of anchoring units. They can bind onto the surface of inorganic nanoparticles. Furthermore, the copolymers consist of repeating units, that can be transformed to a partially graphitic material by pyrolysis. This approach enables the binding of a carbon precursor immediately onto the surface of inorganic particles. Thus, this approach allows a homogeneous distribution of carbon precursors on the nanoparticle surface.

For the synthesis of copolymers (both statistical and block copolymers) RAFT polymerization is applied. This allows the synthesis of well-defined polymers, especially the synthesis of block copolymers. Additionally, a correlation between block length and grafting density of the polymer on the nanoparticle can be obtained, as the molecular weight of the polymers can be well controlled by the RAFT polymerization.

By variation of the anchoring structure, this approach can be applied to a variety of inor-

ganic nanoparticles, as shown in the following sections for TiO_2 nanorods, TiO_2 nanotubes, Au@ZnO multipods and $SnO_2 - x$ sponges. Furthermore, the applied coatings have a positive influence on the battery performances of each material.

The prepared materials are used as electrode materials and are tested in so called Swagelok cells, which are schematically shown in Figure 1.

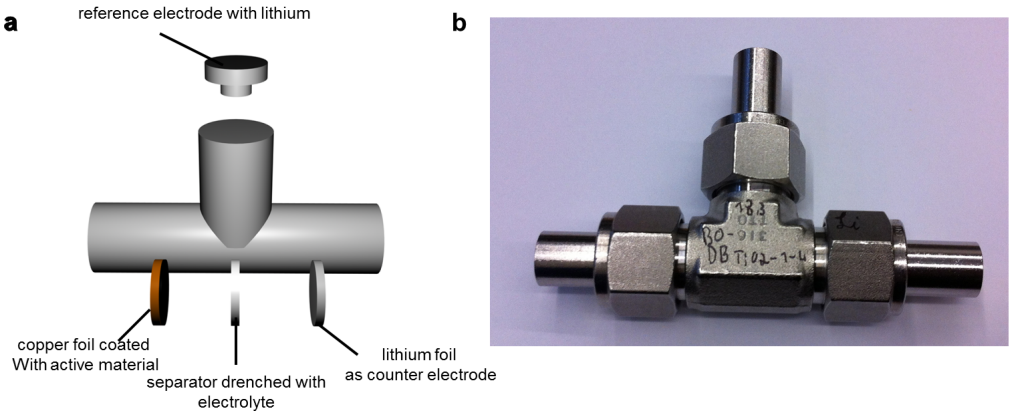

Figure 1: Scheme of a Swagelok cell set-up (a) and foto of an assembled Swagelok cell (b).

4.1.1 Carbon Coating of Titanium Dioxide Anatase Nanorods

The thermal carbon coating approach was first applied to TiO_2 anatase nanorods. TiO_2 is a beneficial material, as it enhances safety in batteries. As a carbon precursor polymer a block copolymer was synthesized by RAFT polymerization. First, the carbon precursor block was synthesized, which consists of polyacrylonitrile. Second, a reactive ester block is copolymerized using the polyacrylonitrile as a macro-chain transfer agent (macro-CTA). As an anchoring structure, catechol containing dopamine was chosen, since dopamine can be incorporated into the polymer by aminolysis of the reactive ester block.

The final carbon content after the pyrolysis can be influenced by the grafting density of the polymers. This grafting density can be varied either by the block length of the polyacrylonitrile block, as described in the following publication, as well as by the number of anchoring repeating units, which was investigated additionally to the data presented in the publication shown in Figure 2. Using an anchoring end-group results in only 8 wt.% loss during ther-

molysis (equivalent to the amount of chemisorbed polymer), whereas anchor blocks with 25 and 60 anchoring repeating units result in 13 wt.% and 14 wt.% loss. In all three cases the PAN block length was about 100 repeating units. Thus, the polymer content as well as the final carbon content can be controlled in a certain range by the variation of block lengths.

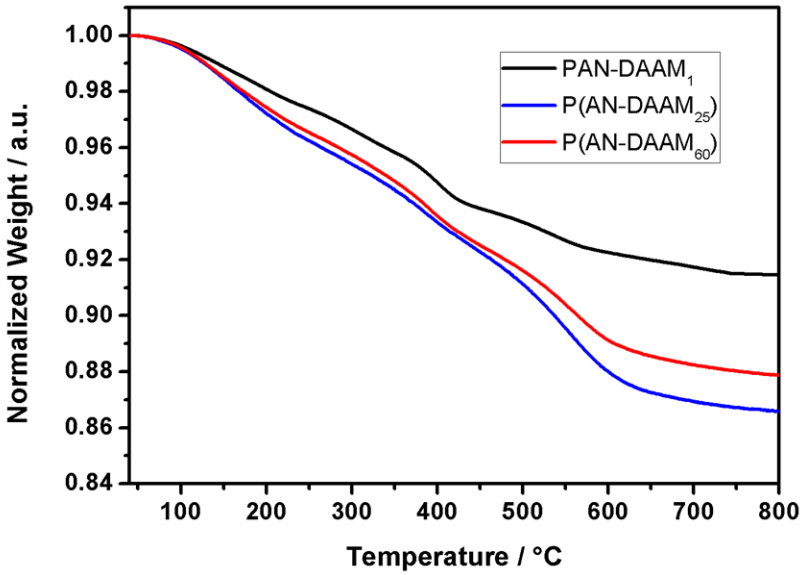

Figure 2: TGA data of grafted polymer under variation of the number of anchoring units.

The successful binding of the polymer onto nanoparticles can be further proven by light scattering, atomic force microscopy and dispersibility tests.

After pyrolysis at 700 °C, the presence of a carbon coating was detected by several methods, such as Raman spectroscopy, high resolution transmission electron microscopy (HRTEM) and thermo gravimetric analysis (TGA). The synthesis related results were published in the following article in Macromolecular Rapid Communication.

A detailed electrochemical characterization was conducted in Münster in cooperation with Dominic Bresser from the Passerini group and was published in Journal of Power Sources. These results prove an enhancement with respect to cycling stability and enhanced C-rate performance for coated particles compared to uncoated particles. More impressively, the coating could avoid a structural degradation of the nanoparticles, which was observed for uncoated particles by means of ex-situ X-ray diffraction. This degradation caused a dramatic

decay of the energy efficiency for uncoated particles, whereas the energy efficiency could be stabilized for coated particles up tp 100 cycles.

The results of the electrochemical characterization techniques, which are presented in the following two publications, suggest an increased electronic conductivity due to the carbon coating. However, the improved battery performance is just an indirect hint. Since conductivity is a major issue in this thesis and in order to prove an increased conductivity by the carbon coating in a macroscopic dimension, an electronic conductivity measurement on a powder of coated and uncoated TiO_2 nanoparticles as a function of an applied pressure was conducted in cooperation with BASF. This method allows the direct detection of the electric resistance of the sample, which can be transformed into electric conductivity. The results are shown in Figure 3. As expected, the coated particles exhibit an increased conductivity compared to the uncoated particles for all applied pressures, whereby at 500 bar the conductivity is $3.79 \cdot 10^{-6}$ S cm^{-1} for coated particles and $6.41 \cdot 10^{-7}$ S cm^{-1} for uncoated particles. Thus, at 500 bar the conductivity of coated particles is about 6 times higher than the conductivity of uncoated particles.

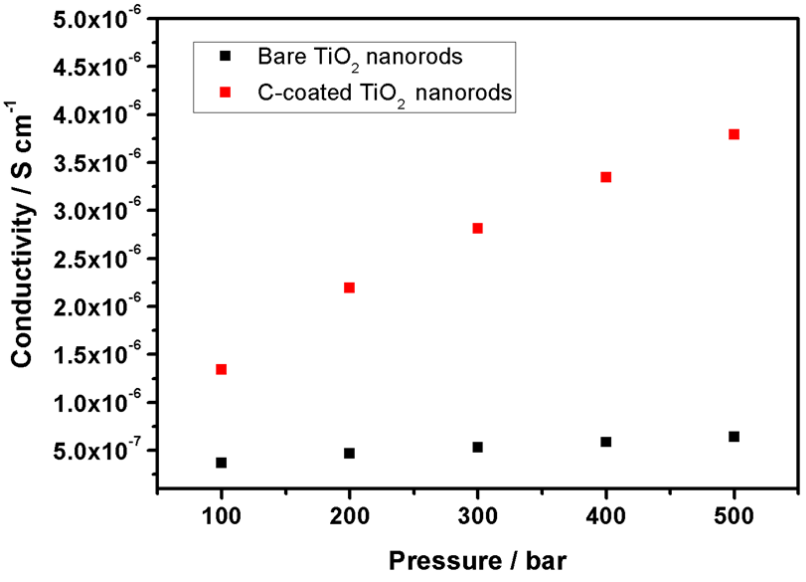

Figure 3: Conductivity measurements of carbon coated TiO_2 nanorods (red) and uncoated TiO_2 nanorods (black).

Muhammad Nawaz Tahir contributed to this work with the synthesis of the inorganic particles. The polymer synthesis and characterization, the hybridization as well as the characterization of the hybrid material was done by myself, whereas light scattering experiments were performed under the supervision of Karl Fischer. The electrochemical characterization of the material was conducted under the supervision of Dominic Bresser.

4.1.1.1 Publication in Macromolecular Rapid Communication, 2013, 34, 1693-1700

Polyacrylonitrile Block Copolymers for the Preparation of a Thin Carbon Coating Around TiO_2 Nanorods for Advanced Lithium-Ion Batteries

Bernd Oschmann, Dominic Bresser, Muhammad Nawaz Tahir, Karl Fischer, Wolfgang Tremel, Stefano Passerini, Rudolf Zentel.

Abstract

Herein, a new method for the realization of a thin and homogenous carbonaceous particle coating, made by carbonizing RAFT polymerization derived block copolymers anchored on anatase TiO_2 nanorods, is presented. These block copolymers consist of a short anchor block (based on dopamine) and a long, easily graphitizable block of polyacrylonitrile. The grafting of such block copolymers to TiO_2 nanorods creates a polymer shell, which can be visualized by atomic force microscopy (AFM). Thermal treatment at 700 °C converts the polyacrylonitrile block to partially graphitic structures (as determined by Raman spectroscopy), establishing a thin carbon coating (as determined by transmission electron microscopy, TEM, analysis). The carbon-coated TiO_2 nanorods show improved electrochemical performance in terms of achievable specific capacity and, particularly, long-term cycling stability by reducing the average capacity fading per cycle from 0.252 mAh g^{-1} to only 0.075 mAh g^{-1}.

1. Introduction

Lithium-ion batteries are currently considered to be one of the most promising electrochemical energy storage devices for future large-scale applications, for instance electric vehicles or stationary energy storage, as they provide superior energy and power densities and a suitable cycle life.[1] However, further improvements in terms of energy and power density are required for such applications, and thus current research activities are inter alia directed towards the search for new electrode active materials like, for instance, $LiFePO_4$, $Li_4Ti_5O_{12}$, or TiO_2.[2] Nevertheless, these materials generally suffer from a relatively low conductivity. In order to overcome this issue, nanostructuring, and thus increasing the electrode/electrolyte contact area and decreasing the diffusion and transport pathways for electrons and lithium ions, has turned out to be a successful strategy.[3] In addition, the application of carbonaceous secondary structures and coatings[3,4] results in an enhanced electronic conductivity and reduces the surface reactivity of nano-sized particles in contact with the electrolyte. Moreover, such coatings prevent the occurrence of surface defect induced structural disorder[5] and have led to a further improvement of the electrochemical performance of such nano-sized active materials. For these reasons, such a carbonaceous coating layer should homogeneously cover the surface of particles, while at the same time it should ideally be rather thin to allow easy diffusion of the lithium ions into the host structure.[6,7]

Polymers play a large role in modern batteries, usually as a solid or gel-type electrolyte[8] or as separator.[9] In addition, they have the potential to act as precursors for thin carbonaceous layers. To date, the realization of such an extremely thin and highly homogenous carbonaceous coating, as is needed for the applications discussed above, still remains a highly challenging issue.[7] Most of the present approaches are based on dispersing the particles within a solution containing the carbon precursor. However, this approach frequently does not result in a homogeneous coating but instead a rather random distribution of precursor on the nanoparticle

surfaces. Grafting precursor polymer to the surface of the nanoparticle would be advantageous in this context. Polyacrylonitrile (PAN) is a well-known graphitic precursor, which is also commercially used to prepare carbon fibers.[10,11] Through pyrolysis of this polymer at temperatures above 600 °C, graphitic structures can be achieved with high carbon yields, up to 50–60%, which underlines the excellent property of PAN as a graphitic precursor.[10,12,13] It is thus challenging to think about the realization of a thin carbon coating based on brushes of PAN grafted onto a nanoparticle surface. Herein, such an approach is reported, based on the graphitization of a block copolymer synthesized by RAFT polymerization, which can anchor onto a nanoparticle surface and can be pyrolyzed. Anatase TiO_2 nanoparticles were utilized as the active material, since they have already been extensively studied as an alternative anode material to avoid the severe safety issues related to the use of graphite anodes.[2,14] It is shown here that carbon-coated anatase TiO_2 nanorods, prepared according to this newly developed procedure, show increased specific capacities and a substantially enhanced cycling stability compared to uncoated TiO_2 nanorods.

2. Experimental Section

2.1 Materials

Dry *N,N*-dimethylformamide (DMF), dopamine hydrochloride, and nitrosonium tetrafluoroborate ($NOBF_4$) were purchased from Sigma Aldrich and used as received. Pentafluorophenyl acrylate and 2-dodecylsulfanylthiocarbonylsulfanyl-2-methyl propionic acid (DMP) were synthesized as described in the literature.[15] α,α-Azoisobutyronitrile (AIBN, Sigma Aldrich) was recrystallized from diethylether. Acrylonitrile (AN, Merck) was distilled before use to remove inhibitor. Titanium(IV)butoxide (TB, 97%), oleic acid (OLEA), and oleylamine (OM, 70–80%) were purchased from ACROS.

2.2 . Preparation of Poly(acrylonitrile-block-dopamineacrylamide)

First, the PAN macroinitiator bearing the trithiocarbonate endgroup was synthesized following a previously reported procedure.[16] This macroinitiator was used to prepare the P(AN-b-PFPA) block copolymer with a short PFPA block using a molar ratio of a PAN:PFPA mole ratio of 1:25. The reaction was conducted in DMF for 48 h at 70 °C and purified by precipitation in methanol. For the polymer analogous reaction, dopamine (40 eq) was added to P(AN-b-PFPA) dissolved in DMF. The reaction was stirred at 50 °C overnight and subsequently precipitated in methanol.

2.3 . Preparation and Surface Modification of TiO_2 Nanorods

The TiO_2 nanorods were synthesized by a method reported by Do and co-workers.[17] OLEA and oleylamine on the surface of the anatase nanorods were replaced by a ligand exchange reaction using nitrosonium tetrafluoroborate.[18] Afterwards, P(AN-b-DAAM) was added to the nanorods dispersed in DMF with a weight ratio of nanorod:polymer of 4:1. After purification by centrifugation the nanorods were dried under vacuum.

FT-IR:ν= 2929 (C–H valence band), 2862 (C–H valence band), 2242 (nitrile valence band), 1661 (NH amide band), 1520 cm^{-1} (NH deformation band). Before pyrolysis, 5 wt% of carbon particles were added.[19]

2.4. Pyrolysis and Reference Sample

The hybrid material was pyrolyzed in two steps under argon. First, the material was heated to 300 °C at a heating rate of 5 °C min^{-1} and kept for 240 min at this temperature. In a second step, the temperature was increased to 700 °C with a heating rate of 5 °C min^{-1} and kept constant for 90 min. For the reference electrode, OLEA-capped nanorods were treated with $NOBF_4$ as described in the literature to remove the electronically insulating OLEA coating.[18] Tetrafluoroborate anions were removed via centrifugation and dialysis in methanol.

2.5. Characterization

A Horiba Jobin Y LabRAM HR Spectrometer with a frequency doubled Nd:YAG laser

was used for performing Raman spectroscopy. High resolution transmission electron microscopy (HRTEM) was performed on a Tecnai F30 ST FEI, which was connected to an Oxford energy dispersive X-ray (EDX) spectrometer. For the investigation of the carbon-coated TiO_2 nanorods, a non-porous silicon window, not containing any carbon, was used. For electrochemical characterization, see the Supporting Information.

3. Results and Discussion

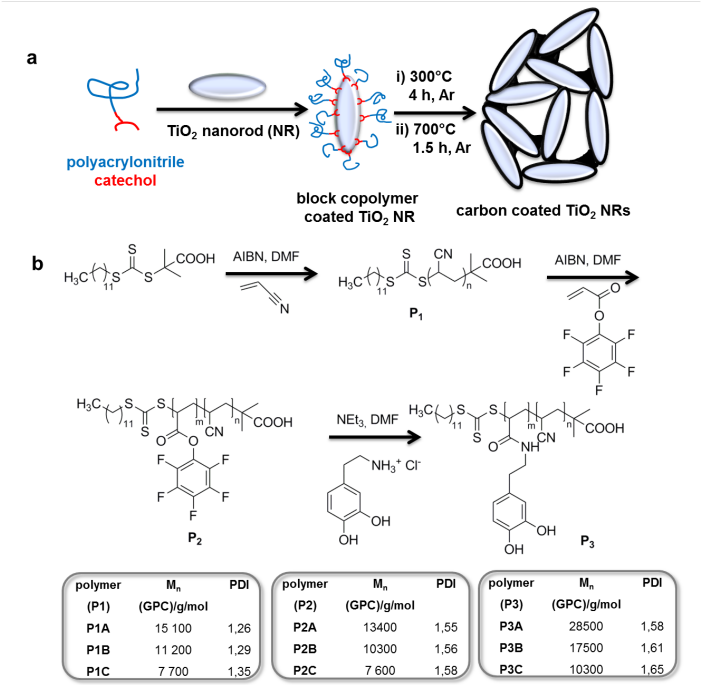

polymer (P1)	M_n (GPC)/g/mol	PDI
P1A	15 100	1,26
P1B	11 200	1,29
P1C	7 700	1,35

polymer (P2)	M_n (GPC)/g/mol	PDI
P2A	13400	1,55
P2B	10300	1,56
P2C	7 600	1,58

polymer (P3)	M_n (GPC)/g/mol	PDI
P3A	28500	1,58
P3B	17500	1,61
P3C	10300	1,65

Figure 1: (a) Schematic illustration of the surface modification using P(AN-b-DAAM) followed by a pyrolysis of the functionalized nanoparticles, resulting in carbon-coated TiO_2 nanorods. (b) Synthetic scheme for poly(acrylonitrile-b-dopamine acrylamide) (P(AN-b-DAAM)) derived from acrylonitrile and pentafluorophenol acrylate through RAFT polymerization followed by the polymer analogous conversion with dopamine.

Figure 1 a describes the newly introduced approach. It is based on PAN block copoly-

mers, which are made by RAFT polymerization and contain a short dopamine anchor block. They can be easily grafted onto the surface of metal oxide active material particles. After surface modification of the active material particles, the polymer coating is carbonized by thermal treatment as schematically illustrated in Figure 1 a.

3.1. Characterization of the Polymer and the Hybrid Material

To prepare the desired block copolymer bearing an anchor block and a graphitizable block, RAFT polymerization was applied (Figure 1 b) as a controlled radical polymerization in order to have access to well-defined polymers and block copolymers. Polyacrylonitrile (PAN) was chosen as a graphitizable block, because it is a well-known graphitic precursor, which is also commercially used to prepare carbon fibers.[10,11] By pyrolysis of this polymer at temperatures above 600 °C, graphitic structures can be achieved with high carbon yields (up to 50–60%), which underlines the excellent property of PAN as a graphitic precursor.[10,12,13] First, acrylonitrile was polymerized using 2-dodecylsulfanylthiocarbonylsulfanyl-2-methyl propionic acid (DMP) as a chain transfer agent (CTA) (see Figure 1 b). Based on the monomer to CTA ratio, polyacrylonitrile polymers (**P1 A-C**) of different molecular weight were synthesized following previously reported procedures.[16,20] After purification, the polymers in the **P1** series were used as a macro-CTA. For the second block, a reactive ester, pentafluorophenol acrylate (PFPA), was chosen as a monomer to prepare the first polyacrylonitrile block copolymers containing an active ester block P(AN-b-PFPA), labeled as P2 A-C . The molecular weight values of P2 as determined by GPC are virtually lower than those of the homopolymers because of the low solubility of the PFPA block in N,N-dimethylformamide (DMF),[21] which is needed to dissolve polyacrylonitrile (see Figure 1 b). By post-polymerization modification methods of the PFPA block with primary amines, many different functional structures can be introduced into the polymer, so that the approach presented here can be applied to a variety of further applications. In this case dopamine was chosen as it is re-

ported to coordinate effectively onto the surface of transition metal oxide nanoparticles.[22] Successful conversion at the post-polymerization step was determined by ^{1}H-NMR spectroscopy (the appearance of dopamine acrylamide signals) and ^{19}-F NMR (the disappearance of ^{19}F signals of PFPA; see Figure S1 and Figure S2a in the Supporting Information).[21] The dopamine containing block copolymers obtained, poly(acrylonitrile-b-dopamine acrylamide) (P(AN-b-DAAM)), were labeled as **P3 A-C**. Comparing the GPC elugrams of the **P1** homopolymers and the **P3** block copolymers, the shift of **P3** to a lower elution volume proves the successful synthesis of these block copolymers, as shown in Figure S2b in the Supporting Information. According to NMR spectroscopy, the length of the dopamine acrylamide block is about 5 repeating units. Using these materials, polymer coated TiO_2 nanoparticles were prepared. Here, nanorods were used because of their large surface to volume ratio and the short diffusion length for Li^+-ion insertion. Transmission electron microscopy (TEM) measurements performed on as-synthesized nanorods show the presence of anisotropic but uniform nanorods. A TEM image of such nanorods is shown in Figure 2 a as a representative example. The size distribution, obtained from TEM measurements, shows that the average length is around 30 nm and the average diameter is approximately 10 nm, which is comparable with an ideal diameter for lithium insertion of 8 nm.[23] According to the X-ray diffraction (XRD) pattern (Figure S3 in the Supporting Information), all observed reflections can be attributed to the anatase structure while no phase impurities are detectable. Due to the fact that the surface of the as-prepared nanorods is stabilized with oleic acid (OLEA) and oleylamine (OAm), these nanorods are soluble in nonpolar solvents like chloroform, dichloromethane, or hexane, whereas polyacrylonitrile is only soluble in polar solvents like DMF or DMSO. Therefore, the synthesized nanorods were phase transferred to DMF using nitrosonium tetrafluoroborate ($NOBF_4^-$) and functionalized using the block copolymer **P3**.[18]

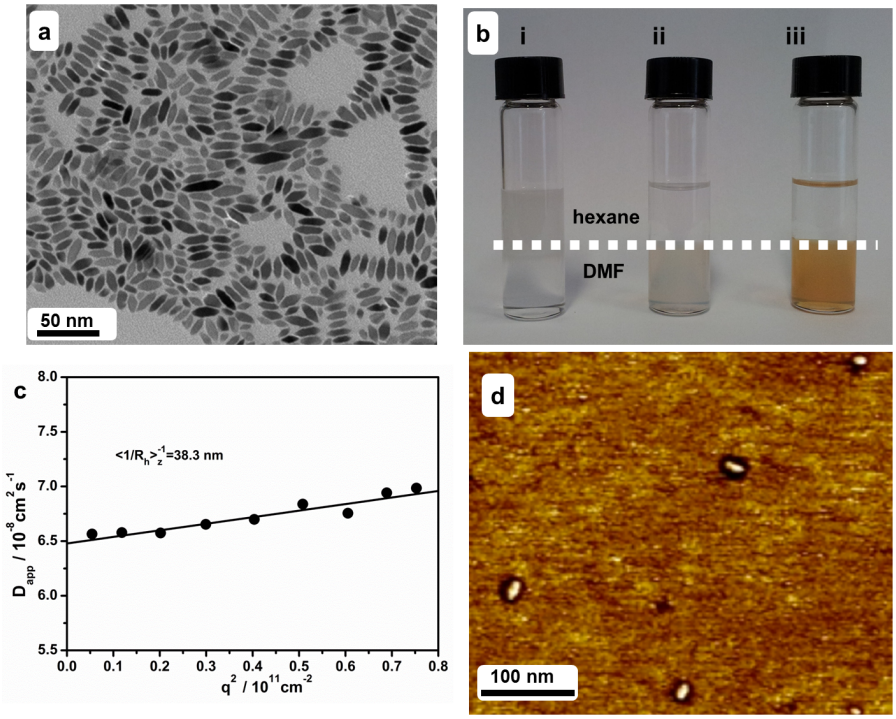

Figure 2: a) TEM image of as-prepared TiO_2 nanorods and b) picture showing the phase transfer of OLEA/OAm-capped nanorods (i) to DMF by surface modification with BF_4 (ii) and **P3** (iii). c) Dynamic light scattering of TiO_2 nanorods in solution functionalized with P(AN-b-DAAM) in DMF (5×10^{-3} M LiBr added, c(TiO_2 $\approx$ 4–5 mg ml^{-1}). d) AFM phase image of P(DEGMEM-b-DAAM)-functionalized TiO_2 nanorods showing a polymer corona around the inorganic nanorods.

The successful ligand exchanges and the bonding of the polymer onto the nanoparticle surface were proven by IR spectroscopy (Figure S4a in the Supporting Information). The phase transfer from hexane to DMF followed by the secondary modification with the synthesized block copolymer is demonstrated in Figure 2b. The obtained hybrid material was characterized by dynamic and static light scattering (DLS and SLS; R_g = 35.3 nm, R_h = 38.3 nm, Figure 2c and S4b in the Supporting Information). All methods give a comparable particle size. The angular dependence of the apparent diffusion coefficient shows a moderate angular dependence, which

excludes the formation of larger aggregates. A detailed discussion of the relation between the (number averaged) length of the nanorods, as obtained by TEM, and the (z-averaged) radii, obtained by static and dynamic light scattering, can be found in a previous publication, which reports TiO_2 nanoparticles coated with different block copolymers.[24] In order to visualize a polymer corona around the nanoparticle, atomic force microscopy (AFM) was applied. Since polyacrylonitrile is a quite hard polymer ($T_g \approx 73$ °C)[25] a contrast between PAN and TiO_2 is hard to visualize in the phase image. Instead of a polyacrylonitrile block, a softer polymer poly(diethylene glycol monomethyl ether) methacrylate (PDEGMEMA) block of similar chain length connected to a dopamine acrylamide block was then used. Due to its low glass transition temperature, around 0 °C, PDEGMEMA is quite soft and it is expected to show a contrast to TiO_2. Indeed, in the AFM phase image (see Figure 2 d) of the hybrid system consisting of TiO_2 nanorods and P(DEGMEMA-DAAM), a homogeneous polymer corona around the nanoparticles can be detected, proving the successful binding of the polymer resulting in a homogeneous coating. According to thermogravimetric analysis (TGA), polymer P3B binds most effectively to the TiO_2 nanoparticles corresponding to an organic material content of 16 wt% of the hybrid material (Figure S4c in the Supporting Information), which is equal to 100–150 polymer chains per TiO_2 nanorod. This polymer was used for further investigations.

3.2. Characterization of the Pyrolyzed Hybrid Material

After drying, the hybrid system was pyrolyzed in two steps. Higher carbon yields are achieved by pyrolysis of polyacrylonitrile if an intermediate stabilization step is performed to favor the formation of ladder structures (Figure S5a in the Supporting Information) prior to a further increase in the pyrolysis temperature.[13] Thus, in a first step, the sample was treated at 300 °C under argon for 4 h. In a second step, the sample was heated to 700 °C to obtain graphitic structures.[12] Temperatures higher than 700 °C cannot be employed to avoid the phase transition of anatase

to rutile (around 850 °C) or the formation of Magneli phases Ti_nO_{2n-1} (around 800 °C).[26] The color change of the sample from the original brown color, due to the bound dopamine, to black indicates macroscopically the desired carbonization of the grafted block copolymer (Figure S5a in the Supporting Information). The received carbon content was 8 wt%, as confirmed by TGA (Figure S5b). The presence of graphitically ordered carbon after pyrolysis was moreover proven by Raman spectroscopy. In the wavenumber range between 1100 cm^{-1} and 1700 cm^{-1}, in fact, the two characteristic graphitic bands, the G-band at 1584 cm^{-1} and the D-band at 1355 cm^{-1} , are observed (Figure 3 a).[27] The preservation of the anatase structure after pyrolysis was proven by means of XRD analysis (Figure S3 in the Supporting Information). The presence of the carbon coating was verified by energy dispersive X-ray spectroscopy (EDX) using scanning transmission electron microscopy (STEM). Figure 3b shows the results of EDX measurements taken from the sample, whereas the corresponding STEM image is shown in Figure S6a in the Supporting Information. The two marked areas of Figure S6a (i) and (ii) were investigated further by EDX. Carbon is detected on the nanorods, but not in the reference area (i) showing only the silicon based TEM window (Figure 3 b). Thus, the carbon in area (ii) is due to the carbonaceous, partially graphitic surface layer on the TiO_2 nanorods (Figure 3 b). Comparing high-resolution TEM (HRTEM) images of coated TiO_2 nanorods after pyrolysis and the as-synthesized nanorods (Figure 3c and 3d), a clear difference can be seen. For the uncoated TiO_2 nanorods there is a bare surface without any visible coating observed (Figure 3d), while for the coated TiO 2 nanorods after pyrolysis, a thin surface film in the range of 1 to 2 nm is apparently formed (Figure 3c).

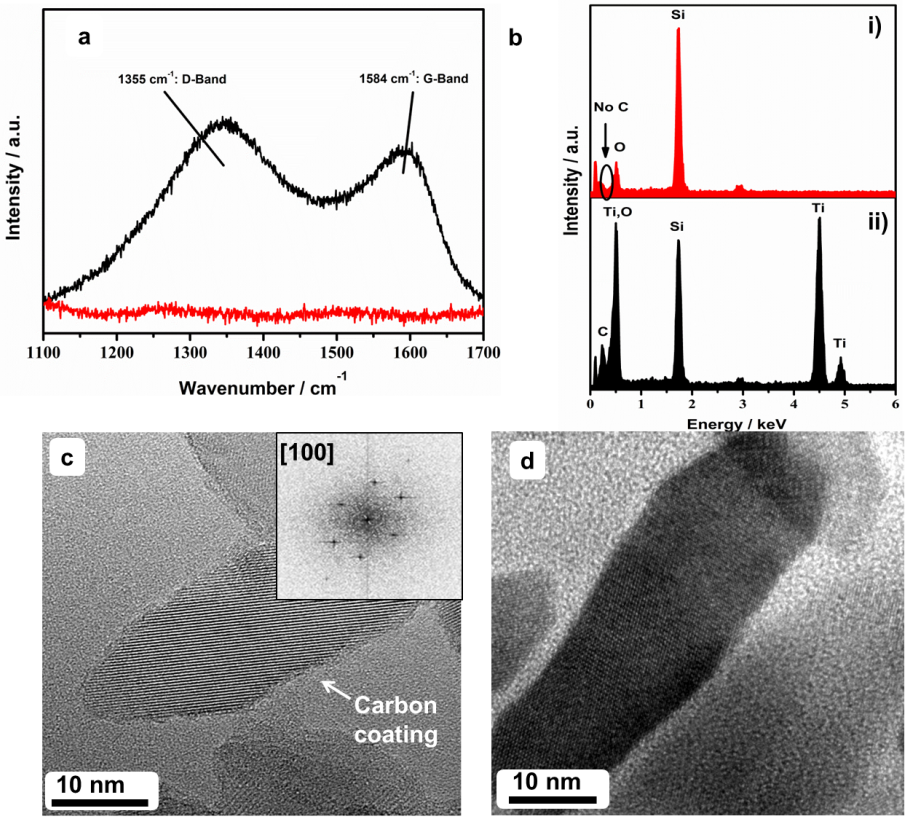

Figure 3: a) Raman spectra in the graphitic carbon region of the coated TiO_2 nanorods before (gray line) and after (black line) pyrolysis. b) EDX spectra of the TEM window only (i) as well as the TEM window covered by the TiO_2/C sample (ii). c) HRTEM image of carbon-coated TiO_2 nanorods with FFT (as an inset nanorods showing a thin carbonaceous layer surrounding the nanorods). d) HRTEM image of as-synthesized nanorods showing no coating layer on the particle surface.

The crystallinity and phase identity of the nanorods after pyrolysis were further confirmed by the fast Fourier transform (FFT) along the [100] direction, as shown in an inset in Figure 3 c. The distances calculated are in good agreement with the theoretical values of anatase reflection of the [100] zone. Summing up the results obtained for Raman, HRTEM, and EDX characterization, it is clear that the polymer film grafted to the titanium dioxide nanorods could be successfully converted into a

homogenous, thin, and partially graphitic carbonaceous surface film.

3.3. Electrochemical Characterization

Carbon-coated TiO_2 nanorods, referred to as TiO_2/C in the following text, were compared with non-coated TiO_2 nanorods (investigated for comparison), which are hereafter referred to as simply TiO_2. To allow a comparison with similar systems, a nanoparticulate conductive carbon was added as is commonly done to prepare lithium-ion electrodes.[28] For a better comparison, both samples contained the same overall carbon content (TiO_2/C: 10 wt% carbon coating and 10 wt% of conductive carbon; TiO 2 : 20 wt% of conductive carbon). The samples were characterized by galvanostatic cycling as presented in Figure 4 , applying a C rate of C/5 (corresponding to a specifi c current of about 34 mA g^{-1}) for the first three cycles and 1C (corresponding to 168 mA g^{-1}) for the following 247 cycles. For both applied specific currents, higher specific capacities can be achieved for TiO_2/C, as demonstrated in Figure 4. After 10 cycles, for example, a specific capacity of 190 mAh g^{-1} and 181 mAh g^{-1}, and after 250 cycles a capacity of 162 mAh g^{-1} and 106 mAh g^{-1}, was obtained for TiO_2/C and TiO_2, respectively. This result indicates the importance of a finely dispersed, percolating conductive network by combining the approach of a carbonaceous coating and the addition of nanoparticulate carbon rather than only adding an excessive amount of conductive carbon.[19] In fact, applying a carbonaceous coating on submicron-sized anatase TiO_2[29] or $Li_4Ti_5O_{12}$[30] particles was already reported to result in a substantially improved conductivity. Moreover, electrodes based on the carboncoated nanorods show a signifi cantly higher cycling stability and a capacity fading of only 0.075 mAh g^{-1} per cycle for the cycles from 50 to 250, while electrodes based on non-coated TiO_2 show a capacity fading of 0.252 mAh g^{-1} per cycle. Indeed, further improvement regarding the electrochemical performance of the coated sample was observed, which is, however, beyond the scope of this article and thus is reported in detail elsewhere.[5]

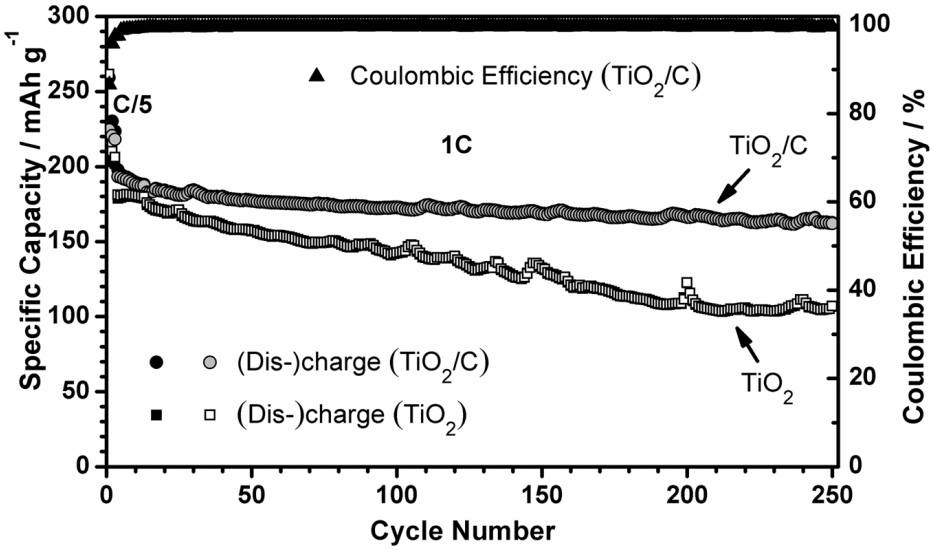

Figure 4: a) Comparison of electrodes made using uncoated (TiO_2) and carbon-coated (TiO_2/C) anatase nanorods subjected to galvanostatic cycling (1C = 168 mA g^{-1}). For reasons of clarity only, the coulombic efficiency for carbon-coated TiO_2 nanorods is presented.

4. Conclusion

In conclusion, a carbon coating process is presented here, based on the carbonization of PAN-based block copolymers (derived by RAFT polymerization) anchored onto anatase TiO_2 nanorods. This carbon coating process resulted in the formation of a homogenous, thin, and partially graphitic carbonaceous surface film. The proposed process can also be applied to other inorganic lithium-ion anode and cathode materials. Electrochemical characterization confirmed that the introduced coating enables a significantly enhanced electrochemical performance of anatase TiO_2 nanorods as an anode material in lithium-ion cells with respect to the achievable specific capacity and, in particular, the longterm cycling stability.

Supporting Information

Supporting Information is available from the Wiley Online Library or from the author.

Acknowledgements:

B.O. would like to thank the “Fonds der Chemischen Industrie” for financial support (stipend). Furthermore, all authors would like to thank Dr. U. Kolb and R. Branscheid for performing HRTEM analysis. Moreover, S.P. and D.B. would like to acknowledge fi nancial support from the European Commission within the AMELIE project (265910) and the ORION project (229036) under the Seventh Framework Programme (7th FWP).

Received: July 10, 2013; Revised: June 9, 2013; Published online: October 2, 2013; DOI: 10.1002/marc.201300531 Keywords: carbon coating ; lithium-ion batteries ; polyacrylonitrile ; RAFT-polymerization ; TiO_2 nanorods

Supporting Information

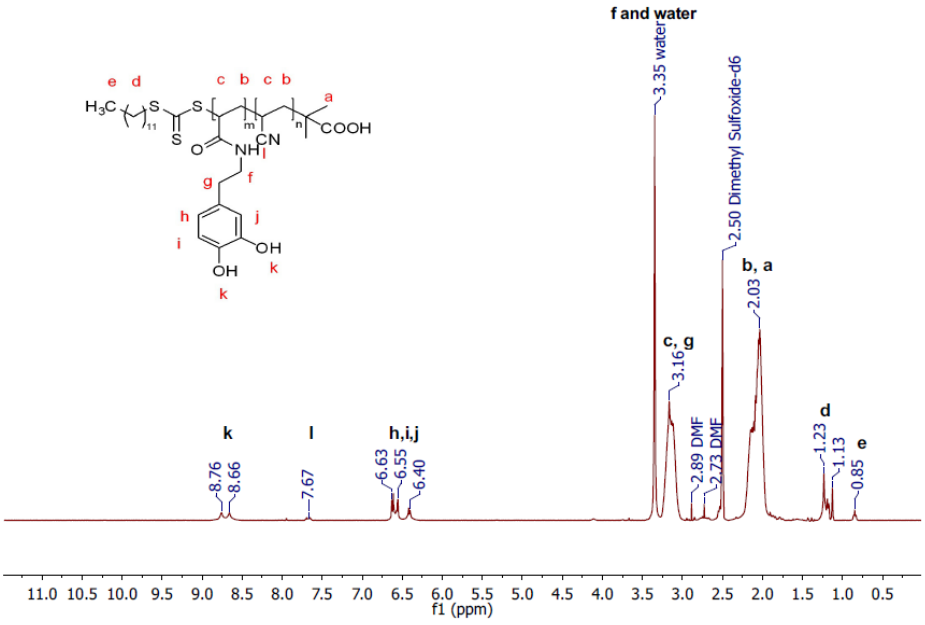

Figure S 1: ^{1}H-NMR of P(AN-b-DAAM) after work-up.

^{1}H-NMR (DMSO-d6, 400 MHz): δ[ppm] =8,71 (br, OH of dopamine); 7,67 (s, NH of dopamine); 6.40 to 6.62(br, ArH of dopamine); 3.0 to 3.2 (br; CH of polymer main chain); 2.0 to 2.2 (br, CH_2 of polymer main chain); 1.13-1.23 (br, S-(CH_2)11-CH3); 0,85 (tr, S-(CH_2)11- CH_3).

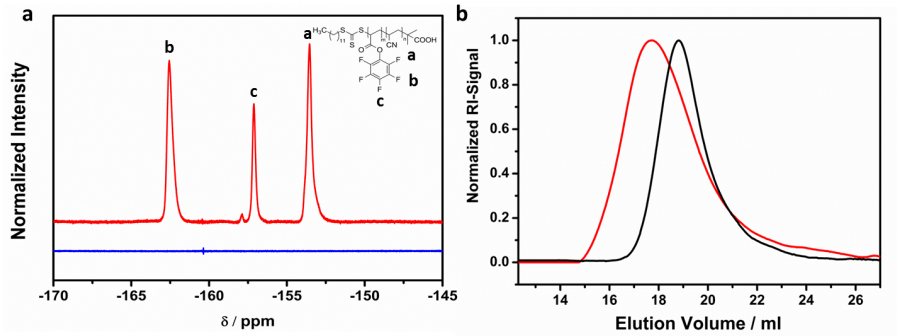

Figure S 2: ^{19}F-NMR spectrum (a) of P(AN-b-PFPA) (red) showing three broad peaks, which are typical for a PFPA polymer block, and of P(AN-b-DAAM) (blue) showing no peak due to the absence of fluorine in this polymer. GPC elugram of P1B (black) and P3B (red) showing a shift to lower elution volume of the block copolymer (b), thus indicating the successful block copolymer synthesis.

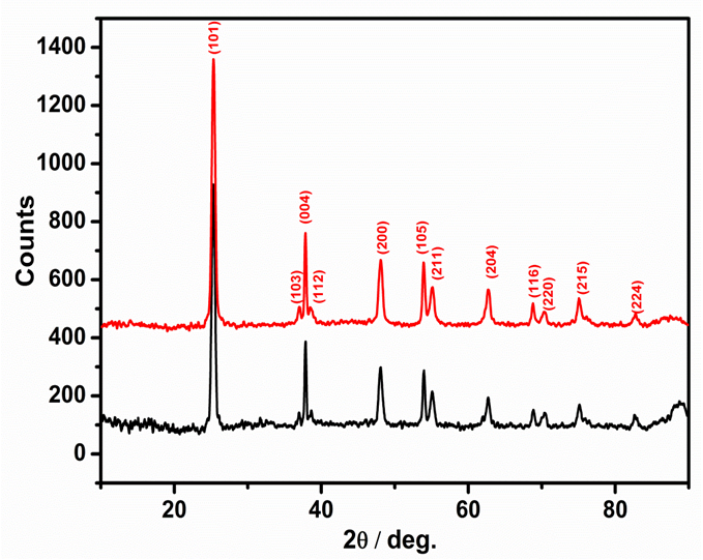

Figure S 3: XRD patterns of TiO_2 nanorods before (red pattern) and after (black pattern) pyrolysis.

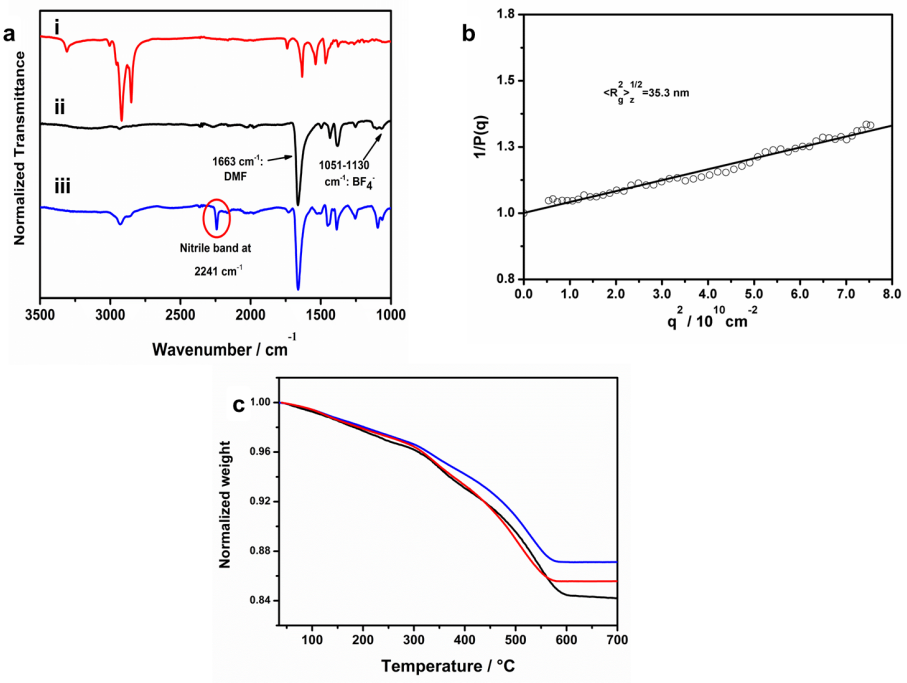

Figure S 4: a) IR data of i) as prepared nanorods functionalized with OLEA and OAm, ii) surface modified nanorods functionalized with DMF and BF_4^- and iii) nanorods functionalized with P(AN-b-DAAM) showing the presence of a nitrile band at 2241 cm^{-1}. Static light scattering (b) of TiO_2 nanorods in solution functionalized with P(AN-DAAM) in DMF ($5*10^{-3}$ M LiBr added, c(TiO_2≈ 4-5 mg/ml). c) TGA of TiO_2 nanorods coated with P3A (red), P3B (black) and P3C (blue).))

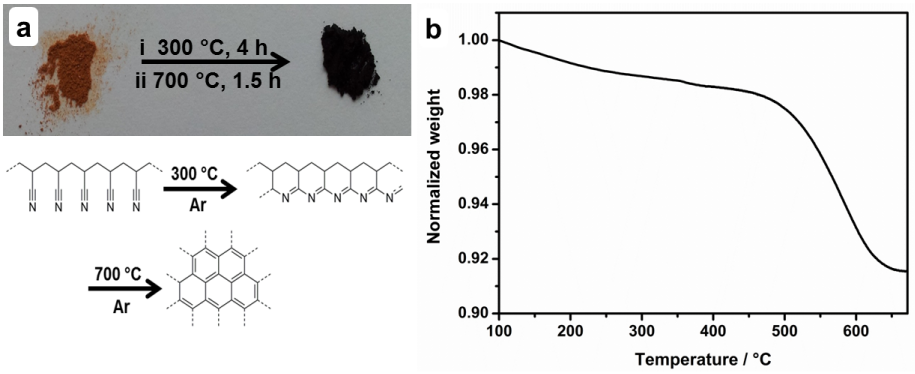

Figure S 5: a) Photo of the functionalized TiO_2 nanorods before (left powder) and after (right powder) pyrolysis (top) and scheme of the structural changes taking place upon pyrolysis of PAN (bottom). TGA of carbon-coated TiO_2 nanorods after pyrolysis (b) showing a weight loss of 8 wt%, indicating the amount of remaining carbonaceous material which remained after pyrolysis (the sample contained 16 wt% of block copolymer prior to this step).

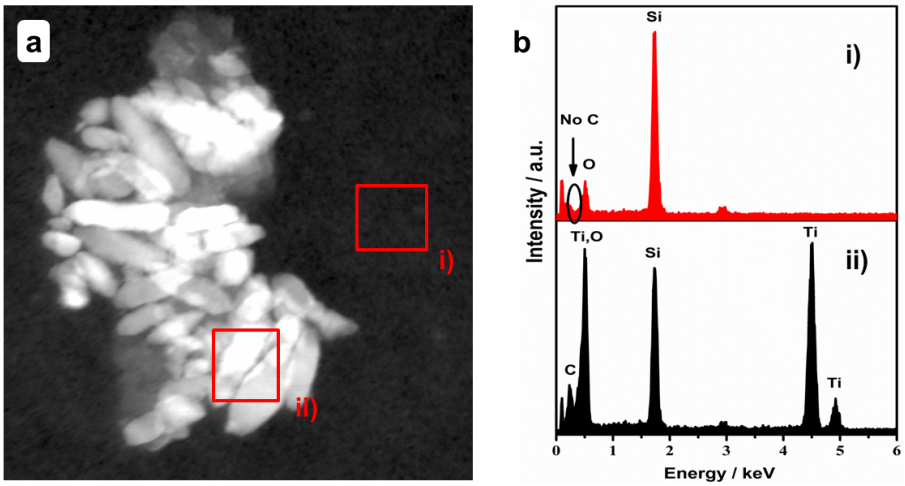

Figure S 6: c) STEM image of pyrolyzed TiO_2 nanorods and d) resulting EDX data for the areas i) and ii).

Electrochemical Characterization:

Electrodes based on carbon-coated anatase TiO_2 nanorods were prepared as follows:

Sodium carboxymethyl cellulose (CMC, Walocel CRT 2000PA, Dow Wolff Cellulosics) was dissolved in deionized water to obtain a 1.25 wt% solution. Subsequently, the carbon-coated TiO_2 nanorods and Super C65 were added. The resulting mixture was homogenized using a planetary ball mill (Vario-Planetary Mill Pulverisette 4, FRITSCH) set at 800 rpm for 2 h. The obtained slurry was coated on dendritic copper foil (SCHLENK) with a wet film thickness of 130 μm and dried at room temperature overnight. Disc electrodes with a diameter of 12 mm were punched and dried overnight at 120 °C under vacuum. The content of active material on the disc electrode ranged between 1.6 and 2.0 mg cm^{-2}. The electrodes had a final composition of 75 wt% of TiO_2, 20 wt% of carbon (comprising 5 wt% of Super C65® resulting from the previous processing, 10 wt% of carbon from the carbonization of the polymer as confirmed by TGA experiments under oxygen, and 5 wt% of Super C65® added upon the electrode preparation), as well as 5 wt% of CMC. Reference electrodes containing non-coated anatase nanorods were prepared analogously. For comparison reasons the amount of Super C65® added during the electrode preparation was 20 wt%. The active material mass loading ranged from 1.7 to 2.1 mg cm^{-2}. Cell assembling using Swagelok™-type cells was carried out in an MBraun glove box with an oxygen and water content below 0.5 ppm. Lithium metal foil (Rockwood Lithium, battery grade) was used as counter and reference electrode. Polypropylene fleeces (Freudenberg FS2190), drenched with the electrolyte (1M $LiPF_6$ in a 3:7 (vol) mixture of ethylene carbonate and diethyl carbonate, UBE) were used as separator. Galvanostatic cycling was conducted in a potential range of 3.0 V to 1.2 V vs. Li/Li^+ using a Maccor Battery Tester 4300.

Further characterization methods:

NMR spectra were obtained by means of a Bruker ARX 400. Thermogravimetric analysis (TGA) was carried out by means of a Perkin Elmer Pyris 6 instrument under oxygen atmosphere. Gel permeations chromatography (GPC) was recorded with

DMF as a solvent. The detector system contained refractive index (Agilent) and UV-vis (Agilent) units. The calibration was performed using polystyrene standards purchased from Polymer Standard Services.

FTIR spectroscopy was performed using a Jasco FT/IR 4100 spectrometer with an ATR unit. The as-prepared and pyrolyzed nanorods were investigated by XRD analysis conducted on a Siemens D5000 using Cu-K-alpha radiation.

References

[1] a) M. Armand, J.-M. Tarascon, *Nature* 2008, 451, 652; b) B. Scrosati, J. Garche, *J. Power Sources 2010*, 195, 2419.

[2] M. Wagemaker, F. M. Mulder, *Acc. Chem. Res.* 2012, 4 , 1206.

[3] P. G. Bruce, B. Scrosati, J.-M. Tarascon, *Angew. Chem. Int. Ed.* 2008, 47, 2930.

[4] A. S. Aricò, P. Bruce, B. Scrosati, J.-M. Tarascon, W. van Schalkwijk, *Nat. Mater.* 2005, 4, 366.

[5] D. Bresser, B. Oschmann, M. N. Tahir, W. Tremel, R. Zentel, S. Passerini, *J. Power Sources* 2013, DOI: 10.1016/j.jpowsour.2013.10.013

[6] N. Ravet, J. B. Goodenough, S. Besner, M. Simoneau, P. Hovington, M. Armand, The Electrochemical Society and The Electrochemical Society of Japan Meeting Abstracts, The Electrochemical Society, Honolulu, HI, 1999, 2, 127.

[7] J. Wang, X. Sun, *Energy Environ. Sci.* 2012, 5, 5163.

[8] a) M. B. Armand, *Annu. Rev. Mater. Sci.* 1986, 16, 245; b) W. H. Meyer, *Adv. Mater.* 1998, 10, 439; c) J. R. MacCallum, C. A. Vincent, Polymer electrolyte reviews, *Elsevier Applied Science*, London, 1989; d) J. Song, Y. Wang, C. Wan, J. Power Sources 1999, 77, 183.

[9] a) P. Arora, Z. Zhang, *Chem. Rev.* 2004, 104, 4419; b) S. S. Zhang, *J. Power Sources 2007*, 164 , 351 ; c) C. Orendorff, *The Electrochemical Society – Interface* 2012, Summer 61.

[10] M. Rahaman, A. Ismail, A. Mustafa, *Polym. Degrad. Stabil.* 2007, 92, 1421.

[11] H. M. Ezekiel, R. G. Spain, *J. Polym. Sci., Part C: Polym. Symp.* 1967, 19, 249.

[12] H. Meier, H. Bäßler, Organic Semiconductors: Dark and photoconductivity of organic solids, Verlag Chemie, Weinheim, 1974, 661 pages.

[13] P. Bajaj, A. K. Roopanwal, *J. Macromol. Sci. C.* 1997, 37, 97.

[14] a) S.-T. Myung, N. Takahashi, S. Komaba, C. S. Yoon, Y.-K. Sun, K. Amine, H. Yashiro, *Adv. Funct. Mater.* 2011, 21, 3231; b) T. Fröschl, U. Hörmann, P. Kubiak, G. Kucerová, M. Pfanzelt, C. K. Weiss, R. J. Behm, N. Hüsing, U. Kaiser, K. Landfester, M. Wohlfahrt-Mehrens, *Chem. Soc. Rev.* 2012 , 41, 5313; c) C. Jiang, J. Zhang, *J. Mater. Sci. Technol.* 2012, 29, 97.

[15] a) M. Eberhardt, R. Mruk, R. Zentel, P. Théato, *Eur. Polym. J.* 2005, 41, 1569; b) J. T. Lai, D. Filla, R. Shea, *Macromolecules*, 2002, 35, 6754.

[16] A. Aqil, C. Detrembleur, B. Gilbert, R. Jérôme, C. Jérôme, *Chem. Mater.* 2007, 19, 2150.

[17] C .-T. Dinh, T.-D. Nguyen, F. Kleitz, T.-O. Do, *ACS Nano* 2 009, 3, 3737.

[18] A. Dong, X. Ye, J. Chen, Y. Kang, T. Gordon, J. M. Kikkawa, C. B. Murray, *J. Am. Chem. Soc.* 2011 , 133 , 998.

[19] D. Bresser, E. Paillard, E. Binetti, S. Krueger, M. Striccoli, M. Winter, S. Passerini, *J. Power Sources* 2012, 206, 301.

[20] a) C. Tang , T. Kowalewski, K. Matyjaszewski, *Macromolecules* 2003, 36, 8587; b) X.-H. Liu, G.-B. Zhang, X.-F. Lu, J.-Y. Liu, D. Pan, Y.-S. Li, *J. Polym. Sci., Part A: Polym. Chem.* 2006, 44, 490.

[21] L. Nuhn, M. Hirsch, B. Krieg, K. Koynov, K. Fischer, M. Schmidt, M. Helm, R. Zentel, *ACS Nano* 2012, 6, 2198.

[22] a) M. Zorn, R. Zentel, *Macromol. Rapid Commun.* 2008, 29, 922 ; b) M. N. Tahir, N. Zink, M. Eberhardt, H. A. Therese, S. Faiss, A. Janshoff, U. Kolb, P. Theato, W. Tremel, *Small* 2007, 3, 829; c) M. I. Shukoor, F. Natalio, V. Ksenofontov, M. N. Tahir, M. Eberhardt, P. Theato, H. C. Schröder, W. E. G. Müller, W. Tremel, *Small* 2007, 3, 1374.

[23] M. Wagemaker, W. J. H. Borghols, F. M. Mulder, *J. Am. Chem. Soc.* 2007, 129,

4323.

[24] S. Meuer, K. Fischer, I. Mey, A. Janshoff, M. Schmidt, R. Zentel, *Macromolecules* 2008, 41, 7946.

[25] J. J. Keavney, E. C. Eberlin, *J. Appl. Polym. Sci.* 1960, 3, 47.

[26] a) Y. Chen, K. S. Kang, K. H. Yoo, N. Jyoti, J. Kim, *J. Phys. Chem. C.* 2009, 113, 19753; b) M. Toyoda, T. Yano, B. Tryba, S. Mozia, T. Tsumura, M. Inagaki, *Appl. Catal. B: Environ.* 2009, 88, 160.

[27] a) F. Tuinstra, *J. Chem. Phys.* 1970, 3, 1126; b) A. C. Ferrari, J. Robertson, *Phys. Rev. B.* 2000, 61, 14095.

[28] V. Palomares, A. Goñi, I. G. de Muro, I. de Meatza, M. Bengoechea, I. Cantero, T. Rojo, *J. Power Sources* 2010, 195, 7661.

[29] J. Moskon, R. Dominko, R. Cerc-Korosec, M. Gaberscek, J. Jamnik, *J. Power Sources* 2007, 174, 683.

[30] G.-N. Zhu, C.-X. Wang, Y.-Y. Xia, *J. Electrochem. Soc.* 2011, 158, A102.

4.1.1.2 Publication in Journal of Power Sources 2014, 248, 852

Stabilizing nanostructured lithium insertion materials via organic hybridization: A step forward towards high-power batteries

Dominic Bresser, Bernd Oschmann, Muhammad Nawaz Tahir, Wolfgang Tremel, Rudolf Zentel, Stefano Passerini.

Abstract

Herein, we present the electrochemical characterization of carbon-coated TiO_2 nanorods, obtained by carbonizing RAFT (reversible addition fragmentation chain transfer) polymerization derived block copolymers anchored on anatase TiO_2 nanorods. These carbon-coated TiO_2 nanorods show an improved electrochemical performance in terms of first cycle reversibility, specific capacity, cycling stability, and high rate capability. More importantly, however, the structural disordering observed in the uncoated TiO_2 nanorods by means of galvanostatic and potentiodynamic cycling as well as ex situ XRD analysis, does not occur for the carbon-coated material. Preventing this structural disordering does not only result in a stabilized cycling performance but, moreover, in substantially enhanced energy storage efficiency (86% vs. only 68% at the 100th cycle) due to the preserved characteristic potential profile of anatase TiO_2.

1. Introduction

Lithium-ion batteries are currently considered as one of the most promising electrochemical energy storage devices for future large-scale applications, as for instance electric vehicles [1-3]. However, beside improvements related to their energy density, current research activities focus on further advances of the obtainable power of such energy storage devices. In fact, the (dis-) charge capability of graphite, the state-of-the-art anode material is inherently limited by the release of the Li^+ solvation shell upon the intercalation of lithium ions through the initially formed solid electrolyte interphase (SEI) [4-6] as well as its very low operational potential and the concomitant safety issue of lithium plating [7,8]. Accordingly, alternative anode materials are investigated offering higher lithium ion (de-)insertion potentials and thus preventing the formation of an SEI layer as well as the risk of metallic lithium deposition at elevated charge/discharge rates. Titanium oxides, as for instance $Li_4Ti_5O_12$ (LTO) or different polymorphs of TiO_2, have gathered a wide interest [9-16] since such materials offer decent specific capacities, due to their higher density with respect to graphite, and lithium (de-)insertion occurs at potentials within the electrochemical stability window of commonly used organic carbonate-based electrolytes. While LTO is already comprised in commercial lithium-ion batteries [2], anatase TiO_2 is certainly a very attractive alternative due to its natural abundance, its already available large-scale production, such as pigments for the paint industry and dye-sensitized solar cells [17-19], as well as its theoretically higher specific capacity (335 mAh g^-1 vs. 175 mAh g^{-1} for LTO). However, micro-sized anatase TiO_2 severely suffers of limited specific capacities especially at high rates [20-22]. Nanostructuring of such active material particles showed substantial improvements in terms of achievable specific capacity, due to the increasing capacity contribution resulting from a second phase formation, which occurs only at the particle surface [23-26]. The high rate capability is also improved by an increasing solid solution domain [24-27], a generally reduced lithium ion and electron diffusion and trans-

port pathways and an increased electrode/ electrolyte contact area [28,29]. Further improvement was achieved by embedding such nanoparticles in carbonaceous host matrices or applying a carbon coating layer in order to enhance the electronic conductivity of such mostly insulating active material [30]. Wang et al. [31], for instance, investigated self-assembled TiO_2-graphene hybrid nanostructures, showing enhanced rate performance, i.e., more than 100 mAh g^{-1} at C rates as high as 30C. Fu et al. [32], Das et al. [33], or Cao et al. [34] followed a rather facile approach using sucrose or glucose as carbon precursor, while Thackeray and co-workers [35] reported an in situ carbon coating procedure utilizing titanium (IV) oxyacetyl acetonate as TiO_2 and carbon precursor and a specially designed autogenic reactor. Using the oleic acid capping agent to form a carbonaceous coating layer on TiO_2 nanorods, Bresser et al. [26] obtained an advanced rate performance, particularly when only the charge (delithiation) rate was increased, and high specific capacities of more than 250 mAh g^{-1}, depending on the cathodic cut-off potential. However, it appears noteworthy that this list of anatase TiO_2-carbon heterogeneous secondary structures presents only a brief overview on previously reported work and is certainly not exhaustive. Generally, for active materials storing lithium ions by insertion mechanism, as inter alia anatase TiO_2, thus undergoing relatively low volume changes upon reversible lithium uptake, homogenous and rather thin coating layers are preferable. This allows an improved electron transport, while at the same time lithium ion diffusion into the active material particles is not slowed down [36], thus resulting in an improved high rate capability of such electrode materials [37]. Very recently, we reported a new approach for the realization of such a carbon coating based on the carbonization of a block copolymer anchored onto the nanoparticles surface and synthesized by RAFT (reversible addition fragmentation chain transfer) polymerization (Fig. 1), showing an improved cycling stability and reduced capacity fading per cycle relatively to the uncoated TiO_2 nanorods [38]. Herein, we will present a detailed and extended electrochemical characterization of these carbon-coated anatase

TiO_2 nanorods, showing their advanced high rate capability, specific capacity, cycling stability, and first cycle reversibility relatively to the uncoated TiO_2 nanorods. Even more remarkably, however, it will be shown that the application of such a carbon coating suppresses a continuously progressing structural disorder observed in uncoated anatase nanorods by means of galvanostatic and potentiodynamic cycling as well as ex situ XRD analysis of cycled electrodes. This structural disordering does not only result in inferior capacity retention but moreover in a substantially reduced energy storage efficiency caused by continuous shortening of the characteristic potential plateau upon lithium (de-)insertion, which is to the best of our knowledge herein investigated and discussed for the first time.

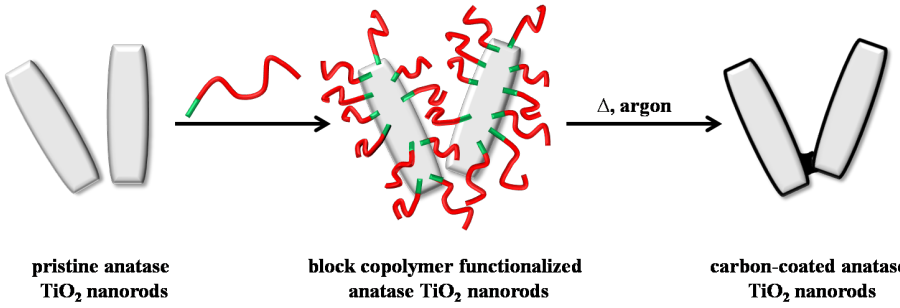

Figure 1: Schematic illustration of the carbon coating approach: as-synthesized TiO_2 nanorods (left) are functionalized by grafting a block copolymer (center), which is subsequently carbonized by a thermal treatment at 300 °C for 4 h and at 700 °C for 1.5 h under argon, resulting in a thin and homogenous carbon coating (right).

2. Experimental section

2.1. Synthesis of carbon-coated and uncoated anatase TiO_2 nanorods

The synthesis of carbon-coated and uncoated anatase TiO_2 nanorods was very recently described in detail by Oschmann et al. [38]. In brief, oleic acid (OLEA, Acros Organics)/oleylamine (OAM, Acros Organics) capped anatase TiO_2 nanorods were synthesized according to a solvothermal method recently reported by Dinh

et al. [39], using titanium butoxide (Acros Organics) as precursor and water vapor as hydrolysis agent. OLEA and OAM were subsequently replaced by tetrafluoroborate (BF_4^-), using nitrosonium tetrafluoroborate ($NOBF_4$, SigmaeAldrich) in dichloromethane solution, according to a ligand-exchange reaction reported by Dong et al. [40]. For the preparation of reference electrodes based on uncoated TiO_2 nanorods, BF_4^- was removed by means of centrifugation and dialysis in methanol. For the preparation of carbon-coated TiO_2 nanorods, the BF_4^--capped nanorods were dispersed in N,N-dimethylformamide (DMF) and mixed with the RAFT (reversible addition fragmentation chain transfer) polymerization-derived block copolymer poly(acrylonitrile-b-dopamine acrylamide) (P(AN-b- DAAM)), comprising polyacrylonitrile (PAN) as carbon precursor and dopamine as anchor block. The polymer to TiO_2 ratio was 1:4. Subsequently, the block copolymer-functionalized TiO_2 nanorods were purified via centrifugation and dried under vacuum. For the carbonization of the block copolymer, the functionalized nanorods were thermally treated under argon (for 240 min at 300 °C and for 90 min at 700 °C; heating rate: 5 °C min^{-1}).

2.2. Morphological and structural characterization The structure of uncoated and carbon-coated anatase TiO_2 nanorods was investigated by means of X-ray diffraction (XRD) analysis using a Siemens D5000 (Cu-Kα radiation, 0.154 nm). Raman spectroscopy was performed by means of a Horiba Jobin Y LabRAM HR Spectrometer, equipped with a frequency doubled Nd:YAG laser. Transmission electron microscopy (TEM) and high resolution transmission electron microscopy (HRTEM) analysis of carbon-coated and uncoated TiO_2 nanorods was conducted using a Tecnai F30 ST FEI. For TEM and HRTEM analysis, the studied samples were dispersed on a nonporous, carbon-free silicon-based sample holder. Ex situ XRD analysis of galvanostatically and potentiodynamically cycled electrodes was carried out using a Bruker D8 Advance (Cu-Kα radiation, 0.154 nm). The patterns were aligned according to the major (101) reflection of anatase TiO_2.

2.3. Electrochemical characterization

Electrodes based on carbon-coated anatase TiO_2 (and for comparison reasons, uncoated TiO_2) nanorods were prepared according the following procedure: Sodium carboxymethyl cellulose (CMC, Walocel CRT 2000PA, Dow Wolff Cellulosics) was dissolved in deionized water (1.25 wt.%). Subsequently, the carbon-coated (and uncoated) TiO_2 nanorods and Super C65 were added. The resulting mixture was homogenized by means of a planetary ball mill (Vario-Planetary Mill Pulverisette 4, FRITSCH) for 2 h set at 800 rpm. The obtained electrode paste was coated on dendritic copper foil (SCHLENK) with a wet film thickness of 130 mm and dried at ambient temperature for around 12 h. Disc electrodes with a diameter of 12 mm were punched and dried for about 24 h at 120 °C under vacuum. The content of active material on the disc electrodes was in a range of 1.6-2.0 mg cm^{-2} for carbon-coated TiO_2 and in a range of 1.7-2.1 mg cm^{-2} for uncoated TiO_2 nanorods. Electrodes based on carbon-coated TiO_2 nanorods had a final composition of 75 wt.% of TiO_2, 5 wt.% of CMC, and 20 wt.% of carbon (5 wt.% of Super C65 resulting from the previous processing, 10 wt.% of carbon coating as confirmed by TGA under O^{-2}, and 5 wt.% of Super C65 added later upon the preparation of the electrodes). Reference electrodes based on uncoated TiO_2 nanorods were prepared replacing the carbon content of the coating layer by additional Super C65, which was added upon the electrode preparation. Swagelok-type cells were assembled in a MBraun glove box with an O_2 and H_2O content of less than 0.5 ppm. Polypropylene fleeces (Freudenberg FS2190), drenched with the utilized electrolyte (1 M $LiPF_6$ in a 3:7 volume mixture of ethylene carbonate and diethyl carbonate, UBE) were used as separator. Since lithium foil (Rockwood Lithium, battery grade) was used as counter and reference electrodes, all potential values given in this manuscript refer to the Li/Li^+ reference couple. Galvanostatic cycling was carried out by means of a Maccor Battery Tester 4300. An applied C rate of 1C corresponds to an applied specific current

of 168 mA g^{-1}, considering x = 0.5 as the reference limit for the insertion reaction: TiO_2 + x(Li^+ + e^-) / Li_xTiO_2. Cyclic voltammetry was performed utilizing a VMP3 potentiostat (BioLogic), applying a scan rate of 0.1 mV s^{-1}.

3. Results and discussion

3.1. Morphological and structural characterization

In a first step, both samples uncoated and carbon-coated TiO_2 nanorods were investigated by means of XRD in order to confirm the preservation of the anatase structure (Fig. 2).

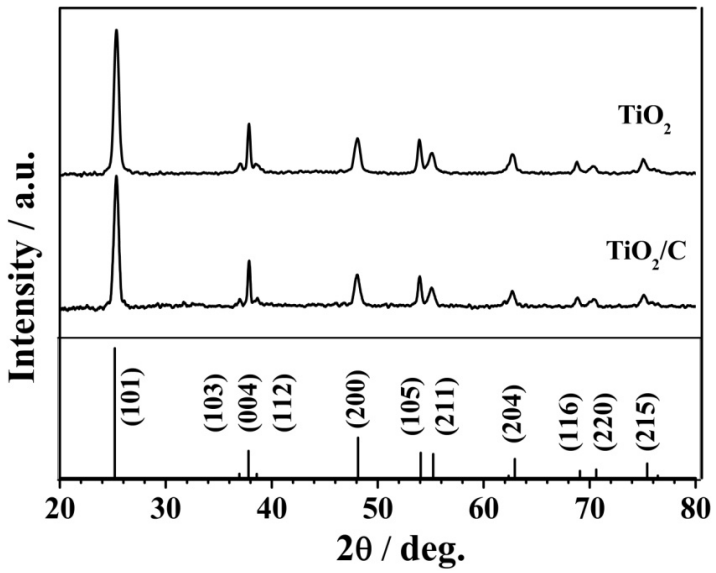

Figure 2: XRD patterns of uncoated anatase TiO_2 nanorods (TiO_2, upper pattern) and after thermal treatment applied in order to carbonize the grafted copolymer (TiO_2/C, lower pattern). The reference ICSD 172914 for anatase TiO_2 is given in the bottom.

Indeed, both patterns show only reflections corresponding to the anatase phase (ICSD 172914) having the space group I41/amd. No additional reflections indicating phase impurities can be observed. Accordingly, the sample does not undergo

a phase change to the principally more stable rutile phase [41,42] upon the thermally induced carbonization of the surface-anchored, RAFT polymerization derived block copolymer.

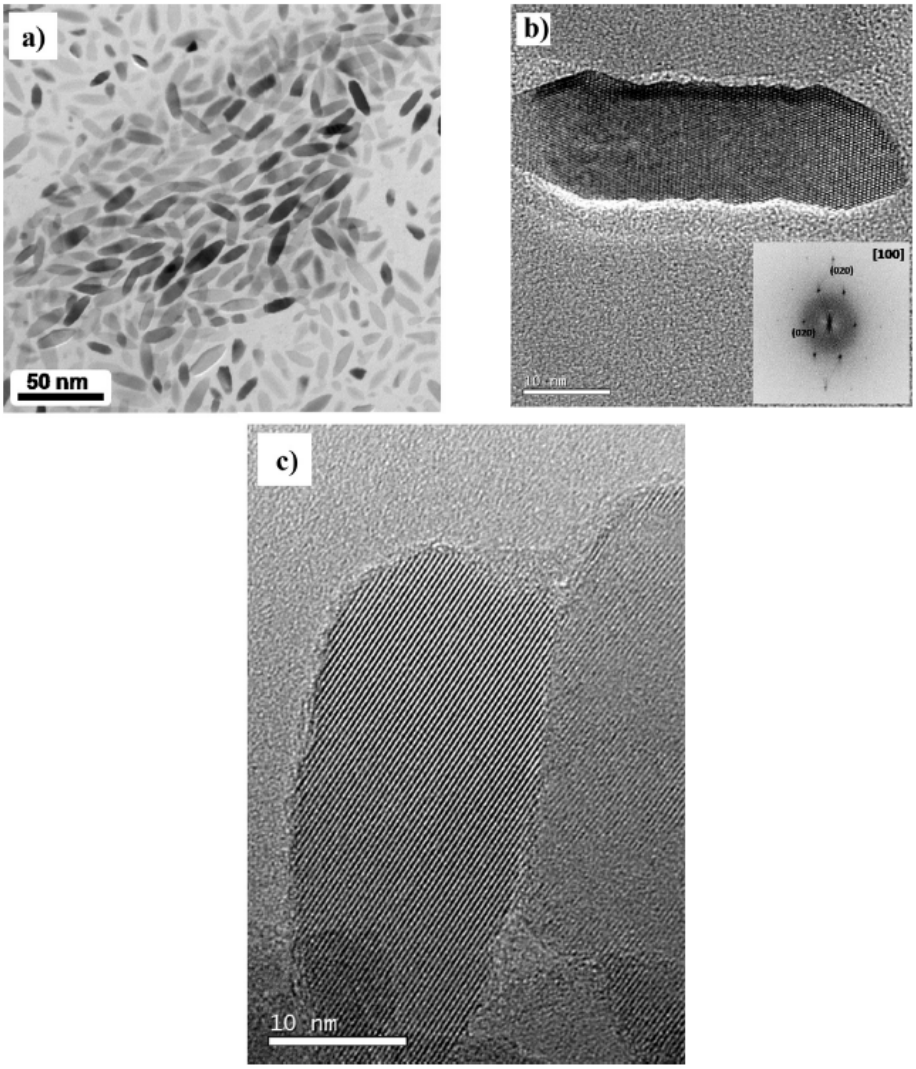

Figure 3: TEM and HRTEM images of uncoated (a and b) TiO_2 nanorods. Inset in b): the Fast Fourier Transform (FFT) showing the [100] direction of anatase TiO_2. c) HRTEM image of carbon-coated TiO_2 nanorods after thermal carbonization of the grafted block copolymer.

This is in good agreement with earlier reported results on anatase TiO_2 nanorods

[26,43], indicating the enhanced stability of the anatase phase relatively to the rutile phase for nano-sized particles due to the increasing impact of the surface free energy, which is lower for the anatase phase compared to the rutile phase, on the total free energy with decreasing particle size [41,42,44].

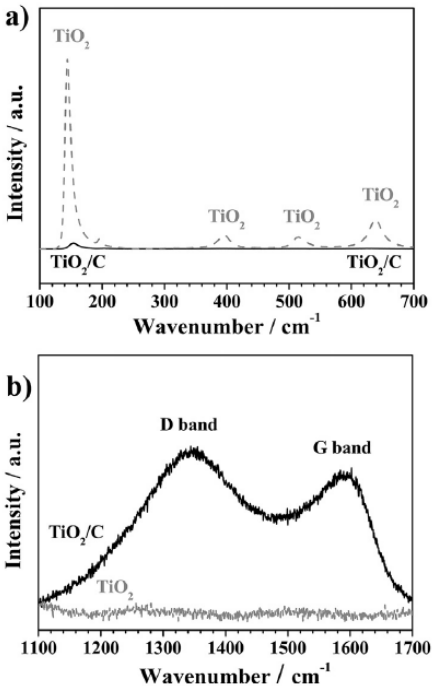

Figure 4: Raman spectra comparing block copolymer-functionalized (gray, dashed line) and carbon-coated (black) anatase TiO_2 nanorods. a) Comparison of the lower wavenumber region for the bands related to anatase TiO_2. b) Comparison of the higher wavenumber region for the bands corresponding to the carbonaceous coating.

The formation of a very thin (approximately 1 nm) and amorphous surface film on the TiO_2 nanorods, having an average length of around 30 nm and an average diameter of about 10-15 nm (Fig. 3a), was confirmed by HRTEM analysis of uncoated (Fig. 3b) and carbon-coated (Fig. 3c) TiO_2 nanorods. In fact, this coating layer is covering the nanorods surface very homogenously. Slight accumulation of carbon is observed only at the boundary of adjacent nanorods (Fig. 3c), as also schematically illustrated in Fig. 1. Such a carbonaceous conductive “bridge”, however, might have a beneficial effect on the electrochemical performance of the sample, enabling a fast electron transfer from one particle to another and finally to the

current collector.

For a further characterization of the carbon coating, Raman spectroscopy was carried out (Fig. 4). While for the copolymer functionalized TiO_2 sample (i.e., prior to the thermally induced carbonization of the grafted polymer; gray dashed spectrum in Fig. 4a) the characteristic Raman bands for anatase TiO_2 [45] are clearly observed, their intensity is significantly decreased for the carbon-coated sample (i.e., after the thermal treatment; black spectrum in Fig. 4a), being in good agreement with previously reported results [26].

In addition, the characteristic G and D bands, appearing at around 1580 and 1355 cm^{-1} and corresponding to the graphitic CeC stretching and induced disorder of sp^2 hybridized carbon [46,47], respectively, are observed only for the carboncoated sample, confirming the presence of a partially graphitic carbonaceous surface layer on the anatase TiO_2 nanorods (Fig. 4b).

3.2. Electrochemical characterization

For the electrochemical characterization of carbon-coated and uncoated TiO_2 nanorods, electrodes were prepared using carboxymethyl cellulose (CMC) as binder, since it was shown that electrodes comprising CMC rather than polyvinylidene fluoride (PVdF) present an improved electrochemical performance [48,49]. Moreover, it appears noteworthy that for the preparation of carboncoated TiO_2-based electrodes, the conductive carbon (Super C65) was added partially before and after the thermal treatment, following a previously reported electrode material processing [26]. Generally, however, electrodes based on carbon-coated TiO_2 nanorods will be hereinafter referred to as TiO_2/C while those based on uncoated TiO_2 nanorods will be simply referred to as TiO_2. In Fig. 5, a comparison of the high rate capability for TiO_2/C and TiO_2 is presented. As expected, TiO_2/C-based electrodes show a significantly improved rate capability. Specific capacities of around 220, 190, 170, and 135 mAh g^{-1} were obtained for TiO_2/C at 0.2C, 1C, 2C, and 5C, respectively, while

TiO_2-based electrodes delivered specific capacities of 10-20 mAh g^{-1} lower for all C rates (see also Table 1).

Table 1: Reversible specific capacity for TiO_2/C- and TiO_2-based electrodes at different C rates and the corresponding cycle number.

Cycle number	**C rate**	**Specific capacity (TiO_2/C)**	**Specific capacity (TiO_2)**
2	C/5	221 mAh g^{-1}	203 mAh g^{-1}
10	1C	191 mAh g^{-1}	180 mAh g^{-1}
20	2C	171 mAh g^{-1}	159 mAh g^{-1}
30	5C	134 mAh g^{-1}	109 mAh g^{-1}
40	10C	96 mAh g^{-1}	72 mAh g^{-1}
50	15C	70 mAh g^{-1}	53 mAh g^{-1}
55	1C	187 mAh g^{-1}	174 mAh g^{-1}
100	1C	183 mAh g^{-1}	154 mAh g^{-1}

More importantly, the cycling stability was dramatically improved as revealed by the lower specific capacity decrease upon continuous cycling at all C rates, and particularly at 1C for the subsequent constant current cycling, evidencing the highly reversible lithium (de-)insertion for carbon-coated TiO_2 nanorods. As a matter of fact, the coulombic efficiency for TiO_2/C approaches 99.97 % upon continuous cycling at 1C, while the efficiency for TiO_2 remains comparably low at about 99.7 %. A more careful analysis of the obtained data performed by plotting the potential vs. the specific capacity (Fig. 6) reveals that the first (dis-)charge profile for carbon-coated (Fig. 6a) as well as for uncoated (Fig. 6b) nanorods shows the characteristic potential profile for nanostructured anatase TiO_2 [20,25,26,50-52].

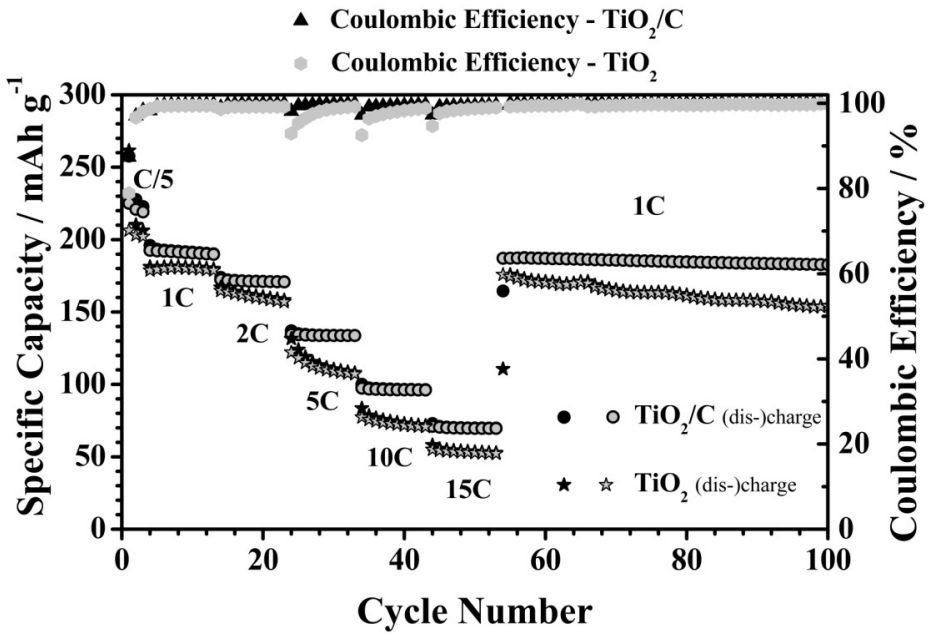

Figure 5: Carbon-coated and uncoated TiO_2 nanorods-based electrodes subjected to galvanostatic cycling at elevated C rates (cycles 1-3 at C/5, followed by each 10 cycles at 1C, 2C, 5C, 10C, and 15C, finally (dis-)charged at 1C again); cut-off potentials: 1.2 and 3.0 V.

Upon the initial rather smooth voltage decrease lithium ions are inserted via solid solution into the Li-poor phase of anatase TiO_2 up to a lithiation degree of around $Li_{0.1}TiO_2$ ($\approx$33 mAh g^{-1}) for carbon-coated TiO_2 (TiO_2/C, Fig. 6a), while retaining the I41/amd space group and its tetragonal symmetry. The subsequent distinct potential plateau at around 1.7 V corresponds to the occurring phase transition and coexistence of the Li-rich $Li_{0.5}TiO_2$ ($\approx$168 mAh g^{-1}, Fig. 6a) phase, having a lithium titanate structure and orthorhombic symmetry (space group: Imma). Finally, the second phase change, occurring only at the nanoparticles surface [24,53-55], from Li-rich lithium titanate back to the anatase phase ($LiTiO_2$, space group $I4_1$/amd) is taking place, as indicated by the following voltage plateau at around 1.5 V [26,54,55]. This results in a total lithiation of the active material up to $Li_{0.77}TiO_2$ (Fig. 6a,

TiO_2/C).

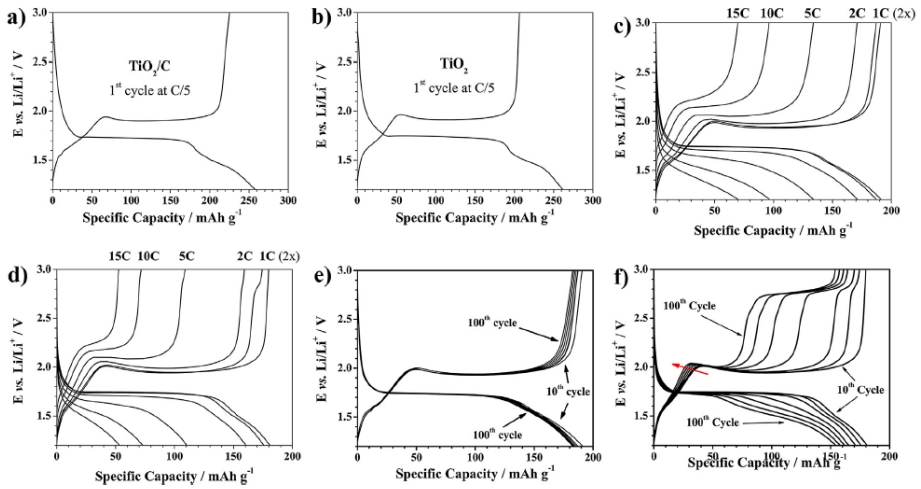

Figure 6: Potential profile of the first galvanostatic cycle (see Fig. 5) for carbon-coated (a) and uncoated (b) anatase TiO_2 nanorods at C/5 (w33.6 mA g^{-1}). Selected potential profiles for carbon-coated (c) and uncoated (d) TiO_2 nanorods at elevated C rates (1C, 2C, 5C, 10C, 15C, and 1C again). Selected potential profiles at a constant C rate of 1C for carbon-coated (e) and uncoated (f) TiO_2 nanorods. Cut-off potentials: 1.2 and 3.0 V.

It should be mentioned here, that other studies have assigned the presence of the second voltage plateau to a kinetically hampered, ongoing lithium insertion in orthorhombic TiO_2 [56], while the increased capacity values for nanostructured materials would be caused by (pseudo-)capacitive lithium storage [56,57]. In fact, within scientific literature it is still under discussion whether the second phase transition is taking place for nanostructured anatase TiO_2 in an electrochemical cell. However, based on the results presented herein, we cannot ultimately exclude one explanation or the other. Actually, both phenomena (second phase transition and (pseudo-)capacitive lithium storage) might contribute to the obtained specific capacities.

However, while for the carbon-coated sample a reversible specific capacity of 225 mAh $g^{-1}$and a coulombic efficiency of 87.4 % are obtained, the uncoated sample deliv-

ers a reversible capacity of only 206 mAh g^{-1} and a coulombic efficiency of 78.9%. This improved first cycle efficiency of TiO_2/C might be related to a reduced surface activity due to the thin carbon layer and thus a decrease of the amount of parasitic surface reactions, inter alia caused by reductive electrolyte decomposition [26]. In addition, the initial lithium trapping inside the TiO_2 host [58] might be reduced due to the enhanced electronic conductivity and thus kinetics of TiO_2/C relatively to TiO_2. In fact, the specific capacity obtained reversibly upon delithiation (charge) up to the appearance of the voltage plateau is higher for TiO_2/C ($\approx$68 mAh g^{-1}) than for TiO_2 ($\approx$55 mAh g^{-1}), indicating an increased contribution of the second phase change from anatase back to titanate. The subsequent slight overvoltage at the onset of the potential plateau (titanate/anatase) appears to be correlated to the primary particle size of the anatase TiO_2 nanoparticles and has been assigned to a nucleation barrier for the initiation of a phase transition [20,59-61]. Selected potential profiles for the different C rates (Fig. 6c and d) show once again the enhanced rate capability and capacity retention after the rate tests of TiO_2/C. Moreover, it is observed that the second phase change, indicated by the second voltage plateau at around 1.5 V appears only for lower (dis-)charge rates, up to 1C, due to kinetic limitations [26,55]. Additionally, however, the potential profile corresponding to cycle 55 for TiO_2 (second profile at 1C, Fig. 6d) presents a new feature at a potential of around 2.8 V. This phenomenon becomes even more obvious by comparing the potential profiles at 1C only up to the 100th cycle (Fig. 6e and f). Indeed, while TiO_2/C presents a stable cycling and only a slight capacity loss caused by a slight shortening of the main voltage plateau (Fig. 6e), TiO_2 presents a more dramatic change of the potential profile upon continuous (de-)lithiation (Fig. 6f). The main voltage plateaus observed around 1.7 and 1.9 V during the discharge (lithiation) and charge (delithiation), respectively, are continuously shrinking (Fig. 6f). Upon 100 cycles the lithium insertionwas mainly taking place at lower potentials (in average at around 1.5 V) while a new voltage plateau at about 2.8 V appeared for the delithi-

ation process, accompanied by a shift of the overvoltage at the onset of the main potential plateau to higher voltages (indicated by the red arrow in web version). It is extremely important to notice that a potential relaxation is observed when a TiO_2-based electrode upon delithiation at 2.8 V is left in open circuit conditions (results not shown). In particular, upon relaxation (a few hours) the potential drops to around 2.0 V thus indicating the kinetic origin of the high voltage delithiation plateau. However, such a modification of the lithium (de-)insertion process results in a dramatically reduced energy storage efficiency of uncoated TiO_2 nanoparticles (Fig. 7).

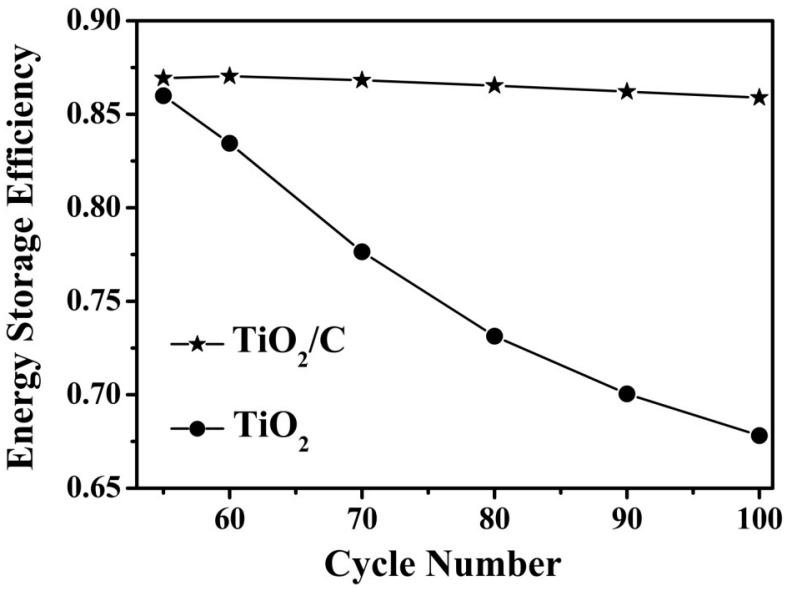

Figure 7: Comparison of the energy storage efficiency for TiO_2/C and TiO_2 (ratio of energy stored upon charge vs. energy released upon discharge according to the theoretically reversed process of charge and discharge in a lithium-ion full-cell within which the TiO_2-based electrode would serve as anode).

A similar behavior was, in fact, already observed by Saravanan et al. [62]. Unfortunately, within their study this phenomenon was neither described nor discussed. In

order to further investigate this phenomenon, cyclic voltammetry was performed on non-coated TiO_2-based electrodes for 50 continuous cyclic sweeps (Fig. 8). Initially, the expected cyclic voltammogram is observed, indicating the two redox couples for the first and second phase transition [26]. Two very minor anodic and cathodic peaks at voltages of around 1.5 and 1.6 V have already been observed in literature and assigned to a reversible pseudocapacitive effect [63] and indeed they are highly reversible even after 50 continuous potentiodynamic sweeps. Kavan and coworkers have very recently reported the electrochemical characterization of TiO_2 (B) and anatase TiO_2 as well as their mixtures, investigating the capacitive contribution for these two titanium oxide phases to the overall lithium storage [64]. According to their results obtained by cyclic voltammetry, particularly with respect to themixture of anatase TiO_2 and TiO_2 (B), these two peaks might also be related to the presence of a very minor impurity of TiO_2 (B), for which, as a matter of fact, the (pseudo-)capacitive lithium storage plays a decisive role [65].

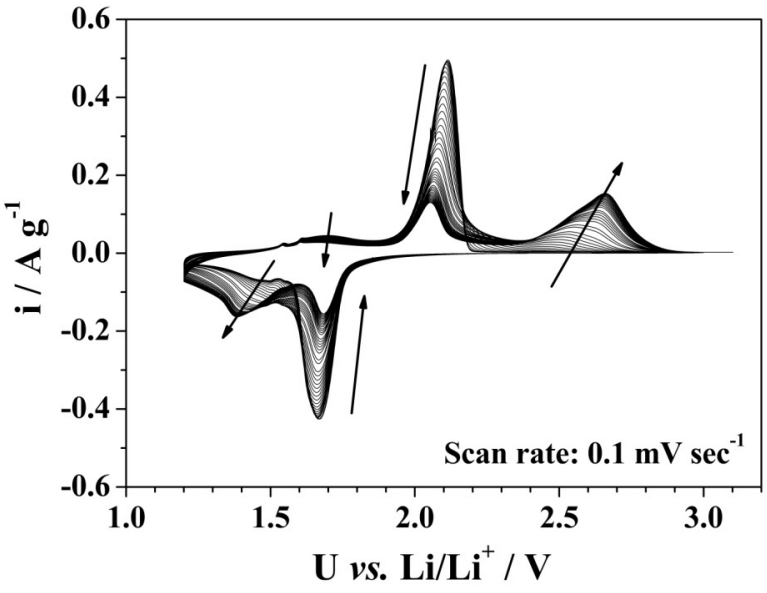

Figure 8: Cyclic voltammogram of an uncoated TiO_2 nanorods-based electrode (TiO_2) from the 5th to the 50th cyclic sweep; reversing potentials: 1.2 and 3.0 V.

Due to an overlap of the major XRD reflections [66], the presence of a very minor amount of TiO_2 (B) within the herein studied anatase TiO_2 nanorods cannot be fully ruled out, particularly if the relative amount is below the XRD detection limit. However, Raman spectroscopy did not reveal the presence of TiO_2 (B), apart from an extremely weak peak at about 200 cm^{-1} (Fig. 4a). In order to verify the presence of TiO_2 (B) impurities, amore careful structural analysis of the samplewould have to be performed, which is beyond the scope of this manuscript. More remarkably, however, is the appearance of a new redox couple at around 1.5-1.35 V and 2.6-2.7 V for the cathodic and anodic sweep, respectively. While these peaks are increasing, the main redox couple is decreasing in terms of specific current (indicated by the black arrows), being perfectly in line with the former results obtained by galvanostatic cycling (Fig. 6d and f). In fact, to the best of our knowledge such a newly appearing redox couple has never been reported so far for anatase TiO_2. For a further investigation of this phenomenon ex situ XRD analysis of the cycled electrodes was carried out (see later in Section 3.3). As it has been shown that the lower cut-off potential has a significant influence on the electrochemical performance of anatase nanoparticles [26],we studied also the influence of the cutoff potential on the appearance of this new potential profile feature, occurring for uncoated TiO_2 nanorods only (Fig. 9). Generally, the previously reported results [26] were confirmed: lowering the cathodic cut-off potential from 1.2 V to 1.0 V resulted in a slightly increased reversible specific capacity in the first cycle (216 vs. 206 mAh g^{-1}; Fig. 9a and b) and for rather low specific currents (187 vs. 180 mAh g^{-1} at 1C in the 10th cycle). However, at higher C rates the situation is reversed (149 vs. 159 mAh g^{-1} at 2C; 83 vs. 109 mAh g^{-1} at 5C; 53 vs. 72 mAh g^{-1} at 10C; 41 vs. 53 mAh g^{-1} at 15C; see also Table 1 for the values for 1.2 V as cut-off potential). In fact, by setting the C rate back to 1C similar capacity values are obtained for both cut-off potentials (171 vs. 174 mAh g^{-1} and 150 vs. 154 mAh g^{-1} for the 55th and 100th cycle and 1.0 vs. 1.2 V as cathodic cut-off potential, respectively), indicating a more pronounced

capacity fading for the lower cut-off potential (Fig. 9a).

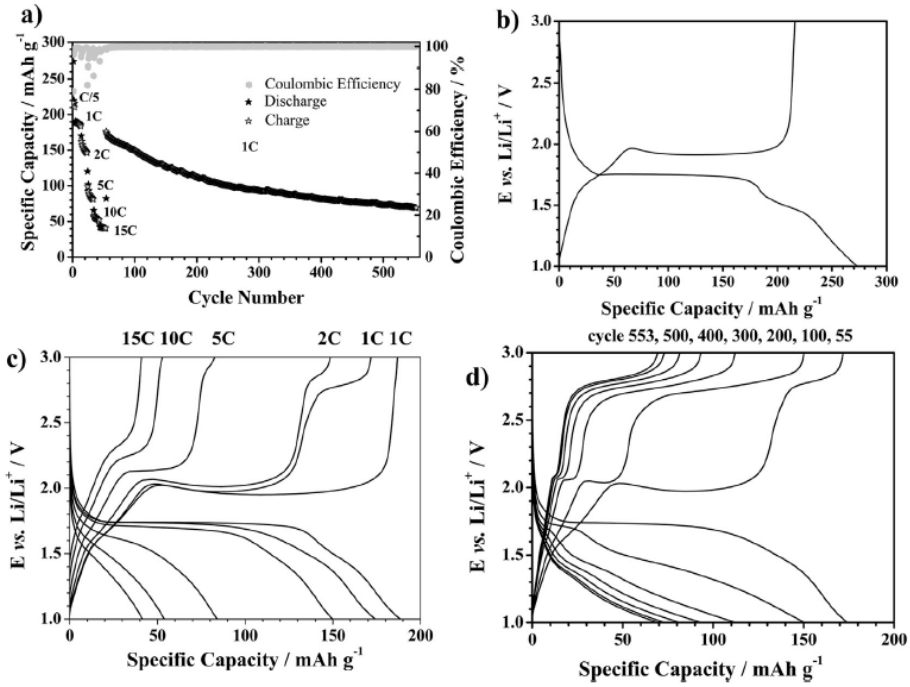

Figure 9: Performance of uncoated TiO_2 nanorod electrode subjected to galvanostatic cycling at elevated C rates (cycles 1-3 at C/5, followed by each ten cycles at 1C, 2C, 5C, 10C, and 15C, finally (dis-)charged at 1C for all subsequent cycles (cut-off potentials: 1.0 and 3.0 V) (panel a)). b) Corresponding potential profile for the 1st cycle. c) Selected potential profiles for elevated C rates (1C, 2C, 5C, 10C, 15C, and 1C again). d) Selected potential profiles for the subsequent cycling at 1C.

A comparison of the potential profiles at elevated C rates (Figs. 9c and 6d), however, reveals that the lower cut-off potential has also an influence on the appearance of the new plateau-like feature at higher potentials of around 2.8 V. It is obvious that this feature appears much earlier for a cut-off potential of 1.0 V, even for elevated rates of 2C and 5C, while it is at the same time much more pronounced for the 55th cycle (1C again). In fact, subjecting a TiO_2- based electrode to more than 550 (dis-)charge cycles confirms that the lengthening of the new plateau-like feature at the expense of shortening of the main voltage plateau is a continuous process (Fig. 9d).

Almost no capacity is obtained anymore along the main voltage plateau, while the major contribution stems from the lithium deinsertion at potentials at around 2.8 V.

3.3. Ex situ XRD analysis

A continuous change of the TiO_2 phase away from anatase towards a new crystalline structure might explain the observed new redox couple (Fig. 8) and the occurrence of a new voltage plateau (Figs. 6f and 9d). Preliminary investigation of cycled electrodes by means of ex situ XRD, however, revealed a preservation of the anatase phase of uncoated TiO_2 nanorods even after extended galvanostatic cycling (Fig. 10a). Nevertheless, a more careful analysis of the obtained XRD patterns revealed that the reflections for the (004) (Fig. 10b) and the (200) plane (Fig. 10c) appear to be slightly shifted to higher and lower 2q values indicating a slight reduction and expansion of the lattice along the [001] and [100] direction, respectively. These findings are, in fact, in good agreement with an earlier report by Rabatic et al. [67], who identified an expansion of the anatase lattice along the [100] direction for the surface layer of TiO_2 nanorods, and particularly at the tips of ellipsoid nanoparticles.

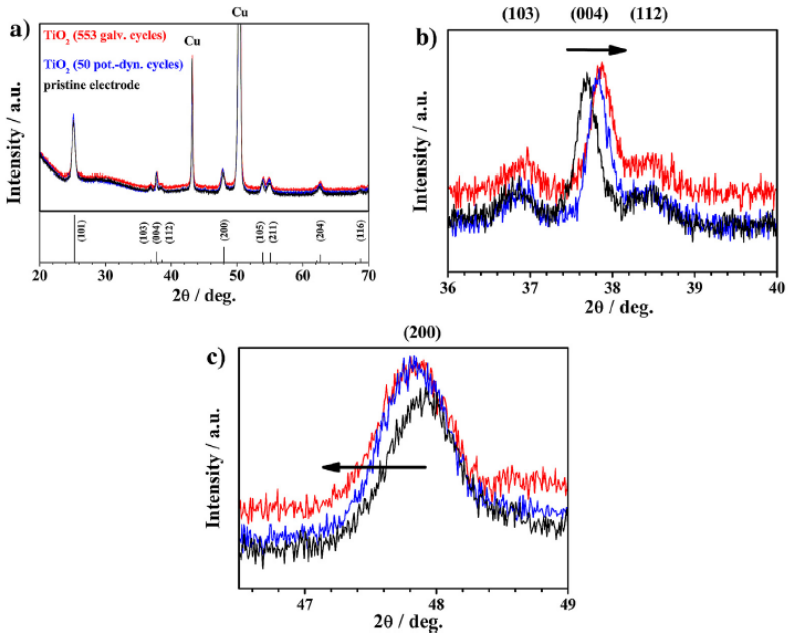

Figure 10: Comparative ex situ XRD investigation of pristine (black pattern), galvanostatically (red pattern, cut-off potentials: 1.0 and 3.0 V, Fig. 9), and potentiodynamically (blue pattern, reversing potentials: 1.2 and 3.0 V, Fig. 8) cycled electrodes based on uncoated anatase TiO_2 nanorods (a). The reference for anatase TiO_2 (ICSD 172914) is given in the bottom. b) and c) show magnifications of the (004) and (200) reflections, respectively. (For interpretation of the references to color in this figure legend, the reader is referred to the web version of this article.)

Indeed, HRTEM images of uncoated anatase TiO_2 nanorods indicate less sharp particle edges at the tip of the rods, leading to the suggestion that particle growth did not reach equilibrium, yet, and thus might be more affected by such kind of surface defects (Fig. 11). Besides, it is agreed in scientific literature that lithium (de-) insertion in anatase TiO_2 occurs preferably along the [001] direction (i.e., along the c-axis) [68,69], meaning that a decrease of the lattice parameter along this direction would result in a kinetic hindrance of lithium diffusion into and within the lattice [68,70], which is in line with the observed shift of the lithium insertion and deinsertion towards lower and higher potentials, respectively, and the previously mentioned

relaxation of the open circuit voltage upon rest.

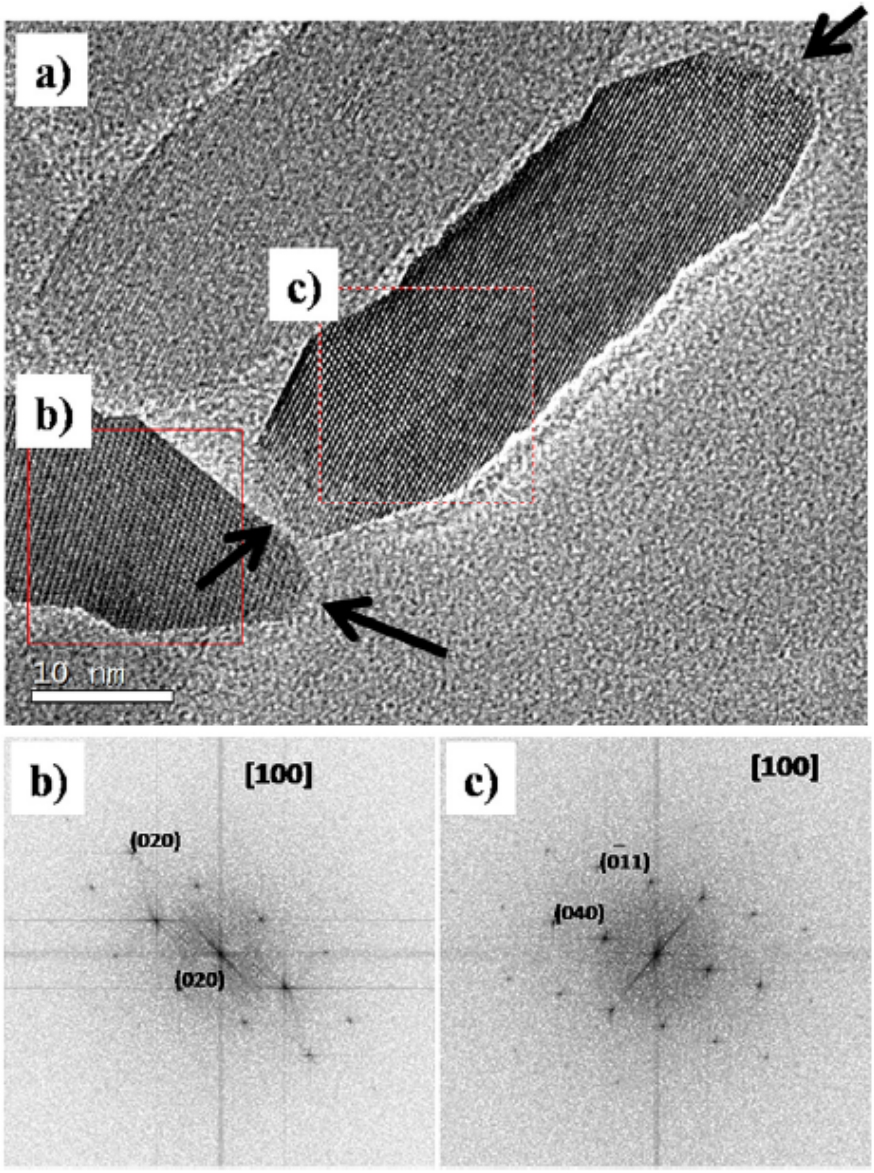

Figure 11: HRTEM image of uncoated anatase TiO_2 nanorods (a). b) and c) show the Fast Fourier Transforms (FFT) for the two nanorods in panel a. The black arrows point on the tip of these nanorods, indicating the crystal growth along the [100] direction.

Moreover, according to the electrochemical results this structural disordering ap-

pears to be a continuously progressing phenomenon upon ongoing lithium ion (de-)insertion e presumably starting from the particle surface and proceeding towards the particle core. Interestingly, Rabatic et al. reported that the lattice distortion in TiO_2 nanorods could be healed by a controlled reaction with dopamine [67], which has been used in the present work as anchor group within the RAFT polymerization as intermediate step upon the carbon coating process. Indeed, ex situ XRD analysis of electrodes based on carbon-coated TiO_2 nanorods does not present any shift of the (200) reflection after about 50 galvanostatic (dis-) charge cycles (results not shown herein) being in good agreement with the results reported by Rabatic et al. [67]. This allows us to suggest that the carbon coating process (including the thermal treatment) might play a fundamental role in preventing the structural disordering for carbon-coated TiO_2 nanorods, thus granting their exceptional long-term electrochemical performance.

4. Conclusions

The effect of a carbon coating process based on the carbonization of PAN-based block copolymers anchored onto anatase TiO_2 nanorods on their performance was presented. This carbon coating process resulted in the formation of a homogenous and thin carbonaceous layer on the TiO_2 nanorods surface. Thus carboncoated TiO_2 nanorods showed a significantly enhanced electrochemical performance in terms of high rate capability, coulombic efficiency, and cycling stability. More remarkably, the application of the carbon coating prevented the appearance of an up to today never discussed alteration of the lithium ion (de-)insertion mechanism of anatase TiO_2 caused by the occurrence of a structural disorder upon continuous lithium storage and release. This structural disordering led to a continuously changing potential profile and the appearance of a new redox couple in the cyclic voltammogram of such electrodes, which finally resulted not only in a less stable cycling performance but moreover in a dramatically reduced energy storage efficiency of such electrodes.

Acknowledgments

D.B. and S. P. would like to thank the European Commission for financial support within the ORION (229036) and the AMELIE (265910) project under the Seventh Framework Programme (7th FWP). B.O. would like to acknowledge financial support by the “Fonds der Chemischen Industrie”. Furthermore, the authors would like to thank Dr. U. Kolb and R. Branscheid for performing HRTEM analysis.

References

[1] M. Armand, J.-M. Tarascon, Nature 451 (2008) 652.

[2] B. Scrosati, J. Garche, J. Power Sources 195 (2010) 2419.

[3] B. Scrosati, J. Hassoun, Y.-K. Sun, Energy Environ. Sci. 4 (2011) 3287.

[4] T. Abe, H. Fukuda, Y. Iriyama, Z. Ogumi, J. Electrochem. Soc. 151 (2004) A1120.

[5] Y. Yamada, Y. Iriyama, T. Abe, Z. Ogumi, Langmuir 25 (2009) 12766.

[6] E. Peled, J. Electrochem. Soc. 126 (1979) 2047.

[7] R. Yazami, Electrochim. Acta 45 (1999) 87.

[8] S. Flandrois, B. Simon, Carbon e Am. Carbon Commun. 37 (1999) 165.

[9] Z. Yang, D. Choi, S. Kerisit, K.M. Rosso, D. Wang, J. Zhang, G. Graff, J. Liu, J. Power Sources 192 (2009) 588.

[10] A. Du Pasquier, C.C. Huang, T. Spitler, J. Power Sources 186 (2009) 508.

[11] T.-F. Yi, L.-J. Jiang, J. Shu, C.-B. Yue, R.-S. Zhu, H.-B. Qiao, J. Phys. Chem. Solids 71 (2010) 1236.

[12] A.S. Prakash, P. Manikandan, K. Ramesha, M. Sathiya, J.-M. Tarascon, A.K. Shukla, Chem. Mater. 22 (2010) 2857.

[13] D. Bresser, E. Paillard, M. Copley, P. Bishop, M. Winter, S. Passerini, J. Power Sources 219 (2012) 217.

[14] S.-T. Myung, N. Takahashi, S. Komaba, C.S. Yoon, Y.-K. Sun, K. Amine, H. Yashiro, Adv. Funct. Mater. 21 (2011) 3231.

[15] C. Jiang, J. Zhang, J. Mater. Sci. Technol. 29 (2013) 97.

[16] T. Froeschl, U. Hormann, P. Kubiak, G. Kucerova, M. Pfanzelt, C.K. Weiss, R.J. Behm, N. Husing, U. Kaiser, K. Landfester, M. Wohlfahrt-Mehrens, Chem.
Soc. Rev. 41 (2012) 5313.

[17] A.L. Linsebigler, G. Lu, J.T. Yates, Chem. Rev. 95 (1995) 735.

[18] U. Bach, D. Lupo, P. Comte, J.E. Moser, F. Weissortel, J. Salbeck, H. Spreitzer, M. Gratzel, Nature 395 (1998) 583.

[19]M. Grätzel, J. Photochem. Photobiol. C Photochem. Rev. 4 (2003) 145.

[20] B. Zachau-Christiansen, K. West, T. Jacobsen, S. Atlung, Solid State Ionics 28e 30 (1988) 1176. [21] T. Ohzuku, T. Kodama, T. Hirai, J. Power Sources 14 (1985) 153. [22] L. Kavan, M. Grätzel, S.E. Gilbert, C. Klemenz, H.J. Scheel, J. Am. Chem. Soc. 118 (1996) 6716.

[23] M. Wagemaker, D. Lützenkirchen-Hecht, A.A. van Well, R. Frahm, J. Phys. Chem. B 108 (2004) 12456.

[24] M. Wagemaker, W.J.H. Borghols, F.M. Mulder, J. Am. Chem. Soc. 129 (2007) 4323.

[25] G. Sudant, E. Baudrin, D. Larcher, J.-M. Tarascon, J. Mater. Chem. 15 (2005) 1263.

[26] D. Bresser, E. Paillard, E. Binetti, S. Krueger, M. Striccoli, M. Winter, S. Passerini, J. Power Sources 206 (2012) 301.

[27] L.J. Hardwick, M. Holzapfel, P. Novák, L. Dupont, E. Baudrin, Electrochim. Acta 52 (2007) 5357.

[28] A.S. Aricò, P. Bruce, B. Scrosati, J.M. Tarascon, W. van Schalkwijk, Nat. Mater. 4 (2005) 366.

[29] P.G. Bruce, B. Scrosati, J.-M. Tarascon, Angew. Chem. Int. Ed. 47 (2008) 2930.

[30] J. Moskon, R. Dominko, R. Cerc-Korosec, M. Gaberscek, J. Jamnik, J. Power Sources 174 (2007) 683.

[31] D. Wang, D. Choi, J. Li, Z. Yang, Z. Nie, R. Kou, D. Hu, C. Wang, L.V. Saraf, J. Zhang, I.A. Aksay, J. Liu, ACS Nano 3 (2009) 907.

[32] L.J. Fu, L.C. Yang, Y. Shi, B. Wang, Y.P. Wu, Microporous Mesoporous Mater. 117 (2009) 515.

[33] S.K. Das, M. Patel, A.J. Bhattacharyya, ACS Appl. Mater. Interfaces 2 (2010) 2091.

[34] F.-F. Cao, X.-L. Wu, S. Xin, Y.-G. Guo, L.-J. Wan, J. Phys. Chem. C 114 (2010) 10308.

[35] V.G. Pol, S.-H. Kang, J.M. Calderon-Moreno, C.S. Johnson, M.M. Thackeray, J.

Power Sources 195 (2010) 5039.

[36] G.-N. Zhu, C.-X. Wang, Y.-Y. Xia, J. Electrochem. Soc. 158 (2011) A102.

[37] J. Wang, X. Sun, Energy Environ. Sci. 5 (2012) 5163.

[38] B. Oschmann, D. Bresser, M.N. Tahir, K. Fischer, W. Tremel, S. Passerini, R. Zentel, Macromol. Rapid Commun. (2013), http://dx.doi.org/10.1002/ marc201300531.

[39] C.-T. Dinh, T.-D. Nguyen, F. Kleitz, T.-O. Do, ACS Nano 3 (2009) 3737.

[40] A. Dong, X. Ye, J. Chen, Y. Kang, T. Gordon, J.M. Kikkawa, C.B. Murray, J. Am. Chem. Soc. 133 (2010) 998.

[41] M.R. Ranade, A. Navrotsky, H.Z. Zhang, J.F. Banfield, S.H. Elder, A. Zaban, P.H. Borse, S.K. Kulkarni, G.S. Doran, H.J. Whitfield, Proc. Natl. Acad. Sci. U. S. A. 99 (2002) 6476.

[42] A.A. Levchenko, G. Li, J. Boerio-Goates, B.F. Woodfield, A. Navrotsky, Chem. Mater. 18 (2006) 6324.

[43] Y. Chen, K.S. Kang, K.H. Yoo, N. Jyoti, J. Kim, J. Phys. Chem. C 113 (2009) 19753.

[44] D.J. Reidy, J.D. Holmes, M.A. Morris, J. Eur. Ceram. Soc. 26 (2006) 1527.

[45] R. Baddour-Hadjean, S. Bach, M. Smirnov, J.-P. Pereira-Ramos, J. Raman Spectrosc. 35 (2004) 577.

[46] D.S. Knight, W.B. White, J. Mater. Res. 4 (1989) 385.

[47] R. Baddour-Hadjean, J.-P. Pereira-Ramos, Chem. Rev. 110 (2010) 1278.

[48] M. Mancini, F. Nobili, R. Tossici, M. Wohlfahrt-Mehrens, R. Marassi, J. Power Sources 196 (2011) 9665.

[49] A. Moretti, G.-T. Kim, D. Bresser, K. Renger, E. Paillard, R. Marassi, M. Winter, S. Passerini, J. Power Sources 221 (2013) 419.

[50] D.W. Murphy, R.J. Cava, S.M. Zahurak, A. Santoro, Solid State Ionics 9e10 (Part 1) (1983) 413.

[51] R.J. Cava, D.W. Murphy, S. Zahurak, A. Santoro, R.S. Roth, J. Solid State Chem. 53 (1984) 64.

[52] M. Wagemaker, R. van de Krol, A.P.M. Kentgens, A.A. van Well, F.M. Mulder, J. Am. Chem. Soc. 123 (2001) 11454.

[53] W.J.H. Borghols, D. Lutzenkirchen-Hecht, U. Haake, E.R.H. van Eck, F.M. Mulder, M. Wagemaker, Phys. Chem. Chem. Phys. 11 (2009) 5742.

[54] U. Lafont, D. Carta, G. Mountjoy, A.V. Chadwick, E.M. Kelder, J. Phys. Chem. C 114 (2010) 1372.

[55] A.A. Belak, Y. Wang, A. Van Der Ven, Chem. Mater. 24 (2012) 2894.

[56] J.-Y. Shin, D. Samuelis, J. Maier, Adv. Funct. Mater. 21 (2011) 3464.

[57] J. Wang, J. Polleux, J. Lim, B. Dunn, J. Phys. Chem. C 111 (2007) 14925.

[58] R. van de Krol, A. Goossens, J. Schoonman, J. Phys. Chem. B 103 (1999) 7151.

[59] C. Jiang, M. Wei, Z. Qi, T. Kudo, I. Honma, H. Zhou, J. Power Sources 166 (2007) 239.

[60] J.W. Kang, D.H. Kim, V. Mathew, J.S. Lim, J.H. Gim, J. Kim, J. Electrochem. Soc. 158 (2011) A59.

[61] R.A. Huggins, J. Power Sources 81e82 (1999) 13. [62] K. Saravanan, K. Ananthanarayanan, P. Balaya, Energy Environ. Sci. 3 (2010) 939.

[63] L. Kavan, M. Kalbác, M. Zukalová, I. Exnar, V. Lorenzen, R. Nesper, M. Graetzel, Chem. Mater. 16 (2004) 477.

[64] B. Laskova, M. Zukalova, A. Zukal, M. Bousa, L. Kavan, J. Power Sources 246 (2014) 103.

[65] M. Zukalová, M. Kalbác, L. Kavan, I. Exnar, M. Graetzel, Chem. Mater. 17 (2005) 1248.

[66] T. Kogure, T. Umezawa, Y. Kotani, A. Matsuda, M. Tatsumisago, T. Minami, J. Am. Ceram. Soc. 82 (1999) 3248.

[67] B.M. Rabatic, N.M. Dimitrijevic, R.E. Cook, Z.V. Saponjic, T. Rajh, Adv. Mater. 18 (2006) 1033.

[68] R. Hengerer, L. Kavan, P. Krtil, M. Grätzel, J. Electrochem. Soc. 147 (2000) 1467.

[69] C.H. Sun, X.H. Yang, J.S. Chen, Z. Li, X.W. Lou, C. Li, S.C. Smith, G.Q. (Max) Lu, H.G. Yang, Chem. Commun. 46 (2010) 6129.

[70] S. Lunell, A. Stashans, L. Ojamäe, H. Lindström, A. Hagfeldt, J. Am. Chem. Soc. 119 (1997) 7374.

4.1.2 Carbon Coating of Titaniumdioxide Anatase Nanotubes

The idea of using TiO_2 nanotubes instead of nanorods is to increase the surface-to-volume ratio. A higher surface-to-volume ratio enables shorter lithium-ion diffusion distances and thus is expected to enable faster charging process when applied as an anode material.

In this project, titanate nanotubes synthesized by Muhammad Nawaz Tahir were coated with optimized block lengths of poly(acrylonitrile-block-dopamine acrylamide), as determined in the previous publications. In addition, the polymer synthesis was optimized with respect to the use of reactive ester monomer: The previously used pentafluorophenyl acrylate polymer is very unpolar and thus could not be used to form long reactive ester blocks, as for the block copolymerization using PAN as a macro-CTA polar solvents like DMF or DMSO are required. In these solvents the formed PFPA reactive ester block collapses and thus avoids the formation of long reactive ester blocks. N-acryloxysuccinimide (NAS) in contrast is a more polar reactive ester. It is more compatible with the polar solvents used for the block copolymerization and could be used for a more controlled reactive ester block copolymerization. Dopamine can be introduced in the resulting P(AN-NAS) polymer by aminolysis as well. After the coordination of the polymer onto the surface of the titanate tubes, the pyrolysis of the tubes transformed the titanate structure into anatase crystal structure, which is favored for the lithium-insertion. At the same time the polymer coating was transformed into a carbonaceous shell. The carbonaceous shell around the tubes is well characterized by electron energy loss spectroscopy (EELS), whereby both line scans and elemental mappings reveal a homogeneous carbon coating around the tubes.

The focus of this work is a detailed comparison of the battery performance of TiO_2 nanotubes with a high surface area (185.6 $m^2\ g^{-1}$ as confirmed by Brunauer-Emmett-Teller method) and TiO_2 nanorods (84.5 $m^2\ g^{-1}$). As expected, for high C-rates, i.e.

for high specific currents and thus for short charging times, the TiO_2 nanotubes exhibit an improved battery performance with respect to specific capacities (130 and 110 mAh g^{-1} for tubes vs. 90 and 65 mAh g^{-1} for rods at 10C and 15C respectively). Furthermore, for the TiO_2 nanotubes a very promising long-term cycling stability up to 500 cycles is observed.

On the other hand, the focus of this publication is the application of TiO_2 anatase nanotubes as an anode material in sodium-ion batteries. Sodium-ion batteries are of interest, because of the higher abundance of sodium compared to lithium. This enables lower costs for energy storage. However, so far only few anode materials for the sodium-ion storage exist. Anatase is a promising candidate for sodium-ion batteries. Indeed, the obtained values for the specific capacities in the first cycles are quite promising (217 mAh g^{-1} in the first cycle), but the cycling stability needs to be improved for a reasonable application in sodium-ion batteries.

In this context, Muhammad Nawaz Tahir participated with the preparation of inorganic materials. All further synthetic and characterization steps were conducted by myself, whereby high resolution microscopy was conducted by Ingo Lieberwirth. The electrochemical characterization was conducted under the supervision of Dominic Bresser and with the help of Franziska Mueller.

4.1.2.1 Publication in Journal of the Electrochemical Society, 2015, 162 (2), A1-A8

Carbon-Coated Anatase TiO_2 Nanotubes for Li- and Na-Ion Anodes

Dominic Bresser*, Bernd Oschmann*, Muhammad N. Tahir, Franziska Mueller, Ingo Lieberwirth, Wolfgang Tremel, Rudolf Zentel, and Stefano Passerini.

Abstract

Carbon-coated, anatase titanium dioxide nanotubes were prepared by carbonizing a polyacrylonitrile-based block copolymer grafted on the as-synthesized titanate nanotubes. As revealed by high resolution transmission electron microscopy (HRTEM) and electron energy loss spectroscopy (EELS), this approach results in a very homogeneous and thin carbon coating, which is advantageous for those active materials storing lithium without undergoing significant volume changes upon ion (de-)insertion. As a matter of fact, thus prepared carbon-coated TiO_2 nanotubes presented an excellent long-term cycling stability for more than 500 cycles (0.02 % capacity fading per cycle) and a very promising high rate performance (about 130 and 110 mAh g^{-1} at 10 C and 15 C, respectively). The influence of the tubular morphology on the rate performance is briefly discussed by comparing carbon-coated nanotubes and nanorods. Finally, the carbon-coated nanotubes were also investigated as sodium-ion anode material, showing a very promising first cycle reversible capacity of around 170, 120, and 100 mAh g^{-1} at C/10, 1 C, and 2 C, respectively, rendering them as versatile anode material for lithium- and sodium-ion applications.

*D.B. and B.O. contributed equally to this work.

Introduction

Efficient energy storage, prospected to pave the way for a fully electrified transportation system and the complete energy supply by renewables, is probably one of the major challenges modern society faces.[1–3] Lithium-ion batteries and, very recently, sodium-ion batteries are considered as two of the most promising energy storage technologies to achieve these highly desired targets. However, further improvements in terms of energy density, rate capability, and safety are needed to make these devices finally suitable for such large-scale applications.[4–14] With respect to stationary energy storage applications, for which weight and volume of the battery are not a real issue while long-term cycling stability, rate performance, and safety are of major importance, in particular, titanium-based materials are considered as highly promising candidates to replace the state-of-the-art lithium-ion anode material graphite.[15–18] Among these, anatase TiO_2 is certainly of special interest due to its natural abundance, low cost, environmental friendliness, non-toxicity, and large-scale availability.[19–21] Additionally, it offers a rather large theoretical specific capacity of 335 mAh g^{-1}, corresponding to the reversible uptake and release of one lithium or sodium per formula unit of TiO_2. The practical limit for micro-sized particles, however, is 0.5 lithium per TiO_2 unit (corresponding to a specific capacity of about 168mAh g^{-1}), due to diffusion limitation in the solid phase.[22–25] Substantial improve ments were realized in recent years by nanostructuring the primary particles[26–30] and the application of carbonaceous coatings[31–42] and matrices,[43–45] resulting commonly in enhanced rate capabilities, cycling stability, and increased specific capacities.[46–48] One-dimensional nanostructures, such as nanowires, nanorods, or nanotubes, have attracted particular interest, as they generally offer high specific surface areas and small particle (or crystallite) size, facilitating lithium ion transport and diffusion in(to) the TiO_2 host lattice.[49–58] For improving also the electron transport, the application of carbonaceous coatings is presumably the most promising strategy, since it combines the advantages of enhanced conductivity,[59] and passivated

and cured-stabilized TiO_2 surfaces from, respectively, parasitic side reaction with the electrolyte[59–61] and potential structural disordering, upon continuous lithium (de-)insertion.[42] Concerning lithium-ion in- sertion materials, which are not affected by large volume changes upon (de-)lithiation, such coatings are preferably rather thin, though very homogenous, to prevent any obstacle to lithium ion diffusion into the active material particle.[31,62]

Very recently, anatase TiO_2 nanostructures (including carbon-coated materials) have attracted also considerable interest as potential sodium-ion anodes[63–69] with advanced rate performance and cycling stabilities.[64–67] The electrochemical reaction upon sodium up- take/release, however, appears to be rather different from a "simple" (de-)insertion mechanism, including the reduction of titanium to the metallic state as well as the formation of sodium oxide and some amorphous sodium titanate.[66]

Herein, we report the synthesis and characterization of carbon-coated anatase TiO_2 nanotubes. The carbon coating was realized by grafting a polyacrylonitrile (PAN)-based block copolymer onto titanate nanotubes, which were prepared by an easily upscalable hydrothermal synthesis route, as schematically illustrated in Figure 1. The subsequent pyrolysis of the polymer-coated nanotubes yielded a very thin, but highly homogenous carbon coating as evidenced by Raman spectroscopy and high-resolution transmission electron microscopy (HRTEM) coupled with electron energy loss spectroscopy (EELS). Simultaneous to the carbonization, the thermal treatment lead to the conversion of the titanate nanotubes in anatase TiO_2 nanotubes composed of very fine nanocrystals, as revealed by HRTEM and X- ray diffraction analysis. These carbon-coated anatase TiO_2 nanotubes were then studied as versatile lithium- and sodium-ion anodes with a particular focus on the influence of the particle morphology on the rate capability. A comparison with the performance of carbon-coated nanotubes and nanorods is also reported.

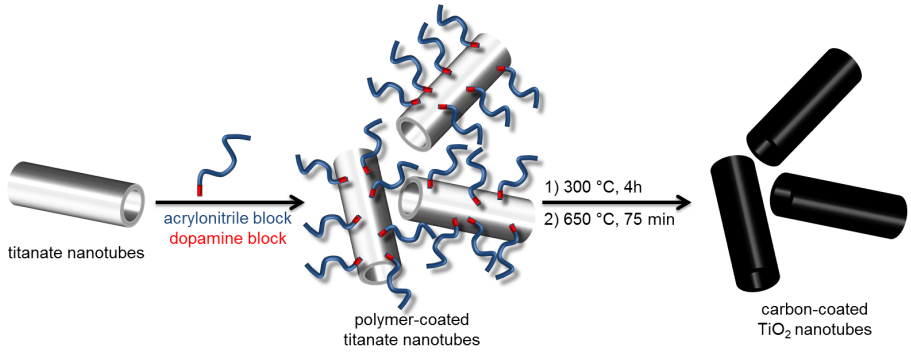

Figure 1: Schematic illustration of the carbon coating approach by grafting a PAN-based block copolymer onto the titanate nanotube surface (left to middle), followed by the thermally induced carbonization of the polymer (middle to right), resulting in carbon-coated TiO_2 nanotubes (right).

Experimental

Materials.

Dry N,N-dimethylformamide (DMF), dry dimethyl sulfoxide (DMSO), and dopamine hydrochloride were purchased from Sigma Aldrich and used as received. N-acryloxy-succinimide (NAS) and 2-dodecylsulfanylthiocarbonylsulfanyl-2-methyl propionic acid (DMP) were synthesized as described elsewhere.[70,71]

α,α-Azoisobutyronitrile (AIBN, Sigma Aldrich) was recrystallized from diethylether. 2,2-azobis(4-methoxy-2,4-dimethylvaleronitrile) (AMDV) was used as received (Sigma Aldrich) Acrylonitrile (AN, Merck) was distilled prior to its use to remove the inhibitor. For the synthesis of TiO_2 nanotubes, anatase TiO_2 (98+%) and NaOH pellets (98 %, extra pure) were purchased from ACROS and used without further treatment.

Synthesis of poly(acrylonitrile-block-dopamine acrylamide).

The block copolymer was synthesized similarly to a previously reported approach under optimized conditions.[41] First, the acrylonitrile (AN) block was synthesized using DMP as charge transfer agent (CTA) and AIBN as a initiator (AN:DMP:AIBN

= 250:1:0.1). After 7 h, the obtained polymer was precipitated in methanol. The block copolymerization with PAN as a macro-CTA, NAS as a monomer, and AMDV as an initiator (NAS:PAN:AMDV = 35:1:0.1) was conducted in dry DMSO for 48 h. The aminolysis of P(AN-block-NAS) with dopamine, using dopamine hydrochloride and triethylamine in DMF, yielded P(AN-block-DAAM). For the polymer characterization, NMR (nuclear magnetic resonance, Bruker ARX 400) and FTIR spectroscopy (Fourier transform infrared, Jasco FT/IR 4100 with an ATR unit) were carried out. Size exclusion chromatography (SEC) was performed with DMF as solvent. The detector system contained refractive index (Agilent) and UV-vis (Agilent) units. The calibration was done using polystyrene standards, purchased from Polymer Standard Services.

^{1}H-NMR (400 MHz, DMSO-d6, δ): 8.74 (s, Ar-OH), 6.20–6.70 (d, Ar-H), 3.32 (s, CONH–CH_2), 3.16 (s, CH of polymer backbone), 2.05 (s, CH_2 of polymer backbone and CONH-CH-CH_2).

Synthesis of carbon-coated TiO_2 nanotubes.

Titanate nanotubes were synthesized by mixing 5 g of anatase titanium dioxide with 120 mL of 10 M NaOH in a polytetrafluoroethylene (PTFE) beaker under vigorous stirring for one hour. Subsequently, the solution was placed in a PTFE-lined autoclave and heated for 24 h at 150 °C. The product was thoroughly washed with 0.1 M HNO_3, 0.1 M HCl, and deionized H_2O until the pH value of the washing solution was seven. The resulting white powder was dried under vacuum at 50 °C. The thus obtained nanotubes were dispersed in DMF and a solution of P(AN-block-DAAM) was added. The dispersion was ultrasonicated for 15 minutes and stirred at 50 °C under argon overnight. As-synthesized titanate nanotubes were characterized by high-resolution transmission electron microscopy (HRTEM) using a Philips EM 420 and XRD analysis conducted on a Siemens D5000 using a Molybdenum-source (0.71073 Å). The reference for anatase TiO_2 given in Figure 4a corresponds to the compound

96–900–8217 registered in the Match! software. Thermogravimetric analysis (TGA) was carried on a Perkin Elmer Pyris 6 instrument under oxygen atmosphere. The polymer coated nanotubes were moreover characterized by IR spectroscopy. For the preparation of carbon-coated TiO_2 nanotubes, the sample was centrifuged, dried, and then pyrolyzed under argon for 3 h at 300 °C and 90 min at 650 °C (heating ramp: 5 °C min^{-1}). The pyrolyzed material was characterized by TGA, XRD analysis, and Raman spectroscopy (Horiba Jobin Y LabRAM HR Spectrometer with a frequency doubled Nd:YAG laser). HRTEM, scanning transmission electron microscopy (STEM), and electron energy loss spectroscopy (EELS) analysis was performed on a Tecnai F 20 (FEI). For the electrochemical characterization, 6 wt% of conductive carbon (Super C65, 160 TIMCAL) was added prior to the pyrolysis.

Electrochemical characterization.

For the electrode preparation, sodium carboxymethylcellulose (CMC, Walocel CRT 2000PA, Dow Wolff Cellulosics), used as binder, was dissolved in deionized water (1.25 wt%). Subsequently, carbon-coated TiO_2 nanotubes and conductive carbon (Super C65, TIMCAL) were added. The resulting slurry was homogenized by ballmilling (Vario-PlanetaryMill Pulverisette 4, FRITSCH) for 2 h (400/-800 rpm). The obtained electrode paste was cast on dendritic copper foil (SCHLENK), with a wet film thickness of 130 μm. After drying at ambient temperature for around 12 h, disc electrodes with a diameter of 12 mm were punched and dried again for about 24 h at 120°C under vacuum. The active material mass loading was in the range from 1.6 to 1.9 mg cm^{-2}. The final electrode composition was 73 wt% TiO_2, 5 wt% CMC, and 22 wt% carbon (including 5.5 wt% conductive carbon added prior to the pyrolysis, 10.5 wt% carbon residue remaining from the carbonized copolymer as confirmed by thermogravimetric analysis (TGA) under O_2, and 6wt% conductive carbon added upon the electrode preparation). For the comparison of the rate performance with carbon-coated anatase TiO_2 nanorods, electrodes were prepared according to our

previous studies.[41,42] The active material mass loading for these electrodes was comprised between 1.6 and 2.0 mg cm^{-2} and the final composition was 75 wt% TiO_2, 5 wt% CMC, and 20 wt% carbon (including 5wt% conductive carbon added prior to the pyrolysis, 10 wt% carbon residue remaining from the carbonized copolymer, and 5 wt% conductive carbon added upon the electrode preparation). All processing steps were performed in the same manner as for carbon-coated TiO_2 nanotubes.

For the electrochemical characterization, three-electrode Swagelok-type cells were assembled using either lithium foil (Rockwood Lithium, battery grade) or sodium metal (99.8 %, Acros Organics) as counter and reference electrodes. The cells were assembled in an MBraun glove box with oxygen and water contents lower than 0.1 ppm. For the characterization as lithium-ion anode material, a stack of polypropylene fleeces (Freudenberg FS2190), drenched with a 1 M solution of $LiPF_6$ in a 3:7 volume mixture of ethylene carbonate (EC) and diethyl carbonate (DEC, UBE), served as separator. Instead, for the investigation as sodium-ion anode material, a sheet of Whatman glass fiber was used as separator, while the 1 M solution of $NaClO_4$ in a 1:1 volume mixture of EC and propylene carbonate (PC) was used as electrolyte, since it was shown to offer the best electrochemical performance for sodium ion insertion into nanostructured anatase TiO_2.[64,66] Galvanostatic cycling was performed with a Maccor Battery Tester 4300. All electrochemical studies were performed at 20 °C ± 2 °C. An applied C rate of 1 C corresponds to a specific current of 168 mA g^{-1}, according to the formula: $TiO_2 + \times Li^+ + \times e^- \rightleftharpoons Li_xTiO_2$ (x = 0.5).

Results and Discussion

Synthesis and characterization of polymer- and carbon-coated TiO_2 nanotubes.

Titanate nanotubes were prepared on gram-scale following a typical hydrothermal synthesis route.[72] HRTEM analysis (Figure 2a) reveals the tubular morphology of the as-synthesized material, having an average outer and inner diameter of about 10 and 6 nm, respectively. While the initial nanotubes were composed of sodium

titanate, the HNO_3 and HCl treatment resulted in hydrogen titanates as revealed by XRD analysis (Figure 2b).

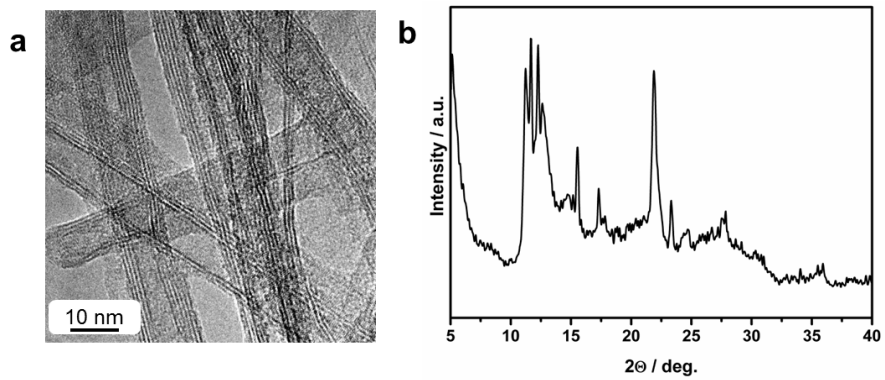

Figure 2: HRTEM micrograph (a) and the recorded XRD pattern (b) of the as-prepared hydrogen titanate nanotubes.

For the polymer coating, a block copolymer, consisting of a short anchor block and a long-chain carbon precursor block, was synthesized by reversible addition-fragmentation chain transfer (RAFT) polymerization (Figure 3a). Firstly, the carbon precursor block polyacrylonitrile (PAN) was synthesized using a trithiocarbonate as chain transfer agent (CTA) and acrylonitrile (AN) as monomer. The average molecular weight was assessed by NMR spectroscopy, revealing 6,200 g mol^{-1} (Figure S1). The polydispersity was 1.24 as determined by gel permeation chromatography (GPC, Figure S2). For the synthesis of the anchor block, initially, a reactive ester block was copolymerized using N-acryloxysuccinimide (NAS). It was shown that using NAS as reactive ester rather than pentafluorophenyl acrylate, which was used in our previous study,[41] is more suitable in case rather polar compounds like N,N-dimethylformamide (DMF)[73] or dimethyl sulfoxide (DMSO)[74] are utilized as solvents for the synthesis. Since catechol structures are suitable for the coordination onto the surface of transition metal oxide nanoparticles,[75,76] dopamine (bearing catechol units) was introduced by a polymer analogous reaction, i.e., the aminolysis of the re-

active ester (see Figure 3a). Performing IR spectroscopy (Figure 3b) confirmed that the desired product poly(acrylonitrile-block-dopamine acrylamide) (P(AN-DAAM)) was obtained, as evidenced by the absence of the reactive ester band (1730 cm^{-1}) and the presence of the amide band (1648 cm^{-1}) as well as the hydroxyl band (3230 cm^{-1}).

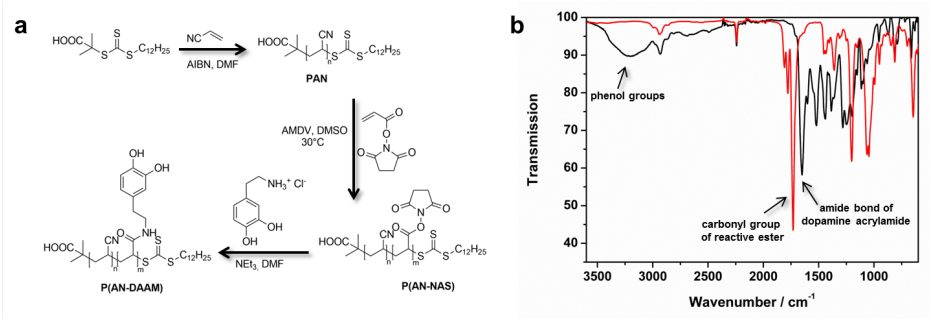

Figure 3: (a) Scheme of the P(AN-DAAM)synthesis by RAFT polymerization starting from PAN and P(AN-NAS). (b) IR spectra of P(AN-NAS) (red) and P(AN-DAAM) (black).

In addition, the GPC elugram of P(AN-DAAM) is shifted to lower elution volumes (Figure S2), indicating an increased volume of the polymer, thus, providing further evidence for the successful synthesis of P(AN-DAAM). The block length of the dopamine acrylamide can be estimated by means of NMR spectroscopy to around 19 repeating units in average (Figure S3).

For the functionalization of the titanate nanotubes, the polymer was dissolved in DMF and the nanotubes were dispersed therein. After the work-up of this hybrid material (consisting of two centrifugation steps to remove excess polymer), the presence of the polymer on the nanotubes was confirmed by IR spectroscopy. Expectedly, the obtained spectrum shows the characteristic polymer bands (Figure S4). Subsequently performed TGA revealed a polymer content of 28 wt%. The polymer-coated nanotubes were then pyrolyzed to transform the polymer coating into a carbonaceous coating, while at the same time the titanate nanotubes are transformed into anatase TiO_2 nanotubes. The overall carbon content derived from the carbonization

of the polymer was 12wt% as determined by TGA. In order to confirm the transformation of the nanotubes from the titanate into the anatase phase, XRD analysis was carried out (Figure 4a). Indeed, the obtained pattern matches the calculated anatase reference very well, excluding the presence of phase impurities or remaining titanate, while the rather broad reflections indicate a rather small crystallite size. Raman spectroscopy, performed to investigate the carbon coating (Figure 4b), showed the characteristic D (1360 cm^{-1}) and G (1595 cm^{-1}) bands corresponding to the induced disorder mode and graphitic C-C stretching mode of sp^2 hybridized carbon, respectively.[77,78]

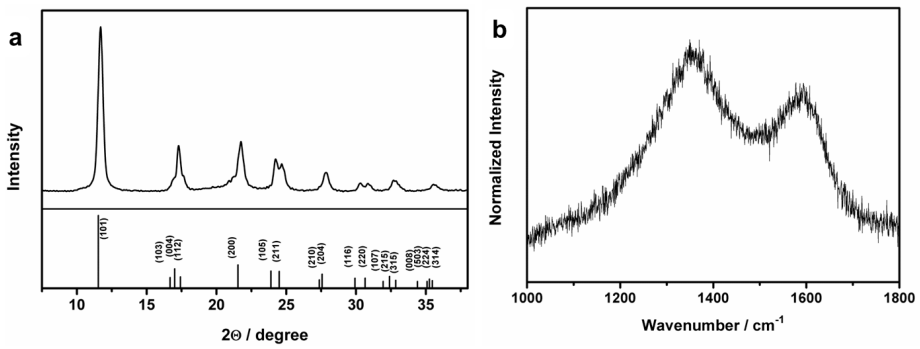

Figure 4: (a) XRD pattern of pyrolyzed nanotubes, having the anatase structure (Mo-source (0.71073 Å); the reference anatase TiO_2 is given in the bottom. (b) Raman spectrum of carbon-coated anatase nanotubes (high wavenumber region).

The carbon-coated anatase TiO_2 nanorods were further characterized by high-resolution transmission electron microscopy (HRTEM) and electron energy loss spectroscopy (EELS). The preservation of the tubular shape is clearly evident from Figures 5a and 5b. (HR)TEM analysis coupled with selected area electron diffraction (SAED, Figure S5) indicates, moreover, that the nanotubes are polycrystalline and to a little extent amorphous. The carbon coating, however, can hardly be visualized, as it is apparently very thin. Thus, EELS was carried out to detect the presence of carbon in the sample. Line scan analysis (Figures 5c and 5d) showed clearly the sig-

nals related to carbon, titanium, and oxygen. In fact, at the edges of the nanotubes, carbon is detected first, prior to oxygen and titanium, indicating that the carbon is deposited on the TiO_2 surface.

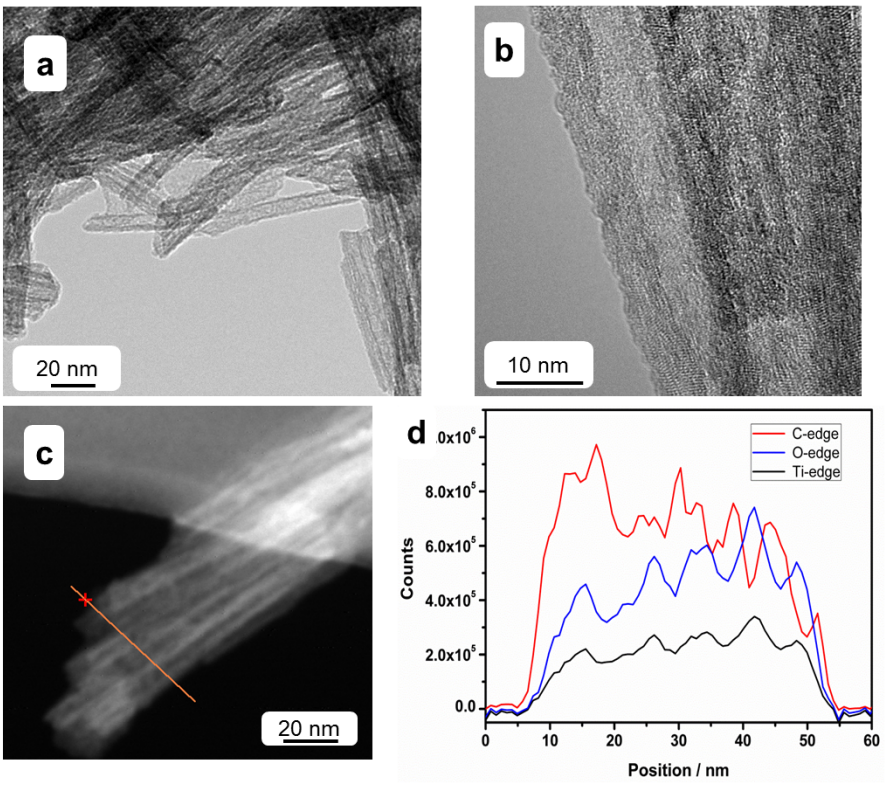

Figure 5: (a) TEM and (b) HRTEM micrographs of pyrolyzed TiO_2 nanotubes at different magnifications. (c) STEM micrograph of the pyrolyzed sample indicating the line, which was investigated by EELS. (d) Detected EELS profile along the line indicated in (c).

Subsequently performed EELS elemental mapping confirmed, in addition, the homogeneous but superficial distribution of carbon on the anatase nanotubes (Figure 6). Finally, the specific surface area was determined according to the Brunauer-Emmett-Teller (BET) method, revealing 277.6 m^2 g^{-1} and 185.6 m^2 $g{-}1$ for the as-synthesized and the pyrolyzed nanotubes, respectively. For comparison, the specific surface area of very similarly treated anatase TiO_2 nanorods (about 10 and 30

nm in width and length, respectively, Figure S6),[41] which electrochemical performance will be later compared with that of the nanotubes, was 107.2 m^2 g^{-1} and 84.5 m^2 g^{-1} after the synthesis and pyrolysis, respectively, i.e., substantially lower than for the nanotubes.

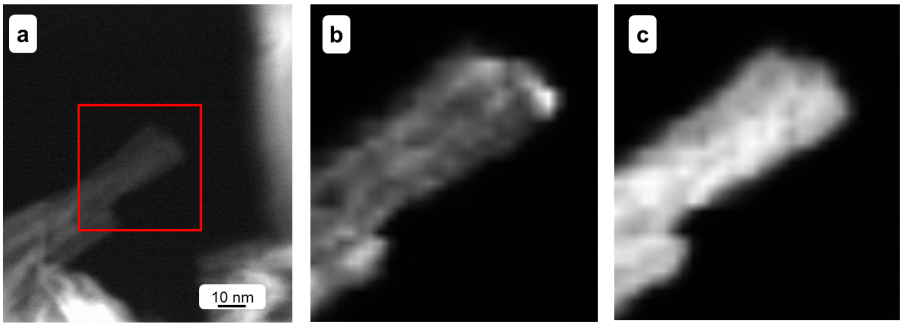

Figure 6: STEM analysis coupled with EELS elemental mapping: (a) STEM micrograph of carbon-coated anatase TiO_2 nanotubes; the area investigated by EELS mapping is marked by the red frame; resulting mapping for carbon (b) and titanium (c).

Electrochemical characterization as lithium-ion anode.

Electrodes comprising carbon-coated anatase TiO_2 nanotubes as active material were subjected to galvanostatic cycling at elevated C rates to study their (dis-)charge capability as lithium-ion hosts (Figure 7). In the first cycle (C/5), a reversible capacity of 215 mAh g^{-1} is obtained corresponding to the reversible storage of about 0.64 lithium per formula unit of TiO_2 (Figure 7a). At 1 C, 2 C, 5 C, 10 C, and 15 C, specific capacities of around 185, 172, 153, 130, and 110 mAh g^{-1} are 299 observed, respectively, highlighting carbon-coated TiO_2 nanotubes as very promising alternative lithium-ion anode material for high-power applications. After applying elevated specific currents and decreasing the (dis-)charge rate back to 1 C, a specific capacity of 187 mAh g^{-1} is obtained, revealing the great stability of the anatase lattice toward lithium ion (de-)insertion. As a matter of fact, the delivered capacity remains highly

stable upon continuous constant current cycling at 1 C, providing still 170 mAh g^{-1} after 500 full (dis-)charge cycles. To evaluate the influence of the particle morphology on the electrochemical performance, in a next step, the same C rate test as in Figure 7a was applied to electrodes based on carbon-coated anatase TiO_2 nanorods prepared by a very similar method (Figure 7c).[41] Obviously, the initial capacity (1st cycle reversible capacity: 225 mAh g^{-1}) is slightly higher than for the nanotubes, presumably due to the poorer crystallization of the latter. Also, at 1 C the specific capacity is slightly higher, while it is the same at 2 C and subsequently decreasing more rapidly at higher rates than for the nanotubes (Figure 7d). Apart from the enhanced rate performance of nanotubes compared to nanorods, these findings are different from the results reported by Kim and Cho,[58] reporting higher capacities for nanotubes than for nanorods at lower rates, too. A careful examination of the corresponding potential profiles may provide an explanation for these findings (Figures 7e and 7f). Generally, both carbon-coated nanotubes and nanorods show the expected potential profile, i.e., the initial solid solution domain, followed by the voltage plateau, related to the phase transition from lithium-poor anatase to lithium-rich titanate,[24,55,79] and, subsequently, a sloped low potential region, within which the diffusion-limited, second phase transition from lithium-rich titanate to fully lithiated anatase occurs.[46,55,80,81]

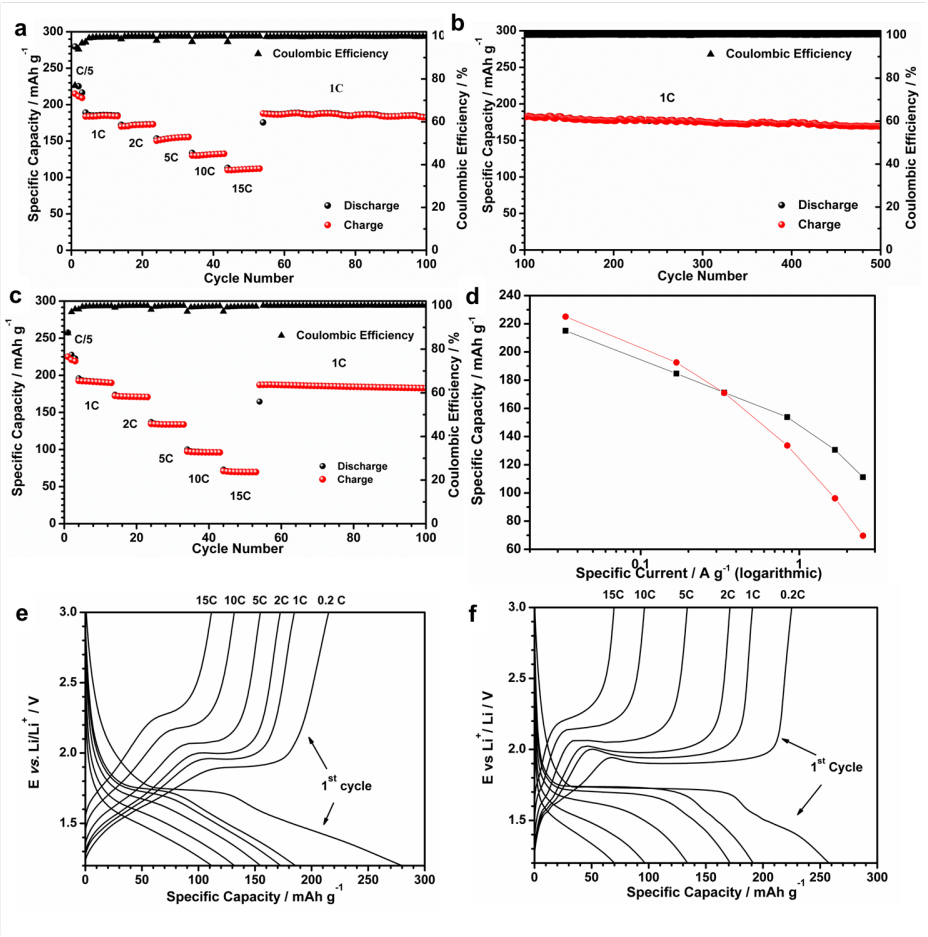

Figure 7: Electrodes based on carbon-coated anatase TiO_2 nanotubes subjected to galvanostatic cycling (cut-off potentials: 1.2 and 3.0 V): (a) capacity vs. cycles at elevated C rates; (b) long-term constant current cycling at 1 C; (c) C rate test for electrodes based on carbon-coated anatase TiO_2 nanorods; (d) comparison of the specific capacity values obtained for carbon-coated TiO_2 nanotubes (black) and nanorods (red) at different C rates; corresponding potential profiles for carbon-coated anatase nanotubes (e) and nanorods (f).

Nevertheless, a comparison of the potential profiles of the two samples reveals some substantial differences. The initial solid solution domain is substantially extended for the nanotubes due to the smaller crystallite size[82] as discussed earlier and obvious also from a comparison of the corresponding XRD patterns (Figure 8).

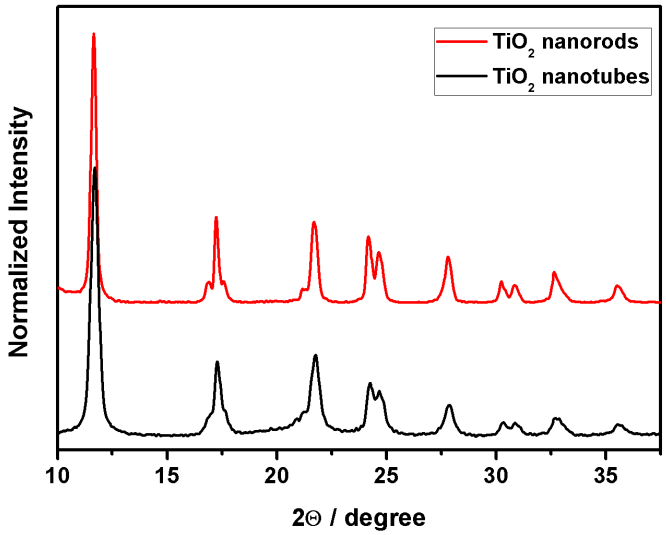

Figure 8: Comparison of the XRD patterns of carbon-coated anatase TiO_2 nanotubes (black) and nanorods (red).

Additionally, the first cycle irreversible capacity is significantly larger for the nanotubes than for the nanorods (Figures 7e and 7f). This might have basically two reasons: First, the specific surface area of the carbon-coated nanotubes (185.6 m^2 g^{-1}) is much higher than that of the nanorods (84.5 m^2 $g^{-}1$). Hence, the contribution of parasitic surface reactions at the electrode/electrolyte interface[40,60,61] is expected to be much larger for the nanotubes. Second, the presence of amorphous TiO_2 in the nanotubes may also contribute to this increased irreversibility as such disordered material may be more affected by initial lithium trapping,[83] commonly resulting in rather high initial charge loss.[84] More remarkable, however, are the differences observed in the voltage plateau and low potential regions in the two carbon-coated materials. While the voltage plateau is significantly shortened for the nanotubes, the low potential region is much more pronounced. Additionally, the potential profile of the nanorods is characterized by some overvoltage at the onset of the voltage plateau. These phenomena are, presumably, related to the different crystallite size. Indeed, although not specifically discussed, it was shown that in-

creasing crystallization accompanied by increasing size of crystallite results in the continuous modification of the potential profile.[85] The study showed that the potential profile of rather small crystallites (13 nm) is composed of a relatively short voltage plateau and a rather long and sloped low potential region (both upon discharge and charge). Upon increasing crystallite size (22, 50, and 91 nm), however, the voltage plateau is seen to become longer, the sloped low potential region shorter, and an increasing overpotential at the onset of the voltage plateau upon charge is observed, commonly assigned to a nucleation barrier for the occurring phase transition[86] from lithium-rich titanate to lithium-poor anatase.[85] Other studies on anatase TiO_2 nanoparticles, investigating various samples with different crystallite sizes, confirm these findings, which may be explained considering the following points.[29,30,55,82,87] First, the extension of the sloped low potential region might partially originate from the presence of amorphous TiO_2, for which generally no voltage plateau is observed.[84,88] Second, the formation of the poorly ionically conductive Li_1TiO_2 phase at the particles surface is much more pronounced for smaller particles, which are intrinsically characterized by a higher surface area, thus hindering further lithium insertion.[80] This may explain the necessity of lower potentials for further lithium ion insertion, particularly considering that nucleation and phase boundary movement in anatase TiO_2 appears to be faster than lithium ion diffusion within the TiO_2 lattice.[80] In accordance with this consideration, the absence of a nucleation barrier at the onset of the voltage plateau might be related to the absence of phase- coexistence in sufficiently small particles.[46,80] In fact, it was proposed that in such case the presence of a voltage plateau would be related to the existence of a many-particle two-phase equilibrium rather than a two-phase equilibrium within every single particle.[89,90] Additionally, the two potential profiles (nanorods and nanotubes) reveal a slight difference in the high potential region above the main voltage plateau. While the potential profiles recorded for carbon-coated nanorods show an almost vertical trend in this region (Figure 7f), the potential profiles recorded for the

nanotubes present a slight slope upon further potential increase (Figure 7e). Considering the significantly higher surface area of the nanotubes, this may be associated to pseudo-capacitive effects.[30,82,91–94] Comparing now the development of the potential profiles at elevated C rates reveals two additional interesting features. First, nanotubes show a reduced ohmic drop at elevated rates. This may be attributed partially to the higher surface area, resulting in a lower current density per unit surface area, as well as a facilitated lithium transport along the interfacial grain boundaries between the single crystals;[52,95] both aspects leading to an enhanced rate performance. More remarkable, however, is the more pronounced shortening of the main voltage plateau for anatase nanorods. Indeed, the length of the voltage plateau appears very similar at 15 C, indicating that the additional capacity at such high C rates, i.e., the enhanced rate performance, originates mainly from the increased lithium (de-)insertion at lower potentials.

Application as sodium-ion anode material.

The suitability of carbon-coated anatase TiO_2 nanotubes as sodium-ion active material was also evaluated (Figure 9). According to a previous study,[64] within which the cycling protocol for anatase TiO_2 nanoparticles was optimized, the cut-off potentials were set to 0.02 and 2.0 V for the initial three formation cycles. For the following cycles, the cathodic cut-off potential was increased to 0.1 V. The initial reversible capacity of about 217 mAh g^{-1} (Figures 9a and 9b) exceeds the reversible capacity obtained for uncoated nanoparticles[64] by far. Nevertheless, also the irreversible capacity loss of around 400 mAh g^{-1} is very high. Beside the irreversible processes, i.e., the formation of metallic titanium, sodium superoxide, and amorphous sodium titanate,[66] this large irreversibility might be related to the high surface area of the carbon-coated nanotubes, presumably leading to an extensive electrolyte decomposition at the electrode/electrolyte interface.

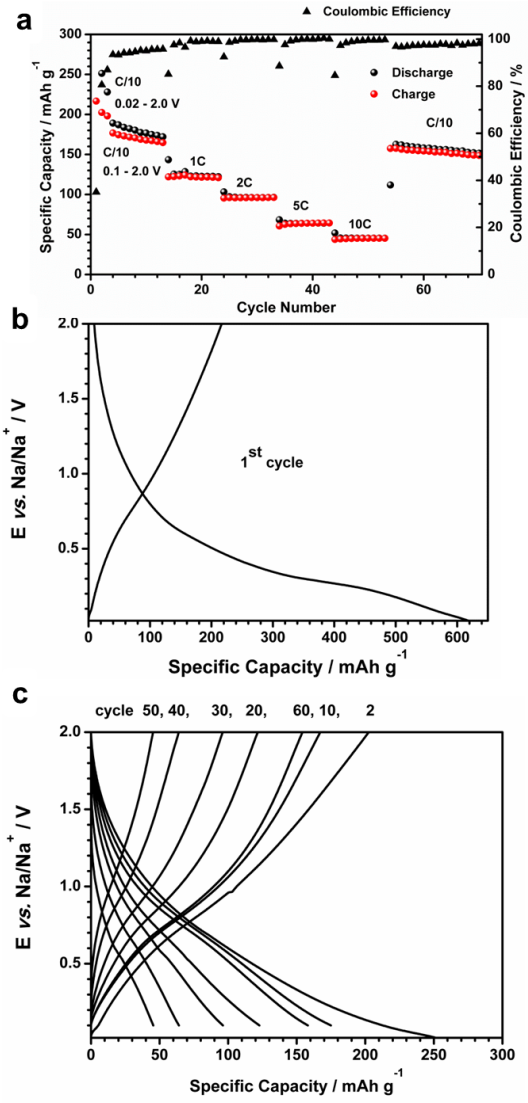

Figure 9: Electrode based on carbon-coated anatase TiO_2 nanotubes subjected to galvanostatic cycling at elevated C rates: (a) specific capacity vs. cycle number; (b) corresponding potential profile for the 1st cycle (C/10, cut-off potentials: 0.02 and 3.0 V); (c) corresponding potential profiles for selected cycles at different C rates (cut-off potentials for the 2nd cycle: 0.02 and 2.0 V, cut-off potentials for the following cycles: 0.1 and 2.0 V).

The shape of the potential profile matches well with those reported in previous

studies,[64,66] indicating that similar, if not the same, electrochemical processes occur, i.e., the reversible (de-)insertion of sodium ions into the initially formed, (quasi-)amorphous sodium titanate.[66] Upon subsequent cycles, however, the reversible capacity decreases to about 200 mAh g^{-1} in the third cycle and to around 170 mAh g^{-1}, when the lower cut-off is increased to 0.1 V (Figure 9a). At 1 C, 2 C, 5 C, and 10 C, specific capacities of about 120, 96, 64, and 45 mAh g^{-1} are obtained, respectively (Figure 9c). Decreasing the C rate to 1 C led to a specific capacity of almost 160 mAh g^{-1} (Figures 9a and 9c), indicating a rather good capacity retention of the active material. It might be noted that the comprised conductive carbon (10 wt%) and the carbon coating (10 wt%) resulting from the carbonization of the polymer contribute with about 8 mAh g^{-1} 66 and 10 mAh g^{-1} to the overall capacity, respectively. The latter value was obtained by subjecting electrodes based on the carbonized polymer only to the same testing protocol and is in good agreement with results reported for electrodes comprising carbonaceous materials derived from the pyrolysis of PAN (about 120 mAh g^{-1} at 100 mA g^{-1}).[96]

Conclusions

Carbon-coated anatase TiO_2 nanotubes were prepared by pyrolysis of PAN-based block copolymer-coated titanate nanotubes. Raman spectroscopy and HRTEM analysis coupled with EELS revealed a very thin and homogeneous carbonaceous coating on the particles surface. Thus prepared carbon-coated nanotubes showed a highly promising cycling stability and superior high rate capability compared to carbon-coated anatase nanorods, when applied as lithium-ion active material. The different rate performance was discussed with a particular focus on the shape of the potential profile. Finally, carbon-coated anatase nanotubes were also investigated as sodium-ion anode material. Galvanostatic cycling at elevated C rates revealed a very high initial reversible capacity and good rate performance, highlighting carbon-coated anatase TiO_2 nanotubes as versatile anode material for lithium- and sodium-ion de-

vices. However, the cycling stability in lithium-ion configuration appears superior, meaning that further improvement will have to be realized for their potential application in practical sodium-ion batteries.

Acknowledgment

B.O. wants to thank the “Fonds der Chemischen Industrie” for financial support. Dominic Bresser and Bernd Oschmann contributed equally to this study.

Supporting Information

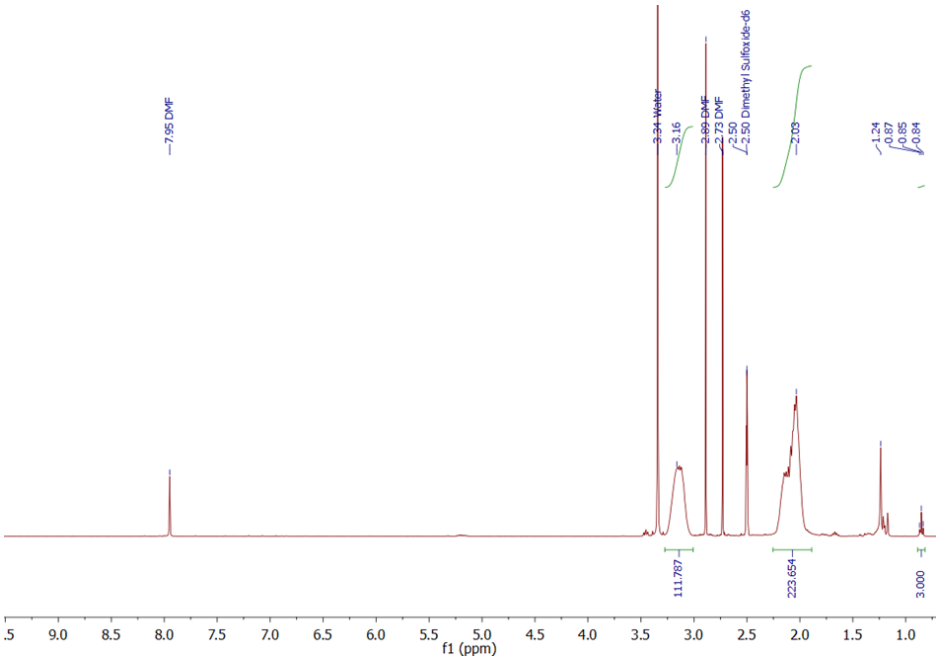

Figure S 1: ^{1}H-NMR spectrum of PAN: the average chain length is estimated by integration of the chain transfer agent methyl group and the signal at 3.16 ppm, corresponding to the –CH-backbone signal.

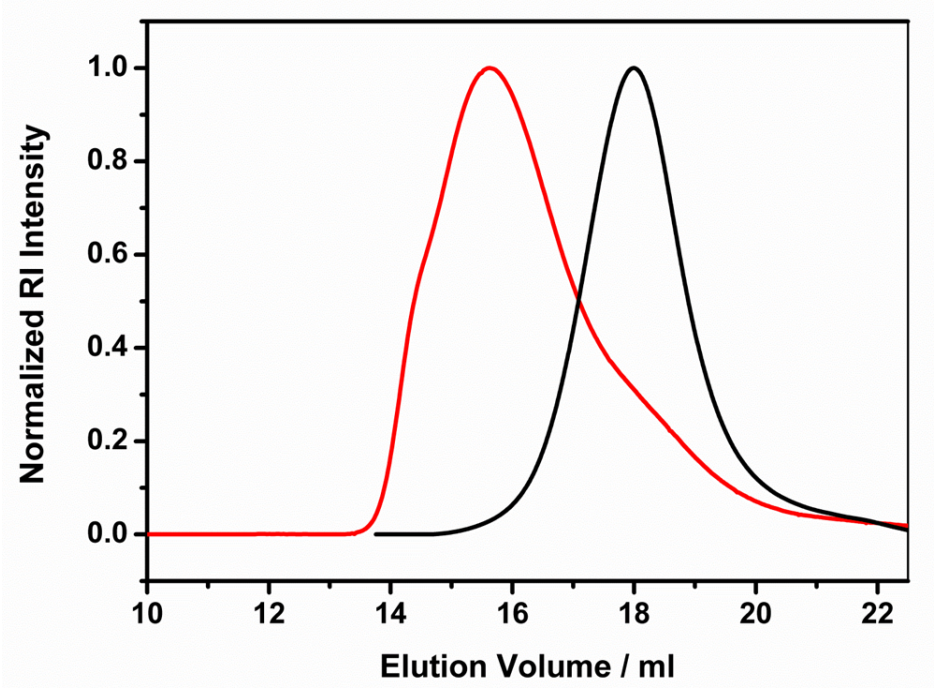

Figure S 2: GPC elugram of P(AN-DAAM) (red) and PAN (black).

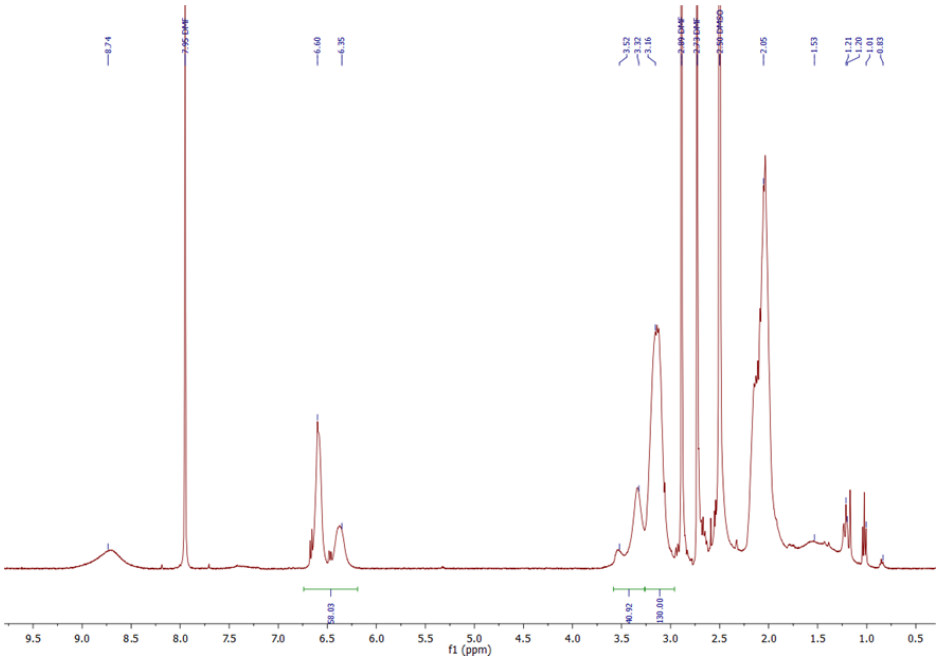

Figure S 3: ^{1}H-NMR spectrum of P(AN-DAAM): the length of the DAAM block is estimated by integration of the dopamine signal and the backbone signal.

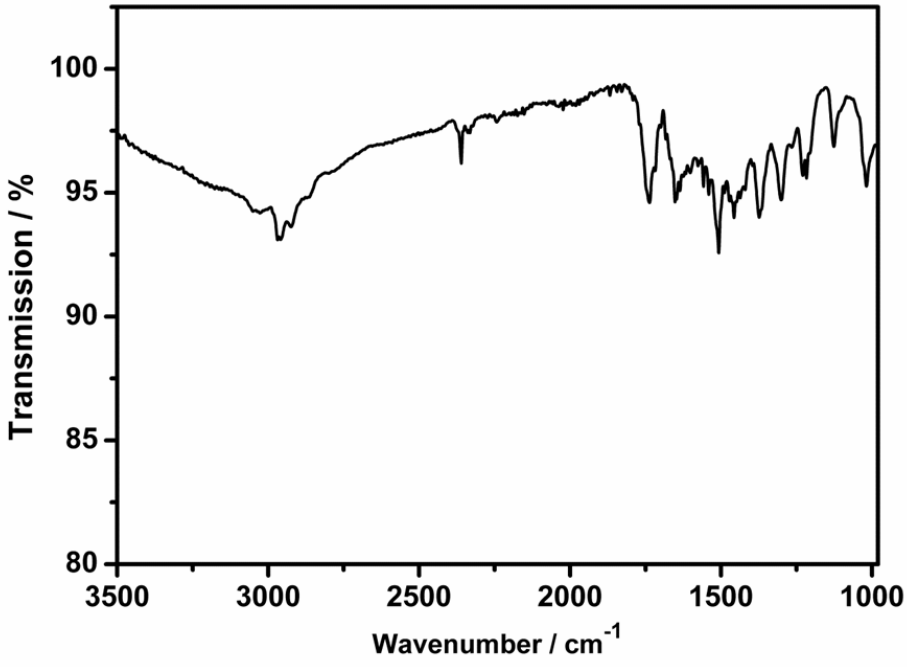

Figure S 4: IR spectrum of polymer-coated TiO_2 nanotubes.

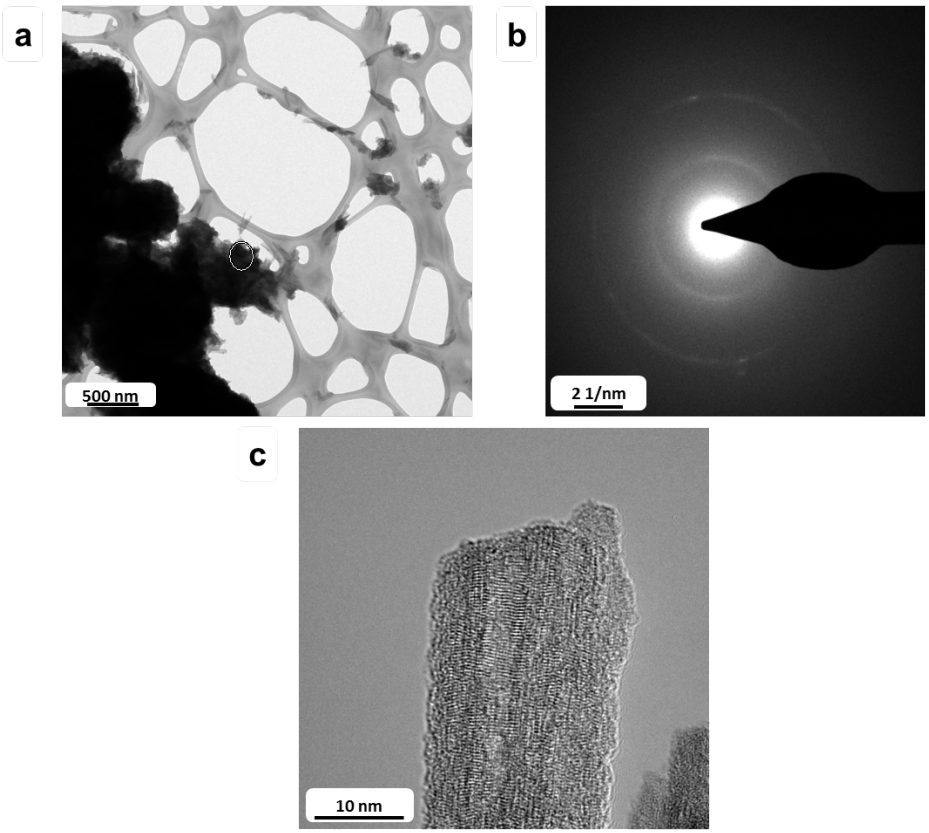

Figure S 5: TEM image (a) and SAED analysis (b) of carbon-coated anatase nanotubes. The white circle in (a) indicates the position at which SAED analysis was performed. (c) HRTEM image of carbon-coated anatase TiO_2 nanotubes.

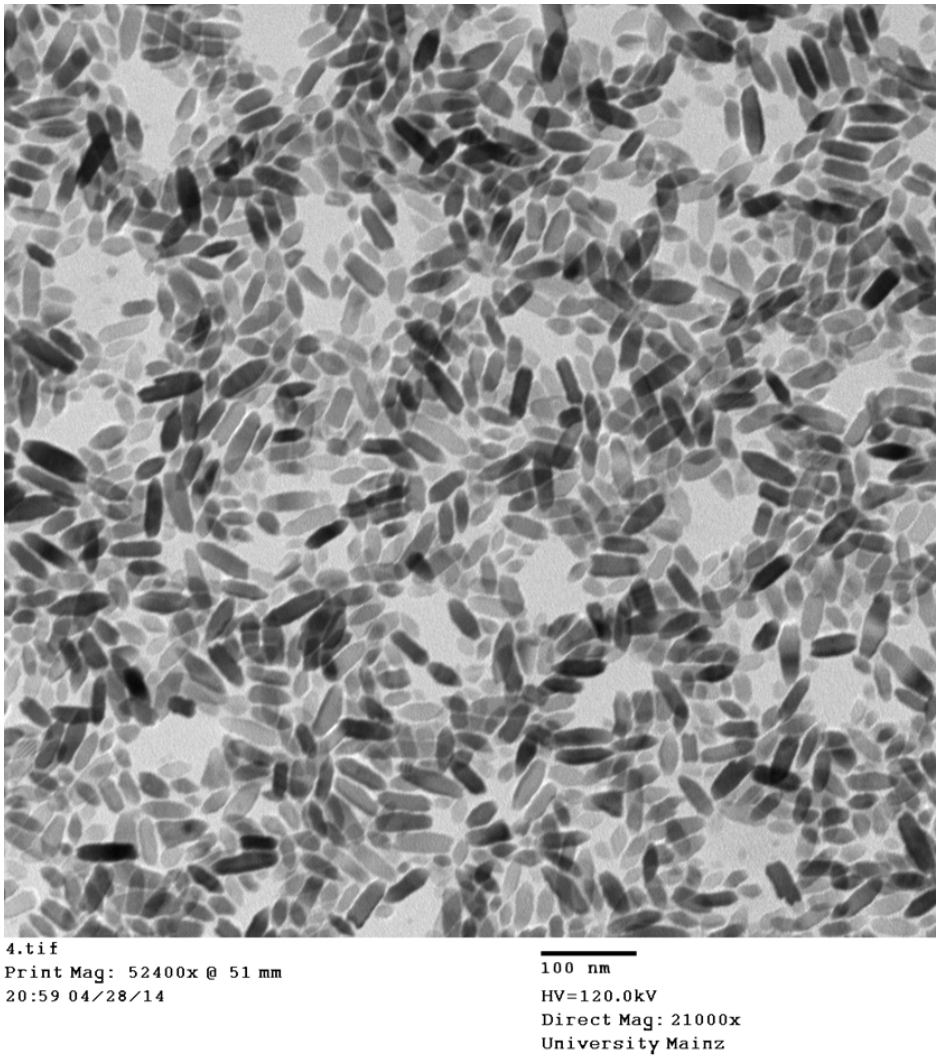

Figure S 6: TEM image of anatase TiO_2 nanorods, synthesized according to the method described in Oschmann et al.41

References

1. M. Z. Jacobson and M. A. Delucchi, Sci. Am., 301, 585 (2009).
2. M. Z. Jacobson and M. A. Delucchi, Energy Policy, 39, 1154 (2011).
3. M. A. Delucchi and M. Z. Jacobson, Energy Policy, 39, 1170 (2011).
4. M. Armand and J.-M. Tarascon, Nature, 451, 652 (2008).
5. B. Scrosati and J. Garche, J. Power Sources, 195, 2419 (2010).
6. B. Scrosati, J. Hassoun, and Y.-K. Sun, Energy Environ. Sci., 4, 3287 (2011).

7. B. Dunn, H. Kamath, and J.-M. Tarascon, Science, 334, 928 (2011).

8. M. M. Thackeray, C. Wolverton, and E. D. Isaacs, Energy Environ. Sci., 5, 7854 (2012).

9. A. Manthiram, J. Phys. Chem. Lett., 2, 176 (2011).

10. V. Palomares et al., Energy Environ. Sci., 5, 5884 (2012).

11. B. L. Ellis and L. F. Nazar, Emerg. Oppor. Energy Storage, 16, 168 (2012).

12. S.-W. Kim, D.-H. Seo, X. Ma, 470 G. Ceder, and K. Kang, Adv. Energy Mater., 2, 710 (2012).

13. M. D. Slater, D. Kim, E. Lee, and C. S. Johnson, Adv. Funct. Mater., 23, 947 (2013).

14. M. R. Palacin, (2014) https://ecs.confex.com/ecs/imlb2014/webprogram/Paper34525.html.

15. T. Xu, W. Wang, M. Gordin, D. Wang, and D. Choi, JOM, 62, 24 (2010).

476 16. Z. Chen, I. Belharouak, Y.-K. Sun, and K. Amine, Adv. Funct.Mater., 23, 959 (2013).

17. N. Takami et al., J. Power Sources, 244, 469 (2013).

18. Z. Yang et al., Chem. Rev., 111, 3577 (2011).

19. X. Chen and S. S. Mao, Chem. Rev., 107, 2891 (2007).

20. P. Roy, S. Berger, and P. Schmuki, Angew. Chem. Int. Ed., 50, 2904 (2011).

21. T. Froeschl et al., Chem. Soc. Rev., 41, 5313 (2012).

22. B. Zachau-Christiansen, K.West, T. Jacobsen, and S. Atlung, Solid State Ion., 28–30, 1176 (1988).

23. T. Ohzuku, T. Kodama, and T. Hirai, J. Power Sources, 14, 153 (1985).

24. R. J. Cava, D. W. Murphy, S. Zahurak, A. Santoro, and R. S. Roth, J. Solid State Chem., 53, 64 (1984).

25. D. W. Murphy, R. J. Cava, S. M. Zahurak, and A. Santoro, Solid State Ion., 9–10(1), 413 (1983).

26. D. Deng, M. G. Kim, J. Y. Lee, and J. Cho, Energy Env. Sci, 2, 818 (2009).

27. C. Jiang and J. Zhang, J. Mater. Sci. Technol., 29, 97 (2013).

28. P. Kubiak et al., Small, 1 (2011).

29. A. K. Rai et al., Electrochimica Acta, 90, 112 (2013).

30. C. Jiang et al., J. Power Sources, 166, 239 (2007).

31. J. Moskon, R. Dominko, R. Cerc-Korosec, M. Gaberscek, and J. Jamnik, J. Power Sources, 174, 683 (2007).

32. L. J. Fu, L. C. Yang, Y. Shi, B.Wang, and Y. P.Wu,MicroporousMesoporousMater., 117, 515 (2009).

33. S. K. Das, M. Patel, and A. J. Bhattacharyya, ACS Appl. Mater. Interfaces, 2, 2091 (2010).

34. F.-F. Cao, X.-L.Wu, S. Xin, Y.-G. Guo, and L.-J.Wan, J. Phys. Chem. C, 114, 10308 (2010).

35. S.-J. Park, Y.-J. Kim, and H. Lee, J. Power Sources, 196, 5133 (2011).

36. S. K. Das, S. Darmakolla, and A. J. Bhattacharyya, J.Mater. Chem., 20, 1600 (2010).

37. L. J. Fu et al., J. Power Sources, 159, 219 (2006).

38. V. G. Pol, S.-H. Kang, J. M. Calderon-Moreno, C. S. Johnson, andM. M. Thackeray, J. Power Sources, 195, 5039 (2010).

39. H. Bai, Z. Liu, and D. D. Sun, J. Mater. Chem., 22, 24552 (2012).

40. D. Bresser et al., J. Power Sources, 206, 301 (2012).

41. B. Oschmann et al., Macromol. Rapid Commun., 34, 1693 (2013).

42. D. Bresser et al., J. Power Sources, 248, 852 (2014).

43. D. Wang et al., ACS Nano, 3, 907 (2009).

44. S. Ding et al., Chem. Commun., 47, 5780 (2011).

45. J. S. Chen, Z. Wang, X. C. Dong, P. Chen, and X. W. (David) Lou, Nanoscale, 3, 2158 (2011).

46. M. Wagemaker, W. J. H. Borghols, and F. M. Mulder, J. Am. Chem. Soc., 129, 4323 (2007).

47. G. Sudant, E. Baudrin, D. Larcher, and J.-M. Tarascon, J. Mater. Chem., 15, 1263 (2005).

48. L. Kavan, J. Rathousky, M. Grätzel, V. Shklover, and A. Zukal, J. Phys. Chem. B, 104, 12012 (2000).

49. X. Gao et al., J. Phys. Chem. B, 108, 2868 (2004).

50. J. Xu, C. Jia, B. Cao, and W. F. Zhang, Electrochimica Acta, 52, 8044 (2007).

51. S.-W. Kim et al., ACS Nano, 3, 1085 (2009).

52. M. Park, X. Zhang, M. Chung, G. B. Less, and A. M. Sastry, J. Power Sources, 195, 53. P. Zhu et al., RSC Adv., 2, 531 (2012).

54. F. Wu et al., J. Alloys Compd., 509, 3711 (2011).

55. V. Gentili et al., Chem. Mater., 24, 4468 (2012).

56. G. S. Zakharova et al., J. Phys. Chem. C, 116, 8714 (2012).

57. H. Zhang et al., J. Phys. Chem. C, 111, 6143 (2007).

58. J. Kim and J. Cho, J. Electrochem. Soc., 154, A542 (2007).

59. H. Li and H. Zhou, Chem. Commun., 48, 1201 (2012).

60. S. Brutti, V. Gentili, H. Menard, B. Scrosati, and P. G. Bruce, Adv. Energy Mater., 2,3 322 (2012).

61. G. Zampardi, E. Ventosa, F. La Mantia, and W. Schuhmann, Chem. Commun., 49, 9347 (2013).

62. G.-N. Zhu, C.-X. Wang, and Y.-Y. Xia, J. Electrochem. Soc., 158, A102 (2011).

63. Y. Xu et al., Chem. Commun., 49, 8973 (2013).

64. L.Wu,D.Buchholz,D.Bresser, L. Gomes Chagas, and S. Passerini, J. Power Sources, 251, 379 (2014).

65. K.-T. Kim et al., Nano Lett., 14, 416 (2014).

66. L. Wu et al., Adv. Energy Mater.,(2014).

67. S.-M. Oh et al., ACS Appl. Mater. Interfaces, 6, 11295 (2014).

68. H. A. Cha, H. M. Jeong, and J. K. Kang, J. Mater. Chem. A, 2, 5182 (2014).

69. J. R. Gonzalez, R. Alcantara, F. Nacimiento, G. F. Ortiz, and J. L. Tirado,

CrystEng- Comm, 16, 4602 (2014).

70. D. E. Bergbreiter, P. L. Osburn, and C. Li, Org. Lett., 4, 737 (2002).

71. J. T. Lai, D. Filla, and R. Shea, Macromolecules, 35, 6754 (2002).

72. D. V. Bavykin, V. N. Parmon, A. A. Lapkin, and F. C. Walsh, J. Mater. Chem., 14, 3370 (2004).

73. H.-C. Chiu, Y.-W. Lin, Y.-F. Huang, C.-K. Chuang, and C.-S. Chern, Angew. Chem. Int. Ed., 47, 1875 (2008).

74. Z. Hu, Y. Liu, C. Hong, and C. Pan, J. Appl. Polym. Sci., 98, 189 (2005).

75. T. Rajh et al., J. Phys. Chem. B, 106, 10543 (2002).

76. E. Faure et al., Top. Issue Polym. Chem., 38, 236 (2013).

77. D. S. Knight and W. B. White, J. Mater. Res., 4, 385 (1989).

78. R. Baddour-Hadjean and J.-P. Pereira-Ramos, Chem. Rev., 110, 1278 (2010).

79. M. Wagemaker, G. J. Kearley, A. A. van Well, H. Mutka, and F. M. Mulder, J. Am. Chem. Soc., 125, 840 (2003).

80. K. Shen, H. Chen, F. Klaver, F. M. Mulder, and M. Wagemaker, Chem. Mater., 26, 1608 (2014).

81. W. J. H. Borghols et al., Phys. Chem. Chem. Phys., 11, 5742 (2009).

82. J. Wang, J. Polleux, J. Lim, and B. Dunn, J. Phys. Chem. C, 111, 14925 (2007).

83. R. van de Krol, A. Goossens, and J. Schoonman, J. Phys. Chem. B, 103, 7151 (1999).

84. W. J. H. Borghols et al., J. Electrochem. Soc., 157, A582 (2010).

85. M. V. Reddy, X. W. Valerie Teoh, T. B. Nguyen, Y. Y. Michelle Lim, and B. V. R. Chowdari, J. Electrochem. Soc., 159, A762 (2012).

86. R. A. Huggins, J. Power Sources, 81–82, 13 (1999).

87. E. Madej, F. La Mantia,W. Schuhmann, and E. Ventosa, Adv. Energy Mater., n/a–n/a (2014).

88. H.-T. Fang et al., Nanotechnology, 20, 225701 (2009).

89. W. Dreyer et al., Nat. Mater., 9, 448 (2010).

90. W. Dreyer, C. Guhlke, and R. Huth, Phys. Nonlinear Phenom., 240, 1008 (2011).

91. T. Brezesinski, J. Wang, J. Polleux, B. Dunn, and S. H. Tolbert, J. Am. Chem. Soc., 131, 1802 (2009).

92. J.-Y. Shin, D. Samuelis, and J. Maier, Adv. Funct. Mater., 21, 3464 (2011).

93. J.-H. Kim, K. Zhu, J. Y. Kim, and A. J. Frank, Electrochimica Acta, 88, 123 (2013).

94. B. Laskova, M. Zukalova, A. Zukal, M. Bousa, and L. Kavan, J. Power Sources, 246, 103 (2014).

95. P. Heitjans and S. Indris, J. Phys. Condens. Matter, 15, R1257 (2003).

96. L. Wu et al., Energy Environ. Sci., 7, 323 (2014).

4.1.3 Carbon Coating of Au@ZnO Multipods

Besides TiO_2, ZnO is also a very attractive alternative electrode material for lithium-ion batteries due to its high theoretical specific capacity. However, it suffers again from low electrical conductivity and from capacity fading due to the irreversible formation of Li_2O and due to volume changes.

The extension of the carbon coating coating approach, introduced in the previous chapters, to another transition metal oxide was the aim of this project. Another focus was the use of an advanced morphology of the inorganic particles. The use of multipod shaped ZnO nanoparticles appeared to be interesting, as the use of tetrapod shaped particles were reported to form a highly interconnected network allowing an advanced percolation network for charge carriers in solar cells. Indeed, the synthesis of multipod shaped ZnO nanoparticles could be achieved in Prof. Tremel's group by Muhammad Nawaz Tahir, whereby the ZnO nanoparticles are synthesized by use of a spherical shaped gold particle as a template for the growth of ZnO branches.

The carbon precursor polymer, especially the anchoring unit, always needs to be adjusted to the inorganic particle. Since thiol groups bind efficiently both onto gold and onto ZnO surfaces, thiol groups were used as anchoring units. These thiol groups were introduced by aminolysis of the NAS reactive ester with cysteamine. Both block copolymer and statistical polymer were synthesized in order to investigate, which polymer structure binds more effectively onto this special multipod morphology. It could be shown that the statistical copolymer binds more effectively onto the Au@ZnO nanoparticles as confirmed by TGA. Pyrolysis of the hybrid material leads to a carbon coating around the particles, which is proven by SEM and EDX as well as by HRTEM. The carbon coated particles were evaluated as an anode material in lithium-ion batteries and compared to uncoated Au@ZnO particles to investigate the influence of the coating and in addition to carbon coated ZnO nanorods in order to investigate the influence of the morphology. The coating has a huge impact on the

battery performance, since capacities twice as high as for uncoated particles can be obtained (831 mAh g^{-1} after 150 cycles for coated particles and only 353 mAh g^{-1} after 10 cycles for uncoated particles). Furthermore, the multipod morphology is advantageous towards a simple rod morphology, since the cycling stability for multipods is higher compared to rods.

Finally, an in-situ XRD analysis during the first charge and discharge cycle of carbon coated Au@ZnO particles was conducted in order to investigate structural changes during (de-)lithiation. This analysis reveals that the gold particles have several functions: Besides the function as a template and as an additional conductive additive, the gold particles participate also in the (de-)lithiation mechanism.

As in the previous publications, Muhammad Nawaz Tahir contributed to this work with the synthesis of inorganic nanoparticles. Electron microscopy was conducted by Ingo Lieberwirth. All further synthesis and characterization steps (except in-situ XRD measurement) were conducted by myself, whereas for the electrochemical characterization I got support from Franziska Mueller and Dominic Bresser.

4.1.3.1 Publication in Macromolecular Rapid Communication, DOI: 10.1002/marc.201400647

Precursor Polymers for the Carbon Coating of Au@ZnO Multipods for Application as Active Material in Lithium-Ion Batteries

Bernd Oschmann, Muhammad Nawaz Tahir, Franziska Mueller, Dominic Bresser, Ingo Lieberwirth, Wolfgang Tremel, Stefano Passerini, and Rudolf Zentel

Abstract

The synthesis of statistical and block copolymers based on polyacrylonitrile, as a source for carbonaceous materials, and thiol-containing repeating units as inorganic nanoparticle anchoring groups is reported. These polymers are used to coat Au@ZnO multipod heteroparticles with polymer brushes. IR-spectroscopy and transmission electron microscopy prove the successful binding of the polymer onto the inorganic nanostructures. Thermogravimetric analysis is applied to compare the binding ability of the block and statistical copolymers. Subsequently, the polymer coating is transformed into a carbonaceous (partially graphitic) coating by pyrolysis. The obtained carbon coating is characterized by Raman spectroscopy and energy dispersive X-ray (EDX) spectroscopy. The benefit of the conformal carbon coating of the Au@ZnO multipods regarding its application as lithium-ion anode material is revealed by performing galvanostatic cycling, showing a highly enhanced and stabilized electrochemical performance of the carbon-coated particles (still 831 mAh g^{-1} after 150 cycles) with respect to the uncoated ones (only 353 mAh g^{-1} after 10 cycles).

1. Introduction

The effective storage of electric energy still remains a main societal challenge and lithium-ion batteries (LIBs) are certainly one of the most promising candidates to address this issue. Current lithium-ion technology is mainly based on insertion or intercalation compounds as active materials, which offer highly efficient energy storage and long-term stable cycling performance, though intrinsically limited capacities. This is also true for graphite, the state-of-the-art anode material in LIB, for which the theoretical maximum specific capacity is nowadays readily achieved (372 mAh g^{-1}). Accordingly, further capacity improvements require the utilization of alternative anode materials like silicon or tin, reversibly alloying with lithium. However, due to the rather extensive volume variations upon (de-)lithiation, these materials are severely affected by rather rapid capacity fading upon long-term cycling.[1–3] To overcome this drawback, metal oxide nanoparticles were proposed, initially forming a volume-changes buffering matrix of lithium oxide (Li_2O). Nano-sized ZnO, for instance, provides a theoretical specific capacity of 978 mAh g^{-1} (assuming the fully reversible formation of this Li_2O matrix)[4] and short lithium-ion and electron diffusion distances due to the high surface-to-volume ratio.[3] However, ZnO nanoparticles suffer from two main issues, namely, low electronic conductivity[3] and the irreversibility of the Li_2O formation. A rather common approach nowadays to overcome the conductivity issue is the realization of (frequently carbonaceous) conductive coatings in combination with the addition of carbonaceous materials.[5–8] Typically, the nanoparticles are dispersed in a dispersion or solution containing the dissolved carbon precursor, for instance, sugar, which is then converted to a carbonaceous surface layer. This frequently results in a rather inhomogeneous carbon distribution, as the usually used precursors are not homogenously deposited on the particles surface. However, a thin and homogeneous coating is commonly desired as it enables the continuous formation of electron conducting pathways while the Li-ion diffusion through it.[9] Beside the gain in electronic conductivity, such a coating

can also prevent parasitic side reactions (for instance, with the electrolyte), buffer the possible volume changes occurring during measurements and reduce problems arising from phase separation during Li_2O formation.[10] Moreover, depending on the coating method, it may stabilize the frequently defect-afflicted nanoparticles surface.[7,11,12] Nevertheless, the realization of a thin and homogeneous carbon film surrounding the nanoparticles is not trivial. One very promising approach is the chemical bonding of polymer brushes onto the inorganic nanoparticles, resulting in a thin and highly homogenous polymer film.[7,13] Another approach to improve the performance of such "challenging" alternative lithium-ion anode materials is the smart design of advanced hierarchical nanostructures such as superparticle morphologies or tubular systems with a high surface area and high interconnectivity.[14–16] Among these, multipod structures are presumably especially advantageous in this context, as multipods span the volume in all three dimensions, thus offering a very high surface area, allowing enhanced interconnectivity and percolation of the nanoparticles, which results, inter alia, in a facilitated charge transfer within the electrode coating layer.[17] Herein, we report the synthesis of statistical and block copolymers as carbon precursors, which are designed to bind onto the branched shape Au@ZnO heteroparticles. The copolymers are based on polyacrylonitrile, a well-known carbon precursor, and repeating units containing thiol groups enabling the binding of the polymer onto the inorganic particles. A thermal treatment converts the polymer coating into a homogeneous carbonaceous coating. Thus, the herein introduced strategy combines the two previously mentioned approaches, i.e., (i) an advanced 3-dimensional particle morphology and (ii) a conformal carbon coating. The carbon-coated particles are characterized by transmission electron microscopy (TEM), Raman spectroscopy, and energy dispersive X-ray spectroscopy to confirm the presence of the carbon coating, as well as X-ray diffraction. The readily synthesized and fully characterized nano-heteroparticles were studied as lithium-ion anode material with a particular focus on the effect of the carbon coating.

2. Results and Discussion

2.1. Synthesis and characterization of carbon-coated Au@ZnO heteroparticles

As active material allowing 3-dimensional percolation, multipods consisting of five to six ZnO nanorods connected to a gold core were chosen due to the rather easy synthesis. For the application of a carbonaceous coating we had to modify a recently reported approach based on the anchoring of a polymer precursor,[7] as schematically depicted in Figure 1a. This polymer (polyacrylonitrile, PAN) is, later on, converted into a carbonaceous coating[22,23] by a facile heat treatment. However, extending this method for the realization of a thin and homogenous carbonaceous coating from TiO_2[7] to Au@ZnO particles required a modification of the polymer design. In fact, to anchor the polymer both to ZnO and gold core thiols were used.[24–27] For the realization of a homogeneous, but rather thin carbonaceous layer (not affecting the Li^+ ion transport into the active material particles), both statistical- and block-copolymers were investigated. Also, the reactive ester monomer was varied accordingly. Due to the required utilization of DMF or DMSO as solvent, resulting from the limited solubility of polyacrylonitrile, it appeared advantageous to use N-acryloylxysuccinimide (NAS) instead of the very unpolar pentafluorophenyl acrylate, as in the previous study.[7] NAS is a reactive ester monomer and can be used to introduce anchoring units by aminolysis of the ester group. Both block- and statistical- copolymers were synthesized by reversible addition fragmentation chain transfer (RAFT) polymerization using 2-dodecylsulfanylthiocarbonylsulfanyl-2-methyl propionic acid (DMP) as a chain transfer agent. The synthesis scheme of the polymers is presented in Figure 1b. The statistical copolymer was obtained by mixing both monomers for the polymerization step (see Figure 1b, i)) resulting in poly(acrylonitrile-r-acrlyoxysuccinimide) (P(AN-r-NAS)). Copolymerization analysis according to Fineman-Ross revealed 0.80 for AN and 0.75 for NAS as copolymerization parameters (see Figure S1). As both parameters are smaller than 1, the

co-monomers should be individualized within the copolymer. According to the NMR spectrum, the use of a monomer ratio of AN:NAS 250:35 yields a copolymer consisting of about 17 reactive ester units and around 99 acrylonitrile units (Figure S2 and Table S1). The thiol anchoring group was introduced by aminolysis of the reactive ester with cysteamine, resulting in poly(acrylonitrile-r-cysteamidacrylate) (P(AN-r-CAA).

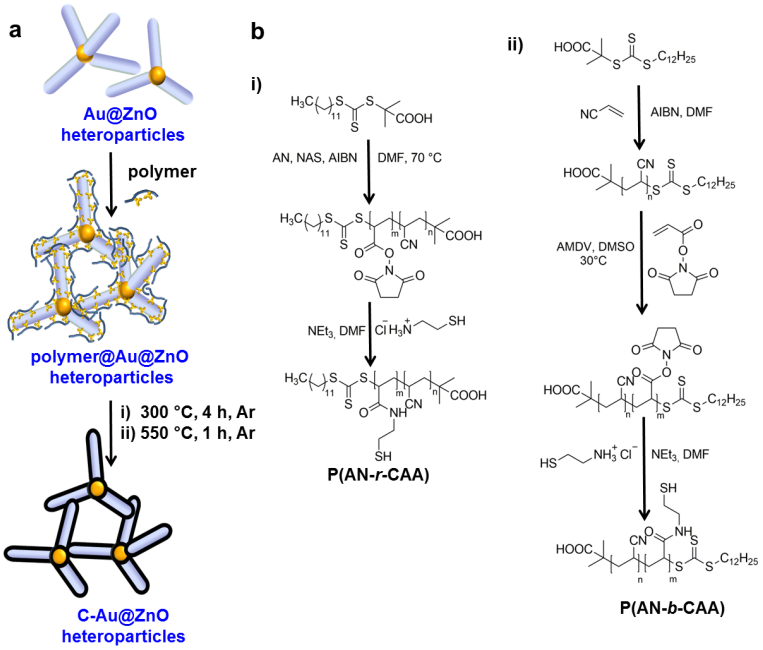

Figure 1: a) Schematic illustration of the synthesis of carbon-coated Au@ZnO nano-heteroparticles. (b) Synthesis route of (i) poly(acrylonitrile-r-cysteamidacrylate) and (ii) poly(acrylonitrile-b-cysteamidacrylate) via RAFT polymerization.

The occurrence of this reaction is confirmed by NMR spectroscopy (Figure S3) and IR spectroscopy (Figure 2a). The reactive ester bond disappears (1705 cm^{-1}) and, instead, an amide bond appears after the polymer analogous reaction (1656 cm^{-1}) as shown in Figure 2a. The polymer was further characterized by size exclusion chromatography (SEC) with hexafluoroisopropanol (HFIP) as solvent as shown in Figure 2b. The molecular weight determined by SEC of P(AN-r-NAS) is 13,500 g mol^{-1} and

the polydispersity is 1.23. After polymer analogous reaction the molar mass appears to be higher (27,500 g mol^{-1}). This increase of the molar mass is presumably related to the polar cysteamine acrylamide units, which are well soluble in HFIP (NAS is not soluble). Consequently, the polymer is more easily swelled in the polar HFIP, leading to an increased hydrodynamic volume of the polymer and a decreased elution volume. Nevertheless, the size distribution of the polymer did not change upon this reaction and the polydispersity index was 1.19. Hence, intermolecular disulfide formation could be successfully avoided (Figure 2b).

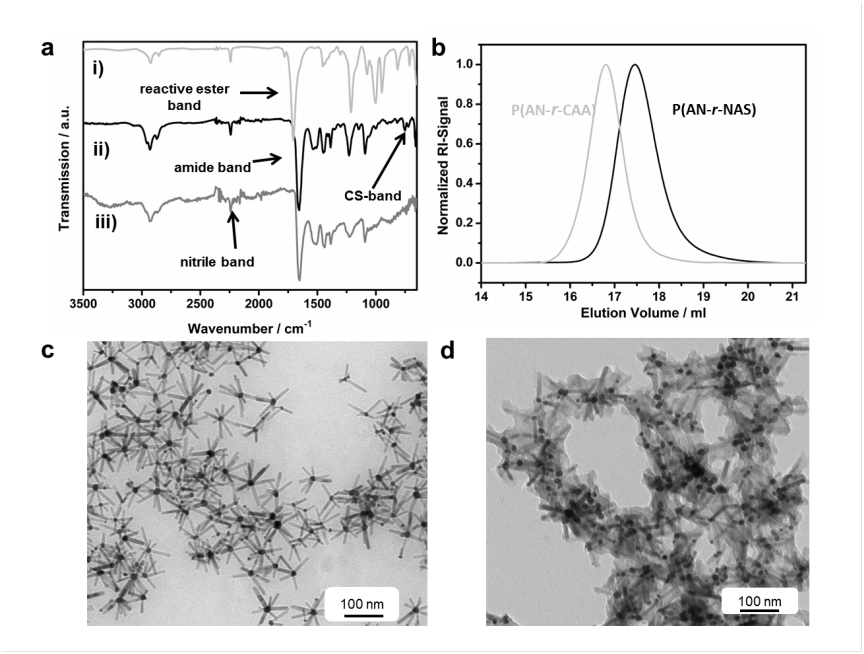

Figure 2: a) IR spectrum of (i) poly(acrylonitrile-r-acrlyoxysucciimid), (ii) poly(acrylonitrile-r-cysteamidacrylate), and (iii) polymer-functionalized Au@ZnO heteronanoparticles, showing typical polymer bands. (b) Size exclusion chromatogram of P(AN-r-NAS) (black) and P(AN-r-CAA) (grey). (c) TEM micrograph of as-synthesized Au@ZnO heteroparticles. (d) TEM micrograph of polymer-coated Au@ZnO particles.

The block copolymer P(AN-b-CAA) was synthesized as schematically illustrated in

Figure 1b (ii) by first polymerizing the acrylonitrile block and then using the PAN as macroinitiator and NAS as the second monomer to obtain P(AN-b-NAS). The conversion of this polymer with cysteamine hydrochloride resulted in P(AN-b-CAA). Zorn et al. reported high grafting densities for block copolymers with a short anchor block (less than 30 anchoring repeating units) and a longer solubilizing block (around 100 repeating units).[13] Thus, a block copolymer with block lengths in these ranges was synthesized as confirmed by NMR, IR, and SEC, yielding a narrowly distributed block copolymer with a PDI of 1.18 (see Figure S4 and Table S2). Furthermore, the monomer composition of the block copolymer is similar to the composition of P(AN-r-CAA) (105 AN units and 24 CAA units), i.e., both systems are comparable from this point of view (see Table S2). The Au@ZnO heteroparticles were synthesized according to a previously reported method,[19] whereby it was possible to scale up the reaction to several gram batches. First, Au nanoparticle intermediates were formed in situ by reduction of the $[AuCl_4]^-$ precursor in presence of oleylamine at 120 °C followed by the heterogeneous nucleation of ZnO on the in situ formed gold nanoparticles.[20] The gold nanoparticles act as structure bearing template to achieve multipod morphology and provide electronic conductivity to the attached ZnO branches when used as anode material. Moreover, the gold itself is electrochemically active during electrochemical cycling forming gold-lithium alloys.[28,28–30] A transmission electron microscopy (TEM) micrograph of the as-synthesized Au@ZnO heteroparticles is given in Figure 2c. The size of the gold particles is estimated to around 8 nm and the average length of the ZnO branches is in the range from $\approx$ 37 to 45 nm (polydispersity index: 1.11) with an average diameter of around 8 nm (polydispersity index: 1.04). The polydispersity of the ZnO branches itself is obviously rather low. However, the gold particles bear a variable number of ZnO branches. The majority of these multipods consists of around five to six ZnO branches per gold particle. According to the results obtained by energy dispersive X-ray spectroscopy, the elemental composition of heteroparticles is around 87 mol%

of ZnO and 13 mol% of gold. The surface modification of Au@ZnO heteroparticles, which are initially stabilized by oleyl amine, with the different polymers was conducted in a DMF/chloroform mixture. In contrast to the oleyl amine-functionalized particles, which are dispersible in non-polar solvents like hexane and chloroform, the polymer-functionalized heteroparticles form stable dispersions in solvents like DMF as shown in Figure S5a. The presence of the polymer coating was further confirmed by IR spectroscopy after work-up of the hybrid system, i.e., the centrifugation to remove excess polymer. The IR spectrum revealed the typical polymer bands such as the nitrile band at 2241 cm^{-1} (Figure 2a). Thermogravimetric analysis (TGA) was conducted to quantify which copolymer structure binds more effectively onto the Au@ZnO heteroparticles. The TGA data shown in Figure S5b revealed that the statistical copolymer binds more effectively onto the special morphology of Au@ZnO particles compared to the block copolymer, since the organic content is 12.5 wt.% for the statistical copolymer and only 11 wt.% for the block copolymer. Also after pyrolysis at 550 °C, the carbon content was higher for the statistical copolymer (8 wt.%) compared to the block copolymer (5 wt.%) as shown in Figure S5c. Thus, for the further investigation the more effectively binding statistical copolymer was used. TEM analysis of the P(AN-r-CAA)-coated Au@ZnO heteroparticles (Figure 2d) confirmed the retention of the multipod morphology after functionalization and the presence of the polymer coating, indicated by the corona (lower contrast) around the particles. For the conversion of the polymer coating into a carbonaceous coating, the hybrid material was pyrolyzed under argon at 550 °C. As evidenced by X-ray diffraction (XRD), the relative position and intensity of both ZnO and Au reflections remain unchanged after the pyrolysis, confirming the absence of phase impurities and the stability of the initial phases under above mentioned pyrolysis conditions (Figure 3a). The successful conversion of the polymer coating into carbonaceous material was confirmed by Raman spectroscopy. After pyrolysis the characteristic D (1349 cm^{-1}) and G band (1590 cm^{-1}), corresponding to disordered and graphitic

C-C stretching of sp^2-hybridized carbon, are observed (Figure 3b).[31,32] The SEM micrograph in Figure 3c shows carbon-coated multipods after pyrolysis, confirming the retention of the branched shape morphology of Au@ZnO heteroparticles. The elemental composition of the hybrid material after pyrolysis was investigated by energy dispersive X-ray (EDX) spectroscopy of the area shown in Figure S6a. The resulting spectrum is presented in Figure 3d.

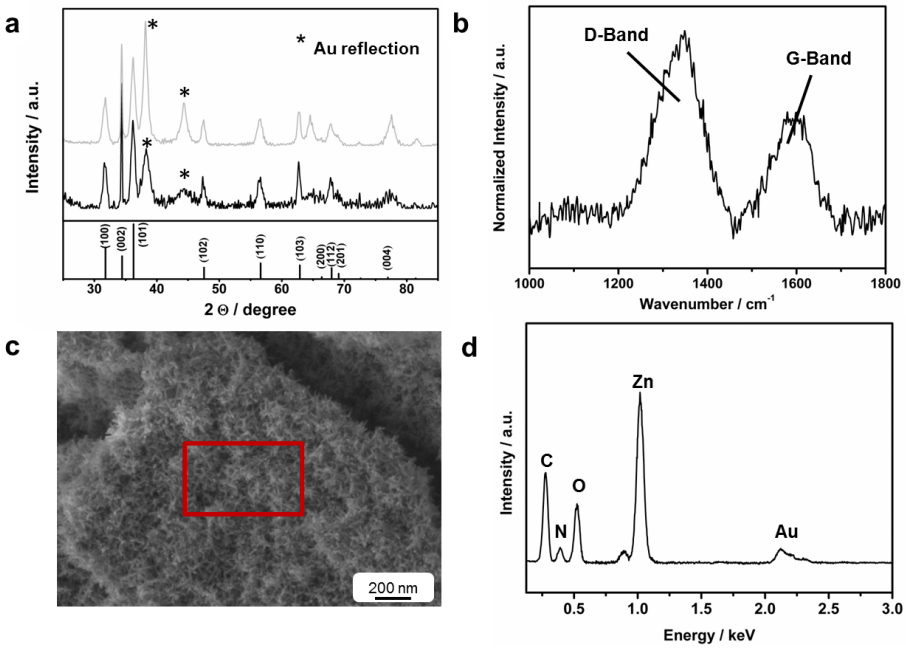

Figure 3: a) XRD patterns of as-synthesized Au@ZnO (black) and carbon-coated Au@ZnO heteroparticles (grey), i.e., before and after pyrolysis, respectively (the JCPDS 01-071-6424 of ZnO is given in the bottom). (b) Raman spectrum of carbon-coated Au@ZnO. (c) SEM micrograph and (d) EDX spectrum of carbon-coated Au@ZnO heteroparticles.

Beside the expected signals from zinc, oxygen, gold, and carbon the EDX spectrum revealed also the presence of nitrogen, which is attributed to the utilization of poly-acrylonitrile as carbon precursor and the formation of N-doped (partially) graphitic material. A thin carbon layer (around 2 nm) could also be imaged by high reso-

lution TEM (Figure S6b). It might be noted that for this initial characterization of the material, no additional carbon was added. To explore the potential application of C-Au@ZnO nanomaterials as lithium-ion anode material, however, conductive carbon was added prior to the pyrolysis (as described in the experimental section), following a previously described processing.[11,21]

2.2. Electrochemical characterization

Figure 4a shows the cyclic voltammogram (CV) of electrodes based on carbon-coated Au@ZnO heteroparticles. In the first cathodic sweep, a broad shoulder between 0.5 – 0.9 V is observed which is presumably related to the decomposition of the electrolyte, commonly occurring at such potential values and resulting in the formation of a solid electrolyte interphase (SEI).[33] The main cathodic peak at 0.4 V can be ascribed to the reduction of ZnO to amorphous Li_2O and metallic Zn.[34] Below 0.3 V the alloying of Zn and gold with Li occurs.[4,34,35] For the subsequent anodic sweep, the characteristic peaks for the stepwise dealloying process of LiZn to Li_2Zn_5 between 0.1 V and 0.8 V during the anodic sweep are less distinct, as described in literature for pure ZnO,[34] and are rather broad. The reason for this latter observation might be the overlapping of the dealloying peaks of Zn/Li and Au/Li, which occur partially in the same voltage range,[35] as well as an increased electronic conductivity due to the presence of carbon and gold. The broad peak at about 1.3 V might be related to the (partial) decomposition of Li_2O.[4] Upon the second cathodic sweep the profile of the CV response is altered significantly, indicating the rather huge structural reorganization of the active material after the first lithiation.[36] Indeed, upon the following cyclic sweeps no substantial further changes of the CV response are observed. To further investigate the contribution of gold to the overall electrochemical (de-)lithiation process in situ XRD analysis was carried out. Beside the recently reported features for ZnO based materials, like the disappearance of the ZnO-related reflections upon lithiation (between 0.2 V and 0.6 V) in the range of 30° and 38° (see Figure 4b),[36] additional features were observed

arising from the presence of gold in these nano-heteroparticles. The intensity of the Au(111) reflection centered at 2Θ of around (38.64°) obviously decreases below 0.2 V as shown in Figure 4c and a new reflection assigned to the formation of an Au/Li alloy phase appears (Figure 4d). This newly appearing reflection decreases in intensity when the electrode is subsequently delithiated (between 0.1 V and 0.6 V, Figure S7), indicating the good reversibility of the Au/Li alloying reaction (Figure S7).[29,37,38]

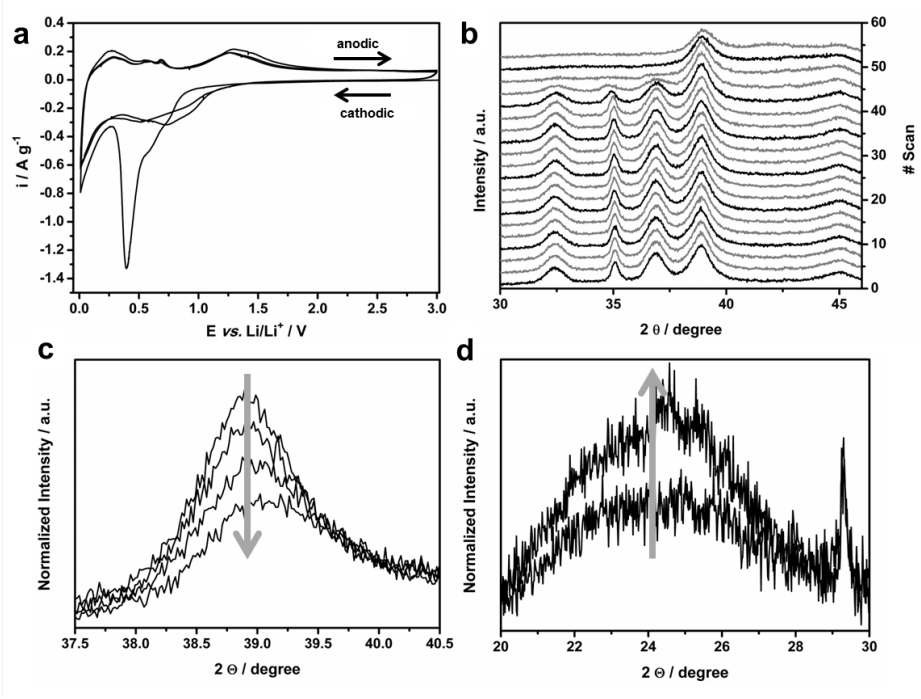

Figure 4: a) Cyclic voltammetry of carbon-coated Au@ZnO heteroparticles. (b) to (d) Excerpts of the in situ XRD analysis upon lithiation: b) the development of selected ZnO and Au reflections upon scan 1 to scan 57 during the initial discharge; (c) the Au (111) reflection upon the scans 54 to 57; and (d) the appearance and development of a new reflection (scan 50 and 57) related to the formation of the Au/Li alloy.

To investigate the influence of the carbon coating on the electrochemical performance, carbon-coated Au@ZnO heteroparticles (in the following abbreviated as C-

Au@ZnO) and uncoated Au@ZnO heteroparticles (Au@ZnO) were studied as anode materials using galvanostatic cycling. Figure 5a and 5b show the results for electrodes based on Au@ZnO and C-Au@ZnO, respectively. The uncoated Au@ZnO delivered an initial specific capacity upon charge of 674 mAh g^{-1}. However, the specific capacity decreases rapidly upon subsequent (dis-)charge cycles before it stabilizes at about 353 mAh g^{-1} (Figure 5a). Electrodes based on C-Au@ZnO (Figure 5b) provided a much higher reversible first cycle capacity (946 mAh g^{-1}), which stabilizes after few cycles at 831 mAh g^{-1}. This value is not only more than twice that delivered by uncoated Au@ZnO, but is very close to the material theoretical capacity, proving that the whole material mass was accessible for the electrochemical processes. The carbon coating obviously enhances the electrochemical performance substantially. It appears noteworthy that the stabilized capacity for branched shape C-Au@ZnO is, by far, exceeding that of Au-ZnO nanoflowers (400 mAh g^{-1}, 120 mA g^{-1}).[28] Furthermore, the positive influence of the multipod morphology becomes apparent by comparison with ZnO nanorods: A rather rapid capacity fading was observed for ZnO nanorod arrays (ZnO arrays on Nickel: 330 mAh g^{-1} at 247 mA g^{-1} after 50 cycles[39] and ZnO nanorods on copper: 338 mAh g^{-1} at a rate of 0.1 mA cm^{-2} after 20 cycles[40]). Finally carbon-coated ZnO nanorods prepared in our group following the same synthesis method showed lower specific capacities and inferior cycling stability compared to the Au@ZnO multipods (see SI, Figure S9). This proves the advantage of the multipod morphology. In Figure 5c and 5d, the corresponding potential profiles of selected cycles for Au@ZnO and C-Au@ZnO are presented, respectively. While Au@ZnO shows a potential profile comparable to the Au-ZnO nanoflower-based profile and a rapid capacity fading (Figure 5c),[4] the potential profile of C-Au@ZnO is obviously altered by the presence of the carbonaceous coating. The capacity retention upon cycling is also clearly improved (Figure 5d). This enhanced reversibility of the electrochemical (de-)lithiation might originate from the increased electronic conductivity within the electrode due to the

3-D conducting multipods C-Au@ZnO structures (this effect might be limited in the uncoated Au@ZnO due to the poor conductivity of ZnO). In addition the carbon coating is supposed to prevent the loss of electronic contact resulting from the large volume changes upon (de-)lithiation, which might inhibit the reversible formation of Li_2O.[10,36]

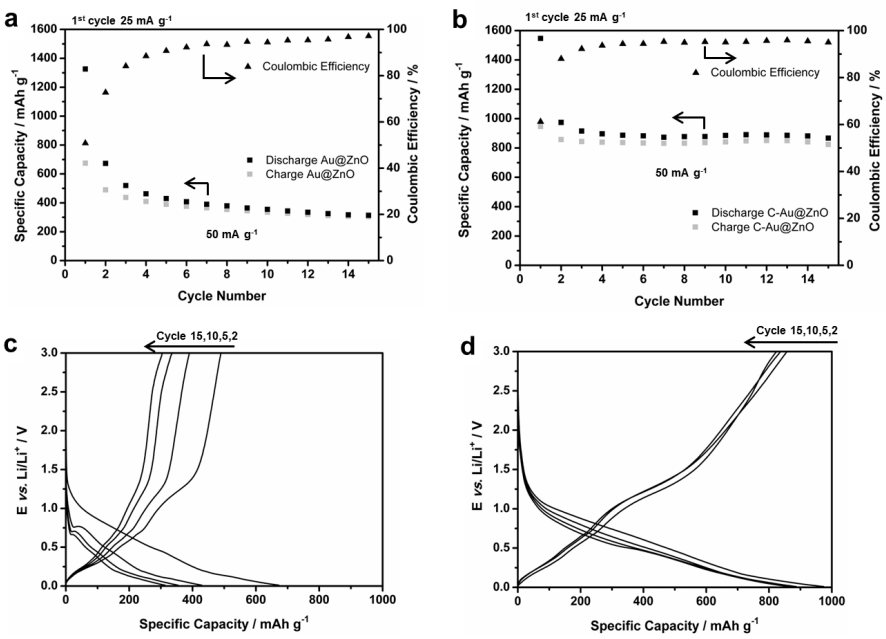

Figure 5: Galvanostatic cycling of a) uncoated Au@ZnO heteroparticles and b) carbon-coated Au@ZnO heteroparticles (1st cycle: 25 mA g^{-1}; following cycles: 50 mA g^{-1}; 0.01 to 3.0 V); corresponding potential profiles of selected cycles for Au@ZnO (c) and C-Au@ZnO (d).

Indeed, one of the major reasons for the fading of Au@ZnO appears to be the capacity loss upon charge at relatively higher potentials ($\geq$ 0.7 V), at which the dealloying should be mostly completed and the reformation of zinc oxide is expected.[4] Finally, in Figure S8 the long-term electrochemical performance of C-Au@ZnO subjected to constant current cycling at 50 mA g^{-1} after several formation cycles is presented, confirming that these nano-heteroparticles provide a highly stable capacity for more

than 150 cycles without significant fading.

3. Conclusions

In summary, we succeeded in the synthesis of block and statistical copolymers containing acrylonitrile as a carbon source and thiol groups as anchoring structures as well as in the synthesis of branched shape Au@ZnO heteroparticles at the gram level. As confirmed by TGA the statistical copolymer anchors more efficiently onto the particle surface. Thus, the statistical copolymer was further used in the present study and thermally transformed into a thin and homogeneous carbon coating surrounding the Au@ZnO heteroparticles. Investigating these carbon-coated Au@ZnO particles as lithium-ion electrode material by means of in situ XRD revealed that the gold nanoparticles, which initially served as structure bearing template, participate in the overall electrochemical reaction by reversibly alloying with lithium. Moreover, the advantageous carbonaceous coating leads to a substantially enhanced cycling stability and increased specific capacity, the latter being only slightly below the theoretical one. As a result, electrodes based on carbon-coated Au@ZnO heteroparticles provide a stable specific capacity of about 870 mAh g^{-1} for more than 150 full (dis-)charge cycles.

Acknowledgements

B.O. wants to thank the “Fonds der Chemischen Industrie”, the MAINZ graduate school, and the IRTG 1404 for financial support. Moreover, B.O. would like to thank Prof. K. Char for the opportunity to work in his laboratory on comparable sulfidic material. All authors would like to thank Gunnar Glasser for SEM measurements.

Supporting Information

Experimental section

Materials:

Dry dimethylsulfoxide (DMSO 99.9 %), dry N,N-dimethylformamide (DMF 99.8 %), cysteamine hydrochloride, tributylphosphine, zinc acetate dehydrate, gold(III) chloride hydrate, and chloroform were purchased from Sigma Aldrich and used as received. Benzyl alcohol, oleylamine and hexane were purchased from Acros and also used without further purification. The reactive ester N-acryloxysuccinimide (NAS) and 2-dodecylsulfanylthiocarbonylsulfanyl-2-methyl propionic acid (DMP), which was used as a chain transfer agent, were synthesized following procedure described already in literature.[18,19]α,α-Azoisobutyronitrile (AIBN, Sigma Aldrich) was recrystallized from diethylether. Acrylonitrile (AN, Merck) was distilled prior to its use to remove the inhibitor. Conductive carbon (Super C65) was supplied by IMERYS.

Synthesis of poly(acrylonitrile-r-cysteamidacrylate):

Acrylonitrile (2.0 ml, 200 eq.), DMP (55.5 mg, 1 eq.), NAS (0,9 ml, 35 eq.), and AIBN (2.5 mg, 0.1 eq.) were dissolved in 6.5 ml DMSO. The solution was degassed by three freeze-pump-thaw cycles. The reaction mixture was stirred overnight at 70 °C and the polymerization was stopped by precipitation in cold methanol. The resulting polymer was dissolved twice more in DMSO and precipitated in cold methanol prior to its drying under reduced pressure. The yield of the yellow powdered polymer poly(acrylonitrile-r-cysteamidacrylate) (PAN-r-NAS) was 45 %.

IR (FTIR): ν = 2924 (w), 2240 (w, -CN), 1705 (s, C=O, reactive ester), 1450 (w), 1211 (s), 998 (s), 954 (w), 652 (w) cm^{-1}.

For the polymer analogues reaction,P(AN-r-NAS) (100 mg, 1 eq.) was dissolved in DMF and a solution of tributylphosphine (0.1 ml) in THF, cysteamine hydrochloride (53 mg, 40 eq.) and triethylamine (65 μl, 40 eq.) were added. The mixture

was stirred overnight and subsequently precipitated in methanol and dried to yield poly(acrylonitrile-r-cysteamidacrylate) (P(AN-r-CAA)), which was characterized by NMR and GPC.

^{1}H NMR (400 MHz, DMSO-d6, δ): 8.37 (bs, NH), 4.15 (bs, SH), 3.34 (bs, CONH-CH_2), 3.09 (s, CH of polymer backbone), 2.25-2.50 (bd, CH_2 of polymer backbone and –CH_2-SH) ppm.

IR (FTIR): ν = 2924 (w), 2240 (w, -CN), 1660 (s, C=O, amide), 1450 (w), 1228 (s), 1091 (s), 659 (w) cm^{-1}.

Synthesis of poly(acrylonitrile-b-cysteamidacrylate):

Acrylonitrile (2.0 ml, 250 eq.), DMP (43.9 mg, 1 eq.) and AIBN (2.5 mg, 0.1 eq.) were dissolved in 6.5 ml DMF. The solution was degassed by three freeze-pump-thaw cycles. The reaction mixture was stirred for 6 hours and the polymerization was stopped by precipitation in cold methanol. The block copolymerization with PAN as a macro-CTA, NAS as a monomer, and AMDV as an initiator (NAS:PAN:AMDV=35:1:0.1) was conducted in dry DMSO for 48 h. The block copolymer was precipitated three times in cold methanol. Finally, P(AN-b-CAA) was obtained by the polymer analogous reaction. Therefore, 40 eq. of cysteamine hydrochloride, 40 eq. of triethylamine and one eq. of P(AN-b-NAS) was dissolved and stirred overnight.

IR (FTIR): ν = 2924 (w), 2240 (w, -CN), 1660 (s, C=O, amide), 1450 (w), 1228 (s), 1091 (s), 659 (w) cm^{-1}.

Synthesis of Au@ZnO heteroparticles, polymer functionalization, and pyrolysis:

The Au@ZnO heteroparticles were synthesized following a previously reported procedure.[19] Briefly, 0.5 mmole of gold(III) chloride hydrate (200 mg) and 5 mmole of zinc acetate dihydrate (1,090 mg) were added to 60 mL of benzyl alcohol and 30 mL of oleylamine. The mixture was heated to 120 °C and kept constant at this temperature for 20 min followed by increasing the temperature to 180 °C for additional 30 min. Afterwards, the solution was slowly cooled down to room temperature. The

product was precipitated from solution by adding an excess of ethanol and subsequently separated by centrifugation (9000 rpm, 10 min, RT).

Polymer and carbon coating of Au@ZnO heteroparticles:

The Au@ZnO heteroparticles were synthesized following a previously reported procedure (for detail see supporting information).[20] For the polymeric surface modification, Au@ZnO heteroparticles were dispersed in chloroform (10 mg ml^{-1}) and P(AN-r-CAA) or P(AN-b-CAA) dissolved in DMF (10 mg ml^{-1}) was added and stirred overnight. For the work-up, the dispersion was twice centrifuged and redispersed in DMF. After drying, the sample was pyrolyzed by heating the sample at temperature 300 °C for 4 h followed by increasing the temperature to 550 °C for additional 1 h (heating ramp: 5 °C min-1). For those batches later-on investigated electrochemically, 5 wt.% of conductive carbon (Super C65®) were added prior to the pyrolysis.[11,21] As reference material, as-synthesized, uncoated Au@ZnO particles were used.[20]

Characterization:

NMR spectra were measured with a Bruker ARX 400. FTIR spectroscopy was conducted on a Jasco FT/IR 4100 spectrometer with an ATR unit. GPC was carried out using a solution of 3 g L^{-1} $K^{+}TFA^{-}$ as eluent at 40 °C. The stationary phase in the columns consists of modified silica. The utilized detector was a refractive index detector (JASCO G1362A RID) and the calculation of the molecular weights was conducted using a calibration with PMMA standards. TEM micrographs were obtained by means of a EM420 (Philips). X-ray diffraction was performed using a Siemens D 5000 (Cu-K-alpha radiation). Thermogravimetric analysis (TGA) was carried out using of Perkin Elmer Pyris 6 under oxygen atmosphere. A Horiba Jobin Y LabRAM HR Spectrometer with a frequency doubled Nd:YAG laser was utilized to perform Raman spectroscopy. Scanning electron microscopy (SEM) was conducted using a HITACHI SU 8000 (Hitachi High-Technologies Europe GmbH, Krefeld; Germany), which was coupled to an XFlash 5010 X-ray detector to obtain simultaneously energy-dispersive

X-ray (EDX)-based elemental analysis.

Electrochemical Characterization:

Electrodes were prepared as following: First, sodium carboxymethyl cellulose (CMC) was dissolved in water. Then Au@ZnO or C-Au@ZnO and conductive carbon (Super C65, IMERYS, Switzerland) were added. The composition in wt.% for both Au@ZnO and C-Au@ZnO was 75:20:5 for Au@ZnO:carbon:CMC (the carbon content includes the conductive carbon as well as the coating in case of C-Au@ZnO). The mixture was ball-milled (Vario Planetary Mill Pulverisette 4, Fritsch) for 2 h at 400/-800 rpm. The resulting slurry was cast on dendritic copper foil (Schlenk) with a wet film thickness of 120 μm. After drying the coated electrode sheets at ambient temperature overnight, disc electrodes were punched and further dried under vacuum at 120 °C for 24 h. The active material mass loading was in the range from 1.8 to 2.3 mg cm^{-2} and 2.2 to 2.4 mg $^{-2}$ for electrodes based on C-Au@ZnO and Au@ZnO, respectively. Three-electrode Swagelok™ cells were assembled in a glove box (MBraun, Germany) with water and oxygen content less than 0.1 ppm. As separSator polypropylene fleeces (FS2190 Freudenberg, Germany) were used, which were drenched with the electrolyte, a 1M solution of $LiPF_6$ in a 3:7 volume mixture of ethylene carbonate and diethyl carbonate (UBE, Japan). Lithium foil (Rockwood Lithium) was used as a counter and reference electrodes. Accordingly, all potentials values given in this manuscript refer to the Li/Li$^+$ redox couple. All electrochemical experiments were conducted at 20 °C $\pm$ 2°C. Galvanostatic cycling was conducted by means of a Maccor Battery Tester 4300 and the applied specific current was 25 mA g^{-1} in the first and 50 mAh g^{-1} in the following cycles. Cyclic voltammetry was performed using a VMP3 potentiostat (BioLogic), applying a sweep rate of 0.05 mV s^{-1} in the range of 3.0 V and 0.01 V. In situ XRD was performed using a self-designed in situ cell.[9] First, the electrode was prepared by dissolving 0.01 g CMC in deionized water and subsequently adding 0.065 g of C-Au@ZnO and 0.025 g of conductive carbon. The obtained dispersion was further homogenized by means of ball-milling.

The resulting slurry was cast on a beryllium disk and dried under vacuum at 40 °C overnight. Cyclic voltammetry was performed using a VSP potentiostat/galvanostat (BioLogic, reversing potentials: 0.01 and 3.0 V with a sweep rate of 0.025 mV). In parallel, XRD analysis was conducted in the 2Θ range from 20° to 65° with a step size of 0.0184°. The time per step was 0.53 sec. Accordingly, each scan lasted 30 min including a rest time of 400 sec prior to each scan. Therefore, during the discharge 57 scans and during charge 67 charge scans were conducted.

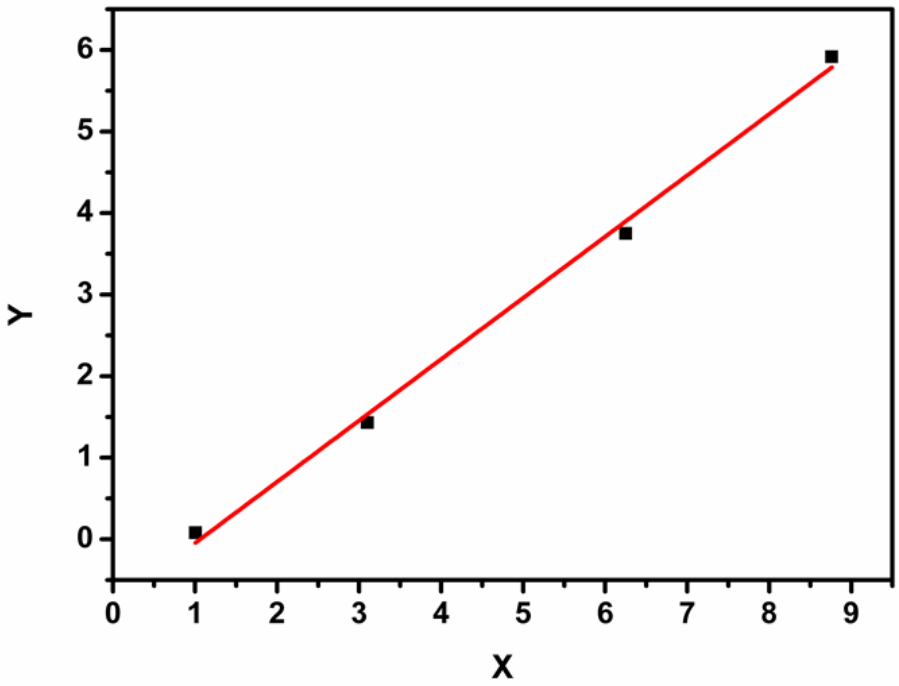

Figure S 1: Fineman-Ross plot for the copolymerization of AN with NAS, whereas $X = \frac{m_2}{m_1} \cdot \frac{[M1]^2}{[M2]^2}$ with m_1: incorporated AN in the polymer, m_2: incorporated NAS in the polymer, $[M_1]$: initial AN monomer concentration, $[M_2]$ initial NAS monomer concentration and $Y = (\frac{m_1}{m_2} - 1)\frac{[M_1]}{[M_2]} \cdot \frac{m_2}{m_1}$. The copolymerization parameter $r_1 = 0.80$ for AN can be obtained from the slope and the copolymerization parameter $r_2 = 0.75$ of NAS can be obtained from the y axis intercept. 4 different M_1 and M_2 were chosen and m_1 and m_2 were determined by NMR spectroscopy (see Figure S2).

Table S1: Parameters for the Fineman-Ross plot.

M_1	M_2	m_1	m_2	X	Y
120	115	52	48	1.01	0.08
170	65	75	34	3.10	1.42
250	50	100	25	6.25	3.75
250	35	99	17	8.76	5.91

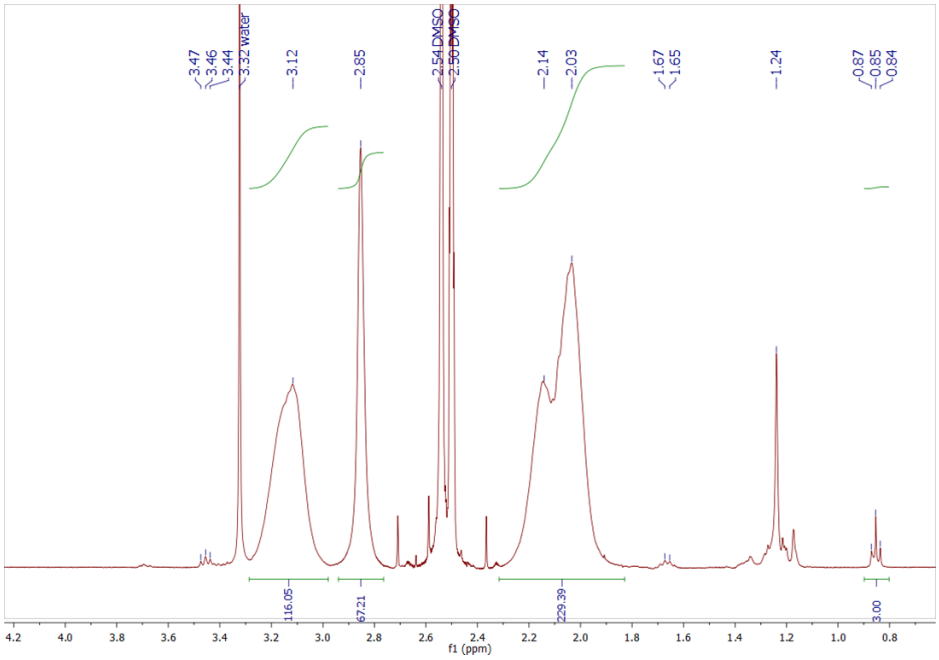

Figure S 2: ^{1}H-NMR spectrum of P(AN-r-NAS): The ratio between NAS and AN units was determined by integration of the signals at 3.12 ppm (corresponding to all –CH polymer backbone signals of both AN and NAS) and 2.85 ppm (corresponding to the CH_2 signals of the NAS side chain) and the CTA end-group signal at 0.85 ppm (-CH_3 of dodecyl end group).

^{1}H-NMR of P(AN-r-NAS)

^{1}H NMR (400 MHz, DMSO-d6, δ): 3.12 (bs, 116 H, CH of polymer backbone), 2.85

(bs, 67 H, CH_2CNO of NAS units), 2.03 (bs, 230 H, CH_2 of polymer backbone), 1.24 (m, dodecyl signals of DMP), 0.85 (t, 3 H, -CH_3 of DMP). M_n (NMR): 8 540 g/mol.

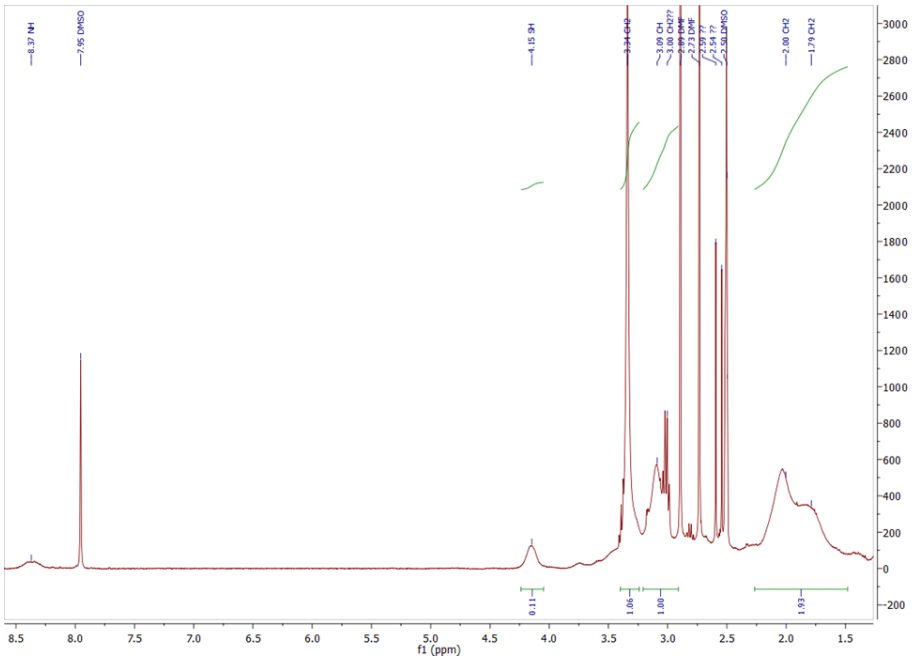

Figure S 3: ^{1}H-NMR spectrum of P(AN-r-CAA).

Table S2: Overview of the synthesized polymers.

Polymer	**M_n (NMR) / g mol^{-1}**	**M_n (SECR) / g mol^{-1}**	PDI
P(AN-r-NAS)	8,970	13,500	1.24
P(AN-r-CAA)	9,580	27,500	1.19
PAN	5,876	8,700	1.17
P(AN-b-NAS)	9,932	14,800	1.20
P(AN-b-CAA)	10,796	30,400	1.18

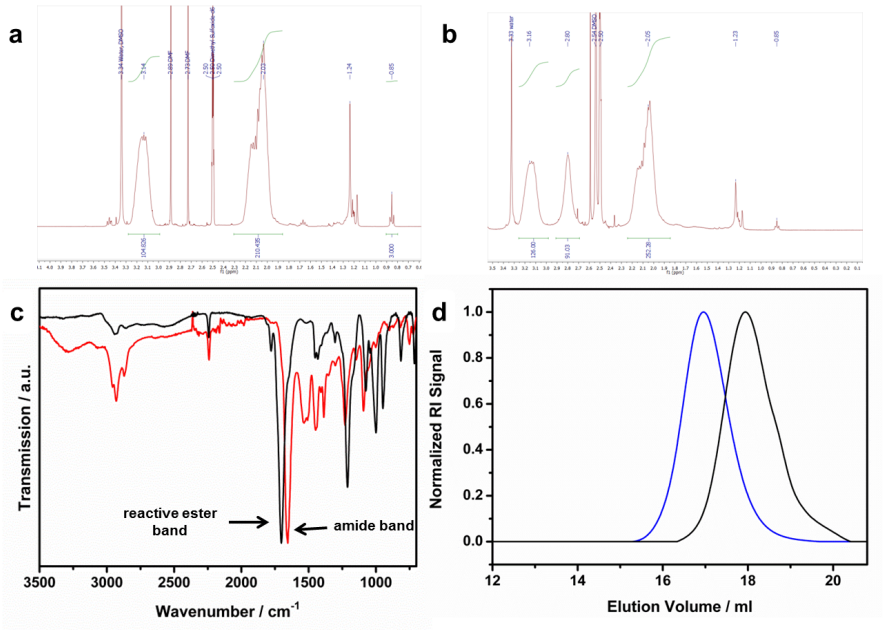

Figure S 4: a) ^{1}H-NMR spectrum of PAN and (b) of P(AN-b-NAS); (c) IR spectra of P(AN-b-NAS) (black) and P(AN-b-CAA) (red); (d) SEC of PAN (black) and P(AN-b-CAA) (blue).

^{1}H-NMR of PAN:

^{1}H NMR (400 MHz, DMSO-d6, δ): 3.14 (s, CH of polymer backbone, 105H), 2.25-2.50 (s, CH_2 of polymer backbone 210H), 1.24 (m, dodecyl rest of CTA), 0.85 (CH_3 of dodecyl rest of CTA, 3H) ppm.

^{1}H-NMR of P(AN-NAS):

^{1}H NMR (400 MHz, DMSO-d6, δ): 3.16 (s, CH of polymer backbone, 126H), 2.80 (CH_2-CH_2 of NAS, 91H), 2.25-2.50 (s, CH_2 of polymer backbone 252H), 1.23 (m, dodecylrest of CTA), 0.85 (CH_3 of dodecylrest of CTA, 3H) ppm.

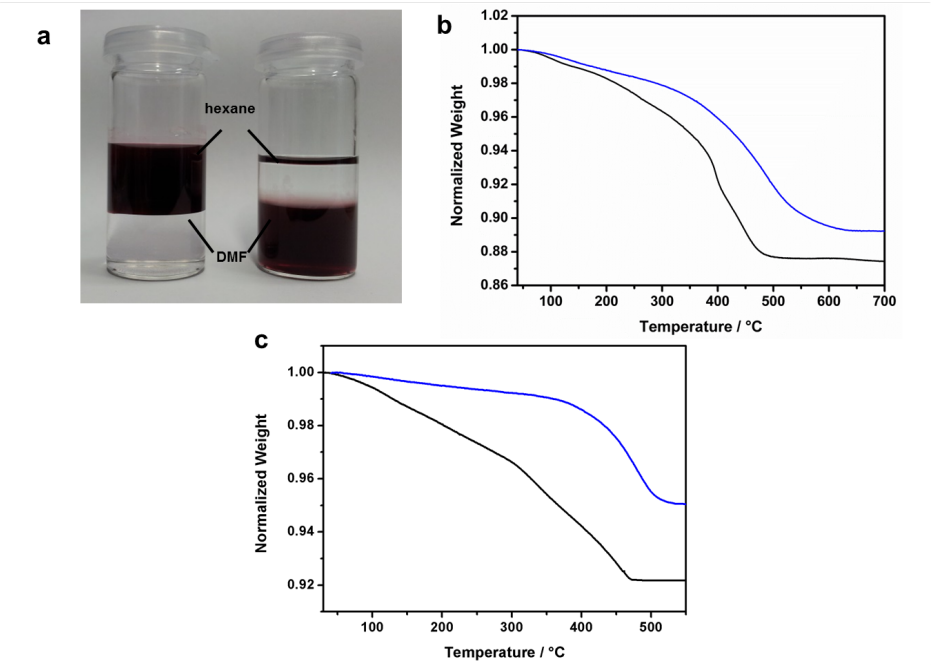

Figure S 5: a) Photograph of oleic acid-functionalized as-synthesized Au@ZnO heteroparticles dispersed in hexane (left) and of P(AN-r-CAA)-functionalized heteroparticles dispersed in DMF (right); (b) TGA data of P(AN-b-CAA) (blue) and P(AN-r-CAA) (black) coated onto Au@ZnO nanoparticles.(c) TGA data of pyrolyzed P(AN-b-CAA)@Au@ZnO (blue) and pyrolyzed P(AN-r-CAA)@Au@ZnO (black).

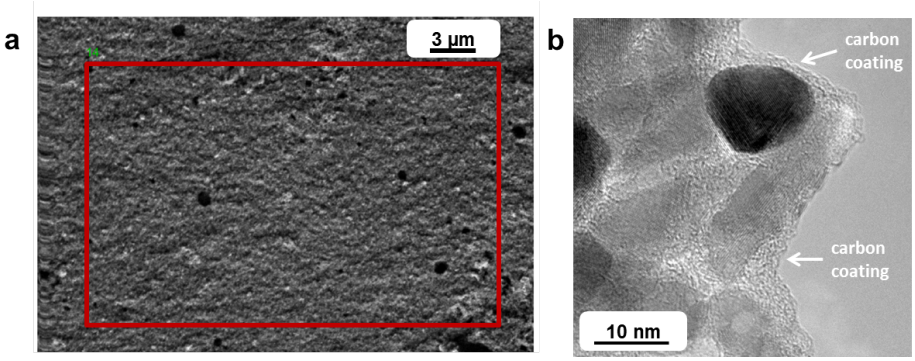

Figure S 6: a) SEM micrograph of carbon-coated Au@ZnO particles (C-Au@ZnO); the red marked area was investigated by EDX spectroscopy (see Figure 3d); (b) High resolution TEM micrograph of carbon-coated Au@ZnO heteroparticles.

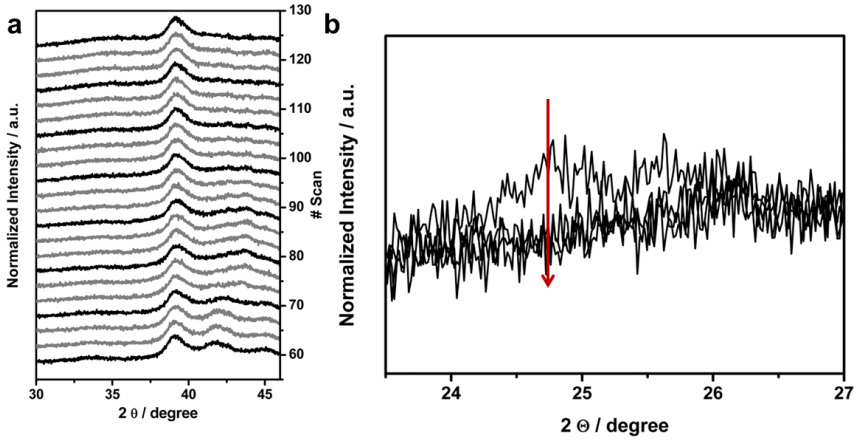

Figure S 7: Excerpt of the in situ XRD measurement of selected scans upon the delithiation process in the range of 30° to 46° (a) and in the range of 23.5° to 27° (b). For the latter, selected scans are presented (60, 70, and 80), showing the decreasing intensity related to the dealloying of gold and lithium.

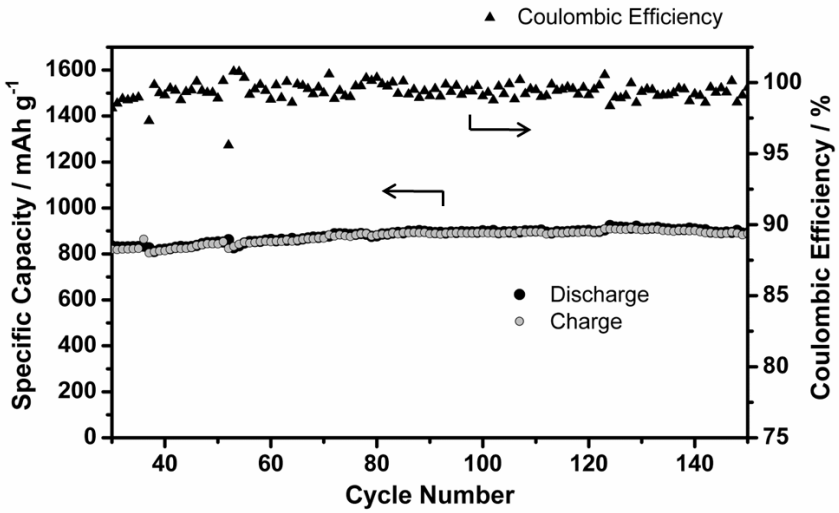

Figure S 8: Long-term constant current cycling of C-Au@ZnO-based electrodes (50 mA g^{-1}; 0.01 – 3.0 V).

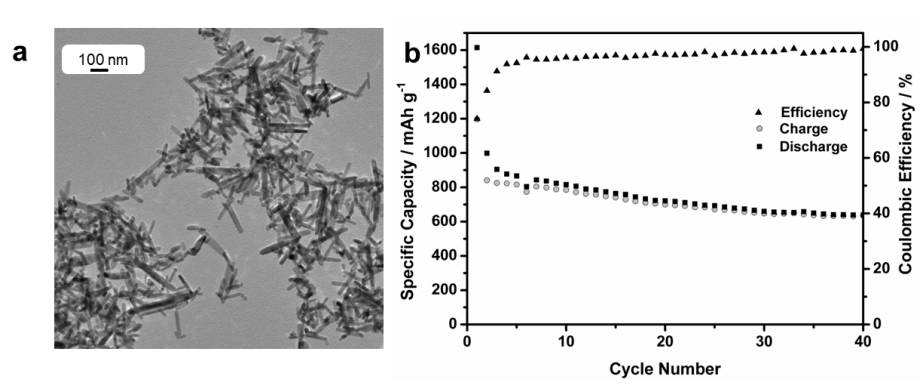

Figure S 9: a) TEM image of as-synthesized ZnO nanorods and b) their electrochemical performance applying a specific current of 50 mA g^{-1}.

Galvanostatic cycling was also conducted for carbon coated ZnO nanorods, which were coated with the same polymer precursor and carbonized analogously. The dimensions of these rods (average: 20 nm width, 112 nm length, see Figure S9a) are comparable to the ZnO branches employed in the multipod morphology. These nanorods were cycled applying the same testing protocol as for the multipod Au@ZnO heteroparticles. The initial reversible specific capacity was 840 mAh g^{-1}. Subsequently, the charge capacity decreased within the first 20 cycles to about 700 mAh g^{-1} and after 40 cycles further to 630 mAh g^{-1} as shown in Figure S9b (given below). Thus, the obtained specific capacities as well as the cycling stability are obviously inferior compared to the results obtained for the Au@ZnO multipods (initial charge capacity: 946 mAh g^{-1}, 888 mAh g^{-1} after 150 cycles).

References

[1] W.-J. Zhang, J. Power Sources2011, 196, 13.

[2] C. Menictas (Ed.), Advances in batteries for medium and large-scale energy storage, Woodhead Publ., Cambridge 2014.

[3] Y.-G. Guo, J.-S. Hu, L.-J. Wan, Adv. Mater.2008, 20, 2878.

[4] H. Wang, Q. Pan, Y. Cheng, J. Zhao, G. Yin, Electrochim.Acta2009, 54, 2851.

[5] H. Li, H. Zhou, Chem. Commun.2012, 48, 1201.

[6] J. Ni, H. Wang, L. Gao, L. Lu, Electrochim.Acta2012, 70, 349.

[7] B. Oschmann, D. Bresser, M. N. Tahir, K. Fischer, W. Tremel, S. Passerini, R. Zentel, Macromol. Rapid Commun.2013, 34, 1693.

[8] D. Bresser, E. Paillard, R. Kloepsch, S. Krueger, M. Fiedler, R. Schmitz, D. Baither, M. Winter, S. Passerini, Adv. Energy Mater.2013, 3, 513.

[9] J. Wang, X. Sun, Energy Environ. Sci.2012, 5, 5163.

[10] F. Mueller, D. Bresser, E. Paillard, M. Winter, S. Passerini, Journal of Power Sources2013, 236, 87.

[11] D. Bresser, B. Oschmann, M. N. Tahir, W. Tremel, R. Zentel, S. Passerini, Journal of Power Sources2014, 248, 852.

[12] D. M. Piper, T. A. Yersak, S.-B. Son, S. C. Kim, C. S. Kang, K. H. Oh, C. Ban, A. C. Dillon, S.-H. Lee, Adv. Energy Mater.2013, 3, 697.

[13] M. Zorn, S. Meuer, M. N. Tahir, Y. Khalavka, C. Sönnichsen, W. Tremel, R. Zentel, J. Mater. Chem.2008, 18, 3050.

[14] J. M. Feckl, K. Fominykh, M. Döblinger, D. Fattakhova-Rohlfing, T. Bein, Angew. Chem. Int. Ed.2012, 51, 7459.

[15] Y. Zhang, Y. Tang, S. Yin, Z. Zeng, H. Zhang, C. M. Li, Z. Dong, Z. Chen, X. Chen, Nanoscale2011, 3, 4074.

[16] G. Huang, F. Zhang, L. Zhang, X. Du, J. Wang, L. Wang, J. Mater. Chem. A2014, 2, 8048-8053.

[17] J. Lim, L. Zur Borg, S. Dolezel, F. Schmid, K. Char, R. Zentel, Macromol. Rapid

Commun.2014, 19, 1685.

[18] D. E. Bergbreiter, P. L. Osburn, C. Li, Org. Lett.2002, 4, 737.

[19] J. T. Lai, D. Filla, R. Shea, Macromolecules2002, 35, 6754.

[20] M. N. Tahir, F. Natalio, M. A. Cambaz, M. Panthöfer, R. Branscheid, U. Kolb, W. Tremel, Nanoscale2013, 5, 9944.

[21] D. Bresser, E. Paillard, E. Binetti, S. Krueger, M. Striccoli, M. Winter, S. Passerini, J. Power Sources2012, 206, 301.

[22] H. M. Ezekiel, R. G. Spain, J. Polym. Sci., C Polym.Symp.1967, 19, 249.

[23] P. Rajalingam, G. Radhakrishxan, J.Macromol. Sci., Part C: Polymer Reviews1991, 31, 301.

[24] P. J. Roth, P. Theato, Chem. Mater.2008, 20, 1614.

[25] E. M. Wong, P. G. Hoertz, C. J. Liang, B.-M. Shi, G. J. Meyer, P. C. Searson, Langmuir2001, 17, 8362.

[26] M. Brust, M. Walker, D. Bethell, D. J. Schiffrin, R. Whyman, J. Chem. Soc., Chem. Commun.1994, 801.

[27] P. W. Sadik, S. J. Pearton, D. P. Norton, E. Lambers, F. Ren, J. Appl. Phys.2007, 101, 104514.

[28] M. Ahmad, S. Yingying, A. Nisar, H. Sun, W. Shen, M. Wei, J. Zhu, J. Mater. Chem.2011, 21, 7723.

[29] G. Taillades, Solid State Ionics2002, 152-153, 119.

[30] S. C. Mui, P. E. Trapa, B. Huang, P. P. Soo, M. I. Lozow, T. C. Wang, R. E. Cohen, A. N. Mansour, S. Mukerjee, A. M. Mayes, D. R. Sadoway, J. Electrochem. Soc.2002, 149, A1610.

[31] D. Knight, W. White, J. Mater. Res., 1989, 4,385.

[32] R. Baddour-Hadjean, J.-P. Pereira-Ramos, Chem. Rev.2010, 110, 1278.

[33] E. Peled, J. Electrochem. Soc.1979, 126, 2047.

[34] F. Belliard, J. Irvine, J.Power Sources2001, 97-98, 219.

[35] L. Yuan, H.K. Liu, A. Maaroof, K. Konstantinov, J. Liu, and M. Cortie, J. of New

Mat. for Elect. Syst.2007, 95.

[36] D. Bresser, F. Mueller, M. Fiedler, S. Krueger, R. Kloepsch, D. Baither, M. Winter, E. Paillard, S. Passerini, Chem. Mater.2013, 25, 4977.

[37] F. Renner, H. Kageyama, Z. Siroma, M. Shikano, S. Schöder, Y. Gründer, O. Sakata, Electrochim.Acta2008, 53, 6064.

[38] P. Bach, A.Seemayer, U.Rütt, O.Gutowski, F. Renner, 223rd ECS Meeting Abstract book, 2013, 187.

[39] J. Liu, Y. Li, R. Ding, J. Jiang, Y. Hu, X. Ji, Q. Chi, Z. Zhu, X. Huang, J. Phys. Chem. C 2009, 113, 5336.

[40] H. Wang, Q. Pan, Y. Cheng, J. Zhao, G. Yin, Electrochimica Acta 2009, 54, 2851.

4.1.4 Carbon Coating of SnO_x Sponge-like Structure

Similar to ZnO, tin oxide based materials are attractive as an anode material for lithium-ion batteries due to the theoretical capacities exceeding 750 mAh g^{-1}. Tin oxide materials are conversion-alloying materials as well and suffer from huge volume changes up to 200 % during the (de-)lithiation mechanism. Thus, concepts for the design of morphologies with free void are interesting.

In this contribution, Nils Mohri from Prof. W. Tremel's group synthesized SnO_x films with a nanoscaled sponge-like morphology, which are attached immediately onto Cu-foil used as current collector. These films can be obtained by anodization technique. For this sample the typical carbon coating approach based on the mixing of carbon precursor molecules with the active material cannot be applied. In contrast, the herein developed carbon coating approach using the previously described carbon precursor block copolymer containing polyacrylonitrile and dopamine units, which can bind onto the sponge-like morphology, can be applied. In cooperation with Nils Mohri, these samples were characterized in detail before and after coating by XPS, SEM, XRD (Nils Mohri) and Raman spectroscopy. The prepared materials were applied as anode materials in lithium-ion batteries and the coated SnO_x films were compared with uncoated SnO_x films in order to investigate the influence of the coating. The coating has a positive influence on the battery performance, as the C-rate performance as well as the longterm cycling could be enhanced.

Several visits at the Helmholtz Institute Ulm for Electrochemical Energy Storage at the group of Prof. S. Passerini gave me the possibility to assemble all batteries and to conduct all electrochemical measurements by myself and thus to learn more about typical approaches in the environment of battery technologies.

Muhammad Nawaz Tahir and Franziska Mueller contributed to this manuscript with helpful discussions and proof reading.

4.1.4.1 Manuscript to be submitted

Synthesis and Characterization of Carbon Coated Sponge-like Tin Oxide (SnO_x) Films and Their Application as Electrode Materials in Lithium Ion Batteries

Nils Mohri,* Bernd Oschmann,* Franziska Mueller, Jan von Zamory, Muhammad Nawaz Tahir, Stefano Passerini, Rudolf Zentel, and Wolfgang Tremel

Abstract

We report on the synthesis of sponge-like tin oxide films on copper foil by anodization of electrochemically deposited tin films. The thin films are functionalized using a surfaceanchoring carbon precursor polymer (poly(acrylonitrile-b-dopamine acrylamide)) followed by annealing at elevated temperature to convert the polymer coating into a carbonaceous coating. The as prepared and the carbon coated films are characterized by X-ray diffraction (XRD), X-ray photoelectron spectroscopy (XPS), scanning electron microscopy (SEM) and Raman spectroscopy. The carbon coated as well as the as-synthesized SnO_x films are applied as anode materials in lithium ion batteries. Carbon coating has a positive effect on the battery performance with respect to the C-rate capability, increasing the capacity by 200 mAh g^{-1} for all applied C-rates. After 20 cycles, the coated sample still shows a reversible specific charge capacity of 497 mAh g^{-1}. Ex situ scanning electron microscopy was applied and shows the retention of the sponge-like morphology even after cycling.

*N.M. and B.O. contributed equally to this work.

1. Introduction

The interest in the synthesis of carbon coated nanostructured materials with a high surface area has increased within the last years due to their enhanced applications in various fields such as catalysis,[1,2] and as electrode materials in energy storage devices, especially in lithium-ion batteries.[3–6] Currently, lithium-ion batteries are the leading energy storage devices in portable electronic devices and are furthermore attractive candidates for up-scale applications such as electric vehicles. However, the state-of-the art batteries contain electrode materials with rather limited specific capacities, whereby on the anode side graphite is applied with a theoretical capacity of 372 mAh g^{-1}. Therefore, the exploration of new electrode materials with higher specific capacities is indispensable, for instance to increase the driving range of electric vehicles. As alternative electrode materials, inter alia tin and tin oxides (SnO or SnO_2) are interesting, due to their theoretical specific capacity of around 790 mAh g^{-1}.[7,8] As conversion-alloying compounds tin oxides first undergo a conversion reaction forming elemental tin and Li_2O. This conversion is followed by alloying reaction of elemental tin and lithium described as follows:[9,10]

$$SnO_2 + 4Li^+ + 4e^- \rightarrow Sn + 2Li_2O \quad (1)$$

$$Sn + xLi^+ + xe^- \leftrightarrow Li_xSn \ (0 \leq x \leq 4.4) \quad (2)$$

These oxides suffer from the irreversible formation of Li_2O and from volume changes during the (de-)alloying progress. Both issues cause a capacity fading during electrochemical cycling.[11–13] Thus, especially in case of tin oxides the architecture of active material morphology has a high impact on the battery performance. Current approaches to address these issues range from the use of zero-dimensional nanoparticles to three-dimensional nano-sized morphologies with hollow structures,[7,14–17], for instance hollow tin dioxide microspheres,[17] whereby the motivation to create hollow structures is driven by the idea that the void space buffers the volume

changes.[18] Furthermore, nanoporous tin oxides have been investigated recently, but suffered from rather short cycling lifetime.[19–21] In addition to the downsizing of active material to nano-size, the application of a carbon coating on the surface of nano-sized active material lowers the intrinsically high electrical resistance within the electrode composite and improves the battery performance, as it has been applied to numerous active materials including also tin oxides.[4,11,22–24] Herein, we report on the synthesis of a carbon coated nanoporous sponge-like morphology of SnO_x films. The sponge-like morphology of SnO_x is derived by first electrodepositing Sn immediately onto Cu-foil, which serves as the current collector, followed by the anodization of the Sn film in an aqueous medium resulting in the nanoporous sponge-like morphology. Thus, for this approach there is no need for the addition of electrochemically inactive binding material and no need of slurry preparation using toxic organic solvents such as N-methyl pyrrolidone (NMP), which is a common procedure in many of the reports in this area of research.[25–27] The motivation for the use of this sponge-like morphology is the nanoporous structure, which might buffer the volume changes during (de-)lithiation, and porous structure enables short diffusion pathways for the lithium-ions due to the nano-sized dimensions. Furthermore, these films are functionalized with block copolymers containing an anchor block and a graphitizable block to obtained homogenous carbon film.[6,24,28] As a carbon source polyacrylonitrile is used and a rather low pyrolysis temperature (350 °C) is applied. At this temperature a flexible carbonaceous material (also described as cyclized polyacrylonitrile) is obtained, a strategy similarly reported to buffer volume changes of silicon, a further alloying based electrode material for lithium-ion batteries.[29] A detailed structural and morphological characterization of the as-synthesized material as well as the carbon coated material is described in this manuscript. Furthermore, the synthesized materials are applied as an electrode material in lithium-ion batteries and the influence of the carbon coating is investigated by comparing as anodized and carbon coated material. Ex-situ scanning

electron microscopy was applied after electrochemical cycling of the SnO_x material to investigate the morphology and structural changes after electrochemical cycling.

2. Results and Discussion

Structural and morphological characterization

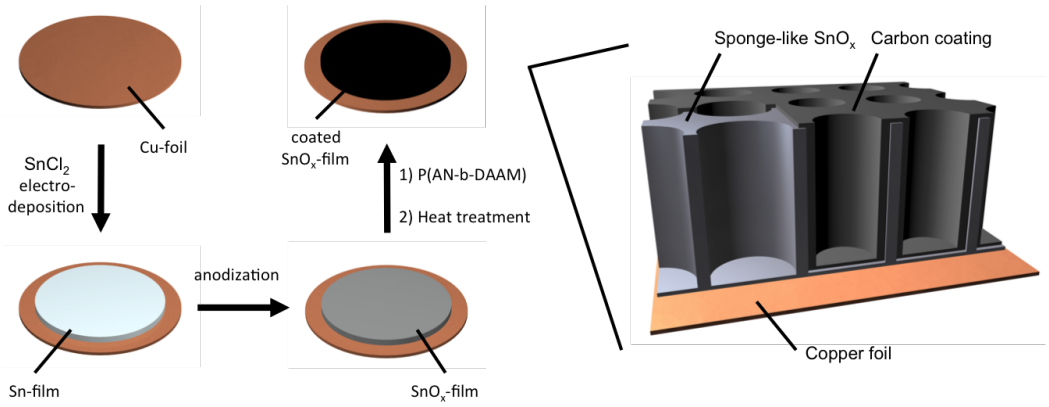

Figure 1: Scheme showing the different steps of sample preparation (left) and magnification of the schematic sample structure (right).

A Tin film is electrodeposited from a tin(II) chloride and tri-ammonium citrate containing solution[30] onto copper foil, which can be used as the current collector of the electrode in the lithium-ion battery setup (see Figure 1). SEM image of the deposited tin film is shown in Figure 2a. The surface exhibits a pre-structuring of tin resulting from intertwined single crystals grown during tin deposition. By applying a common anodization technique,[31] a sponge-like SnO_x film can be formed as shown by the SEM image in Figure 2b, as the anodization of tin generates large amounts of oxygen. The formed oxygen is the reason for pore breaking and inhibits regular pore growth, thus resulting in the well-known sponge-like structure as reported before.[20,31] Images at higher magnifications prove the sponge-like morphology with pore diameters of 30-60 nm and wall thicknesses of 10-15 nm as shown in Figure 2c.

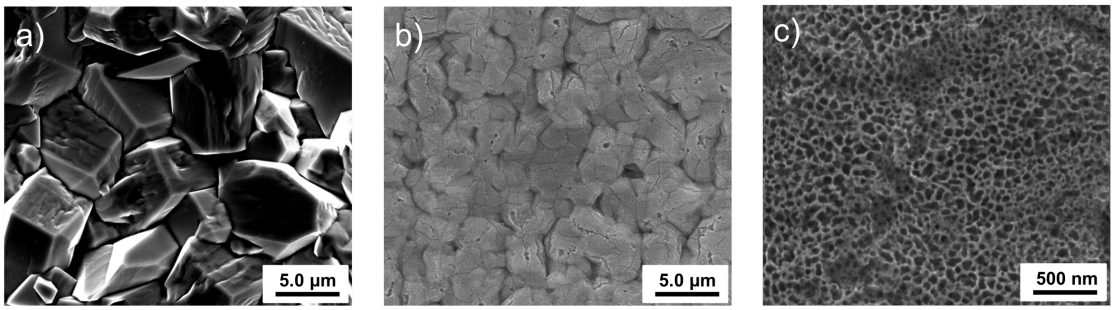

Figure 2: SEM images of tin surface after deposition and anodization. a) Deposited metallic tin with different oriented single crystalline tin domains, b) anodized SnO_x surface, c) high resolution image of sponge-like SnO_x surface.

Cross section measurement of the anodized sample reveals a nanoporous SnO_x film thickness of 20 - 25 μm (Figure 3).

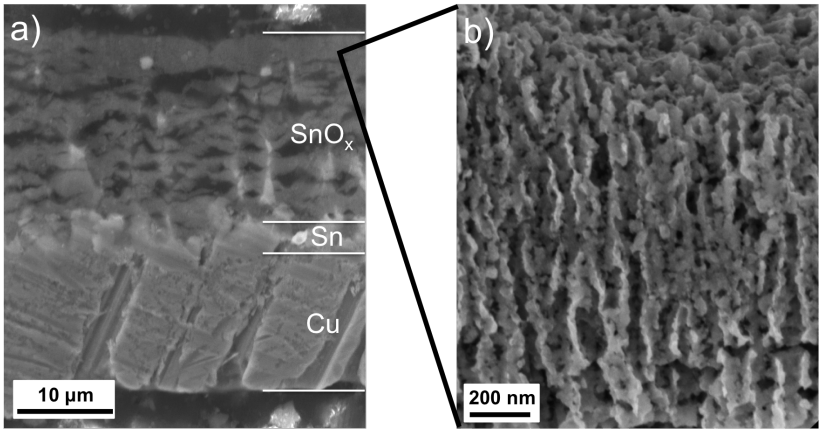

Figure 3: a) Cross section SEM image of anodized sample. Top: Sponge-like nanoporous SnO_x (grey), cracks from oxygen evolution breaking up regular tubular structure (black). Middle: Thin tin gluing layer connecting nanoporous tin oxide to underlying copper foil. Bottom: Copper foil. b) High resolution cross section SEM image of the SnO_x layer showing the nanoporosity.

Longer anodization times than the herein applied time of 6 min result in spallation of the oxide layer, because once the reaction reaches the bottom of the tin layer,

oxygen evolution results in detachment of the SnO_x from the copper foil . Thus, anodization was interrupted shortly before the copper surface was reached. A thin layer of non-oxidized tin remained, gluing the porous tin oxide to the copper foil. The crystallinity of the film was investigated by X-ray diffraction (XRD) as shown in Figure 4. As commonly observed for SnO_x, broad reflections appear, which can be attributed to SnO_2.[32,33] Sharp reflections of low intensity originate from metallic Sn of the gluing layer. Remaining high intensity reflections can be attributed to the underlying copper foil. Reflections from SnO_x could not be detected due to the highly amorphous nature of the film.[34]

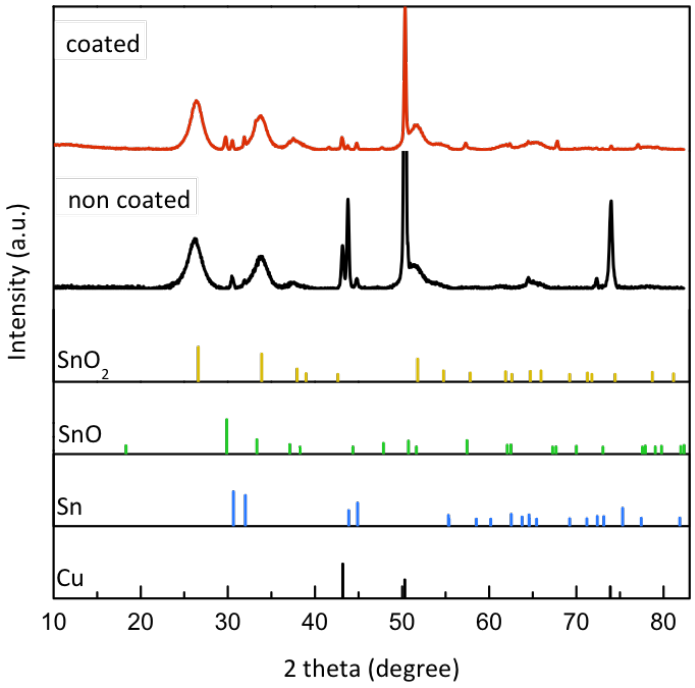

Figure 4: XRD patterns before (black) and after coating and tempering (red), reference patterns of SnO_2 (JCPDS 00-041-1445), SnO (JCPDS 01-085-0423), Sn (JCPDS 01-065-0296) and Cu (JCPDS 01-070-3038).

A recently developed carbon coating approach based on the use of a block copolymer containing was applied to the sponge-like SnO_x thin film.[6,28] The block copolymer contains a carbon precursor block, in this case polyacrylonitrile (PAN), and a

block, that can coordinate onto a metal oxide surface. As a coordinating species, dopamine was chosen and incorporated into the polymer, as dopamine containing polymers were reported to bind onto SnO_2 nanoparticle surfaces.[35] The reversible addition-fragmentation chain transfer (RAFT) polymerization based synthesis route is described in Figure 5.

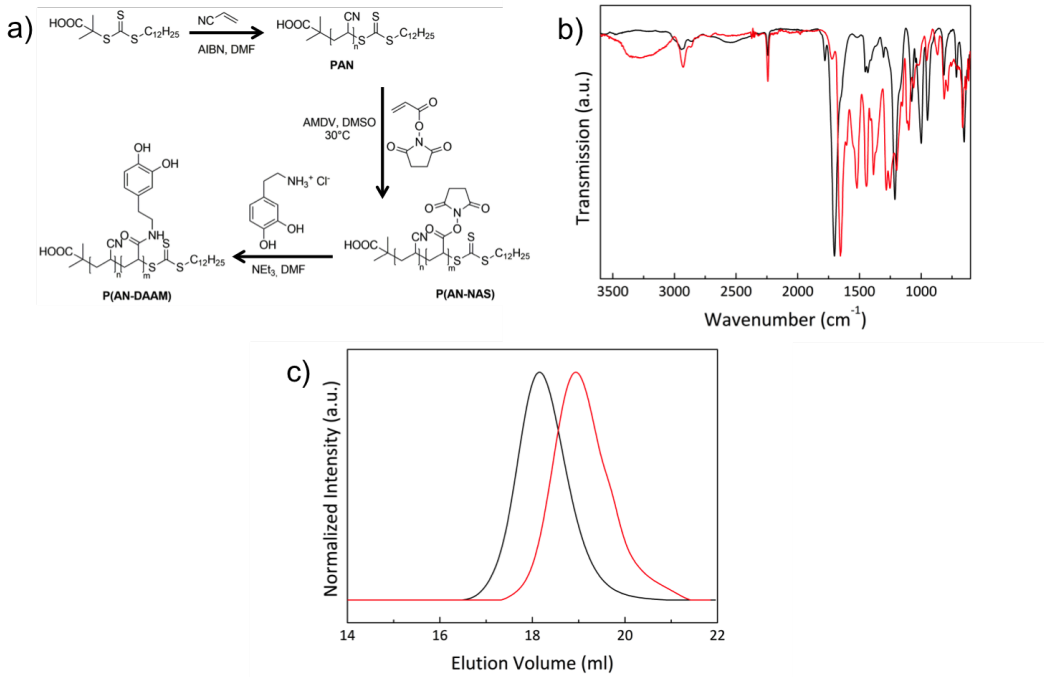

Figure 5: a) Reaction scheme for the synthesis of P(AN-b-DAAM). b) IR spectra of P(AN-b-NAS) (black) and P(AN-b-DAAM) (red). c) SEC of P(AN) (red) and P(AN-b-DAAM) (black).

Briefly, first the polyacrylonitrile block is synthesized with an averaged number of repeating units 70 as confirmed by NMR spectroscopy (see Supporting Information Figure S1). Dopamine is attached to the polymer after the block copolymerization with a reactive ester monomer by the aminolysis of the reactive ester to finally obtain poly(acrylonitrile-dopamine acrylamide) (P(AN-DAAM)) with an average dopamine containing repeating unit 23 (see NMR spectra in Figure S2). The successful syn-

thesis of the polymer can be proven by IR spectroscopy, which proves the attachment of dopamine due to the presence of the amide band (1702 cm^{-1}) and the disappearance of the reactive ester band (1654 cm^{-1}) (see Figure 5b), size exclusion chromatography (SEC) showing a shift to lower elution volumes after the block copolymerization (Figure 5c), and NMR spectroscopy (see Supporting Information Figure S2 and S3).

The polymer was bound onto the sponge-like inorganic structure by dipping the inorganic material into a polymer solution in DMF under inert atmosphere for 6 h. Unbound polymer was removed by repeated washing with DMF. The polymer coating is transformed into a carbonaceous coating by pyrolysis at 350 °C.

Cross-section SEM of embedded samples showed the structure to be unchanged after coating and heat treatment (see Supporting Information Figure S4). In XRD measurement, new reflections appear (Figure 4) after the coating, which can be attributed to tin(II) oxide, as the heat treatment increases the crystallinity of SnO.

Energy dispersive x-ray (EDX) spectroscopy was used to further investigate the composition of the sponge-like SnO_x (Figure 6). In contrast to the constant Sn:O ratio observed for the as anodized sample, which is determined to be around 1:1 throughout the whole sample (Figure 6a and S5), the Sn:O ratio of the heat treated and carbon coated sample is 1:1 in volume fraction close to the Cu foil, but increases starting from the middle of the sponge in direction of the surface (see Figure 6b and S6). In contrast to previous reports observing an increasing oxidation state upon heat treatment of the sponge, [36,37] the combination of polymer coating and heat treatment in oxygen free atmosphere seem to create a reducing atmosphere. The gradient in oxygen concentration further supports the assumption of a reduction of tin oxide during the heat treatment in the presence of carbonaceous material as the effect occurs predominantly on the surface of the sample where most of the polymer is expected to coordinate. A constant concentration of carbon between 2.1 - 3.6 % throughout the sample cross section was measured for the coated sample (see Figure

6b), confirming the homogeneous carbon distribution within the sponge, whereas no carbon signal could be detected in the case of the uncoated sample.

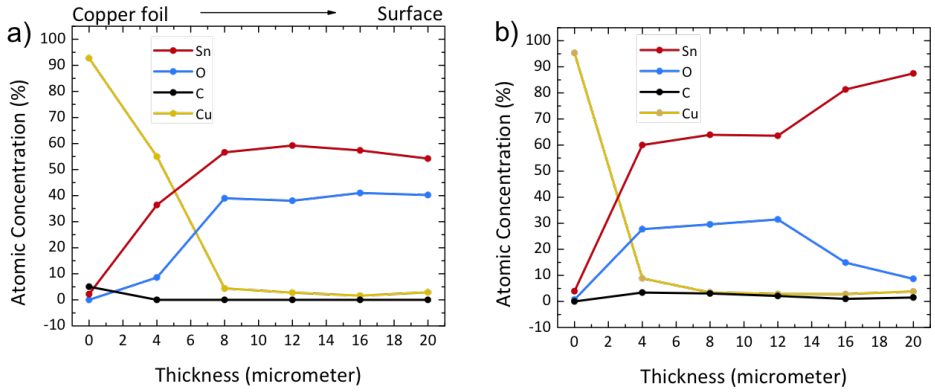

Figure 6: EDX cross-section analysis before (a) and after coating and tempering (b). Corresponding cross-section SEM images are shown in Figure S5 and S6.

The elemental composition of the film was further studied by X-ray photoelectron spectroscopy (XPS). High-resolution spectra of C and Sn elements before and after coating and annealing are shown in Figure 7a-b. Representative survey spectra are shown in Figure 7c. In the case of the non-coated sample, a low intensity carbon signal could be detected. Since XPS is a surface sensitive technique and as no carbon signal could be detected by EDX analysis, we assume the signal to originate from adventitious carbon. Curve fitting showed the signal to exhibit the typical peaks at 284.6, 286.2 and 288.9 eV resulting from C-C, C-O and C=O components respectively.[38] After coating, an increase in intensity of 18 % was observed for the C 1s-peak while the intensity of the Sn 3d5- and O 1s-peak decreased. A slight shift to lower binding energies indicates a lower oxidation state of the carbon as expected for the polymer. Two additional peaks appear at 287.7 and 292.6 eV. The peak at 287.7 eV can be attributed to the C-N bond resulting from nitrogen incorporated in the conjugated organic structure of the coating after pyrolysis.[39] A second peak is expected to appear at 285.9 eV originating from the C-N double bond. Because of

the large overlap with the C-O peak, it was not possible to distinguish them, but the increase in intensity observed for the C-O peak compared to the non-coated sample points towards an additional contribution from the C-N double bond in the coating. Furthermore, a N 1s peak was observed at a binding energy of 400.1 eV in the coated sample, but not visible in the non-coated one (Figure 6d). Since cyanide groups appear at lower binding energies and the peak is rather broad (FWHM = 3.4 eV), we assume it to be the result from an overlap of the C-N bond and double bond peaks as suggested by Boyd et. al.[40]

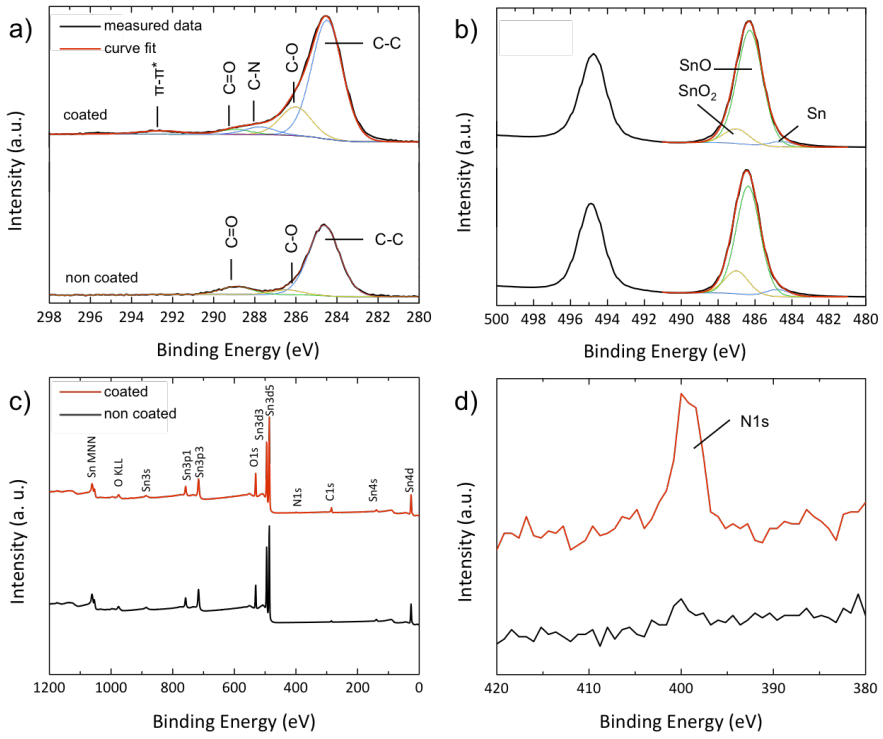

Figure 7: XPS spectra before and after coating and tempering. (a-b) High-resolution spectra from C1s and Sn3d peaks. c) Survey of anodized sample before (black) and after (red) coating and tempering. d) Magnification of N1s peak from survey.

The broad, low-intensity peak at 292.6 eV is the result of π-π* transitions (shake up) in the conjugated system. The Sn 3d5-signal consists of three components at

484.6, 486.3 and 487.0 eV, which could be attributed to Sn(0), Sn(II) and Sn(IV) respectively, further confirming the appearance of SnO in the sample. The ratio of $Sn/Sn^{2+}/Sn^{4+}$ was calculated to be 5%/78%/17%. The ratio of Sn to O was found to be 1:1.12, which is in good agreement with the results from EDX analysis. After coating, the Sn(II) signal increases to 85% while the Sn(IV) signal shows a decrease to 11%, reaffirming the observation of reduced SnO_2 due to the heat treatment.

The Raman spectrum in Figure 8 shows the presence of two bands typically observed for carbonaceous material, namely the D-band (1355 cm^{-1}) and the G-band (1591 cm^{-1}), which can be attributed to a delocalized sp^2 π-bonding.[41] As expected, none of these bands are observed for the uncoated sample.

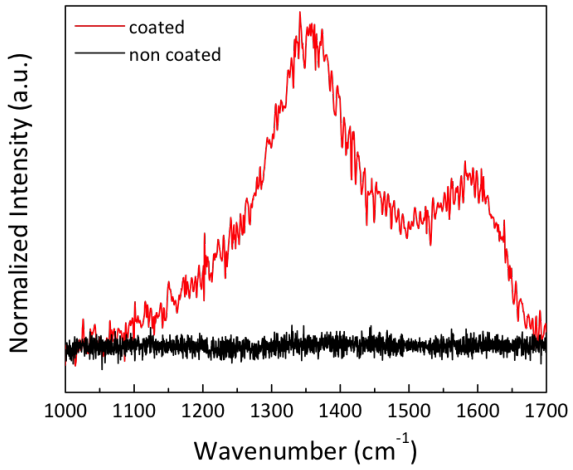

Figure 8: Raman spectrum of SnO_x sponge before (black) and after (red) coating

Electrochemical characterization of carbon coated SnO_x sponges

Electrodes based on as-synthesized and carbon coated SnO_x sponges were applied as anodes in a lithium-ion battery half-cell set-up. Figure 9 shows the results of cyclic voltammetry for the uncoated and coated sample. In the first cathodic sweep of the carbon coated sponges a reduction peak at 0.9 V with a shoulder at 1.2 V can be observed, which is ascribed to the partially irreversible stepwise formation of elemental Sn and Li_2O as well as the formation of the solid electrolyte interface due

to the decomposition of the electrolyte.[42–44]

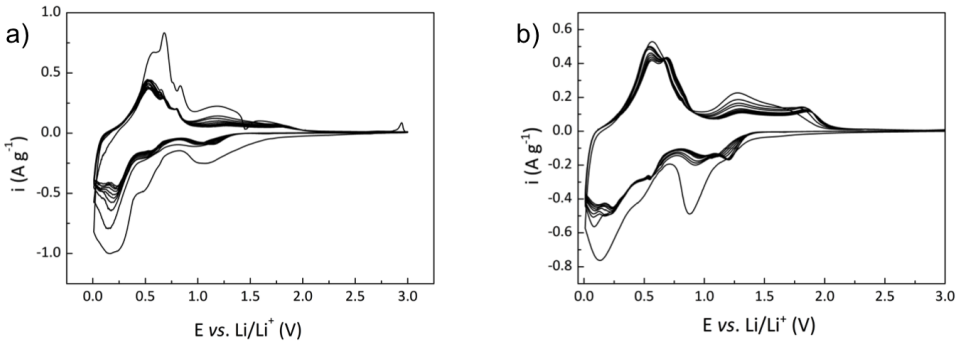

Figure 9: Cyclic voltammogram of uncoated SnO_x sponges (a) and carbon coated SnO_x sponges (b).

A shoulder at 0.45 V is followed by the main cathodic peak of the first cycle at 0.15 V, whereby the reactions occurring in the range of 0 to 0.6 V are ascribed to the formation of Li_xSn alloys.[45,46] The anodic main peak at 0.55 V as well as a second peak at 1.28 V are correlated to the stepwise dealloying processes of the Li_xSn alloys.[46] The peak at 1.6 V is ascribed to the at least partial decomposition of Li_2O.[46,47] The second as well as the following cycles show some differences compared to the first cycle, as the cathodic peak at 0.9 V is less pronounced and a peak shows up at 1.2 V. Furthermore, the main cathodic is less pronounced. There is no change with respect to the anodic main peak, however, the intensity of the anodic peak at 1.28 V is decreased and a second peak shows up at 1.8 V due to the decomposition of Li_2O.[11] Compared to the carbon coated SnO_x sample, the uncoated sample shows similar features including an intensive cathodic peak due to the SEI formation, a cathodic main peak due to the alloying as well as the dealloying peaks. However, in the following cycles, the intensity of the cathodic peak at 1.2V and the anodic peak at 1.8 V is strongly reduced. Thus, the partial decomposition of Li_2O seems to be more reversible in the presence of the carbon coating.

In Figure 10 a comparison of the rate capability of coated and uncoated SnO_x

sponges is presented. At the applied specific currents of 50, 100, 200 and 500 mA g^{-1} specific charge capacities of 400, 287, 220 and 102 mAh g^{-1}, respectively can be obtained for the uncoated SnO_x sponges. Significantly higher charge capacities of 600, 505, 431 and 260 mAh g^{-1} respectively can be obtained for the coated, which is for all applied specific currents more than 200 mAh g^{-1} higher compared to the uncoated sample, proving the positive influence of the carbon coating.

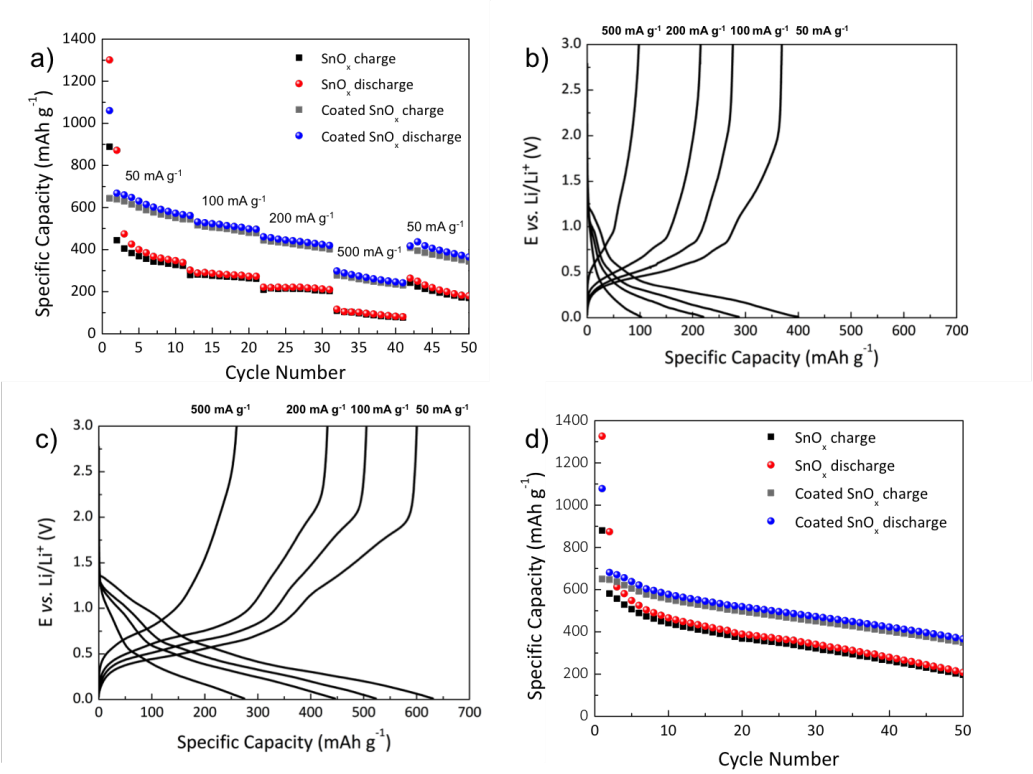

Figure 10: C-rate performance of uncoated and carbon coated SnO_x sponges (a) and corresponding selected potential profiles at the different applied specific currents of uncoated (b) and coated (c) SnO_x sponges. d) Cycling at a constant specific current of 50 mA g^{-1}; cut-off potentials: 0.01 and 3.0 V.

Selected potential profiles of coated and uncoated sponges for the different specific currents are shown in Figure 10b and c respectively and are in a good agreement with the results from cyclic voltammetry. A voltage plateau at 0.45 V can be observed

during the discharge and plateau at 0.5 V during the charge due to the alloying and dealloying reactions. These plateaus are more pronounced at lower specific currents and are more pronounced for the coated sample compared to the uncoated sample. Furthermore, in case of the coated sample a higher gain of specific capacity can be observed during charge in the region of 1.25 V to 2.0 V related to a higher reversibility of the decomposition of Li_2O due to the presence of a conductive carbon coating.[24] Figure 10d shows 50 cycles of the carbon coated and uncoated SnO_x sponges at 50 mA g^{-1}. In case of the uncoated sponges the charge capacity drops rapidly within the first 10 cycles from 880 to 441 mAh g^{-1}. In contrast, the initial charge capacity of the coated sample is lower (650 mAh g^{-1}), but the capacity retention is higher, as the discharge capacity after 10 cycles is still 555 mAh g^{-1}. The obtained specific capacity for the coated sample is up to the 50th cycle constantly 120 mAh g^{-1} higher compared to the uncoated sponges.

Potential profiles of selected cycles up to cycle 20 shown in Figure S7 and prove the enhanced cycling performance of coated SnO_x sponges. In case of uncoated sponges the plateau of the charge profile in the voltage region between 0.5 and 0.75 V decreases, but more dramatically is even the decrease of capacity gain above 1.0 V upon cycling, whereas the plateau between 0.5 and 0.75 V related to the dealloying reaction appears to be very reversible in case of the coated sample. Compared to previous reports on nanoporous tin oxide, which report capacities of less than 300 mAh g^{-1} after 20 cycles in the voltage range of 0.01 V to voltages higher than 1.8 V,[19,20] the carbon coated sponge-like SnO_x shows a strongly enhanced battery performance, as still a discharge capacity of 497 mAh g^{-1} can be obtained.

The morphology of the sponge-like structure was investigated after galvanostatic cycling by ex situ SEM measurements as shown in Figure 11 for carbon coated SnO_x samples after the first and fifth charge. Obviously, the sponge-like morphology could be retained upon continuous (dis-)charging, as the porous structure is clearly observable after cycling.

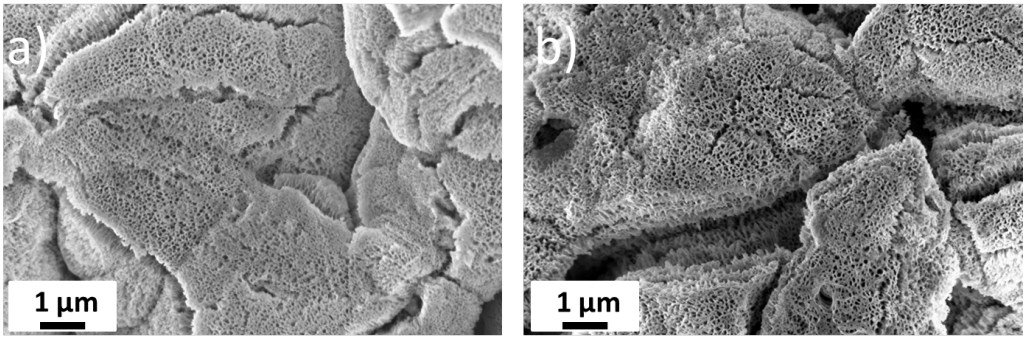

Figure 11: SEM images of carbon coated SnO_x electrodes after a) the first charge and b) after the fifth charge showing the preservation of the sponge-like morphology even after cycling.

3. Conclusions

In summary, we report on the synthesis of sponge-like SnO_x films deposited onto copper foil. The film was coated with a block copolymer containing carbon precursor polymer, followed by annealing to get a thin homogeneous carbon film. Composition of the SnO_x film was investigated before and after coating using XRD, EDX, XPS and Raman-spectroscopy and proves the sponge-like morphology and the presence of a carbon film in case of the coated sample. The tin oxide film was found to mainly consist of tin(II) oxide prior to coating, while a partial reduction was observed during the heat treatment. Electrochemical characterization shows that the coated SnO_x sponge exhibits an increased specific capacity and higher cycling stability as compared to the non-coated sample. The porous structure of the SnO_x film could be retained even upon cycling as proven by ex situ SEM measurements.

4. Methods and Experimental

Synthesis of SnO_x Sponges on Copper Foil.

Copper foil (Schlenk) was cut into round pieces of 15 mm in diameter. The passivation layer on the surface was then removed by applying 1 ml of a solution consisting of 300 mL (52.47 wt%) of methanol ($\geq$ 99.8 %, Sigma-Aldrich), 200 mL (35.79 wt%) of 1-butanol (99 % extra pure, Acros Organics), 29.16 mL (10.69 wt%) of

perchloric acid (70% solution in water, Acros Organics) and 4.71 mL (0.01 wt%) of MilliQ-Water were used. After 30 s the samples were cleaned with MilliQ-Water and air-dried. For electrodeposition and anodization, the foil was mounted in a setup consisting of a PTFE-cylinder and a copper block as the anode. For electrodeposition, a solution consisting of 0.22 mol/l tin (II) chloride dihydrate ($\geq$ 99.99 %, Sigma-Aldrich) and tri-ammonium citrate ($\geq$ 97 %, Alfa Aesar) and deionized warter was used. Electrodeposition was carried out at a constant current of 4 mA applied via a Voltcraft PSP 1803 voltage source for 25 min. After electrodeposition, the solution was removed, the foil rinsed with MilliQ-Water and air-dried. For the anodization, a solution consisting of 5.9 wt% oxalic acid dihydrate ($\geq$ 99.5 %, Sigma-Aldrich) and deionized water (Millipore) was used. Anodization was carried out under a constant anodic bias of 10 V applied by a Voltcraft Digi 35 voltage source for 6 min. After anodization, the solution was removed, the sample rinsed with deionized water and air-dried.

Carbon Coating of SnO_x Sponges.

The carbon precursor block copolymer was synthesized according to a previous synthesis strategy. [6] Briefly, acrylonitrile (AN) was polymerized by RAFT polymerization technique using 2-dodecylsulfanylthiocarbonylsulfanyl-2-methyl propionic acid (DMP) [48] as a chain transfer agent and α,α-azoisobutyronitrile (AIBN) as initiator. The ratio of AN:CTA:AIBN was set to be 250:1:0.1. For the block copolymerization, PAN was chosen as a macro-CTA and N-acryloxysuccinimide (NAS) [49] as the monomer and 2,2-azobis(4-methoxy-2,4-dimethylvaleronitrile) (AMDV) as the initiator. The molar ratio was NAS:PAN:AMDV = 25:1:0.2) and the reaction was conducted in DMSO for 48 h at 30 °C. Finally, the reactive ester was aminolyzed by the use of dopamine hydrochloride in DMSO resulting in P(AN-b-DAAM).

^{1}H-NMR (DMSO-d6, 400 MHz): δ[ppm] = 6.20–6.70 (d, Ar-H), 3.42 (s, CONH–CH_2), 3.14 (s, CH of polymer backbone), 2.03 (s, CH_2 of polymer backbone and CONH-CH-*CH_2*).

FT-IR: 2940 (C-H valence band), 2443 (nitrile valence band), 1702 (NH amide band), 1520 (NH deformation band), 1444, 1384, 1282, 1251 cm^{-1}.

The copper foil with the deposited SnO_x sponges was placed in 1 ml of a 20 mg ml[50] solution of P(AN-b-DAAM) in DMSO. The foil was removed after 8 h from the solution and washed with DMF to remove unbound polymer. The sample was dried under vacuum and then pyrolyzed. The heat treatment was conducted in two steps by first heating to 300 °C for 240 min and then heating to 350 °C for 45 min.

X-ray photoelectron spectroscopy (XPS).

XPS spectra were measured on a PHI 5600 Multi-Technique XPS (Physical Electronics, Lake Drive East, Chanhassen, MN) using monochromatized Al Kα at 1486.6 eV. Prior to measurement, the surface was sputtered for 1 s with Ar^+ ions to remove adsorbed CO2. Atomic concentrations were calculated using MULTIPAK 9.4.1.2 software.

X-ray diffraction (XRD).

The crystal structure of was examined via room temperature x-ray diffraction on a Bruker D8 Discover instrument operated in reflection geometry with a CuKα1,2 x-ray source.

Scanning electron microscopy (SEM).

Surface topography was analyzed using a high-vacuum mode scanning electron microscope (SEM; FEI Quanta 200 FEG Environmental-SEM, FEI Deutschland GmbH, Frankfurt / Main, Germany) at an acceleration voltage of 15 kV.

Cross-section measurement.

Samples were embedded in PMMA using DuroFix-2 Kit by Struers GmbH. PMMA cylinder were then cut into disks of approx. 1 mm thickness with an EXAKT 300CP diamond band saw. Disks were glued on Plexiglas slides and polished by Struers RotoPol-31 for 30 seconds with polishing paper of a grain size of 1200 and 2 minutes with a grain size of 4000. Polished samples were then applied to an aluminum stub and measured in SEM using low vacuum mode.

Characterization of the polymer.

For the polymer characterization, NMR (nuclear magnetic resonance) spectroscopy was conducted using a Bruker ARX 400, and FTIR spectroscopy (Fourier transform infrared) was carried out using Jasco FT/IR 4100 with an ATR unit. Size exclusion chromatography (SEC) was performed with hexafluoroisopropanol as solvent. The detector system contained refractive index (Agilent) and UV-vis (Agilent) units. The calibration was done using polymethylmethacrylate standards, purchased from Polymer Standard Services.

Electrochemical Characterization of SnO_x Sponge.

The content of SnO_x was in average 2.89 mg. SwagelokTM cells were assembled in a glove box (MBraun) with water and oxygen content of less than 0.1 ppm. Polypropylene fleeces (FS2190 Freudenberg, Germany) were used as separator and were drenched with an ethylene carbonate: diethyl carbonate 3:7 electrolyte containing 1M LiPF6. As a counter and reference electrode lithium foil (Rockwood Lithium) was used, so that all given potentials refer to the Li/Li^+ redox couple. The electrochemical experiments were conducted at 20 °C $\pm$ 2 °C. A Maccor Battery Tester was used for galvanostatic cycling experiments. Cyclic voltammetry was performed using a VMP3 potentiostat (BioLogic), applying a sweep rate of 0.05 mV/s in the range of 0.01 V and 3.0 V.

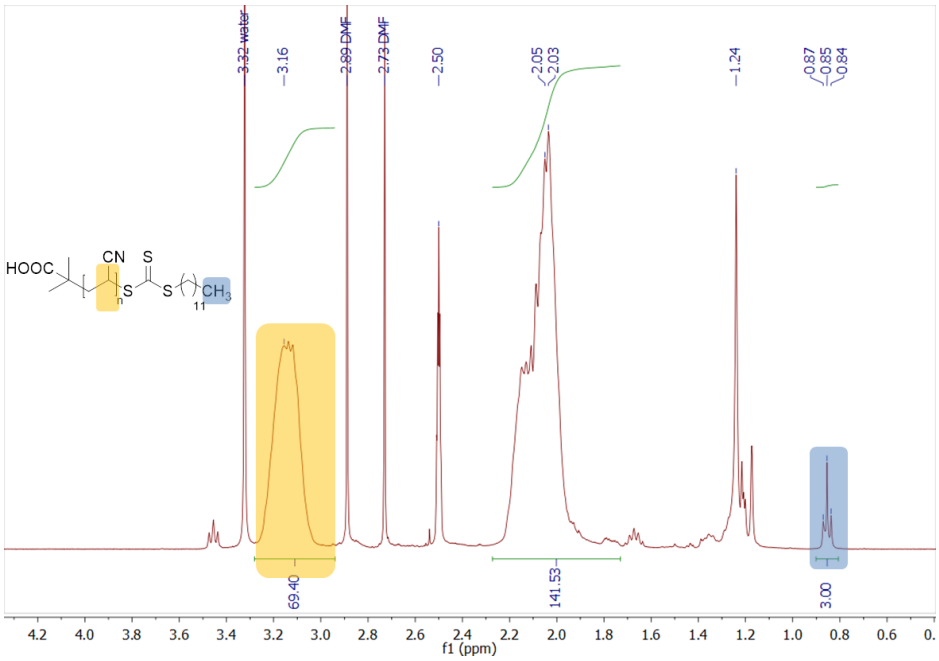

Figure S 1: ^{1}H-NMR spectrum of polyacrylonitrile. The number average of the molecular weight is determined to be 70, as confirmed by the ratio of the integrals of the signals at 0.85 ppm (CH_3-group of the chain transfer agent end-group) and the signal at 3.16 ppm (CH-backbone signal of the polyacrylonitrile).

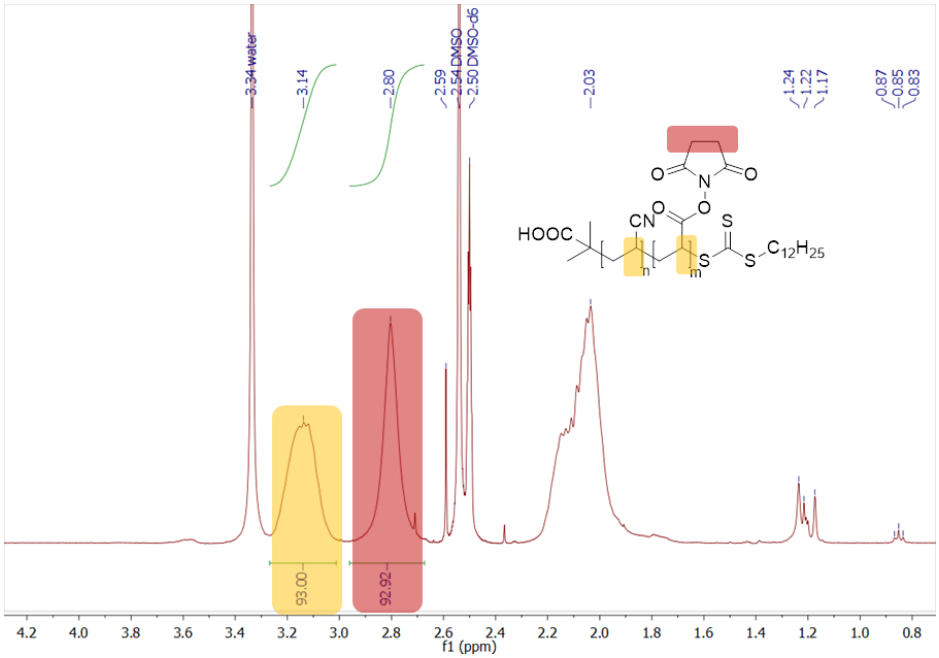

Figure S 2: ^{1}H-NMR spectrum of poly(acrylonitrile-block-N-acryloxysuccinimide).

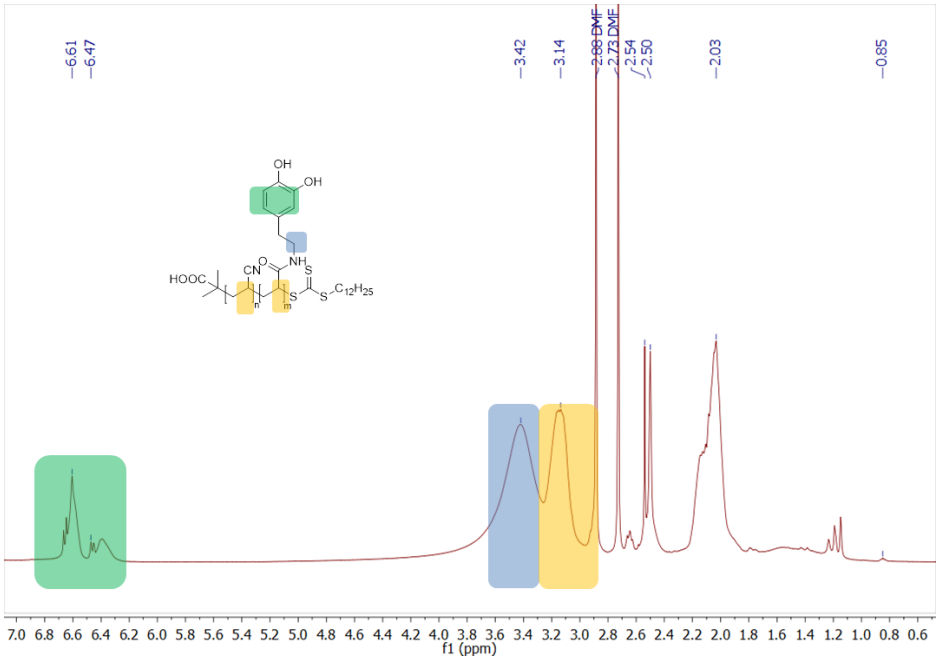

Figure S 3: ^{1}H-NMR spectrum of poly(acrylonitrile-block-dopamine acrylamide) showing both the typical polyacrylonitrile signals and the dopamine acrylamide signals.

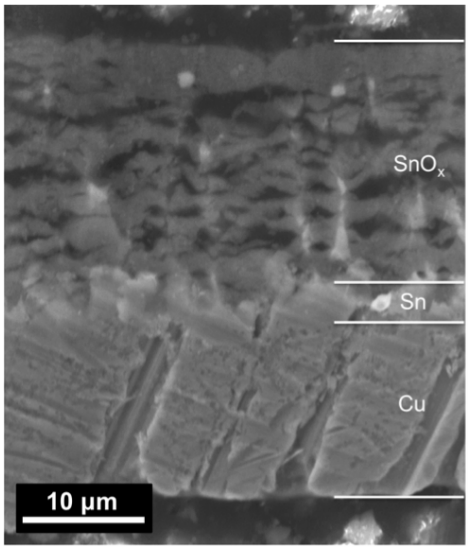

Figure S 4: Cross section SEM image of coated sample. Top: Sponge-like nanoporous SnO_x (grey), cracks from oxygen evolution breaking up regular tubular structure (black). Middle: Tin gluing layer connecting nanoporous tin oxide to underlying copper foil. Bottom: Copper foil.

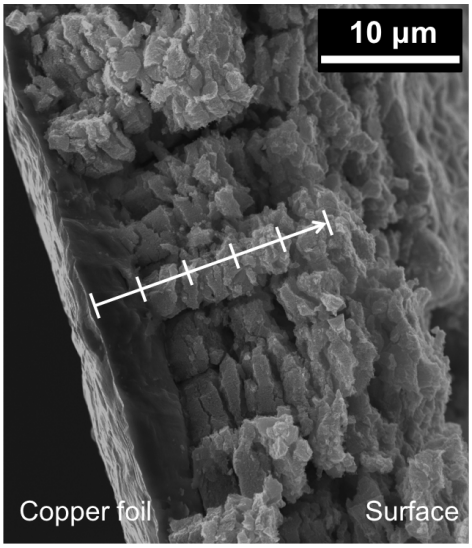

Figure S 5: Cross section SEM image of uncoated SnO_x sponge. Numbers indicate measuring points for EDX, the arrow shows the direction of measurement.

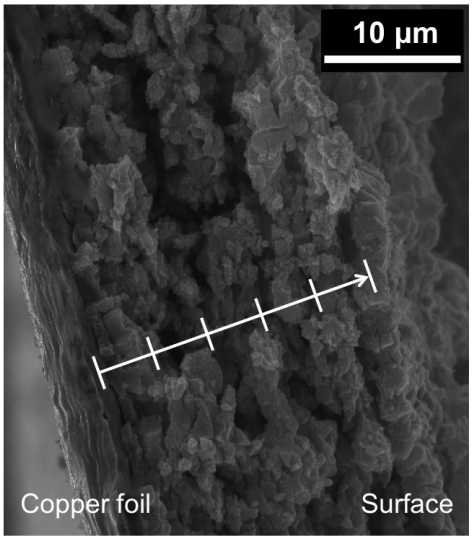

Figure S 6: Cross section SEM image of carbon coated SnO_x sponge. Numbers indicate measuring points for EDX, the arrow shows the direction of measurement.

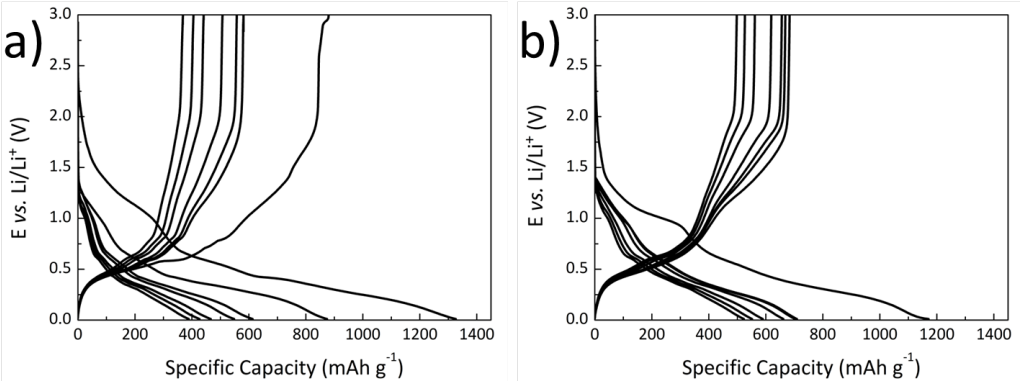

Figure S 7: Potential profiles of cycles 1, 2, 3, 5, 10, 15, 20 for uncoated SnO_x (a) and coated SnO_x (b) at 0.05 C. Cut-off potentials: 0.01 and 3.0 V vs. Li/Li^+.

References

[1] S. Shanmugam, A. Gedanken, Small 2007, 3, 1189.

[2] C. Mahendiran, T. Maiyalagan, K. Scott, A. Gedanken, Materials Chemistry and Physics 2011, 128, 341.

[3] A. S. Aricò, P. Bruce, B. Scrosati, J.-M. Tarascon, W. van Schalkwijk, Nat. Mater. 2005, 4, 366.

[4] H. Li, H. Zhou, Chem. Commun. 2012, 48, 1201.

[5] P. G. Bruce, B. Scrosati, J.-M. Tarascon, Angew. Chem. Int. Ed. 2008, 47, 2930.

[6] B. Oschmann, D. Bresser, M. N. Tahir, K. Fischer, W. Tremel, S. Passerini, R. Zentel, Macromol. Rapid Commun. 2013, 34, 1693.

[7] J. S. Chen, X. W. D. Lou, Small 2013, 9, 1877.

[8] Y. Idota, Science 1997, 276, 1395.

[9] J.-M. Tarascon, M. Armand, Nature 2001, 414, 359.

[10] J. S. Chen, Y. L. Cheah, Y. T. Chen, N. Jayaprakash, S. Madhavi, Y. H. Yang, X. W. Lou, J. Phys. Chem. C 2009, 113, 20504.

[11] X. W. Lou, J. S. Chen, P. Chen, L. A. Archer, Chem. Mater. 2009, 21, 2868.

[12] D. Larcher, S. Beattie, M. Morcrette, K. Edström, J.-C. Jumas, J.-M. Tarascon, J. Mater. Chem. 2007, 17, 3759.

[13] J. BESENHARD, M. HESS, P. KOMENDA, Solid State Ionics 1990, 40-41, 525.

[14] L. Zhang, G. Zhang, H. B. Wu, L. Yu, X. W. D. Lou, Adv. Mater. 2013, 25, 2589.

[15] X. W. Lou, L. A. Archer, Z. Yang, Adv. Mater. 2008, 20, 3987.

[16] C. Wang, G. Du, K. Ståhl, H. Huang, Y. Zhong, J. Z. Jiang, J. Phys. Chem. C 2012, 116, 4000.

[17] S. Han, B. Jang, T. Kim, S. M. Oh, T. Hyeon, Adv. Funct. Mater. 2005, 15, 1845.

[18] L. Zhang, H. B. Wu, X. Wen Lou, Mater. Horiz. 2013, 1, 133.

[19] G. F. Ortiz, P. Lavela, P. Knauth, T. Djenizian, R. Alcántara, J. L. Tirado, J. Electrochem. Soc. 2011, 158, A1094.

[20] J.-W. Lee, S.-J. Park, H.-C. Shin, Korean Journal of Materials Research 2011, 21, 21.

[21] S.-J. Park, H.-C. Shin, Korean Journal of Materials Research 2012, 22, 1.

[22] X. Ji, X. Huang, J. Liu, J. Jiang, X. Li, R. Ding, Y. Hu, F. Wu, Q. Li, Nanoscale Res Lett 2010, 5, 649.

[23] P. Wu, N. Du, H. Zhang, J. Yu, Y. Qi, D. Yang, Nanoscale 2011, 3, 746.

[24] B. Oschmann, M. N. Tahir, F. Mueller, D. Bresser, I. Lieberwirth, W. Tremel, S. Passerini, R. Zentel, Macromol. Rapid Commun. 2015.

[25] A. Moretti, G.-T. Kim, D. Bresser, K. Renger, E. Paillard, R. Marassi, M. Winter, S. Passerini, J. Power Sources 2013, 221, 419.

[26] A. Magasinski, B. Zdyrko, I. Kovalenko, B. Hertzberg, R. Burtovyy, C. F. Huebner, T. F. Fuller, I. Luzinov, G. Yushin, ACS Appl. Mater. Interfaces 2010, 2, 3004.

[27] J. Drofenik, M. Gaberscek, R. Dominko, F. W. Poulsen, M. Mogensen, S. Pejovnik, J. Jamnik, Electrochimica Acta 2003, 48, 883.

[28] D. Bresser, B. Oschmann, M. N. Tahir, F. Mueller, I. Lieberwirth, W. Tremel, R. Zentel, S. Passerini, Journal of the Electrochemical Society 2015, 162, A3013.

[29] D. M. Piper, T. A. Yersak, S.-B. Son, S. C. Kim, C. S. Kang, K. H. Oh, C. Ban, A. C. Dillon, S.-H. Lee, Adv. Energy Mater. 2013, 3, 697.

[30] A. He, Q. Liu, D. G. Ivey, J Mater Sci: Mater Electron 2008, 19, 553.

[31] H.-C. Shin, J. Dong, M. Liu, Adv. Mater. 2004, 16, 237.

[32] X. Hou, Y. Hu, H. Jiang, Y. Li, W. Li, C. Li, J. Mater. Chem. A 2015, 3, 9982.

[33] D. M. Mukhamedshina, K. A. Mit', N. B. Beisenkhanov, E. A. Dmitriyeva, I. V. Valitova, J Mater Sci: Mater Electron 2008, 19, 382.

[34] L. Zaraska, N. Czopik, M. Bobruk, G. D. Sulka, J. Mech, M. Jaskuła, Electrochimica Acta 2013, 104, 549.

[35] M. Zorn, S. Meuer, M. N. Tahir, Y. Khalavka, C. Sönnichsen, W. Tremel, R. Zentel, J. Mater. Chem. 2008, 18, 3050.

[36] J.-H. Jeun, H.-S. Ryu, S.-H. Hong, J. Electrochem. Soc. 2009, 156, J263.

[37] A. Palacios-Padrós, M. Altomare, K. Lee, I. Díez-Pérez, F. Sanz, P. Schmuki, CHEMELECTROCHEM 2014, 1, 1133.

[38] T. L. Barr, J. Vac. Sci. Technol. A 1995, 13, 1239.

[39] J. F. Moulder, J. Chastain, Handbook of x-ray photoelectron spectroscopy: A reference book of standard spectra for identification and interpretation of XPS data,

Physical Electronics Division, Perkin-Elmer Corp., Eden Prairie, Minn ©1992.

[40] K. J. Boyd, J. Vac. Sci. Technol. A 1995, 13, 2110.

[41] A. C. Ferrari, J. Robertson, Philosophical Transactions of the Royal Society A: Mathematical, Physical and Engineering Sciences 2004, 362, 2477.

[42] I. A. Courtney, J. Electrochem. Soc. 1997, 144, 2045.

[43] Z. Wen, F. Zheng, H. Yu, Z. Jiang, K. Liu, Materials Characterization 2013, 76, 1.

[44] E. Peled, J. Electrochem. Soc. 1979, 126, 2047.

[45] X. W. Lou, C. M. Li, L. A. Archer, Adv. Mater. 2009, 21, 2536.

[46] M. Mohamedi, S.-J. Lee, D. Takahashi, M. Nishizawa, T. Itoh, I. Uchida, Electrochimica Acta 2001, 46, 1161.

[47] T. Brousse, J. Electrochem. Soc. 1998, 145, 1.

[48] J. T. Lai, D. Filla, R. Shea, Macromolecules 2002, 35, 6754.

[49] D. E. Bergbreiter, P. L. Osburn, C. Li, Org. Lett. 2002, 4, 737.

[50] K. Mizushima, P. Jones, P. Wiseman, J. Goodenough, Mater. Res. Bull. 1980, 15, 783.

4.1.5 In situ Polymer Functionalization and Carbon Coating of TiO_2 Nanoparticles and Their Application in Na-ion Batteries

Commonly, for the synthesis of nanoparticles the use of surfactants is required to enable a controlled particle growth and to avoid the formation of aggregations, as also shown in the chapters 4.1.1 and 4.1.3. Thus, for the carbon coating approach developed in this thesis, several synthetic steps are required to obtain polymer coated nanoparticles including the synthesis of the nanoparticles using typical surfactants such as oleylamine or oleic acid, the exchange of surfactant by the use of nitrosonium tetrafluoroborate (see chapter 4.1.1) and finally the attachment of the polymer. Motivated by the idea to reduce the number of synthetic steps, a further synthetic approach was developed and is introduced in this chapter. Instead of using common surfactants the use of the carbon precursor polymer itself as the surfactant should be applied for the nanoparticle synthesis. Therefore, a block copolymer was synthesized consisting of the already introduced polyacrylnitrile as the carbon precursor block and consisting of a block containing hydroxamic acid, which functions as the surface protecting and coordinating group in the polymer. Using hydroxamic acid instead of dopamine, which was used in the previous chapters, is supposed to offer several advantageous: First of all, it is not redox sensitive as the catechol groups, which undergo oxidation forming o-chinone structures, which are no more able to coordinate onto inorganic nanoparticle surfaces. Secondly, the binding of catechol groups is very strong and this might prevent a particle growth during the synthesis. Thus, a weaker coordinating species such as hydroxamic acid might be more useful in this respect.

As shown in this contribution, TiO_2 nanoparticles can obtained by the use of poly-(acrylonitrile-b-hydroxamic acid) as a surfactant with a very small primary nanoparticle size of 8 nm. By the application of pyrolysis, the polymer coating can be transformed into a carbonaceous shell. As the obtained nanoparticles are very small, this

material was expected to be very promising for Na-ion batteries, as in the case of Na-ion batteries, size of nanoparticles and thus diffusion distances for the Na-ions is expected to matter even more compared to Li-ions, as the size of Na-ions is bigger compared to Li-ions. In this study, we applied the TiO_2 nanoparticles obtained by the in-situ functionalization approach as an anode material in Na-ion batteries and proved the huge impact of the nanoparticle size on the battery performance by comparing the battery performance of 8 nm sized coated particles with the battery performance of 30 nm sized carbon coated nanoparticles. Furthermore, the influence of carbon coating was demonstrated one more time, as 8 nm sized uncoated TiO_2 nanoparticles were applied as anode material as well. The coated TiO_2 particles with a size of 8 nm show a significantly enhanced battery performance with respect to the obtained capacities for an applied C-rate test. Furthermore, the carbon coated small particles exhibit a very impressive longterm cycling stability for several hundreds of cycles at different applied C-rates, which is currently rather exceptional for electrode materials in Na-ion batteries.

In this contribution polymer synthesis was conducted by myself, whereas the synthesis of inorganic particles using the polymers was conducted by Muhammad Nawaz Tahir. Ingo Lieberwirth was responsible for electron microscopy. The electrode fabrication and cell assembly was conducted by myself, whereby Xinwei Dou supported me by assembling about 20 % of the total number of cells. Daniel Buchholz and Liming Wu supported me with ideas to reasonably characterize the material.

4.1.5.1 Manuscript to be submitted

Synthesis of Carbon Coated TiO_2 Nanoparticles Obtained by in situ Carbon Precursor Polymer Functionalization and its Advanced Sodium-Ion Battery Performance

Bernd Oschmann, Muhammad Nawaz Tahir, Daniel Buchholz, Xinwei Dou, Liming Wu, Ingo Lieberwirth, Wolfgang Tremel, Stefano Passerini, and Rudolf Zentel

Abstract

The synthesis of in situ polymer-functionalized anatase TiO_2 particles using an anchoring block copolymer is reported, which yields in gram amounts of particles with a small crystallite size (about 8 nm). A thermal annealing converts the polymer brushes into a carbonaceous coating as proven by high resolution TEM and Raman spectroscopy, allowing an advanced battery performance of the carbon coated particles when applied as an anode material in sodium ion-batteries. The strong impact on the battery performance of i) down-sizing to small nanoparticles and of ii) the presence of a carbon coating is proven by comparing the presented material with reference systems. Extraordinary high degree of reversible insertion of sodium is enabled by the herein introduced synthetic approach (0.69 Na/TiO_2), whereas uncoated particles of same size (0.61 Na/TiO_2) and bigger particles (about 30 nm) with carbon coating (0.51 Na/TiO_2) show a decreased battery performance. Enhanced C-rate capability, improved coulombic efficiency and high capacity retention are further key features of the particles obtained by the in situ functionalization approach, as even after 300 cycles at 1C a charge capacity of 177 mAh g^{-1} can be obtained corresponding to a retention of 102 % .

1. Introduction

Currently, lithium-ion batteries are the dominating technology for energy storage, especially in portable electronic devices[1] due to their high energy density. They are promising candidates for future large scale applications such as in the field of electromobility and in combination with renewable energy sources. However, driven by the concern over the limited abundance of lithium, which might not cover the world-wide demand of energy storage based on long-term considerations,[2] the development of post-lithium battery technologies has attracted more and more researchers. In this regard, sodium-ion battery technology takes the privilege over other promising stationary energy storage devices including lithium ion batteries due to its cost effectiveness and natural abundance, which are two very important parameters to meet the future demands of technology. Sharing similar electrochemical behaviour with lithium, it is possible to adopt the rocking chair battery set-up of lithium-ion batteries to sodium-ion batteries, where the alkali-ion shuttles between the electrodes back and forth. Therefore, sodium ion batteries have become the target of vigilant eyes of attraction for nanotechnologists. However, developing suitable electrode materials, especially anode materials, accommodating the bigger Na-ions and enabling reversible (de-)sodiation reactions with a long and stable cycling behaviour, is still challenging.

Conversion-alloying compounds are rather challenging, as they suffer from large volume changes and capacity fading. However, alloying based materials such as Sn[3–6] and Sb[7–9] as well as insertion and intercalation based materials such as hard carbon [10–12], recently graphite[13] and titanium based insertion materials like $Na_2Ti_3O_7$[14,15] and TiO_2[16] are very promising candidates as anode materials. Especially TiO_2 in different polymorphs like TiO_2(B),[17,18] amorphous TiO_2[19,20] as well as anatase TiO_2[21–33] has attracted attention due to the low cost, environmental friendliness and attractive theoretical specific capacity of 335 mAh g^{-1}. However, challenges of pristine anatase TiO_2 are the rather low electrical

conductivity in the range of 10-12 S cm^{-1} and the low ion diffusion coefficients. An approach to lower ion diffusion distances is the downsizing of the active material to nanostructured particles, which is proven to be successful for lithium-ion batteries[34] and which is even more critical for the bigger sodium-ions. Various strategies including doping of TiO_2 with foreign atoms such as N,[21] Nb[35] or Sn[36], carbon coating or the use of graphene as a conductive additive are employed to increase the electrical conductivity of TiO_2 as anode materials.[16,26,32] However, the use of graphene on industrial scale is still challenging due to the fact that cost effective up-scaled synthesis of graphene needs to be established. Additionally, homogeneous and precise amount of foreign atom doping poses a big challenge for synthetic chemists as well. As reported in numerous reports carbon coating approaches applied to nanomaterials could successfully improve battery performances.[25,27,28] Common strategies to obtain carbon coated nanoparticles often involve at least three steps, starting with the synthesis of the inorganic particle followed by mixing of particles with a carbon precursor (for example glucose) and finally the pyrolysis of carbon precursors at elevated temperature.[24,28,37,38] The major drawback related to this method is the solubility incompatibility which often results in agglomeration of nanoparticles and ultimately in a rather inhomogeneous distribution of carbon coating. Additionally, scaling up the amount of electrode materials is rather challenging due to a multistep process. Advanced strategies also based on post functionalization method, include the coordination of a carbon precursor polymer onto the nanoparticle resulting in rather homogeneously coated particles.[39,40] This method could improve the electrode performance, but as it is based on post functionalization strategy of nanomaterials it could not reduce the number of steps to obtaine final electrode material.

To address these problems, we report on the synthesis of carbon precursor polymeric ligand coated TiO_2 nanoparticles using an in situ surface functionalization approach. The carbon precursor block used as ligand consists of a well-graphitizable

polyacrylonitrile block and a hydroxamic acid anchor-block, as hydroxamate units are reported to bind to transition metals.[41] The block copolymer plays a dual role: (i) the surface chelating block (hydroxamate) controls the growth, size and crystallinity of nanoparticles from nucleation stage and ensures the binding of carbon precursor polymer to every nuclei, (ii) the graphitizable block shileds the nanoparticles, controls mesoporosity and provides the long electron pathways upon pyrolysis. This synthetic strategy reduces the number of required synthesis steps, to obtain electrode material with very small crystallite domains (about 8 nm). Thus, this material is expected to be beneficial, as it offers low diffusion distances for ions and a very well interconnected carbon network with an increased electrical conductivity. Additionally, the amount of active materials can be scaled up to gram amounts very easily. These carbon coated particles are applied as an anode material in sodium-ion batteries. By comparing the herein described material with uncoated TiO_2 of the same particle size (about 8nm) and with carbon coated particles of bigger size (about 30nm), we demonstrate the high impact of particle size and carbon coating. The small particles obtained by in situ functionalization synthesis show an advanced electrochemical performance with respect to C-rate capability, long-term cycling and capacity retention, as cycling for more than 500 cycles without capacity fading is possible.

2.Results and Discussion

Synthesis and characterization of carbon coated TiO_2 particles

A schematic illustration for the synthesis of carbon coated TiO_2 nanoparticles is shown in Figure 1. The block copolymer containing acrylonitrile block as carbon precursor moiety and hydroxamic acid is used as an in situ functionalization ligand to control the nucleation and growth process of TiO_2 nanoparticles. As a coordinating species hydroxamic acid was chosen, since it is reported to coordinate the transition metals cations on thin films.[41] However, it is worth to mention that (to

the best of our knowledge) it has not been used as an in situ anchor group to synthesize well crystalline metal oxide nanoparticles. Moreover, hydroxamate appears more attractive compared to the well-established catechol coordination chemistry applied in our previous works,[30,39,42,43] as it is not susceptible to oxidation.

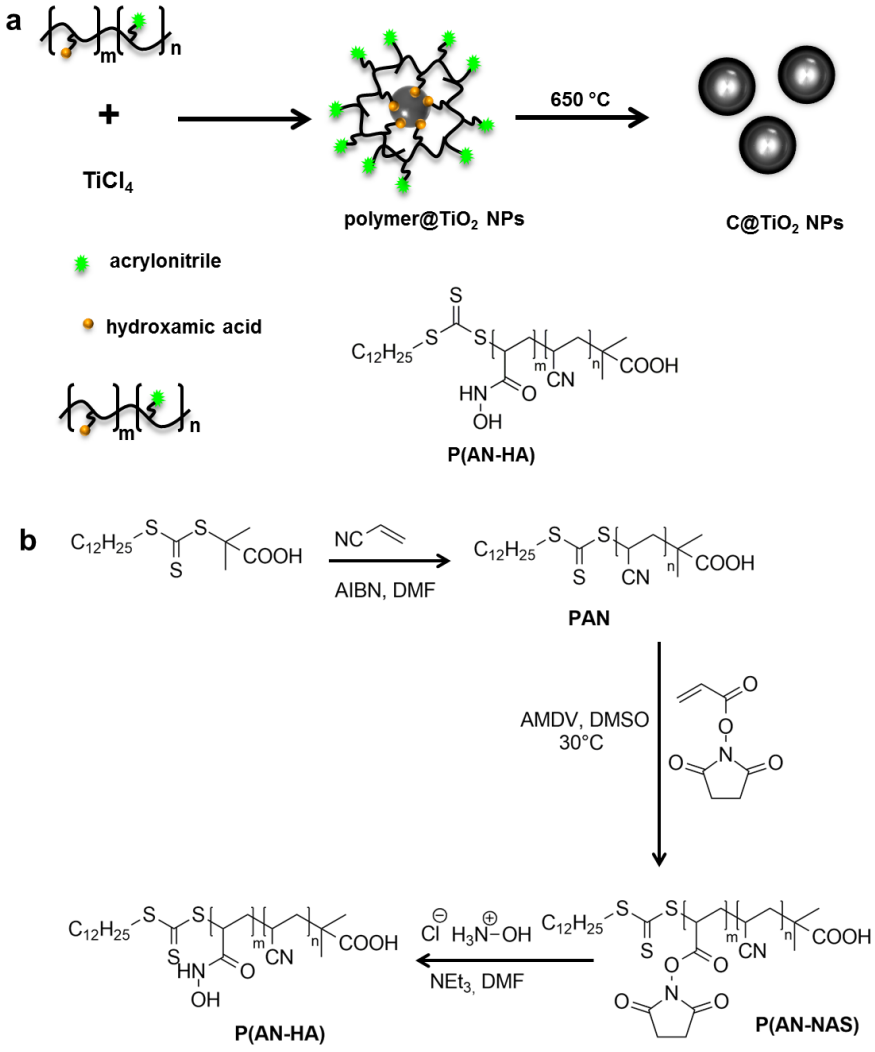

Figure 1: a) Schematic synthesis route for carbon coated TiO_2 nanoparticles obtained by in situ polymer functionalization and b) synthesis route of the block copolymer.

The hydroxamic acid containing block copolymer is synthesized by reversible addition-

fragmentation chain transfer (RAFT) polymerization. The synthesis scheme is shown in Figure 1b. As previously reported,[39] first the carbon precursor block consisting of polyacrylonitrile is synthesized, whereby the average block length is 80 repeating units as determined by NMR spectroscopy (see Figure S1). Hydroxamic acid as an anchor group is introduced using reactive ester chemistry. Therefore, N-acryloyloxysuccinimide (NAS) is used as a second monomer for the block copolymerization and polyacrylonitrile (PAN) is used as the macro-RAFT agent to obtain P(AN-b-NAS). The block length of the reactive ester is about 31 repeating units, as estimated by NMR spectroscopy (see Figure S2). Aminolysis of the reactive ester with hydroxylamine yields in the hydroxamic acid containing polymer poly(acrylonitrile-b-hydroxamic acid) (P(AN-b-HA) as confirmed by IR-spectroscopy (Figure S3a) and NMR spectroscopy (Figure S4). As sown in Figure S3a the reactive ester band (1732 cm^{-1}) of NAS, observeable prior to the aminolysis, is no more present after aminolysis. Instead, an amide band (1648 cm^{-1}) and a hydroxyl band are observed indicating the successful conversion. Furthermore, the polymer was characterized by size exclusion chromatography (SEC). Figure S3b shows the elugrams of polyacrylonitrile (PDI: 1.20) and of P(AN-b-HA) (PDI: 1.28). After aminolysis the polymer still shows a rather low polydispersity, suggesting that no cross-linking occurred. The clean reaction is also proven by the absence of ester bands, which might occur due to the alcoholysis of the hydroxyl group of hydroxylamine.

The resulting polymeric ligand is used as an in situ functionalizing ligand to synthesize the carbon coated TiO_2 nanoparticles. The hydroxamic acid block acts as metal chelating ligand to synthesize TiO_2 nanoparticles. Thereafter the acrylonitrile block can be graphitized upon pyrolysis. The overall synthesis is based on a modified benzyl alcohol synthetic methodology reported by Nieberger et al.[44,45] As shown in Figure 1a, $TiCl_4$ and P(AN-b-HA) are solved in a benzyl alcohol/DMF mixture and the reaction mixture is stirred at 80 °C under inert conditions to obtain gram amounts of polymer coated TiO_2 (see Figure S5). The resulting particles are

characterized by high resolution transmission electron microsopy (TEM) and corresponding images are shown in Figure 2a.

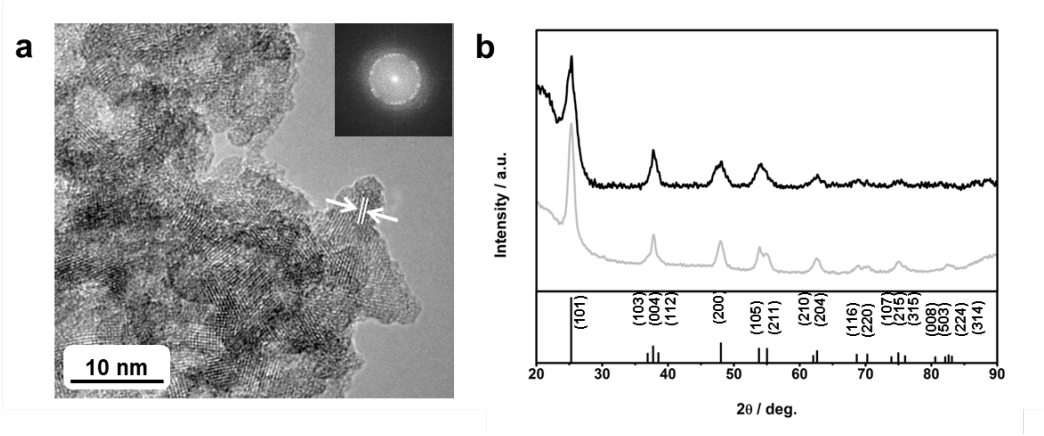

Figure 2: a) High resolution TEM image of as-synthesized TiO_2 particles with the FFT (inset) indicating a lattice spacing of 3.5 Å corresponding to the (101) reflection. b) XRD pattern of as-synthesized TiO_2 particles (black) and carbon coated TiO_2 particles (grey).

The single-crystalline nature of the nanoparticles, with perfect anatase structure, is clearly visible from the fast fourier transform (FFT) and by measuring fringe spacing as estimated to be 0.35 nm. This is close to the (101) lattice spacing of anatase TiO_2. The average size of the resulting nanoparticles is around 8 nm. Furthermore, the anatase crystal structure is confirmed by means of X-ray diffraction (XRD) shown in Figure 2b. All reflections can be attributed to the phase pure anatase and no other reflections are observed. In order to estimate the organic content of the as-synthesized particles, thermograviemtric analysis (TGA) was conducted. The total weight loss is 40 wt.%, whereby two shoulders can be observed in the TGA data as shown in Figure S6a. The first shoulder at around 250 °C is ascribed to the presence of benzyl alcohol, and the second shoulder at around 500 °C is ascribed to the bound polymer. The thus roughly estimated weight ratio between polymer and TiO_2 is 23:77. Furthermore, IR spectrum of the hybrid material includes typical polymer

bands, especially the nitrile group at 2246 cm^{-1} (see Figure S6b). The hydroxyl band at 3200 cm^{-1} indicates the presence of benzyl alcohol, which is in agreement with the observation of the TGA data. By the application of a heat treatment at 650 °C the polymer shell around the particles can be transformed into a carbonaceous shell. The content of organic material after pyrolysis decreases to 12 wt.% as proven by TGA (see Figure 3a).

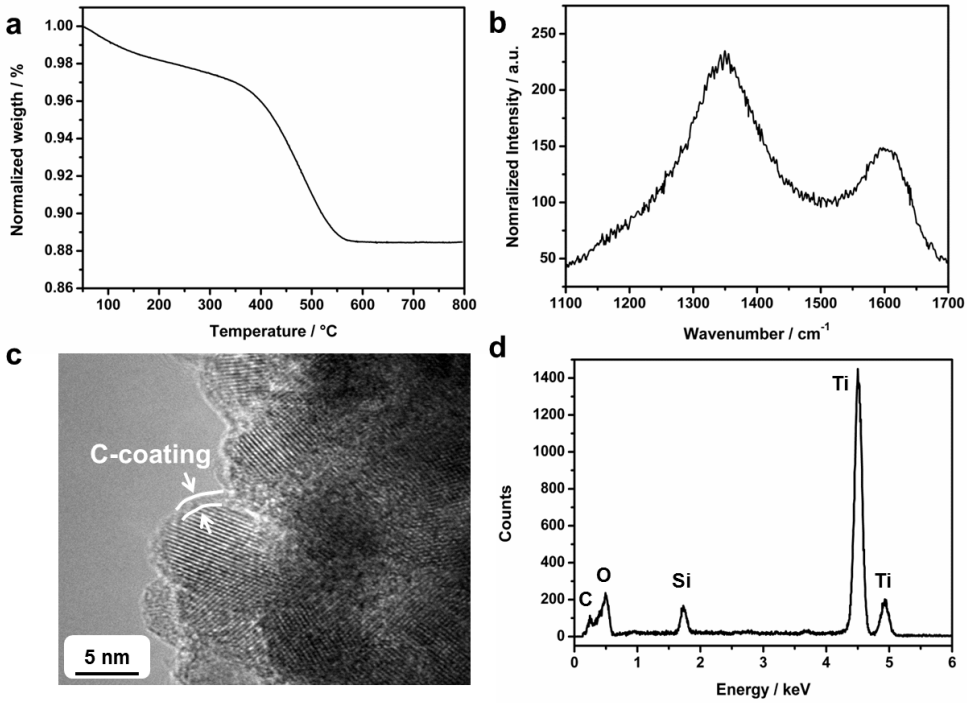

Figure 3: a) TGA data of carbon coated TiO_2 particles b) Raman spectrum of carbon coated TiO_2 particles. c) HRTEM image d) EDX data corresponding to the area scan indicated in Figure S7 of carbon coated TiO_2 particles.

This is in good agreement with the results of CHN elemental analysis, where a carbon content of 10.4 wt.% and a nitrogen content of 1.4 wt.% is detected, whereby the presence of nitrogen can be attributed to not completed removal of nitrogen present in the polyacrylonitrile. Raman spectroscopy (see Figure 3b) indicates the

presence of carbonaceous material after pyrolysis due to the presence of the D-band at 1349 cm^{-1} and the G-band at 1601 cm^{-1}. As proven by XRD (shown in Figure 2b) the anatase crystal structure is remained even after pyrolysis at 650 °C and no phase transformation is observed. The specific surface area was determined after pyrolysis by means of the Brunauer-Emmet-Teller (BET) method, revealing a value of 132.9 m^2 g^{-1}. High resolution TEM images show a thin amorphous layer (about 1-2 nm thickness) around the inorganic particles, as presented in Figure 3c. Finally, an EDX area scan proofs the presence of carbon on the surface of the inorganic particles (Figure 3d and Figure S7).

Electrochemical characterization of carbon coated TiO_2 nanoparticles

The carbon coated TiO_2 particles with a size of 8 nm, in the following abbreviated as C-TiO_2(8), were applied as an electrode material in sodium-ion batteries. Figure 4 shows the results of cyclic voltammetry for C-TiO_2(8) cycled in a voltage range of 0.05V and 2.0 V at a scan rate of 0.1 mV s^{-1}.

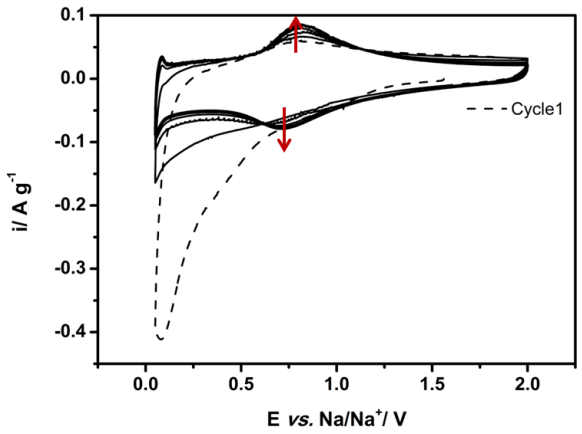

Figure 4: Figure 4: Cyclic voltammetry of C-TiO_2(8).

The main cathodic peak of the first scan starting at around 0.8 V is attributed to both irreversible reactions related to the formation of a solid electrolyte interface due to electrolyte decomposition, to a partial conversion of TiO_2 to metallic titanium and sodium peroxide,[22,24,31,46] and to the reversible sodiation of TiO_2 resulting in

the formation of a sodium titanate.[22] During the first anodic sweep a broad peak in the range of 0.5 V to 1.1 V can be observed. It is ascribed to the desodiation reaction of the sodium titanate.[22] For the following cathodic and anodic sweeps, broad and highly reversible peaks with slightly increasing intensities are observed in the range of 0.55 V to 1.2 V and 0.6 V to 1.3 V respectively.

In order to investigate the influence of the particle size and of the coating on the battery performance, the sample C-TiO_2(8) was applied to a C-rate test (Figure 5a) and compared to reference samples: Therefore, i) carbon coated particles of 30 nm size in diameter (see SEM image in Figure S8) obtained by applying a carbon coating approach to commercial TiO_2 particles (Sigma Aldrich) using the same polymer as a carbon precursor, in the following abbreviated as C-TiO_2(30), and ii) uncoated TiO_2 particles with a primary particle size of 8 nm (see TEM image in Figure S9), abbreviated as TiO_2(8), were used. In the case of C-TiO_2(30) and C-TiO_2(8) the specific capacities presented in Figures 5,6 and S10 are based on the weight of C-TiO_2, i.e. both TiO_2 and the carbon coating are included in the weight of active mass. The specific current applied in the first cycle was 0.02C, whereby 1C is defined as 335 mA g^{-1}, and the specific charge capacity for the smaller particles, i.e. for TiO_2(8) and C-TiO_2(8) are 233 and 231 mA g^{-1} respectively and thus significantly higher compared to the specific charge capacity of C-TiO_2(30) with 184 mA g^{-1}. Removing the contributions to the specific capacities of conductive carbon particles added during electrode preparation and of carbon coating, which were calculated to be 75 mA g^{-1} and 125 mA g^{-1} as reported in our previous studies,[22,30] enables the calculation of the specific capacities based on TiO_2 only. In case of C-TiO_2(30) the obtained value for the specific charge capacity of the first cycle is 171 mA g^{-1} corresponding to 0.51 Na per TiO_2, whereas higher capacities can be obtained for TiO_2(8) with 204 mA g^{-1} (0.61 Na/TiO_2) and for C-TiO_2(8) with 230 mA g^{-1} (0.69 Na/TiO_2).

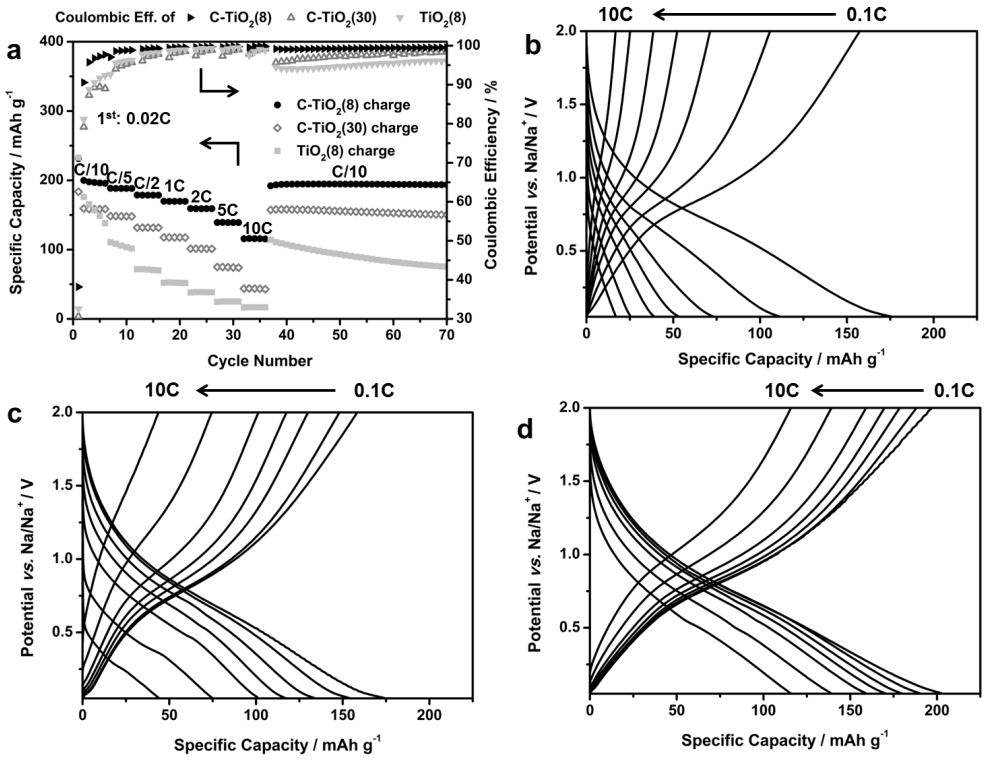

Figure 5: a) Cycling performance of TiO_2(8), C-TiO_2(30) and C-TiO_2(8) at various C-rates and corresponding selected potential profiles of TiO_2(8) (b), C-TiO_2(30) (c) and C-TiO_2(8) (d) at 0.1C, 0.2C, 0.5C, 1C, 2C, 5C and10C.

This proves that a higher degree of reversible sodium extraction can be achieved by the use of smaller nanoparticles, as these offer shorter diffusion distances for the sodium ions. It should be pointed out that we reported a maximum possible degree of sodiation of 0.69 Na/TiO_2 in our previous study, which is limited by the partially irreversible decomposition of TiO_2 to metallic titanium.[22] Thus, the ability to extract 0.69 Na/TiO_2 brings us close to the limit of anatase TiO_2 sodium-ion battery performance. Further cycling, especially cycling at elevated C-rates, shows a capacity fading for the uncoated TiO_2(8) (Figure 5a). This might be related to the fact that the small particles undergo a relatively high volume change due to the relatively high degree of sodiation causing the loss of electrical contact of active material. In

contrast, the bigger C-TiO_2(30) particles show a more stable cycling performance obtaining higher specific capacities compared to TiO_2(8) as from the fifth cycle, as the degree of (de-)sodiation and thus the volume changes are relatively lower. Additionally, the carbon coating of C-TiO_2(30) buffers the volume changes and increases the electrical contact between the particles. However, even more impressive is the comparison of the C-rate performance of C-TiO_2(8) with C-TiO_2(30) and TiO_2(8), as highest capacities for all applied C-rates as well as a highly stable cycling performance can be accomplished for C-TiO_2(8), thus highlighting both the importance of a small particle size enabling a high degree of (de-)sodiation and the importance of a carbon coating enabling a very stable cycling performance. For instance, reversible charge capacities of 197, 170 and 116 mA g^{-1} (based on C-TiO_2) can be obtained at 0.1C, 1C and 10C respectively. Obtained values for C-TiO_2(30) are only 158, 118 and 44 mA g^{-1} and for TiO_2(8) only 157, 52 and 17 mA g^{-1}. Besides the enhanced C-rate performance, C-TiO_2(8) shows an advanced capacity retention, as the capacity retention with respect to the first cycle at 0.1C after 70 cycles is 96.9 %, whereas the capacity retention for C-TiO_2(30) is 94.2 % and for TiO_2(8) even only 42.8 %. Coulombic efficiencies at the first cycle are for all three materials rather low (38.2 %, 32.6 % and 30.6 % for C-TiO_2(8), C-TiO_2(30) and TiO_2(8)) due to the side reactions occurring during the first cycle. However, coulombic efficiencies obtained for C-TiO_2(30) and TiO_2(8) are lower compared to C-TiO_2(8), as for instance the coulombic efficiencies at cycle 50 are 94.7 % (C-TiO_2(30)), 97.5 % (TiO_2(8)) and 99.3 % (C-TiO_2(8)). Selected voltage profiles for several C-rates are shown in Figure 5 b), c) and d) for TiO_2(8), C-TiO_2(30) and C-TiO_2(8) respectively, clearly revealing the advanced C-rate performance of C-TiO_2(8), as the slope of the continuously decreasing discharge profiles for C-TiO_2(8) is decreased compared to the two reference systems. Additionally, the voltage region from 0.75 V to 1.25 V in the charge profile is more pronounced in case of C-TiO_2(8) for all applied C-rates.

As the battery performance of C-TiO_2(8) is obviously the most advanced of the herein

presented materials, a more detailed characterization with respect to long-term cycling experiments was conducted for C-TiO_2(8). As shown in Figure S10, C-TiO_2(8) exhibits a very stable cycling performance when applied to an extended cycling at several C-rates ranging from 0.1C, 1C to 5C. Figure 6 a) shows the remarkable long-term cycling performance of C-TiO_2(8) at 1C and presents a stable cycling performance without any substantial loss of specific capacity.

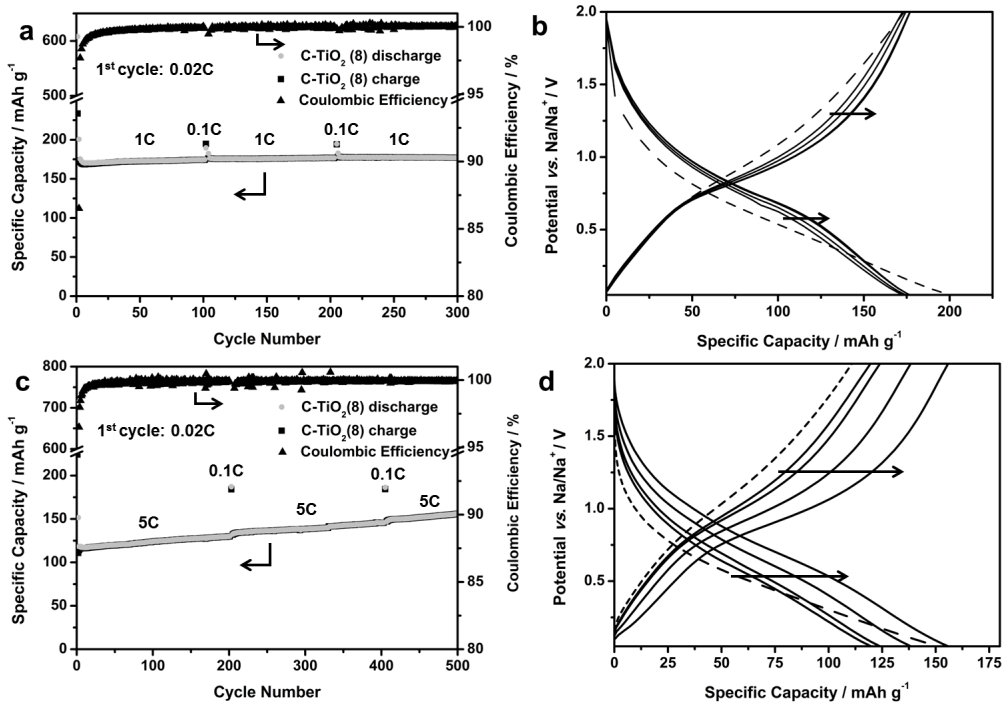

Figure 6: Long-term cycling performance of C-TiO2(8) at 1C (a) and selected potential profiles of cycle number 2, 50, 100, 200 and 300 at 1 C (b). c) Long-term cycling of C-TiO2(8) at 5C and corresponding potential profiles of cycles 2, 50, 100, 300 and 500 (d).

In contrast, as shown for selected voltage profiles ranging from the cycle 2 to cycle 300, even a slight gain of capacity can be observed starting from 174 mA g^{-1} (second cycle, i.e. first cycle at 1C) to 177 mA g^{-1} at the 300th cycle. Additionally, the

coulombic efficiency increases from 86.5 % (second cycle) to an impressively high value of 99.8 % in average. Finally, increasing the C-rate to 5C still allows a highly reversible cycling, whereby the effect of increasing capacity upon cycling is even more pronounced compared to cycling at 1C, as shown in Figure 6 c) and d). Starting with a charge capacity of 111 mA g^{-1} the capacity obtained after 500 cycles is 156 mA g^{-1} with an average coulombic efficiency exceeding 99.9 %. Thus, C-TiO_2(8) appears to be a very promising candidate as an anode material for sodium-ion batteries approaching the limits of anatase TiO_2 battery performance . Remaining challenges, which need to be addressed to actually enable a commercial application of anatase TiO_2, are the low coulombic efficiency of the first cycle related to the irreversible reactions and the formation of metallic titanium as well as the need of preventing a gas formation especially upon the first (dis-)charge.

3. Conclusion

The up-scalable synthesis of TiO_2 particles with a size of 8 nm applying an in situ functionalization approach by the use of an anchoring block copolymer carbon precursor results in homogeneously carbon coated TiO_2 particles. The high impact of the particle size and of the carbon coating is demonstrated by comparing the battery performance of carbon coated 8 nm sized particles with the battery performance of 8 nm sized uncoated and 30 nm sized coated particles. A highly improved battery performance can be observed for the small coated particles with respect to C-rate capability, capacity retention and coulombic efficiency. Moreover, the downsizing and carbon coating approach enables an outstanding long-term cycling with even slightly increasing capacity up to 500 cycles at 5C.

4. Experimental

Synthesis of P(AN-b-HA):

The reactive ester N-acryloxysuccinimide (NAS) and 2-dodecylsulfanylthiocarbonylsulfanyl-

2-methyl propionic acid (DMP), which was used as a chain transfer agent, were synthesized following procedure described already in literature.[47,48] P(AN-b-NAS) was synthesized following a previously reported method.[30] Briefly, acrylonitrile (AN, Merck, purified by destillation), DMP and α,α-Azoisobutyronitrile (AIBN, Sigma Aldrich, recrystallized from diethylether) were dissolved dry N,N-dimethylformamide (DMF 99.8 %, Acros Organics). After degassing by freeze-pump-thaw cycles, the reaction mixture was stirred 7 h at 70 °C. After wok-up by precipitation in methanol PAN was used as a macro-CTA, NAS as a monomer, 2,2-azobis(4-methoxy-2,4-dimethylvaleronitrile) (AMDV, Sigma Aldrich) as an initiator and dimethyl sulfoxide (DMSO 99.9 %, Acros Organics) as a solvent. After stirring for 48 h at room temperature the polymer was worked-up by precipitation in methanol.

FT-IR: ν= 2941 (w, CH), 2240 (w, -CN), 1731 (s, C=O, reactive ester), 1203 (s), 1045 (s), 951 (w), 812 (w) cm^{-1}.

^{1}H-NMR (DMSO-d6, 400 MHz): δ[ppm] = 3.19 (bs, 111, C*H* of polymer backbone), 2.79 (bs, 125, CH_2-CH_2 of NHS), 2.03 (bs, 279, CH_2 of polymer backbone), 1.23 (m, CTA dodecyl chain), 0.85 (t, 3, dodecyl-CH_3 of CTA). SEC (eluent: hexafluoroisopropanol HFIP): 10,300 g mol^{-1}, PDI: 1.30

P(AN-b-NAS) (1 eq.), hydroxylamine hydrochloride (40 eq.), triethylamine (40 eq.) are dissolved in DMF and stirred over night at room temperature. The polymer was purified by precipitation in methanol to obtain poly(acrylonitrile-b-hydroxamic acid) P(AN-b-HA). The yield was about 85 wt.%.

FT-IR:ν=3260 (w, -OH), 2925 (w, CH), 2240 (w, -CN), 1648 (s, C=O, amide), 1386 (m), 1096 (m) cm^{-1}.

^{1}H-NMR (DMSO-d6, 400 MHz): δ[ppm] = 3.34 (bs, C*H*CONHOH) , 3.14 (bs, C*H*CN), 2.04 (bs, CH_2-CHCN), 1.55 (CH_2-CHCONHOH), 1.23 (m, CTA dodecyl chain), 0.85 (t, CTA-CH_3).

SEC (eluent: HFIP): 14,300 g mol^{-1}, PDI: 1.29

Synthesis of in situ functionalized TiO_2 nanoparticles:

200 mg of hydroxamic acid containing polymer ligand was dissolved in 10 ml of DMF and was added to 30 ml of benzyl alcohol (Sigma Aldrich). The polymer solution was heated to 80 °C and degassed under vacuum for 5 minutes. The flask was then filled with argon and kept at this temperature. 1.6 ml of $TiCl_4$ (Sigma Aldrich) was slowly injected through the septum to the hydroxamic acid containing polymer containing solution under vigorous stirring at 80 °C. With continuous stirring the solution was kept at 80 °C for 72 hours. The resulting brown suspension was centrifuged and the precipitate was thoroughly washed twice with $CHCl_3$. The product was dried under vacuum at room temperature.

Pyrolysis of polymer coated TiO_2 nanoparticles:

Polymer coated TiO_2 nanoparticles were pyrolyzed in two steps. First, the powder was heated up to 300 °C with 5 °C min^{-1} as a heating rate and kept at this temperature for 240 minutes. Afterwards the temperature was increased to 650 °C with 5 °C min^{-1} and kept at this temperature for 60 minutes.

Synthesis of TiO_2 reference samples:

TiO_2 particles with a size of about 30 nm (Sigma Aldrich, used as received) were coated with P(AN-b-HA) and pyrolyzed under the same conditions as the in situ functionalized particles. Uncoated TiO_2 particles with a size of about 8 nm were synthesized by a method reported previously.[44] Briefly, benzyl alcohol (20 ml) was sealed in a Schlenk flask (100 ml) in a glovebox, and was removed from the glovebox. $TiCl_4$ (0.8 mL) was slowly injected through the septum to the solution of ligand in benzyl alcohol under vigorous stirring at room temperature. With continuous stirring the solution was heated to 80 °C for 24 h under Ar conditions. The resulting white suspension was centrifuged, and the precipitate was thoroughly washed twice with $CHCl_3$. The product was dried in air at room temperature.

Electrochemical Characterization:

For the electrode preparation, first a slurry was prepared consisting of the C-TiO_2(8) active material, conductive carbon additive (Super C65®, IMERYS, Switzerland)

and PVDF binder solved in NMP (Solef 5130) resulting in a final electrode composition of TiO_2:carbon (including both coating and Super C65®): PVDF of 65:25:10, whereas the exact compositions for the samples was TiO_2:carbon coating:carbon particle:PVDF of 65:12:13:10. This slurry was further homogenized by means of ball-milling (Vario Planetary Mill Pulverisette 4, Fritsch) for 2 h at 400/-1200 rpm. The slurry was then blade cast on dendritic copper foil (Schlenk), whereby the wet film thickness was set to 120 μm. The coated copper foil was first dried at ambient temperature overnight and disc electrodes were punched out of the copper foil. The electrodes were further dried at 120 °C under vacuum for 24 h. The final active material mass loading was determined to be in the range of 1.2 to 1.5 mg cm^{-2}. Electrodes of the references samples C-TiO_2(30) and TiO_2(8) were processed in the same way, whereby the electrode composition of C-TiO_2(30) was TiO_2:carbon coating: carbon additive: PVDF of 65:9:16:10 and the composition of TiO_2(8) was TiO_2:carbon additive:PVDF of 65:25:10. The active material mass loading was determined to be in the range of 1.8 mg cm^{-2} (C-TiO_2(30)) and 1.2 mg cm^{-2} (TiO_2(8)). Three-electrode Swagelok™ cells were assembled in a glove box (MBraun, Germany) with water and oxygen content less than 0.1 ppm. As a separator a sheet of WhatmanTM glass fiber was used. The separator was drenched with the electrolyte consisting of 1M $NaClO_4$ (98 % SIGMA ALDRICH) solved in a 1:1 volume mixture of ethylene carbonate (EC, UBE) and propylene carbonate (PC, SIGMA ALDRICH).

Sodium metal (99.8 %, ACROS ORGANICS) was used as a counter and reference electrode. Thus, all given potentials in this manuscript refer to the Na/Na^+ reference couple. Cyclic voltammetry and galvanostatic cycling was performed with a VMP3 Potentiostat in the voltage range of 0.05V and 2.0 V at a scan rate of 0.1 mV s^{-1} (BIOLOGIC) and a Maccor Battery Tester 4300, respectively. All electrochemical studies were performed at 20 °C ± 2 °C. An applied C-rate of 1C corresponds to a specific current of 335 mAh g^{-1}.

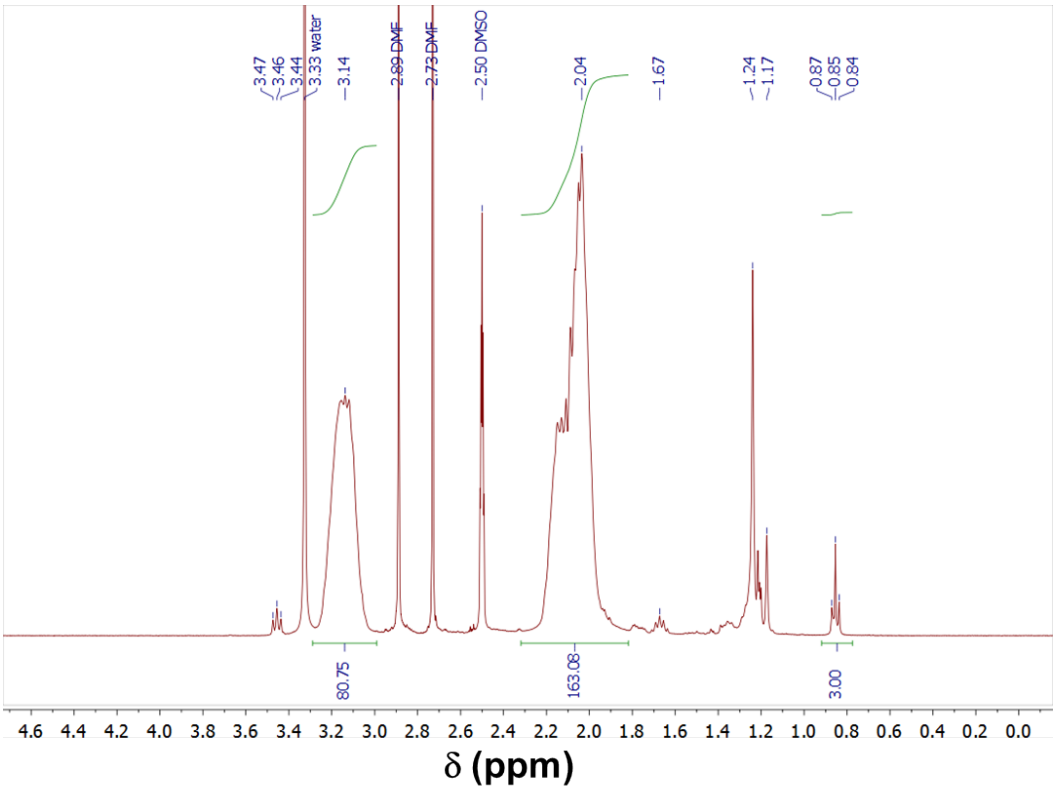

Figure S 1: ^{1}H-NMR spectrum of PAN.

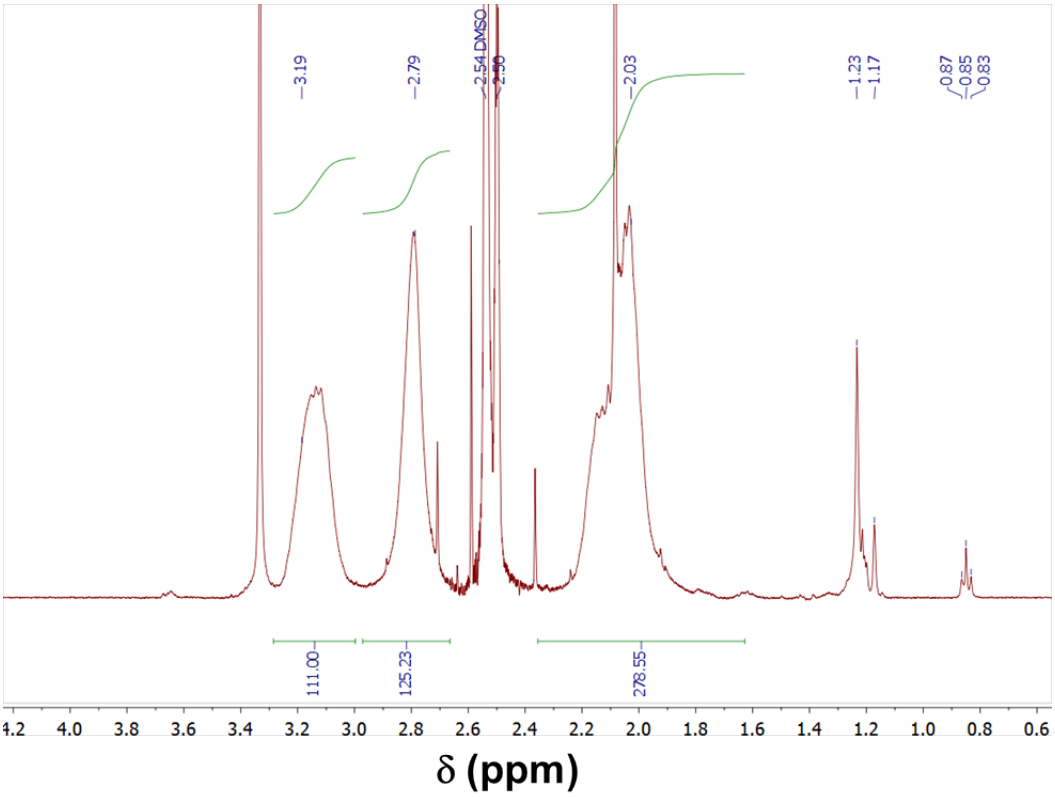

Figure S 2: ^{1}H-NMR spectrum of P(AN-b-NAS).

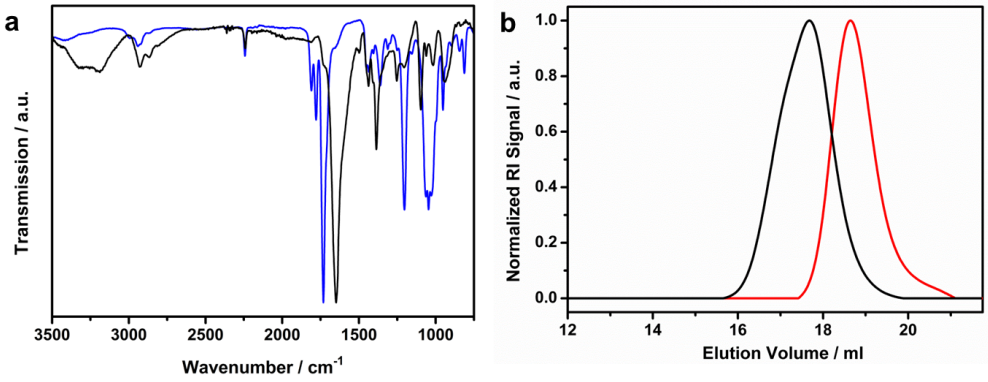

Figure S 3: a) IR-spectrum of P(AN-b-NAS) (blue) and P(AN-b-HA) (black). b) SEC of PAN (red) and P(AN-b-HA) (black).

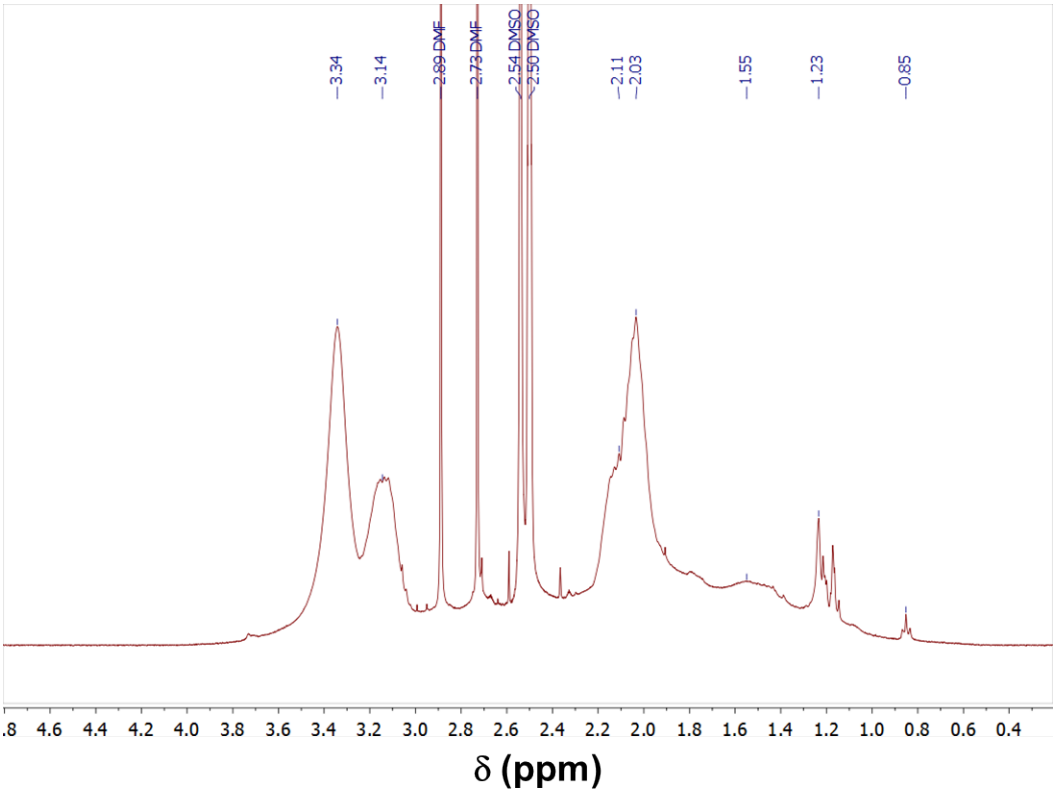

Figure S 4: ^{1}H-NMR spectrum of P(AN-b-HA).

Figure S 5: Fotograph of as-synthesized in situ polymer functionalized TiO_2 particles showing the possibility to synthesize material in gram amounts.

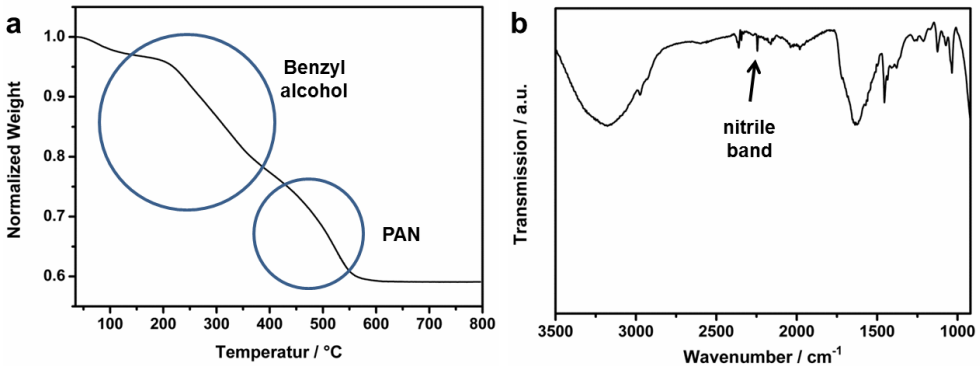

Figure S 6: a) TGA data and b) IR data of polymer coated TiO_2 particles.

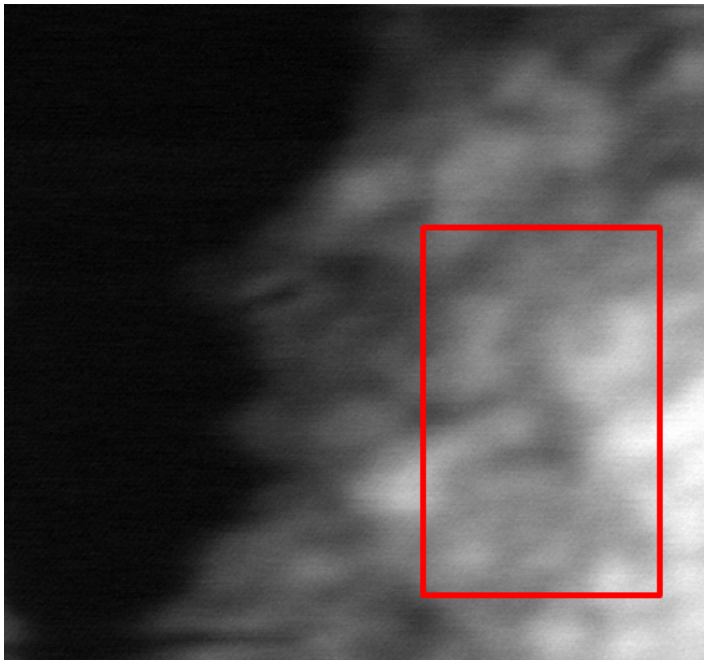

Figure S 7: TEM image to the corresponding EDX area scan shown in Figure 3d.

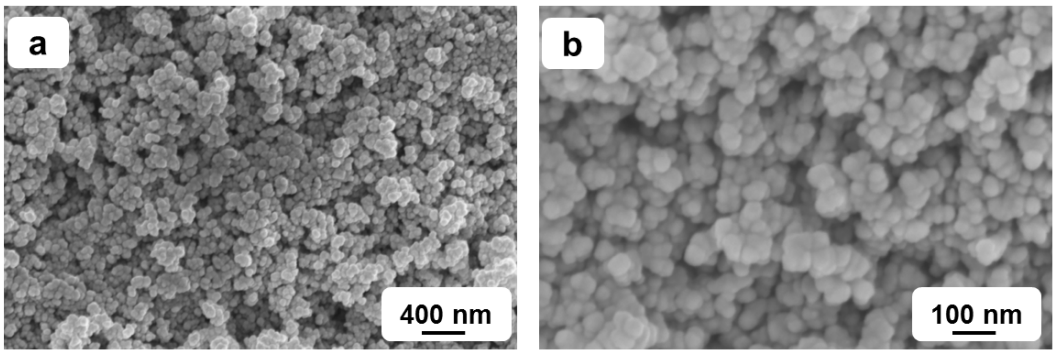

Figure S 8: SEM image of uncoated TiO_2(30).

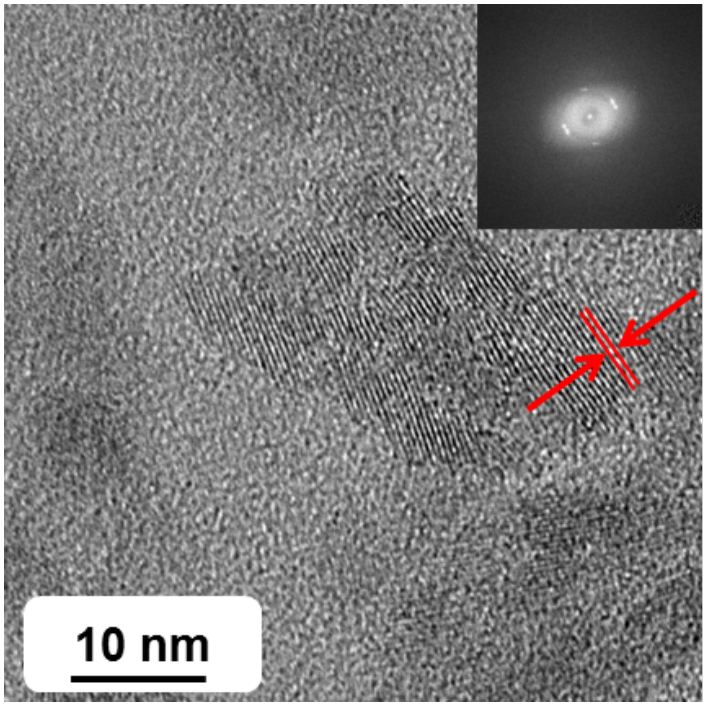

Figure S 9: High resolution TEM image of uncoated TiO_2(8). The inset shows the FFT indicating a lattice spacing of 0.35 nm ascribed to the (101) reflection.

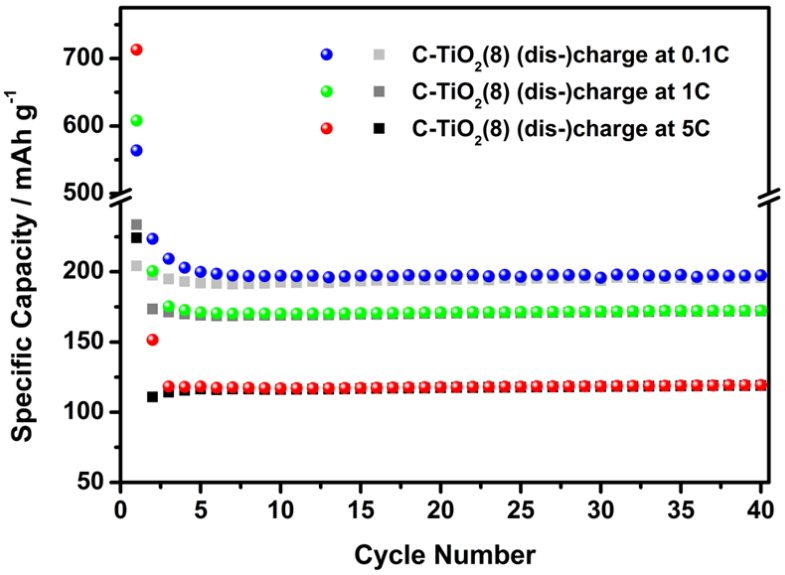

Figure S 10: Cycling performance of C-TiO_2 at 0.1C, 1C and 5C.

References

[1] J.-M. Tarascon, M. Armand, Nature 2001, 414, 359.

[2] P. W. Gruber, P. A. Medina, G. A. Keoleian, S. E. Kesler, M. P. Everson, T. J. Wallington, Journal of Industrial Ecology 2011, 15, 760.

[3] J. W. Wang, X. H. Liu, S. X. Mao, J. Y. Huang, Nano Lett. 2012, 12, 5897.

[4] L. D. Ellis, T. D. Hatchard, M. N. Obrovac, Journal of the Electrochemical Society 2012, 159, A1801.

[5] D. Bresser, F. Mueller, D. Buchholz, E. Paillard, S. Passerini, Electrochimica Acta 2014, 128, 163.

[6] S.-M. Oh, S.-T. Myung, M.-W. Jang, B. Scrosati, J. Hassoun, Y.-K. Sun, Phys. Chem. Chem. Phys. 2013, 15, 3827.

[7] Y. Zhu, X. Han, Y. Xu, Y. Liu, S. Zheng, K. Xu, L. Hu, C. Wang, ACS Nano 2013, 7, 6378.

[8] A. Darwiche, C. Marino, M. T. Sougrati, B. Fraisse, L. Stievano, L. Monconduit, J. Am. Chem. Soc. 2012, 134, 20805.

[9] L. Wu, X. Hu, J. Qian, F. Pei, F. Wu, R. Mao, X. Ai, H. X. Yang, Y. Cao, Energy Environ. Sci. 2013.

[10] S. Komaba, W. Murata, T. Ishikawa, N. Yabuuchi, T. Ozeki, T. Nakayama, A. Ogata, K. Gotoh, K. Fujiwara, Adv. Funct. Mater. 2011, 21, 3859.

[11] A. Ponrouch, A. Goñi, M. R. Palacín, Electrochemistry Communications 2013, 27, 85.

[12] Y. Cao, L. Xiao, M. L. Sushko, W. Wang, B. Schwenzer, J. Xiao, Z. Nie, L. V. Saraf, Z. Yang, J. Liu, Nano Lett. 2012, 12, 3783.

[13] B. Jache, P. Adelhelm, Angew. Chem. Int. Ed. 2014, 53, 10169.

[14] H. Pan, X. Lu, X. Yu, Y.-S. Hu, H. Li, X.-Q. Yang, L. Chen, Adv. Energy Mater. 2013, 3, 1186.

[15] P. Senguttuvan, G. Rousse, V. Seznec, J.-M. Tarascon, M. Palacín, Chem. Mater. 2011, 23, 4109.

[16] C. Chen, Y. Wen, X. Hu, X. Ji, M. Yan, L. Mai, P. Hu, B. Shan, Y. Huang, Nat Comms 2015, 6, 6929.

[17] L. Wu, D. Bresser, D. Buchholz, S. Passerini, Journal of the Electrochemical Society 2014, 162, A3052.

[18] J. P. Huang, D. D. Yuan, H. Z. Zhang, Y. L. Cao, G. R. Li, H. X. Yang, X. P. Gao, RSC Adv. 2013, 3, 12593.

[19] Z. Bi, M. P. Paranthaman, P. A. Menchhofer, R. R. Dehoff, C. A. Bridges, M. Chi, B. Guo, X.-G. Sun, S. Dai, Journal of Power Sources 2013, 222, 461.

[20] H. Xiong, M. D. Slater, M. Balasubramanian, C. S. Johnson, T. Rajh, J. Phys. Chem. Lett. 2011, 2, 2560.

[21] X. Yang, C. Wang, Y. Yang, Y. Zhang, X. Jia, J. Chen, X. Ji, J. Mater. Chem. A 2015, 3, 8800.

[22] L. Wu, D. Bresser, D. Buchholz, G. Giffin, C. R. Castro, A. Ochel, S. Passerini, Adv. Energy Mater. 2014.

[23] L. Wu, D. Buchholz, D. Bresser, L. Gomes Chagas, S. Passerini, Journal of Power Sources 2014, 251, 379.

[24] K.-T. Kim, G. Ali, K. Y. Chung, C. S. Yoon, H. Yashiro, Y.-K. Sun, J. Lu, K. Amine, S.-T. Myung, Nano Lett. 2014, 14, 416.

[25] Y. Yang, X. Ji, M. Jing, H. Hou, Y. Zhu, L. Fang, X. Yang, Q. Chen, C. E. Banks, J. Mater. Chem. A 2015, 3, 5648.

[26] G. Qin, X. Zhang, C. Wang, J. Mater. Chem. A 2014.

[27] J. Lee, Y.-M. Chen, Y. Zhu, B. D. Vogt, ACS Appl. Mater. Interfaces 2014, 6, 21011.

[28] Y. Ge, H. Jiang, J. Zhu, Y. Lu, C. Chen, Y. Hu, Y. Qiu, X. Zhang, Electrochimica Acta 2015, 157, 142.

[29] S.-M. Oh, J.-Y. Hwang, C. S. Yoon, J. Lu, K. Amine, I. Belharouak, Y.-K. Sun, ACS Appl. Mater. Interfaces 2014, 6, 11295.

[30] D. Bresser, B. Oschmann, M. N. Tahir, F. Mueller, I. Lieberwirth, W. Tremel, R.

Zentel, S. Passerini, Journal of the Electrochemical Society 2015, 162, A3013.
[31] Y. Xu, E. Memarzadeh Lotfabad, H. Wang, B. Farbod, Z. Xu, A. Kohandehghan, D. Mitlin, Chem. Commun. 2013, 49, 8973. [32] H. A. Cha, H. M. Jeong, J. K. Kang, J. Mater. Chem. A 2014.
[33] J. R. Gonzalez, R. Alcantara, F. Nacimiento, G. F. Ortiz, J. L. Tirado, Journal of the Electrochemical Society 2014, 162, A3007.
[34] A. S. Aricò, P. Bruce, B. Scrosati, J.-M. Tarascon, W. van Schalkwijk, Nat. Mater. 2005, 4, 366.
[35] H. Usui, S. Yoshioka, K. Wasada, M. Shimizu, H. Sakaguchi, ACS Appl. Mater. Interfaces 2015, 7, 6567.
[36] D. Yan, C. Yu, Y. Bai, W. Zhang, T. Chen, B. Hu, Z. Sun, L. Pan, Chem. Commun. 2015.
[37] D. Bresser, E. Paillard, R. Kloepsch, S. Krueger, M. Fiedler, R. Schmitz, D. Baither, M. Winter, S. Passerini, Adv. Energy Mater. 2013, 3, 513.
[38] S. Jeong, D. Bresser, D. Buchholz, M. Winter, S. Passerini, Journal of Power Sources 2013, 235, 220.
[39] B. Oschmann, D. Bresser, M. N. Tahir, K. Fischer, W. Tremel, S. Passerini, R. Zentel, Macromol. Rapid Commun. 2013, 34, 1693.
[40] B. Oschmann, M. N. Tahir, F. Mueller, D. Bresser, I. Lieberwirth, W. Tremel, S. Passerini, R. Zentel, Macromol. Rapid Commun. 2015.
[41] W. R. McNamara, R. C. Snoeberger III, G. Li, C. Richter, L. J. Allen, R. L. Milot, C. A. Schmuttenmaer, R. H. Crabtree, G. W. Brudvig, V. S. Batista, Energy Environ. Sci. 2009, 2, 1173.
[42] A. Klegeris, Free Radical Biology and Medicine 1995, 18, 215.
[43] T. Rajh, L. X. Chen, K. Lukas, T. Liu, M. C. Thurnauer, D. M. Tiede, J. Phys. Chem. B 2002, 106, 10543.
[44] M. Niederberger, M. H. Bartl, G. D. Stucky, J. Am. Chem. Soc. 2002, 124, 13642.
[45] M. N. Tahir, M. Eberhardt, P. Theato, S. Faiß, A. Janshoff, T. Gorelik, U. Kolb, W.

Tremel, Angew. Chem. Int. Ed. 2006, 45, 908.

[46] D. Bresser, E. Paillard, E. Binetti, S. Krueger, M. Striccoli, M. Winter, S. Passerini, J. Power Sources 2012, 206, 301.

[47] D. E. Bergbreiter, P. L. Osburn, C. Li, Org. Lett. 2002, 4, 737.

[48] D. V. Bavykin, V. N. Parmon, A. A. Lapkin, F. C. Walsh, J. Mater. Chem. 2004, 14, 3370.

4.1.6 Versatility of the Carbon Coating Approach and Its Limits

Introduction

As already shown in the previous chapters, the polymer and carbon coating approach could be successfully applied to a variety of different inorganic particles. Different anchor groups (dopamine, thiol, hydroxamic acid) were introduced by the aminolysis of a reactive ester enabling the binding to different inorganic particles. The extension of this approach to sulfides, especially pyrite FeS_2 and Li_2S, was also intended within this thesis. Li_2S and FeS_2 are interesting alternative cathode materials for lithium-ion batteries due to their theoretically high specific capacities (Li_2S:1166 mAh g^{-1} and FeS_2: 890 mAh g^{-1}). However, it is necessary to coat or encapsulate these materials to avoid the dissolution of polysulfides and to avoid the shuttle mechanism as discussed in chapter 2.3.3. However, coordination of these compounds is quite difficult and requires the introduction of further anchoring units.

The scope of this chapter is to give a brief summary of the attempts to coat these sulfides with polymer followed by a carbon coating approach. In addition, the limits of the carbon coating approach will be demonstrated.

Results and Discussion

For the coating approach, the previously described carbon coating approach should be applied to Li_2S and FeS_2. Further anchor groups were attached as a block to polyacrylonitrile, whereby in the case of FeS_2 sulfonate groups were reported to coordinate well onto the surface and in the case of Li_2S polyvinylpyrrolydone (PVP) as well as polyethyleneglycol (PEG) were reported to interact strongly with the surface.[1–4] PVP was attached as a second block to PAN by RAFT polymerization, whereas PEG was attached to the RAFT agent followed by the RAFT polymerization of AN as shown in Figure 1 and 2 and successful conversions were proven by NMR-, IR-spectroscopy (not shown here) as well as SEC (see Figure 1b and 2b) showing

a shift to lower elution volumes, i.e. higher hydrodynamic radii and proves the preparation of the block copolymers.

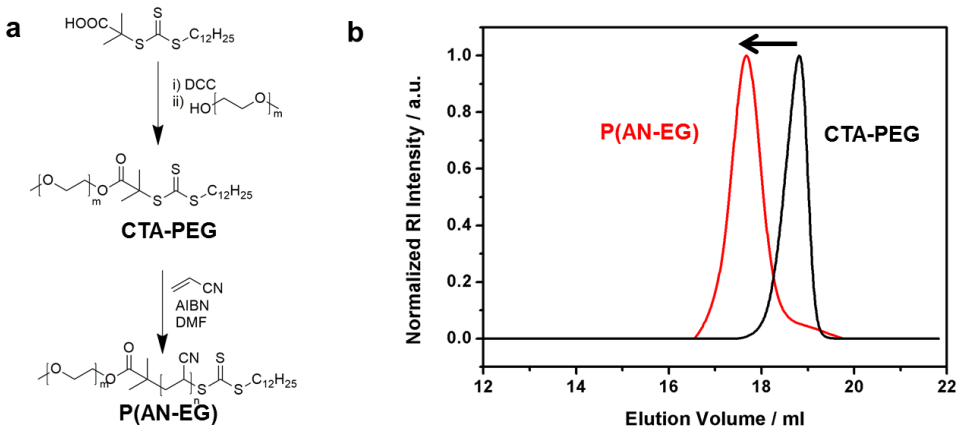

Figure 1: Synthesis route to obtain P(AN-b-EG) (a) and SEC of P(AN-EG) (red) and the PEG-containg CTA (black).

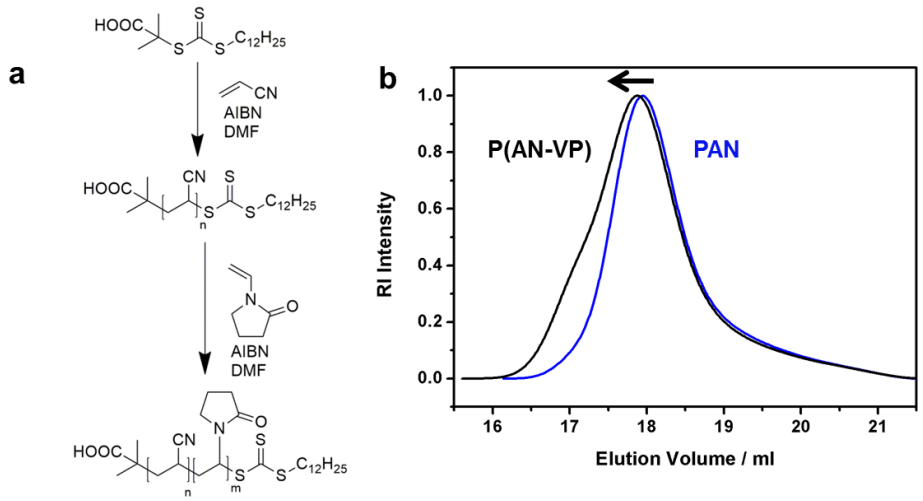

Figure 2: Synthesis route to obtain P(AN-b-VP) (a) and SEC of PAN (black) and the P(AN-VP) CTA (blue).

Sulfonate groups were attached by the block copolymerization of PAN and sodium

styrene sulfonate (SS) to obtain P(AN-SS) as shown in the following figure leading to P(AN-b-SS).

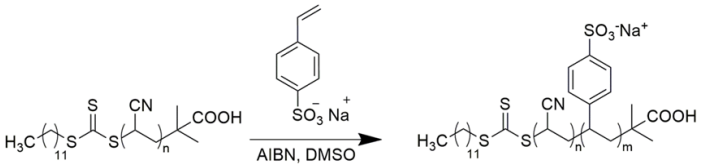

Figure 3: Synthesis route to obtain P(AN-b-SS).

The successful conversion could be proven by NMR-spectroscopy, IR spectroscopy (not shown) and diffusion ordered NMR spectroscopy (DOSY) as shown in Figure 4. Only one diffusing species could be observed, which correlates both with the typical PAN signals as well as with signals attributed to the sulfonate repeating units. The obtained polymer is a block copolymer.

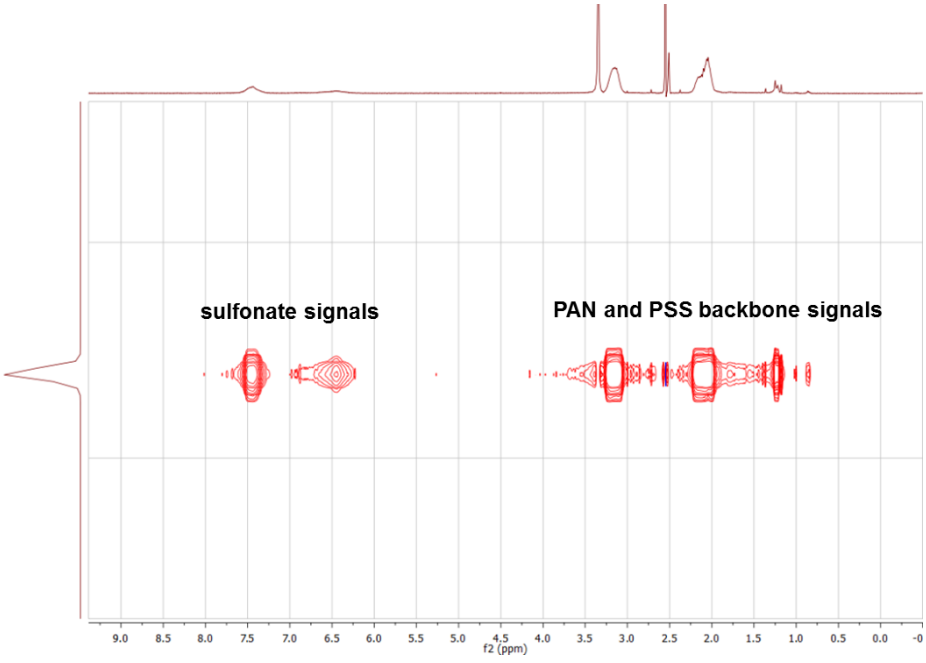

Figure 4: DOSY of P(AN-b-SS).

Hybridization steps were conducted in DMSO, where both polymer and particles were soluble or dispersable. In case of Li_2S the polymer shell could be transformed

to a carbonized shell around the particles as proven by SEM images before and after coating and by Raman spectroscopy after pyrolysis as shown in Figure 5. SEM images after coating show a diffuse shell around the particles.

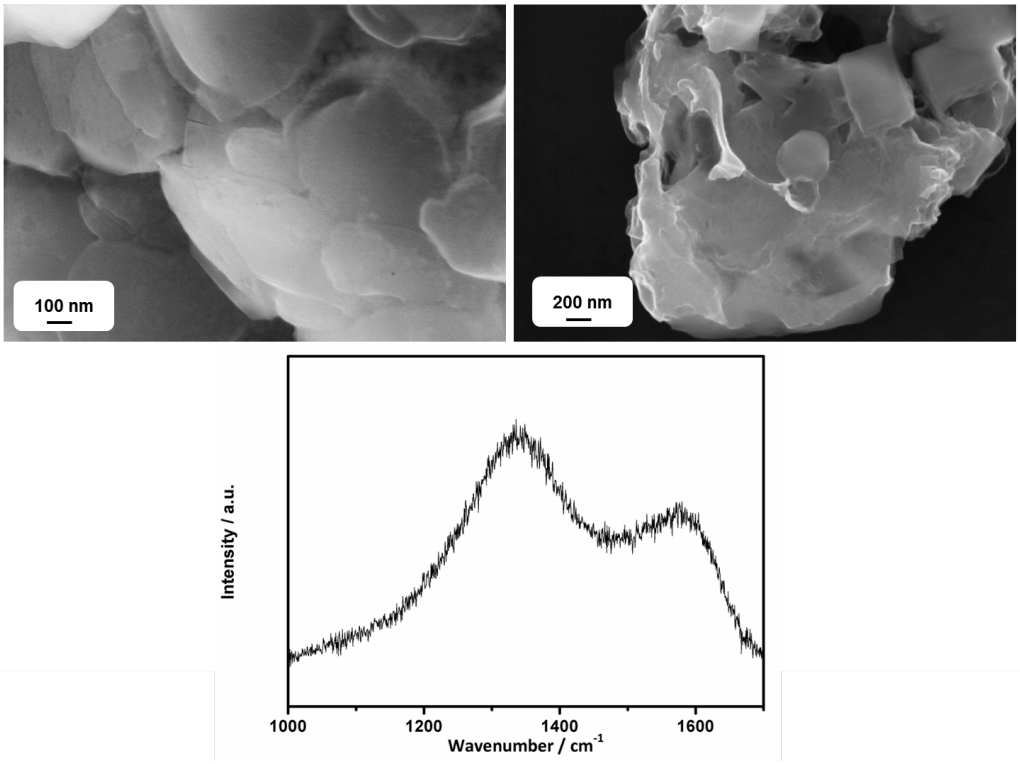

Figure 5: a) SEM image of uncoated Li_2S and b) of carbon coated Li_2S. c) Raman spectrum of carbon coated Li_2S.

The pyrolysis of polymer coated FeS_2 reveals the limits of the developed carbon coating approach, as the obtained FeS_2 nanoparticles (synthesized by Muhammad Nawaz Tahir) were thermally not stable and degraded at temperatures higher than 350 °C according to the following equation:

$$FeS_2 \rightarrow FeS + S \tag{7}$$

This reaction could be detected by XRD measurements showing reflections attributed

to FeS after pyrolysis at temperatures higher than 350 °C:

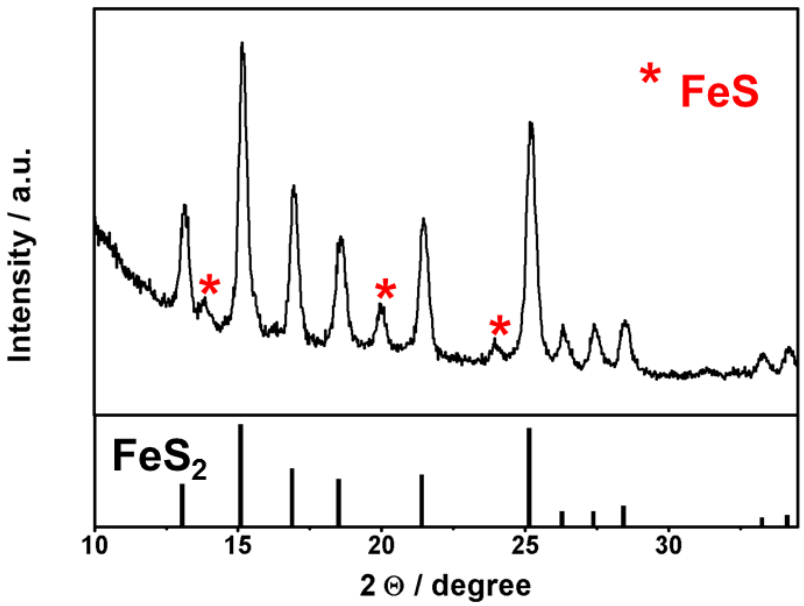

Figure 6: XRD pattern of coated FeS_2 after pyrolysis at 400 °C.

Pyrolysis at lower temperatures than 350°C are possible without structural degradation, but might not create a conductive carbonized shell, as conductivity increases with pyrolysis temperature.[5]

Coated Li_2S and coated pyrite (pyrolyzed at 350 °C) were applied in lithium-ion batteries, but neither for uncoated nor for coated materials reasonable results could be obtained, which might be attributed to an unexpected electrochemicyl inactivity of the inorganic material itself, non-optimized electrode compositions, electrolyte compositions as well as to the battery set-up, and are not supposed to be presented here.

In summary, the polymer coating approach can be also extended to sulfides, but heat treatment at elevated temperatures can cause the degradation of particles due to the loss of sulfur, i.e. active material. Thus, the introduced carbon coating approach is a very powerful tool for thermally stable particles as proven in the previous chapters, but is limited to only thermally stable particles. Due to this, other coating approaches need to be developed for thermally unstable promising electrode materials, which

was the motivation for the use of graphene derivatives and conducting polymers as described in the following chapters.

Experimental

Synthesis of pol(acrylonitrile-b-vinylpyrrolidone)

Polyacrylonitrile (PAN) was synthesized by RAFT polymerization as previously reported.[1] For the block copolymerization PAN (1 eq., 0.049 mmol, 365 mg) as a macro-CTA was solved in 5.8 ml of DMF and N-vinylpyrrolidone (VP, 40 eq., 1.95 mmol, 216 g) and AIBN (1 eq., 0.049 mmol, 7.9 mg) was added. The reaction mixture was degassed by three freeze-pump-thaw cycles and the polymerization was conducted at 70 °C for 14 hours. The polymer was precipitated in methanol.

^{1}H-NMR (DMSO-d6, 400 MHz): δ [ppm] = 3.5-4.0 (b, CH backbone of VP), 3.12 (CH of AN and N-CH_2 of VP), 2.04 (b, CH_2-CH_2-CO of VP and CH_2 of AN), 1.62 (CH_2 of VP backbone).

SEC (eluent: HFIP): 9,330 g mol^{-1}, PDI: 1.45.

Synthesis of poly(acrylonitrile-b-ethyleneoxide)

The chain transfer agent DMP was modified by PEGylation following a literature procedure.[7] Briefly, DMP (1 eq., 4.11 mmol, 1.5 g) and oxalyl chloride (5 eq., 20.57 mmol, 2.61 g) were solved In 8.3 ml dichloromethane and stirred at room temperature until no more gas evolution was observed. The solvent and excess reagents were removed under reduced pressure and the residue was dissolved in 17 ml of dry dichloromethane. Polyethylenglycolmonomethylether (750 g mol^{-1}, 0.7 eq., 2.88 mmol, 2.16 g) was added. The reaction mixture was stirred for 24 h at room temperature. The solvent was partially removed and the desired product was precipitated in cold diethyl ether.

^{1}H-NMR (DMSO-d6, 400 MHz): δ [ppm] = 4.24 (t, 2H, -CH_2-OCO-), 3.63 (b, 77 H, -OCH_2CH_2O-), 3.37 (3H, s, O-CH_3), 3.25 (t, 2H, -S-CH_2-), 1.69 (b, 8H, 2 -CH_3 and –S-CH_2-CH_2), 1.24 (m, 18H, -$(CH_2)_9$-), 0.87 (t, 3H, CH_3).

The PEG-CTA (1 eq., 0,11 mmol, 100 mg), acrylonitrile (300 eq., 0.027 mol, 1.47 g) and AIBN (0.1 eq., 0.011 mmol, 1.8 mg) were dissolved in 3 ml DMF and stirred at 70 °C for 10 hours. The polymer was precipitated in methanol. The polymer was dissolved and precipitated two more times. The yield of the polymer was 42 %.
^{1}H-NMR (DMSO-d6, 400 MHz): δ [ppm] = 4.15 (m, -CH_2-OCO-), 3.51 (b, -OCH_2CH_2O-), 3.13 (b, 73H, CH backbone), 2.03 (b, 142 H, CH_2 backbone), 1.24 (m, -$(CH_2)_9$-), 0.85 (t, 3H, CTA-CH_3).
SEC (eluent: HFIP): 13,400 g mol^{-1}, PDI: 1.13
Synthesis of poly(acrylonitrile-b-sodium styrene sulfonate)
Polyacrylonitrile (PAN) was synthesized by RAFT polymerization as previously reported.[6] PAN (1eq., 0.05 mmol, 300 mg) was used as a macro-CTA and sodium styrene sulfonate (50 eq., 2.5 mmol, 0.57 g) was used as a monomer. Both reagents were solved in 3 ml DMSO and AIBN (0.1 eq., 0.005 mmol, 0.82 mg) was added. After three freeze-pump-thaw cycles the reaction mixture was stirred at 70 °C for12 hours. The product was precipitated in methanol. The yield was 84 %.
^{1}H-NMR (DMSO-d6, 400 MHz): δ [ppm] = 7.44 (b, aromatic signal ortho to SO_3H), 6.47(b, aromatic signal meta to SO_3H, 3.16 (b, CH of AN), 2.26-1.10 (b, CH_2 of AN, CH_2 und CH SS, dodecyl, 0.85 (t, CH_3 CTA).
IR (FTIR): ν = 3440 (s, OH), 2919 (w, CH), 2240 (w, -CN), 1641 (w), 1181 (s), 1127 (s), 1036 (s), 1008 (s) cm^{-1}.

References

[1] K. Mizushima, P. Jones, P. Wiseman, J. Goodenough, Mater. Res. Bull. 1980, 15, 783.
[2] J. Puthussery, S. Seefeld, N. Berry, M. Gibbs, M. Law, J. Am. Chem. Soc. 2011, 133, 716.
[3] Y. Bi, Y. Yuan, C. L. Exstrom, S. A. Darveau, J. Huang, Nano Lett. 2011, 11, 4953.
[4] Z. W. Seh, Q. Zhang, W. Li, G. Zheng, H. Yao, Y. Cui, Chem. Sci. 2013, 4, 3673.

[5] K. Jobst et al, Synthetic Metals 1992, 47, 279-285

[6] B. Oschmann, D. Bresser, M. N. Tahir, K. Fischer, W. Tremel, S. Passerini, R. Zentel, Macromol. Rapid Commun. 2013, 34, 1693.

[7] L. Tao, J. Xu, D. Gell, T. Davis, Macromol., 2010, 3721.

4.2 Non-thermal Coating Approach of Inorganic Particles Using Functionalized Reduced Graphene Oxide Sheets

As discussed in section 4.1.6, the thermal carbon coating approach using anchoring carbon precursor block copolymers is limited to thermally stable inorganic materials. However, there are a lot of thermally unstable attractive materials with theoretically high specific capacities, which suffer from low electrical conductivity and volume changes, for instance Fe_2O_3 and FeS_2. Thus, non-thermal approaches need to be developed in order to overcome the challenges of the thermal unstable materials.
For a non-thermal coating approach graphene is a very attractive material, as it contains a conjugated hexagonal carbon structure with a high electrical conductivity and is additionally voluminous and might be able to buffer occurring volume changes of the electrochemically active material. Graphene can be obtained by several methods as already discussed in section 2.7. Most coating approaches using graphene are based on a thermal reduction of graphene oxide and thus require a thermal step, which is not an option for thermally unstable materials. Other approaches are based on the chemical reduction of graphene oxide using hydrazine, a very toxic reagent.
In cooperation with Gregor Backert, an alternative coating approach based on graphene was developed. This approach does not require a thermal heat treatment for the reduction of graphene oxide and instead, graphene oxide is reduced by the treatment with oleum and at the same time sulfate groups are introduced into the graphene oxide sheet resulting in sulfated and reduced graphene oxide (srGO), as proven by Raman spectroscopy and XPS. The introduction of sulfate groups enables the interaction of the negatively charged graphene sheets with positively charged inorganic nanoparticles. Thus, the prepared sulfated graphene sheets can be used for the post functionalization of a certain variety of inorganic nanoparticles. Examplarily, thermally unstable Ni@Fe_2O_3 superparticles, which were synthesized by Muhammad Nawaz Tahir from Prof. Tremel's group, were coated with srGO and the hybrid

material was investigated by HRTEM and SEM measurements (conducted by Ingo Lieberwirth) proving the presence of a coating on the nanoparticle surface. The hybrid material was applied as an anode material in lithium-ion batteries. Comparing uncoated particles with srGO coated particles, we can conclude that the C-rate performance of the coated particles is significantly improved due to the presence of the graphene coating. Graphene sheets were also used to coat Fe_2O_3 nanorice and FeS_2 nanoparticles to prove that the coating approach can be extended to further materials.

Gregor Backert contributed by the synthesis of the graphene based materials, whereas the hybridization steps as well as all electrochemical characterizations (including electrode preparation, cell assembly and interpretation of the electrochemical data) was conducted by myself. Franziska Mueller contributed by discussing about the electrochemical data.

4.2.1 Manuscript to be submitted

Non-Thermal Hybridization of Ni@Fe_2O_3 Superparticles with Functionalized Reduced Graphene Oxide and its Application as Anode Material in Lithium-Ion Batteries

Gregor Backert*, Bernd Oschmann*, Muhammad Nawaz Tahir, Franziska Mueller, Ingo Lieberwirth, Benjamin Balke, Wolfgang Tremel, Stefano Passerini, Rudolf Zentel

Abstract

The application of metal oxide-graphene composites in lithium-ion batteries has attracted a huge interest within the recent years, as graphene reduces the electrical resistance and compensates during charging and discharging volume changes. In our present work we developed a novel graphene wrapping approach using modified graphene oxide, which interacts with the surface of nanoparticles, whereby this approach is applied to Ni@Fe_2O_3 superparticles. In contrast to most of the recent works, no thermal treatment and no toxic agents like hydrazine are required for the reduction of graphene oxide. The successful wrapping can be proven by energy dispersive X-ray spectroscopy, high resolution transmission electron microscopy and Raman spectroscopy. This composite material is applied as an anode material in lithium-ion batteries and is compared to unwrapped particles proving the positive influence of the graphene wrapping, as it increases the cycling performance enabling a charge capacity of 1082 mAh g^{-1} for graphene wrapped Ni@Fe_2O_3 particles, whereas 475 mAh g^{-1} is achieved with unwrapped Ni@Fe_2O_3 at 0.05C after 30 cycles . The C-rate capability is improved and obtained capacities are about twice as high compared to unwrapped particles.

*G.B. and B.O. contributed equally to this work.

1. Introduction

Lithium-ion batteries are currently the market-leading energy storage devices applied in portable electronic equipments because they offer high energy densities and no memory effect.[1,2] However, despite of the commercialization of a variety of lithium-ion based batteries, there is still a growing demand of more efficient energy storage devices, especially with respect to the desire of establishing electric vehicles as green mode of transportation, where a high energy density device plays a key role and remains a very challenging issue. Therefore, improving the energy density of the current lithium-ion batteries would be a step forward to realize electromobility. One approach to achieve this goal is the development of alternative electrode materials with higher specific capacities than the one currently used in batteries presently on the market. Graphite is used on the anode side in state-of-the art lithium-ion batteries with a theoretical specific capacity of 372 mAh g^{-1}. Within the last years different kind of alternative electrode materials have been investigated, including alloying materials such as Si,[3–5] Sn,[6] and Sb[7] with very high theoretical capacities, e.g. 4200 mAh g^{-1} for Si. In addition, transition metal oxides undergoing conversion reactions (in some cases also followed by alloying reactions) have been proposed as further promising alternatives to substitute graphite on the anode side.[8] For instance, ZnO (theoretical capacity: 978 mAh g^{-1}),[9] $ZnFe_2O_4$ (1007 mAh g^{-1}),[10] and especially Fe_2O_3 (1005 mAh g^{-1})[11] are promising candidates due to their high capacity, low cost and non-toxicity. However, these alternative materials suffer from several challenges such as rather low electronic conductivity, low ionic conductivity and volume changes during charging and discharging processes, causing a loss of electrical connection from current collectors. These issues cause an incomplete utilization of the active material and poor rate capability, as well as capacity fading during cycling.[7,12] Lowering ionic diffusion distances by downsizing of the active material to a nanometer scale as well as the use of advanced morphologies, such as interconnected particles, are approaches to overcome

the ionic conductivity issue and to enhance the battery performance.[2,2,9,13–15] Carbon coating approaches were developed to increase the electronic conductivity, and impressive improvements of the battery performances for a variety of materials could be observed.[10,16–19] Also graphene has been utilized as a conductive carbon-based coating or wrapping to overcome the conductivity problem.[20–30] Due to its outstanding properties, including both electrical conductivity and mechanical flexibility,[31,32] graphene is lowering the electrical resistance within the electrode and stabilizes the volume changes. In most graphene coating approaches for metal oxides, graphene is obtained from graphene oxide coated particles using thermal reduction which is also the case for carbon coating approaches. Alternatively it is obtained by chemical reduction using toxic chemicals like hydrazine as reducing agents.[23,30,33–41] Thus, many of the already reported procedures are limited to those materials which are thermally stable.

Herein, we report on a benign protocol based on post functionalization methodology to synthesize non-thermal graphene wrapping of nanoparticles, exemplarily applied to Ni@Fe_2O_3 superparticles. Superparticles themselves are an interesting class of nanomaterials due to their interconnectivity of various nanodomains. It is worth mentioning that generally Fe_2O_3 is thermally reduced to Fe_3O_4 in the presence of carbonaceous material[42] which limits its use for any method involving thermal annealing. Therefore, Fe_2O_3 based superparticles are the suitable and reasonable choice for our non-thermal approach. Our strategy involves the use of sulfated and reduced graphene oxide (srGO), which is negatively charged due to the presence of sulfate groups and can interact with the inorganic nanoparticles[43–45] as schematically shown in Figure 1. As-synthesized particles and graphene-based materials are well characterized using various methods, including electron microscopy, X-ray photoelectron spectroscopy , X-ray diffraction (XRD), and Raman spectroscopy. The obtained hybrid material consisting of srGO wrapped particles is applied as an electrode material in lithium-ion battery. The influence of the graphene wrapping

is investigated by comparing the battery performance of wrapped and unwrapped Ni@Fe_2O_3 superparticles.

2. Results and Discussion

Structural and morphological characterization

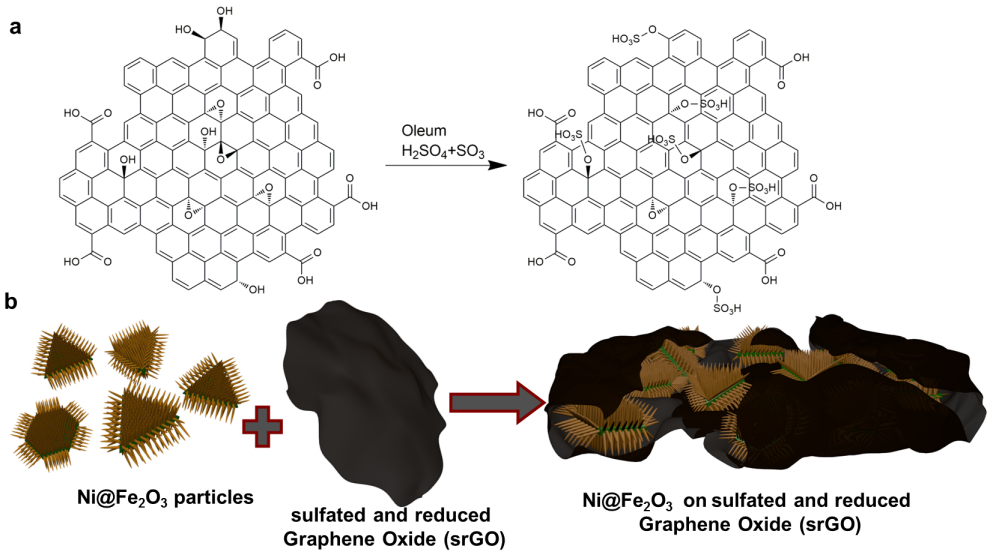

Figure 1: a) Scheme for the synthesis of srGO and b) schematic illustration for the wrapping of Ni@Fe_2O_3.

The Ni@Fe_2O_3 superparticles are synthesized following a method published earlier[46] using in situ grown nickel nanoplates as a substrate to grow epitaxially γ-Fe_2O_3 nanorods on top resulting in a superparticle like morphology as shown in the transmission electron microscope (TEM) image of the as-synthesized Ni@Fe_2O_3 (Figure 2a). The average length of the as-synthesized nanorods is 30 nm with a diameter of about 10 nm. X-ray diffraction (XRD) pattern of the as-synthesized particles (Figure 2b) show both reflections obtained by γ-Fe_2O_3 and reflections due to the presence of the Ni nanoplates. According to atomic absorption spectroscopy (AAS), the as-synthesized particles consist of 86 wt.% Fe_2O_3 and 14 wt.% Ni.

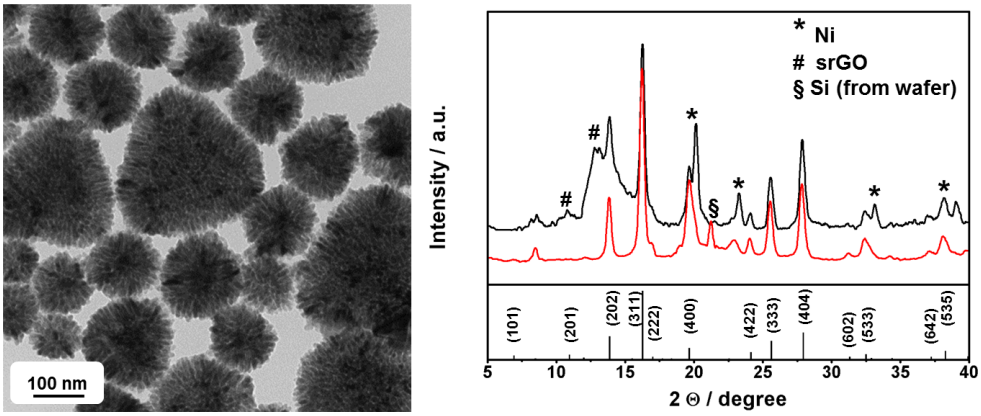

Figure 2: a) TEM image of as-synthesized Ni@Fe_2O_3 superparticles and b) XRD pattern of unwrapped (red) and wrapped Ni@Fe_2O_3 superparticles (black), the JCPDS 96-900-0596 reference for γ-Fe_2O_3 is given in the bottom.

The sulfated and reduced graphene oxide is derived from graphene oxide as a precursor, which is obtained via a modified Hummers method.[47] The treatment of graphene oxide with oleum, first reported by Liu et al.[48], results on one hand in the elimination of hydroxyl groups within the graphene oxide layer causing an extension of the conjugated sp^2-carbon system. On the other hand it introduces sulfate groups into the graphene oxide layer as schematically shown in Figure 1a. Raman spectroscopy is used to prove the increase of interconnected sp^2-hybridized areas on the treated graphene oxide when comparing the intensity ratio of D- to G-band:[49–51] The original graphene oxide shows an I_D/I_G-ratio of 1.69, whereas the oleum-treated material shows a decrease in the intensity ratio with an I_D/I_G-ratio of 1.25 (Figure 3a). With the change of color (Figure S1), there comes a change in elemental composition due to the reaction with oleum: As determined by elemental analysis, the amount of carbon rises from 46.7% in GO to 61.1% in srGO and a sulfur content of 3.4% can be found in srGO. In good agreement with the elemental analysis is the information obtained from XPS of the two materials as shown in Figures

3b and S3.

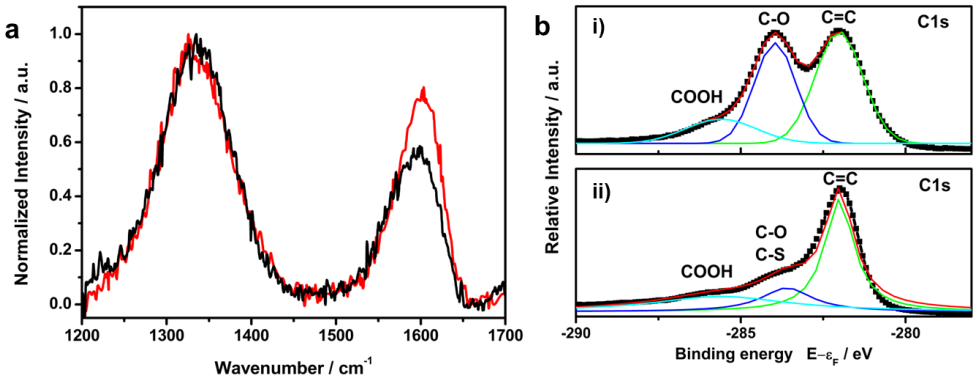

Figure 3: a) Raman spectrum of graphene oxide (black) and srGO (red) and b) high resolution XPS of the C1s signal of i) GO and ii) srGO.

The ratio of the integrated C1s peak and O1s peak C1s:O1s is 2.3 in case of GO. As expected, this ratio increases upon reduction by the treatment with oleum to 5.1 in case of srGO (see Figure S2). Figure 3b shows the high resolution C1s spectra of GO (i) and srGO (ii). The peak can be fitted into three components, i.e. contributions from C=C (-282.0 eV), C-O (-284.0 eV) and –COOH (-285.6 eV). The contributions of oxygenated carbons clearly decrease in case of srGO compared to GO due to the occurring reaction, which completes the overall impression of basal plane reduction in oleum.

In contrast to the reported synthesis of srGO by Liu et al. we used a modified and "greener" workup procedure by dropping the srGO-oleum-dispersion into water instead of diethyl ether. Thorough washing with water and dialysis with subsequent freeze drying gives a black powder. Due to this process, traces of water may still be adsorbed to the srGO surface. Nevertheless, the IR spectrum (Figure S3a) of this material shows only very weak traces of O-H-valence vibrations. Moreover one can find red-shifts of the carbonyl- and aromatic-ring-vibration-bands. Also the epoxy-related bands around 1200 cm^{-1} disappear, while in the same area sulfate related

bands (SO_2 and –S=O valence vibrations) can be observed. The TGA curve of srGO (Figure S3b) also shows a diminished amount of volatile oxygen containing groups. Up to 250 °C the mass loss is just below 20 wt.%, whereas the original GO shows a loss of about 40 wt.%. As it can be seen in the SEM images of srGO (Figure S4), the sheets decrease in size due to the repeated ultrasound treatment. Furthermore, single sheets are mostly spread out separately.

The wrapping of the superparticles could be achieved by dispersing both particles and graphene sheets in the same solvent, in this case in a triethylamine containing N,N-dimethylformamide (DMF) solution. Due to the presence of the sulfate functional groups within the srGO sheets, it can bind to the Fe_2O_3 nanoparticles surfaces. The graphene wrapped on the Ni@Fe_2O_3 surfaces is characterized using Raman spectroscopy, scanning electron microscopy (SEM) as well as high resolution TEM and energy-dispersive X-ray (EDX) spectroscopy methods. The scanning electron microscopy image in Figure 4a shows sheet-like structures on the surface of the particles. An energy-dispersive X-ray (EDX) area scan furthermore proves the presence of carbon (Figure 4b and S4). Besides, high resolution transmission electron microscopy images (HRTEM) show a thin layer of a rather amorphous material on the surface of the particles as shown in Figure 4c. An EDX line scan – conducted in combination with the HRTEM instrument – identified carbonaceous material on a single superparticle, which confirms the presence of the srGO on the surface of the particles (see Figure S6). Raman spectroscopy of the hybrid material clearly shows the D- and G-band already observed for srGO and no difference to the Raman spectrum of the pure srGO can be observed as demonstrated in Figure 4d.

Derived from the Brunauer-Emmett-Teller method, the surface area is determined to be 29.3 $m^2\ g^{-1}$ for the as-synthesized Ni@Fe_2O_3 particles. This is lower compared to the srGO wrapped particles with a surface area of 81.6 $m^2\ g^{-1}$ due to the presence of the graphene derivative.

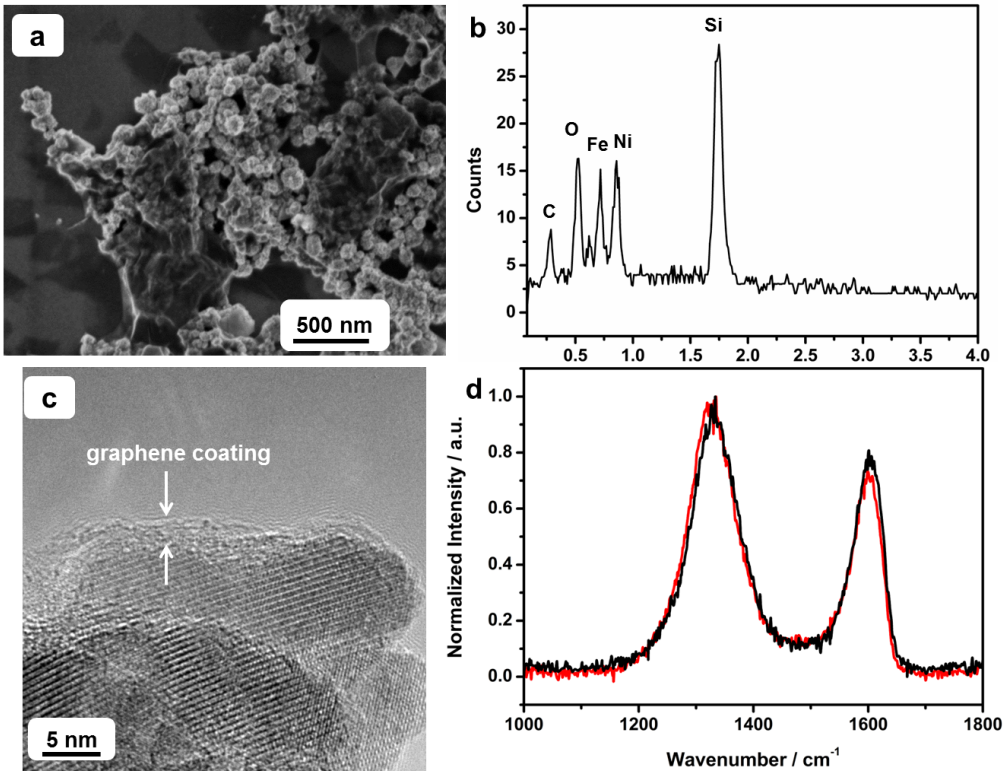

Figure 4: a) SEM image of graphene wrapped Ni@Fe_2O_3 particles. b) EDX results of an area scan of srGO wrapped Ni@Fe_2O_3 particles of the area shown in Figure S5. c) High resolution TEM image of srGO wrapped Ni@Fe_2O_3 superparticles and d) Raman spectrum of pure srGO (red) and wrapped Ni@Fe_2O_3 particles.

Electrochemical Characterization

Figure 5 shows the cyclic voltammetry profiles of 20 cycles at a 1 mV s^{-1} scan rate of unwrapped and wrapped Ni@Fe_2O_3 particles. During the cathodic sweep two peaks can be observed. The first peak at about 1.35 V can be attributed to an intercalation of Li^+ into the Fe_2O_3 spinel structure, as this has been also reported for γ-Fe_2O_3.[52,53] The second cathodic peak at 0.42 V in the first cycle is attributed to the electrolyte decomposition and the formation of the solid electrolyte interface (SEI) as well as to the reversible conversion reaction of Fe_2O_3 with lithium-ions ac-

cordingly Fe_2O_3 + 6 Li^+ + 6 e^- → 3 Li_2O + 2 Fe^0.[53,54] During the first anodic sweep a peak at 1.85 V is observed. This peak is attributed to the oxidation of Fe(0) to Fe(III) as well as the decomposition of the amorphous Li_2O.[55] The main cathodic peak of the following sweeps is shifted to higher voltages (0.6 V) and also the anodic peak shifts slightly to higher voltages of around 2.0 V. In the case of the unwrapped particles the peak intensities of both the cathodic and the anodic main peaks decrease significantly within the first 20 cycles. In contrast, a higher reversibility can be observed for the wrapped particles, as there is a minor decrease of the peak intensities in comparison with the unwrapped particles.

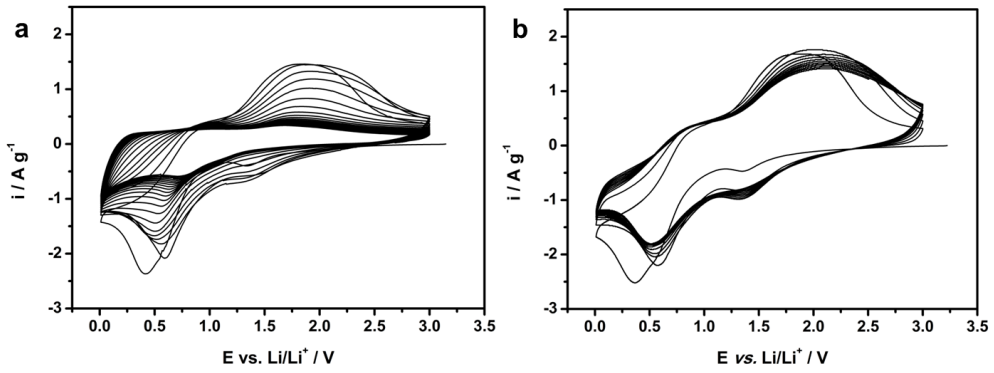

Figure 5: Cyclic voltammetry of unwrapped Ni@Fe_2O_3 superparticles (a) and srGO wrapped Ni@Fe_2O_3 particles (b) with a scan rate of 1.0 mV s^{-1} in the voltage range from 0.01 V to 3.0 V.

Both wrapped and unwrapped Ni@Fe_2O_3 particles were applied to a galvanostatic C-rate test as shown in Figure 6a. The obtained initial discharge and charge specific capacity at 0.05C (1C is defined as 1000 mA g^{-1}) of unwrapped particles is 1298 and 929 mA g^{-1}, whereas for the particles wrapped with srGO it is improved to 1371 and 1004 mA g^{-1}. The coulombic efficiency of the first cycle is rather low due to the formation of the SEI and slightly improved for the wrapped particles (73.3 %) compared to the unwrapped particles (71.6 %). However, there is a gradual increase

to 96 % in the second and 97 % as from the 4th cycle in the case of the wrapped particles, whereas the coulombic efficiency for the unwrapped sample remains below 94 % within the first 10 cycles. The C-rate performance of the srGO wrapped sample is significantly improved as the specific capacities for the charging process of the unwrapped sample are 677, 564, 388, 176, 57, 20 and 3 mA g^{-1} at 0.05C, 0.1C, 0.2C, 0.5C, 1C, 2C and 5C, whereas the specific capacities obtained for the srGO wrapped samples are 1057, 1006, 867, 625, 427, 296 and 131mA g^{-1}.

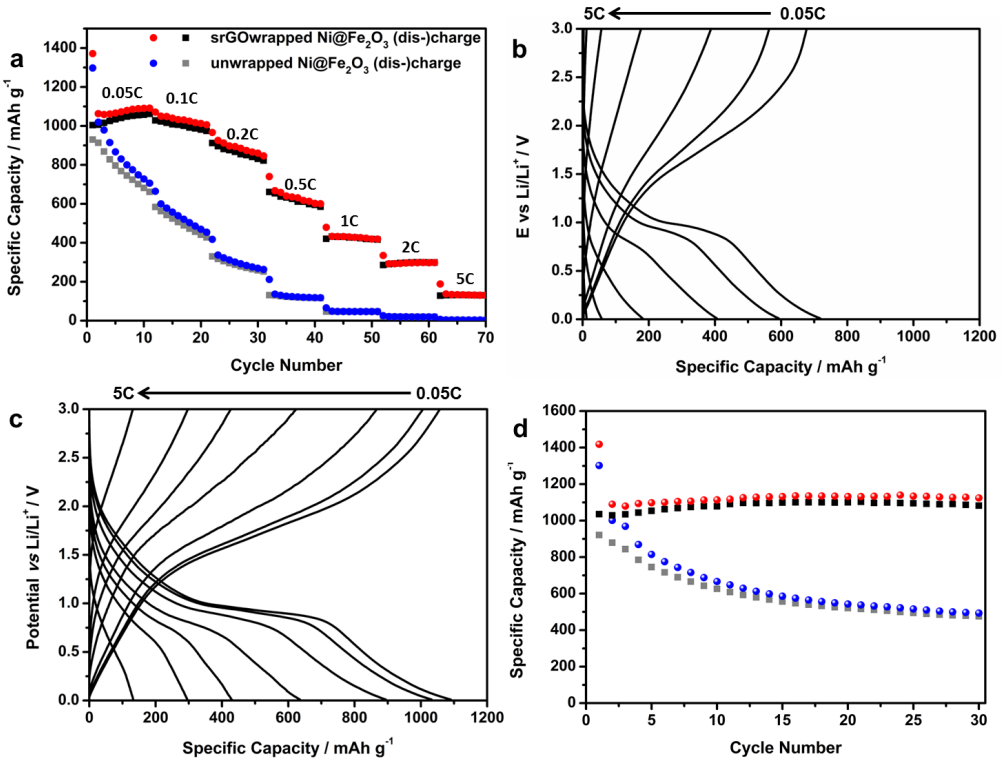

Figure 6: a) C-Rate performance of srGO wrapped Ni@Fe_2O_3 and unwrapped Ni@Fe_2O_3. Selected voltage profiles of srGO unwrapped Ni@Fe_2O_3 (b) and wrapped Ni@Fe_2O_3 (c) particles. Extended cycling performance of wrapped Ni@Fe_2O_3 and unwrapped Ni@Fe_2O_3 at 0.05C

The enhanced battery performance of the wrapped sample can be explained by an increased electrical conductivity within the hybrid material as well as by the abil-

ity of the srGO sheets to mechanically buffer volume changes. In the case of the wrapped sample the high capacities at lower C-rates exceed the theoretical value for the specific capacity of 1005 mA g^{-1}. This can be explained by side reactions with the electrolyte and a reversible SEI formation.[56] Potential profiles of unwrapped and wrapped particles at several C-rates are shown in Figure 6b and 6c. For both discharge profiles a plateau at around 1.0 V can be observed. This plateau completely disappears for the unwrapped sample at elevated C-rates higher than 0.5C. In contrast, this plateau is more pronounced for the wrapped sample and readily identifiable even at 2C, which might be attributed to an increased conductivity due to the presence of homogeneously incorporated srGO wrapping. In case of the charge profiles, a gradual decrease of capacity can be observed in the voltage range from 1.25 V to 2.5 V with rising C-rate. This region is again more stable and pronounced for the wrapped particles.

The extended cycling performance at 0.05C is shown in Figure 6d. The charge capacity of unwrapped Ni@Fe_2O_3 decreases within 30 cycles to 475 mA g^{-1}, whereas the charge capacity of wrapped Ni@Fe_2O_3 constantly exceeds 1000 mAh g^{-1} and 1082 mA g^{-1} are obtained after 25 cycles. It should be pointed out that this wrapping strategy using srGO is not only applicable to the herein described Ni@Fe_2O_3 nanoparticles, but it can also be applied to further inorganic nanoparticles. To show the versatility of this approach the wrapping strategy was also applied to Fe_2O_3 nanorice and FeS_2 nanoparticles, which are currently characterized electrochemically. SEM images of the wrapped particles are shown in Figure S7 and S8.

3. Conclusion

In summary, we introduced a non-thermal wrapping strategy using sulfated and reduced graphene oxide, which can coordinate onto inorganic nanoparticles. The graphene sheets are reduced by the treatment with oleum and the extension of the conjugated system could be proven by XPS and Raman spectroscopy. Exem-

plarily, Ni@Fe_2O_3 superparticles synthesized using Ni nanoplates as a substrate to grow Fe_2O_3 nanorods on the surface were used to be wrapped with the srGO sheets. The wrapping strongly enhances the battery performance with respect to the C-rate capability and stabilizes the capacity retention at a constant C-rate of 0.05C compared to unwrapped particles. Furthermore, the versatility of this approach could be demonstrated by the application of the wrapping to further inorganic nanoparticles especially metal chalcogenides (FeS_2) and Fe_2O_3 nanorice.

4. Experimental

Materials

Graphite (graphite flake natural, -325 mesh, 99.8%) was purchased from AlfaAesar. All other substances were acquired from Acros Organics and used without purification.

Physical characterization

FT-IR spectra were measured on a Jasco FT/IR-4100 spectrometer equipped with a PIKE Technologies ATR unit (MIRacleTM single reflection). TGA of the products was carried out on a PerkinElmer Pyris 6 TGA applying air-atmosphere. Raman spectra were performed on a HORIBA Jobin Yvon LabRAM HR system with a frequency doubled Nd:YAG-Laser (532.2 nm). HRTEM, scanning transmission electron microscopy (STEM), and energy dispersive X-ray spectroscopy (EDX) was carried out on a Tecnai F 20 (FEI). Scanning electron microscopy (SEM) was performed using a HITACHI SU 8000 (Hitachi High-Technologies Europe GmbH, Krefeld; Germany), which was coupled to an XFlash 5010 X-ray detector to obtain simultaneously energy-dispersive X-ray (EDX)-based elemental analysis. X-ray diffraction was performed using a Siemens D 5000 (Cu-K-alpha radiation). Elemental analysis was performed with an Elementar Vario EL cube. For electrochemical characterization see the experimental descriptions. Atomic absorption spectroscopy was carried out on a Perkin Elmer 5100 ZL spectrometer.

Synthesis of sulfated graphene oxide

Graphene oxide was synthesized according to a modified Hummers-Offeman[47,57] method. In a first pre-oxidation step, concentrated H_2SO_4 (40 mL) was mixed with $K_2S_2O_8$ (8.6 g) and P_2O_5 (8.6 g) in small portions at 80 °C. This was followed by a slow addition of graphite powder (10 g) and stirring for 4.5 h. After cooling to room temperature, 300 mL of deionized (DI) water was added carefully and stirring was continued for 12 h. The mixture was centrifuged and redispersed 5 times with DI-water with subsequent drying of the sediment in air at room temperature. The black powder was suspended in 230 mL of sulfuric acid. To this mixture $KMnO_4$ (60 g) was added successively, keeping the temperature below 10 °C. After stirring for 2 h at 35 °C the mixture was diluted with 500 mL DI-water and stirred over night. While stirring vigorously 50 mL aqueous H_2O_2-solution (18 wt.%) was added dropwise. After obtaining a homogenous dispersion, it was left to stand overnight. The mixture was centrifuged and the sediment was washed with 1M aqueous HCl three times, followed by successive washing and dilution with DI-water until pH 5 was reached. After ultrasonication and centrifugation to remove unexfoliated graphite oxide, further purification was achieved by dialysis (Visking, reg. cellulose, MWCO 14000). The dilute brown graphene oxide dispersion was then lyophilized obtaining a light-brown spongy material.

Raman spectroscopy: 1336 cm^{-1}: D-band; 1597 cm^{-1}: G-band

FT-IR: ν= 3370 (b, -OH), 1732 (m, COOH carbonyl group), 1624 (s, C=C in-plane vibration), 1370 (w), 1064 (s, epoxide) cm^{-1}.

Elemental analysis: C: 46.66%; H: 3.40%; N: 0%; S: 1.29%.

Graphene oxide was functionalized with sulfate groups and reduced simultaneously by the treatment with oleum as reported.[48]Therefore, graphene oxide (63 mg) is dispersed in 31 mL of oleum (20% SO_3) and ultrasonicated for 70 min. The viscous suspension is stirred for 48 hours. The resulting suspension is added dropwise to ice cold water. Using DI-water, the product is repeatedly washed and centrifuged until a pH of 4. Further purification is achieved by dialysis (Visking, reg. cellulose, MWCO

14000) against DI-water. After lyophilizing and drying in vacuum at 120 °C, 30 mg of a black powder are obtained. Raman: 1336 cm^{-1}: D-band; 1603 cm^{-1}: G-band. FT-IR: ν= 3370 (w, -OH), 1725 (w, COOH carbonyl group), 1574 (s, C=C in-plane vibration and aromatic ring vibrations), 1310-890 (s, -S=O and SO_2 valence vibrations) cm^{-1}.

Elemental analysis: C: 61.09%; H: 0.81%; N: 0.26%; S: 3.35%.

Synthesis of Ni@Fe_2O_3 particles

The Ni@Fe_2O_3 heteroparticles were synthesized according to a literature.[46] Briefly, the superparticles were synthesized by mixing 62.25 mg (0.25 mmol) of nickel acetate Ni(ac)2, 7 mL of oleylamine, 1 mmol of trioctylphosphine, and 2 mmol of oleic acid and stirring them for 20 min under the inert condition before increasing the temperature. The mixture was heated to 120 °C for 20 min. Subsequently, 67.55 μL of Fe(CO)5 were added and the solution was heated to 180 °C for 30 min and cooled slowly down to room temperature. A black product was precipitated from the solution by adding an excess of ethanol. The precipitate was separated by centrifugation (9000 rpm, 10 min, RT). Finally, the product was dispersed in toluene, flushed with argon (Ar) and stored at 4 °C. The surfactants of the heteroparticles were removed by the use of $NOBF_4$ as described previously.[58] *Functionalization of inorganic nanoparticles*

The sulfated graphene oxide was added to a solution of DMF and triethylamine (2.6 wt. % TEA) resulting in a 0.3 mg/ml srGO containing dispersion and was ultrasonicated until a stable dispersion of srGO sheets was obtained. Dispersed in DMF, the inorganic particles were added slowly to the dispersion of srGO sheets while ultrasonicating. The weight ratio between nanoparticles and sulfated graphene oxide was about 92:8. The dispersion was stirred over night at 40 °C. The reaction mixture was centrifuged and the sediment was redispersed and centrifuged in order to remove excess surfactants of the nanoparticles.

Raman spectroscopy: 1336 cm^{-1}: D-band; 1603 cm^{-1}: G-band

Electrochemical characterization:

Electrodes were prepared as following: A slurry consisting of srGO wrapped Ni@Fe_2O_3 nanoparticles, conductive carbon additive (Super C65, IMERYS, Switzerland) and polyvinylidene fluoride (PVDF) as a binder solved in NMP resulting in a weight ratio of Ni@Fe_2O_3:Carbon (including srGO and Super C65):PVDF 70:20:10 was prepared. The reference sample contains 20 wt. % of carbon additive and no graphene based material. The slurries were homogenized by ball milling (Vario-Planetary Mill Pulverisette 4, Fritsch) for 2 h (400/-800 rpm). The resulting slurry was coated on dendritic copper foil with a wet film thickness of 120 μm. After drying over night at room temperature, disc electrodes were punched with a diameter of 12 mm and further dried at 120 °C under vacuum overnight. The active mass loading was in the range of 2.2 mg cm^{-2} and 2.6 mg cm^{-2}. Swagelok cells were assembled under inert conditions in an MBraun glove box with oxygen and water contents of less than 0.1 ppm. Lithium foil (Rockwood Lithium, battery grade) was used as a counter and reference electrode. Polypropylene fleeces (Freudenberg FS2190) as a separator was drenched with a 1 M solution of $LiPF_6$ in a 3:7 volume mixture of ethylene carbonate (EC) and diethyl carbonate (DEC, UBE). Cyclic voltammetry was conducted using a VMP3 potentiostat (BioLogic) applying a scan rate of 1.0 mV/s in the range of 0.01 V to 3.0 V. Galvanostatic cycling was carried out by means of a Maccor Battery Tester 4300.

Supporting Information

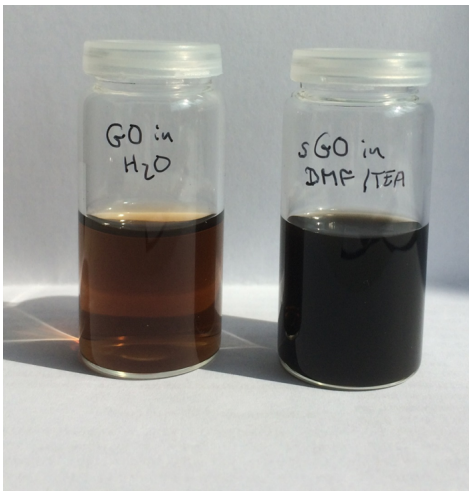

Figure S 1: Photograph of a GO dispersion (left) in water and srGO dispersion (right) in DMF.

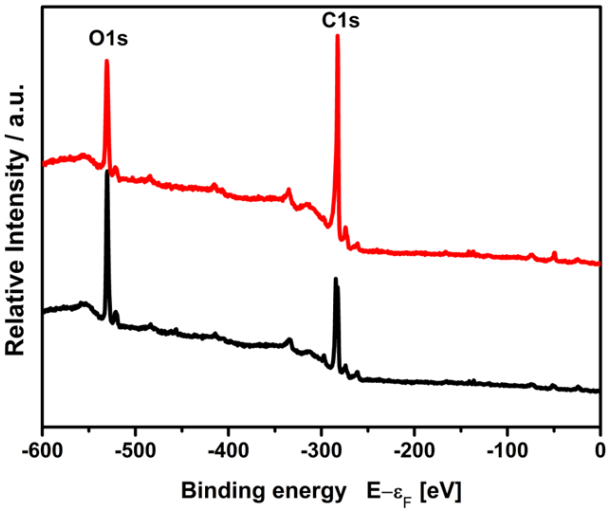

Figure S 2: XPS survey spectra of GO (black) and srGO (red).

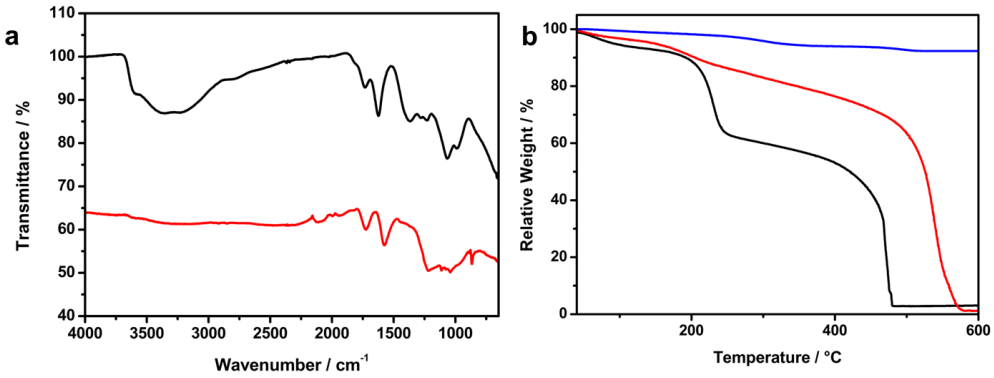

Figure S 3: FT-IR spectra (a) of GO (black) and srGO (red) and TGA data (b) of GO (black), srGO (red) and Ni@Fe_2O_3 wrapped with srGO (blue).

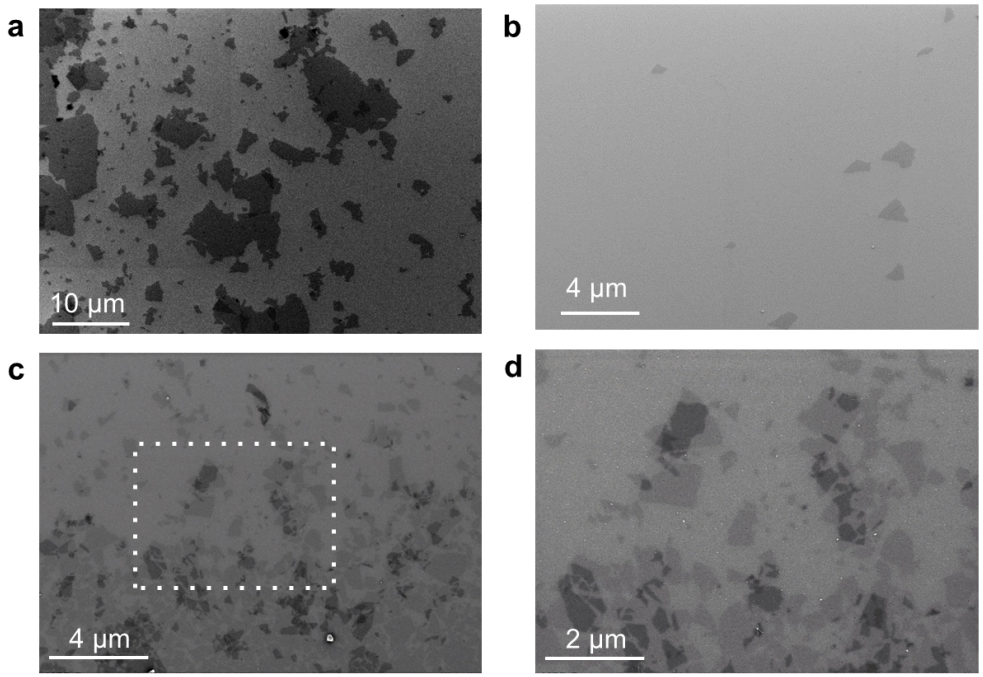

Figure S 4: SEM images of GO (a and b) and of srGO (c and d).

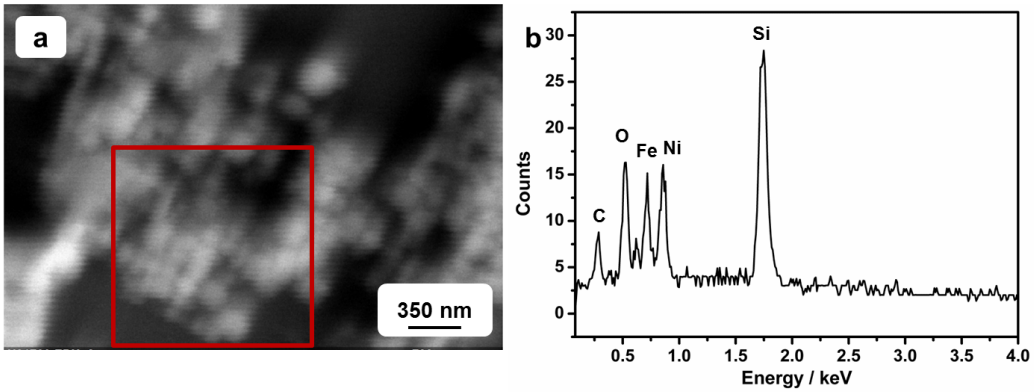

Figure S 5: a) SEM image and b) corresponding EDX data of the area shown in a).

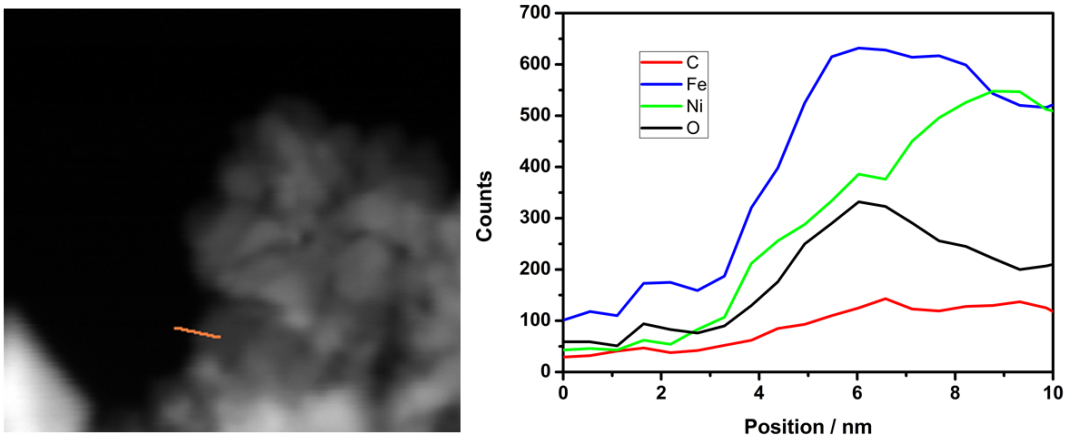

Figure S 6: STEM micrograph of the srGO wrapped Ni@Fe_2O_3 and b) detected EDX profiles along the line indicated in a).

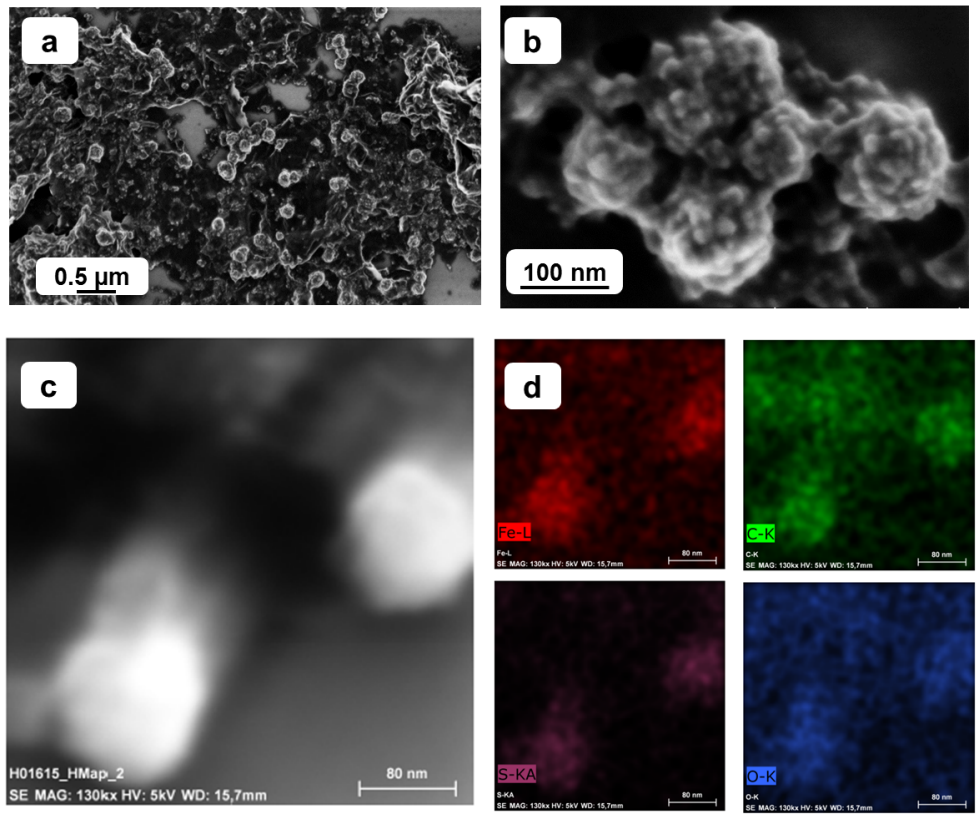

Figure S 7: SEM images of srGO wrapped FeS_2 particles (a and b). SEM image of srGO wrapped FeS_2 particles (c) and corresponding elemental mapping images of Fe, C, S, O (d).

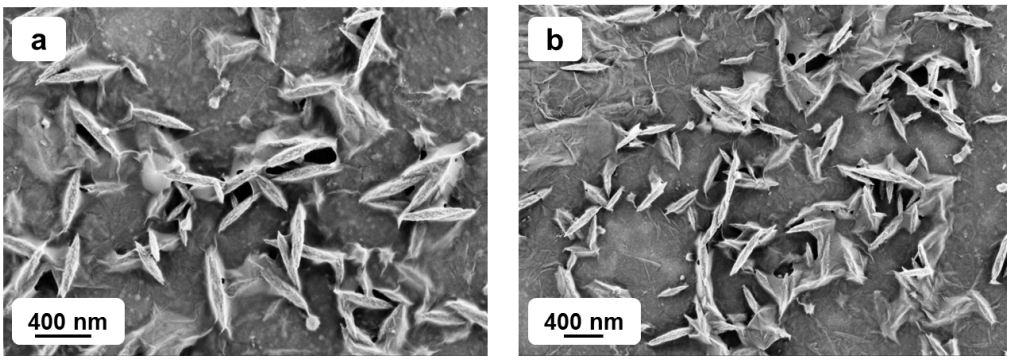

Figure S 8: SEM images of srGO wrapped Fe_2O_3 nanorice (a and b).

References

[1] M. Armand, J.-M. Tarascon, Nature 2008, 451, 652.

[2] A. S. Aricò, P. Bruce, B. Scrosati, J.-M. Tarascon, W. van Schalkwijk, Nat. Mater. 2005, 4, 366.

[3] N. Liu, Z. Lu, J. Zhao, M. T. McDowell, H.-W. Lee, W. Zhao, Y. Cui, Nature Nanotech 2014, 9, 187.

[4] N. Liu, H. Wu, M. T. McDowell, Y. Yao, C. Wang, Y. Cui, Nano Lett. 2012, 12, 3315.

[5] P. G. Bruce, S. A. Freunberger, L. J. Hardwick, J.-M. Tarascon, Nat Mater 2011, 11, 19.

[6] D. Bresser, F. Mueller, D. Buchholz, E. Paillard, S. Passerini, Electrochimica Acta 2014, 128, 163.

[7] W.-J. Zhang, Journal of Power Sources 2011, 196, 13.

[8] J.-M. Tarascon, P. Poizot, S. Laruelle, S. Grugeon, L. Dupont, Nature 2000, 407, 496.

[9] B. Oschmann, M. N. Tahir, F. Mueller, D. Bresser, I. Lieberwirth, W. Tremel, S. Passerini, R. Zentel, Macromol. Rapid Commun. 2015.

[10] D. Bresser, E. Paillard, R. Kloepsch, S. Krueger, M. Fiedler, R. Schmitz, D. Baither, M. Winter, S. Passerini, Adv. Energy Mater. 2013, 3, 513.

[11] L. Zhang, H. B. Wu, X. W. D. Lou, Adv. Energy Mater. 2014, 4, n/a.

[12] M. V. Reddy, G. V. Subba Rao, B. V. R. Chowdari, Chem. Rev. 2013, 113, 5364.

[13] P. G. Bruce, B. Scrosati, J.-M. Tarascon, Angew. Chem. Int. Ed. 2008, 47, 2930.

[14] T. Fröschl, U. Hörmann, P. Kubiak, G. Kučerová, M. Pfanzelt, C. K. Weiss, R. J. Behm, N. Hüsing, U. Kaiser, K. Landfester, M. Wohlfahrt-Mehrens, Chem. Soc. Rev. 2012, 41, 5313.

[15] S. H. Lee, S.-H. Yu, J. E. Lee, A. Jin, D. J. Lee, N. Lee, H. Jo, K. Shin, T.-Y. Ahn, Y.-W. Kim, H. Choe, Y.-E. Sung, T. Hyeon, Nano Lett. 2013, 13, 4249.

[16] H. Li, H. Zhou, Chem. Commun. 2012, 48, 1201.

[17] Y.-D. Cho, G. T.-K. Fey, H.-M. Kao, Journal of Power Sources 2009, 189, 256.

[18] B. Oschmann, D. Bresser, M. N. Tahir, K. Fischer, W. Tremel, S. Passerini, R. Zentel, Macromol. Rapid Commun. 2013, 34, 1693.

[19] N. Yan, X. Zhou, Y. Li, F. Wang, H. Zhong, H. Wang, Q. Chen, Sci. Rep. 2013, 3.

[20] S. Yang, X. Feng, S. Ivanovici, K. Müllen, Angew. Chem. Int. Ed. 2010, 49, 8408.

[21] Z. Wang, C.-J. Liu, Nano Energy 2015, 11, 277.

[22] R. Raccichini, A. Varzi, S. Passerini, B. Scrosati, Nat Mater 2014, 14, 271.

[23] G. Kucinskis, G. Bajars, J. Kleperis, Journal of Power Sources 2013, 240, 66.

[24] M. Srivastava, J. Singh, T. Kuila, R. K. Layek, N. H. Kim, J. H. Lee, Nanoscale 2015, 7, 4820.

[25] C. Xu, B. Xu, Y. Gu, Z. Xiong, J. Sun, X. S. Zhao, Energy Environ. Sci. 2013, 6, 1388.

[26] X. Yang, L. Zhang, F. Zhang, Y. Huang, Y. Chen, ACS Nano 2014.

[27] X. Zhu, J. Hu, W. Wu, W. Zeng, H. Dai, Y. Du, Z. Liu, L. Li, H. Ji, Y. Zhu, J. Mater. Chem. A 2014.

[28] Y. Wen, Y. Zhu, A. Langrock, A. Manivannan, S. H. Ehrman, C. Wang, Small 2013, 9, 2810.

[29] W. Wei, S. Yang, H. Zhou, I. Lieberwirth, X. Feng, K. Müllen, Adv. Mater. 2013, 25, 2909.

[30] J. Zhu, D. Yang, Z. Yin, Q. Yan, H. Zhang, Small 2014, 10, 3480.

[31] K. S. Novoselov, A. K. Geim, S. V. Morozov, D. Jiang, M. I. Katsnelson, I. V. Grigorieva, S. V. Dubonos, A. A. Firsov, Nature 2005, 438, 197.

[32] A. Fasolino, J. H. Los, M. I. Katsnelson, Nat Mater 2007, 6, 858.

[33] J. Zai, X. Qian, RSC Adv. 2015, 5, 8814.

[34] Y. Jiang, X. Ling, X. Cai, Z. Jiao, L. Cheng, L. Bian, M. Nguyen, Y. Chu, B. Zhao, J. Mater. Res. 2015.

[35] X. Li, Y. Ma, L. Qin, Z. Zhang, Z. Zhang, Y.-Z. Zheng, Y. Qu, J. Mater. Chem. A 2015, 3, 2158.

[36] M. Zhang, B. Qu, D. Lei, Y. Chen, X. Yu, L. Chen, Q. Li, Y. Wang, T. Wang, J. Mater. Chem. 2012, 22, 3868.

[37] Y. Zou, J. Kan, Y. Wang, J. Phys. Chem. C 2011, 115, 20747.

[38] L. Tian, Q. Zhuang, J. Li, C. Wu, Y. Shi, S. Sun, Electrochimica Acta 2012, 65, 153.

[39] L. Wang, Q. Chen, Y. Zhu, Y. Qian, Chin. Sci. Bull. 2014, 59, 4271.

[40] X. Zhu, Y. Zhu, S. Murali, M. D. Stoller, R. S. Ruoff, ACS Nano 2011, 5, 3333.

[41] D. Chen, W. Wei, R. Wang, J. Zhu, L. Guo, New J. Chem. 2012, 36, 1589.

[42] K. Xie, Z. Lu, H. Huang, W. Lu, Y. Lai, J. Li, L. Zhou, Y. Liu, J. Mater. Chem. 2012, 22, 5560.

[43] J. M. Lucas, C.-C. Tuan, S. D. Lounis, D. K. Britt, R. Qiao, W. Yang, A. Lanzara, A. P. Alivisatos, Chem. Mater. 2013, 25, 1615.

[44] J. Lu, J. Fan, R. Xu, S. Roy, N. Ali, Y. Gao, Journal of Colloid and Interface Science 2003, 258, 427.

[45] Z. Xu, C. Huang, L. Wang, X. Pan, L. Qin, X. Guo, G. Zhang, Ind. Eng. Chem. Res. 2015, 54, 4593.

[46] Muhammad Nawaz Tahir, Jana Herzberger, Filipe Natalio, Oskar Köhler, Robert Branscheid, Enrico Mugnaioli, Teuta Gasi, Vadim Ksenofontov, Martin Panthöfer, Ute Kolb, Holger Frey, Wolfgang Tremel, Submitted Manuscript 2015.

[47] Z. Xu, C. Gao, ACS Nano 2011, 5, 2908.

[48] J. Liu, Y. Xue, L. Dai, J. Phys. Chem. Lett. 2012, 3, 1928.

[49] M. A. Pimenta, G. Dresselhaus, M. S. Dresselhaus, L. G. Can?ado, A. Jorio, R. Saito, Phys. Chem. Chem. Phys. 2007, 9, 1276.

[50] S. Stankovich, D. A. Dikin, R. D. Piner, K. A. Kohlhaas, A. Kleinhammes, Y. Jia, Y. Wu, S. T. Nguyen, R. S. Ruoff, Carbon 2007, 45, 1558.

[51] Y. Zhou, Q. Bao, L. A. L. Tang, Y. Zhong, K. P. Loh, Chem. Mater. 2009, 21, 2950.

[52] J. Chen, L. Xu, W. Li, X. Gou, Adv. Mater. 2005, 17, 582.

[53] D. Larcher, C. Masquelier, D. Bonnin, Y. Chabre, V. Masson, J.-B. Leriche, J.-M. Tarascon, J. Electrochem. Soc. 2003, 150, A133.

[54] H. Liu, G. Wang, J. Park, J. Wang, H. Liu, C. Zhang, Electrochimica Acta 2009, 54, 1733.

[55] M. V. Reddy, T. Yu, C. H. Sow, Z. X. Shen, C. T. Lim, G. V. Subba Rao, B. V. R. Chowdari, Adv. Funct. Mater. 2007, 17, 2792.

[56] M. N. Obrovac, J. R. Dahn, Electrochem. Solid-State Lett. 2002, 5, A70.

[57] W. S. Hummers, R. E. Offeman, J. Am. Chem. Soc. 1958, 80, 1339.

[58] A. Dong, X. Ye, J. Chen, Y. Kang, T. Gordon, J. M. Kikkawa, C. B. Murray, J. Am. Chem. Soc. 2011, 133, 998.

4.3 Coating of Inorganic Particles Using Conductive Polymer

4.3.1 Introduction

As discussed in section 4.1.6, a thermal carbon coating approach is limited to thermally stable particles. Thus, developing approaches that do not require a thermal treatment are necessary for thermally unstable active materials. In this chapter, the synthesis and use of a semiconductive polymer is described, which is conductive and electrochemically active within a certain voltage range.[1–3] In contrast to the approach using polyacrylonitrile (described in section 4.1), this approach does not require a thermal heat treatment to increase the electronic conductivity and is suitable to thermally unstable alternative cathode materials. Parts of the synthetic results shown here result from Yannick Nyquist's and Jonathan Kiehl's Bachelor thesis conducted under my supervision.[17-18]

The herein used polymer is poly(3-hexylthiophene-2,5-diyl) (P3HT), which was synthesized by GRIM polymerization. The polymer should be functionalized with dopamine units enabling the coordination onto inorganic transition metal oxide particles as schematically shown in Figure 1.

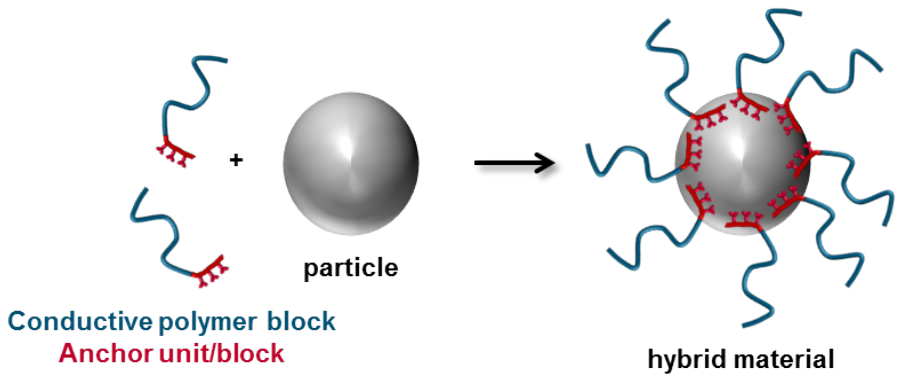

Figure 1: Functionalization of an inorganic particle with a conductive polymer.

The introduction of the anchoring group should be achieved by the introduction of a single anchoring end-group as well as by the introduction of an anchoring block.

$LiNi_{0.33}Co_{0.33}Mn_{0.33}O_2$ (in the following termed as NMC) is used as an exemplary cathode material. The lithiation of NMC takes place at a voltage range of 3.5-4.0 V,[4] whereby the electrochemical doping of P3HT is reported to be in the same voltage range.[5] This electrochemical doping increases the electric conductivity of P3HT, which is typically a semiconductive material in the undoped state due to the lack of free charge carriers, by several orders. Thus, it is expected that the electronic conductivity can be increased during the lithiation of NMC, if P3HT is applied as a coating around NMC particles.

4.3.2 Results and discussion

The anchoring P3HT is synthesized by two strategies, one following the combination of GRIM polymerization and RAFT polymerization in order to synthesize P3HT with an anchoring block copolymer. The other strategy is following the intention to introduce a single anchoring unit.

The synthetic scheme to obtain the anchoring block copolymer is shown in Figure 2.

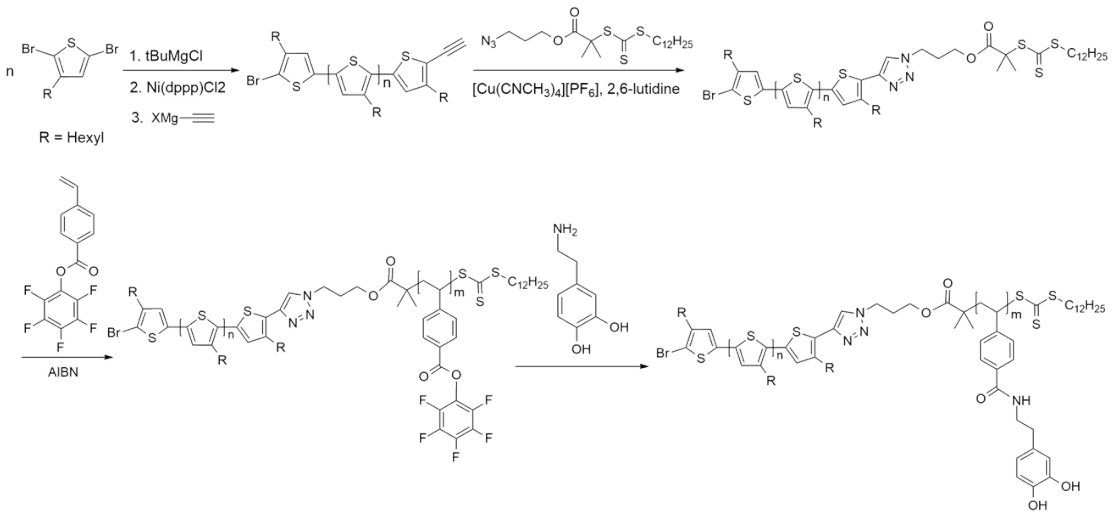

Figure 2: Synthesis route to obtain a polythiophene with an anchoring block.

First, the P3HT is synthesized applying GRIM polymerization. The polymer should be end-capped with an ethynyl group,[6] which enables the further modification

to conduct a RAFT polymerization derived second block as described later. The ethynyl end-group functionalized P3HT is characterized by NMR spectroscopy as sown in Figure 3. The presence of the end-group can be proven by the signal at 3.53 ppm in the NMR spectrum. The integration of this signal and the comparison of the integrated signal at 6.98 ppm corresponding to the aromatic hydrogen of the thiophene allows a rough estimation of the degree of polymerization and the number average of the molecular weight, which is estimated to be 27 (degree of polymerization) and 4,482 g mol^{-1} (see Figure 3) by this method.

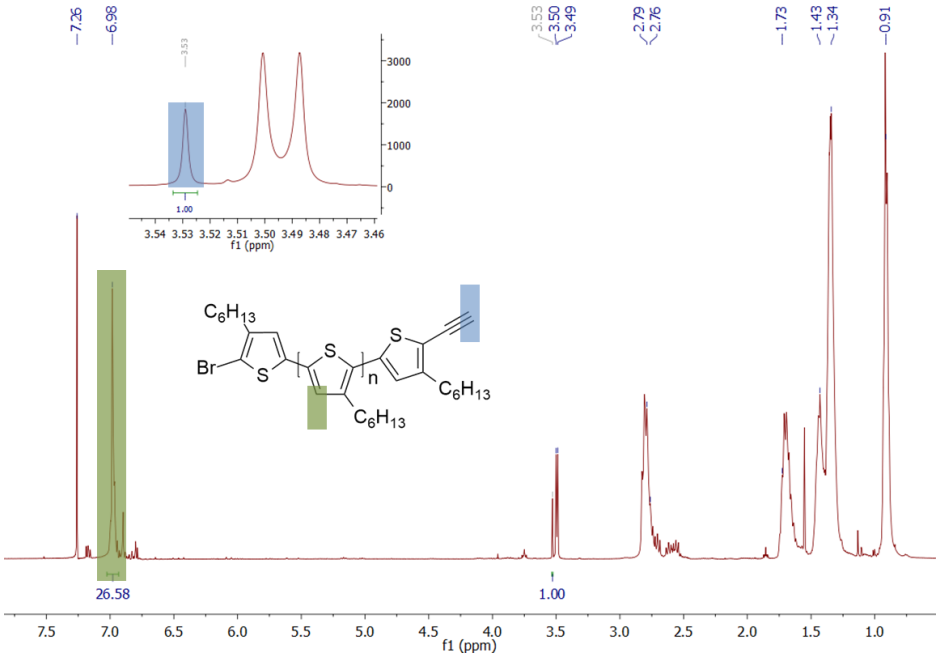

Figure 3: ^{1}H-NMR spectrum of ethynyl-terminated P3HT.

The polymer was not further purified by soxhlet extraction as commonly done for polymers synthesized by GRIM polymerization, as the ethynyl end-group was reported to undergo side reactions in the presence of residual catalyst amounts during the soxhlet extraction.[8] Thus, the polydispersity of the polymer determined by size exclusion chromatography (shown in Figure 4) is about 1.26 for the as-synthesized polymer. This value is higher compared to polythiophenes purified by soxhlet ex-

traction. The molecular weight determined by SEC was 5174 g mol^{-1} and is higher compared to the NMR derived value. This may be caused by the fact that polystyrene was used as a calibration standard, which behaves very differently in solution compared to P3HT.

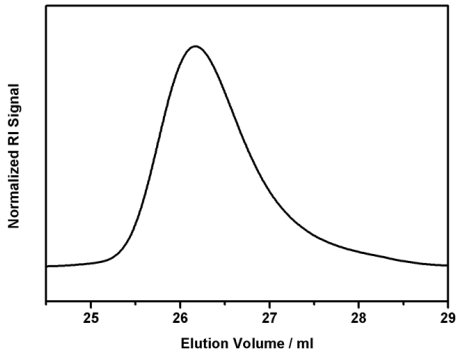

Figure 4: Size exclusion chromatography of ethynyl terminated P3HT.

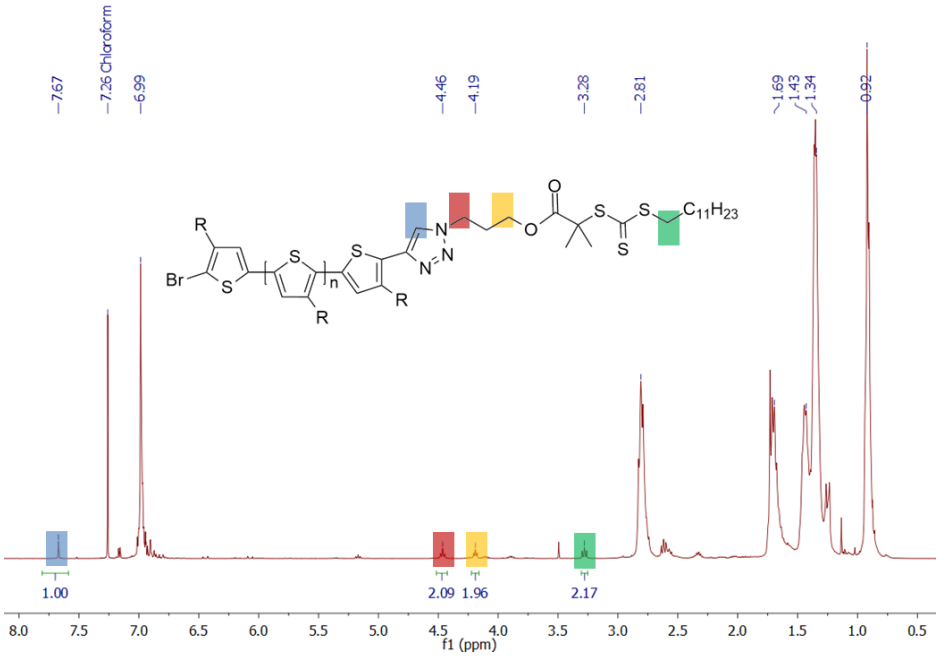

Figure 5: ^{1}H-NMR spectrum of CTA terminated P3HT.

A chain transfer agent was attached to the polymer by a 1,3 dipolar cycloaddition of the azide bearing CTA and the ethynyl terminated polymer, catalyzed by

a Cu(I) species (see Figure 2). The CTA (2-Dodecylsulfanylthiocarbonylsulfanyl-2-methylpropionic acid 3-azidopropyl ester) was synthesized following a previously reported method and could be obtained in a high purity as confirmed by NMR spectroscopy.[13] As proven by NMR spectroscopy (see Figure 5), the CTA could be successfully incorporated into the polymer as an end-group.

The macro-CTA was used to apply RAFT polymerization. A reactive ester monomer was chosen for the block copolymerization, as the reactive ester enables the introduction of several anchoring units yielding in a block of anchoring units.[9] In this case, pentafluorophenyl-4-vinylbenzoate (PFP4VB) was used, as it is suitable for the polymerization using a trithiocarbonate based CTA. The resulting block copolymer P(3HT-b-PF4VB) was characterized by ^{1}H- and ^{19}F-NMR as shown in Figure 6a) and b).

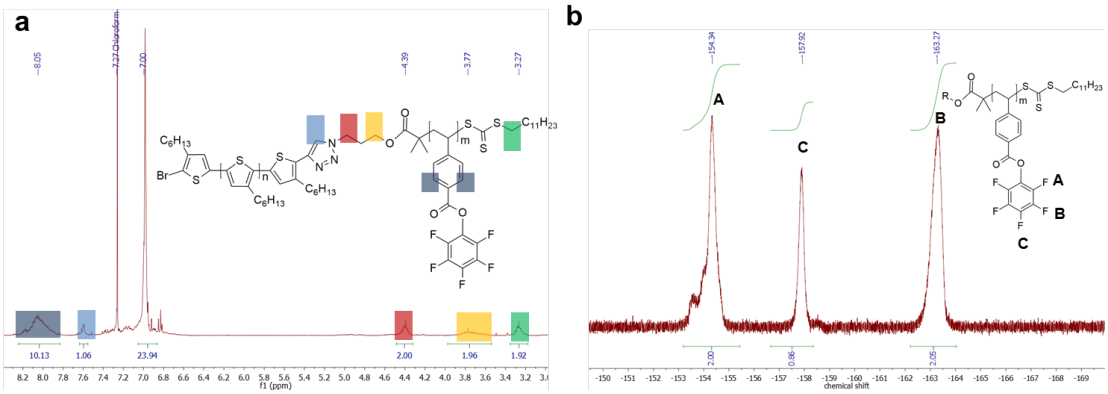

Figure 6: a) ^{1}H-NMR spectrum and b) ^{19}F-NMR spectrum of P(3HT-b-PF4VB).

The obtained polymer shows in the ^{1}H-NMR spectrum typical peaks of the aromatic ring of PF4VB unit and in the ^{19}F the three typically observed broad signals due to the pentafluorophenyl unit. Furthermore, SEC proves the successful reaction, as the elution volume shifts as expected to a lower elution volume for the block copolymer (see Figure 7) due to an increased hydrodynamic radius after block copolymerization. Furthermore, the PDI is slightly increased from 1.26 to 1.31 and the calculated

molecular weight is increased from 5,147 g mol^{-1} to 6,193 g mol^{-1}.

Dopamine was introduced by the aminolysis of the reactive ester block as shown in Figure 2. The successful reaction can be proven by SEC as well as by IR- and NMR-spectroscopy. The elugram of the dopamine containing polymer shows a shift to higher elution volumes compared to the reactive ester containing block copolymer (Figure 7).

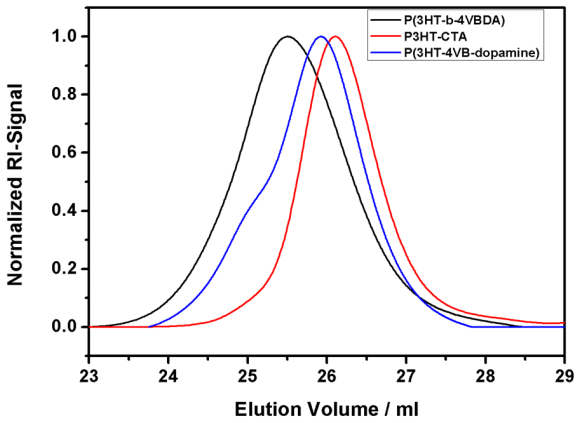

Figure 7: SEC of P(3HT-CTA) (red), P(3HT-b-4VBDA) (black) and P(3HT-4VB-dopamine) (blue).

The reason for this is the lower solubility of the dopamine block compared to the high solubility of the reactive ester block in THF, which is the solvent of the SEC set-up. The lower solubility of the dopamine block causes a reduced volume of the anchoring block inducing a lower hydrodynamic volume of the whole polymer. Furthermore, in the IR-spectrum (Figure 8) the ester band at 1761 cm^{-1} of the reactive ester containing polymer disappears and a new amide band at 1633 cm^{-1} appears after the aminolysis.

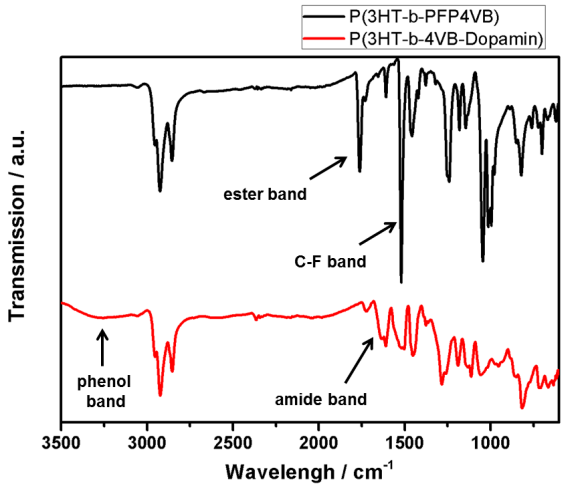

Figure 8: IR spectra of P(3HT-b-4VBDA) (black) and P(3HT-4VB-dopamine) (red).

In the NMR spectrum (Figure 9) typical dopamine signals at 6.68 ppm can be observed proving the presence of the incorporated dopamine.

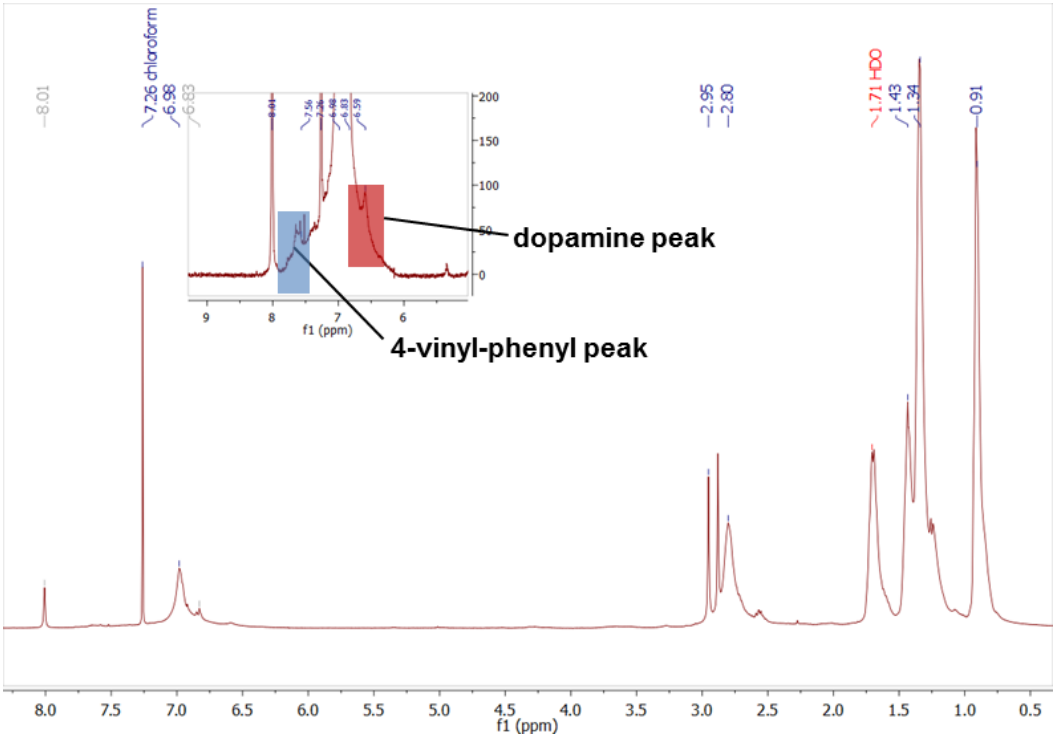

Figure 9: ^{1}H-NMR spectrum of P(3HT-4VB-dopamine).

Besides the introduction of dopamine as a block, dopamine should be also introduced as an end-group. The synthesis route for this product is shown in Figure 10.

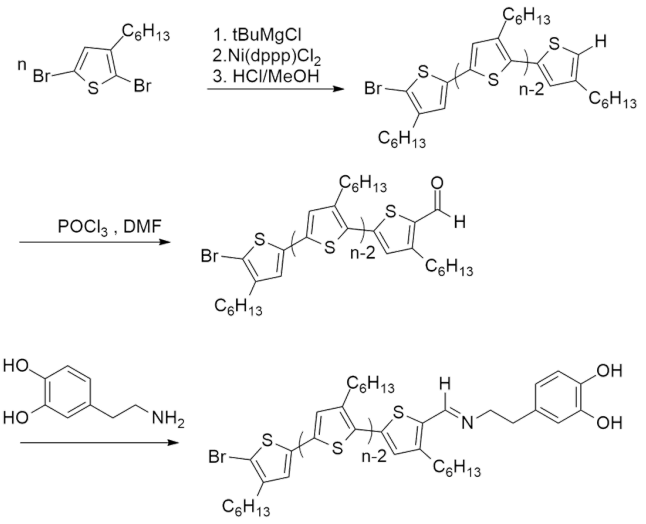

Figure 10: Synthesis route to obtain dopamine end-group functionalized P3HT.

First, P3HT is polymerized applying GRIM polymerization. In order to obtain bromine/hydrogen terminated P3HT, the polymerization was quenched in hydrochloric acid as described in literature.[10] After soxhlet extraction polymers with low PDI of 1.14 and molecular weights of around 5,800 g mol^{-1} could be obtained as confirmed by SEC. The aromatic hydrogen end-group overlaps in the ^{1}H-NMR spectrum with the other aromatic signals. Thus, the determination of the average chain length cannot be estimated by NMR spectroscopy. The introduction of a carbonyl end-group can be achieved by the application of the Vilsmeier reaction as shown in the reaction scheme. The formylation of P3HT can be proven by NMR spectroscopy, where a typical hydrogen signal of an aldehyde can be observed at 10.02 ppm as shown in Figure 11. The integration of this signal and the ratio of this integral and the integral of the signal of the aromatic backbone signal at 6.98 ppm allows the estimation of the chain length (25 units, 4150 g mol^{-1}) by NMR spectroscopy and meets our expectations according to our previous experiences from the SEC results.

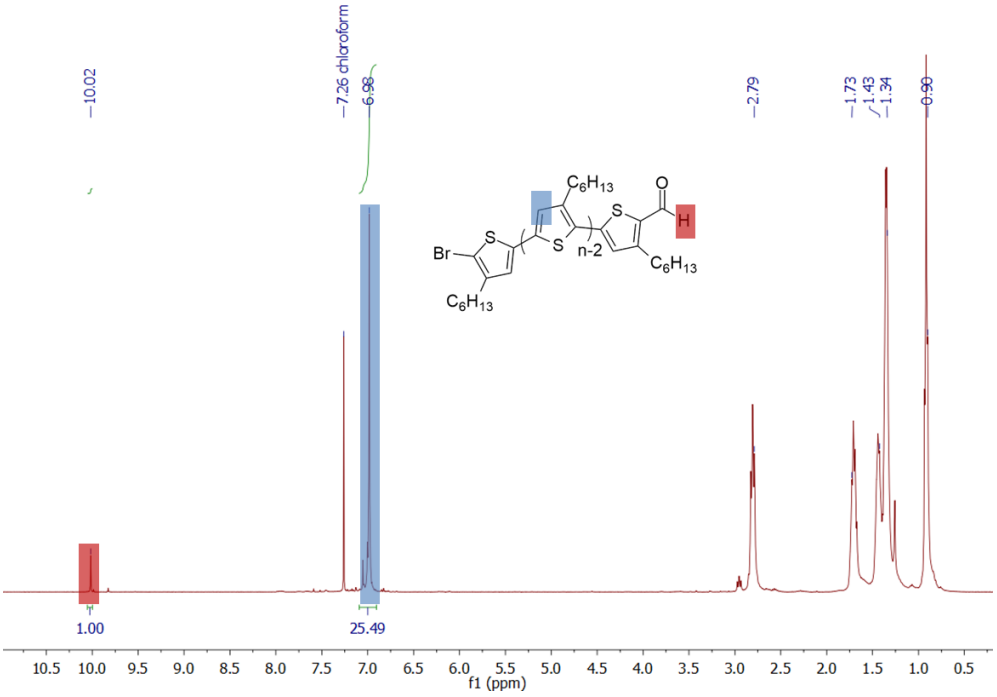

Figure 11: ^{1}-NMR spectrum of aldehyde terminated P3HT.

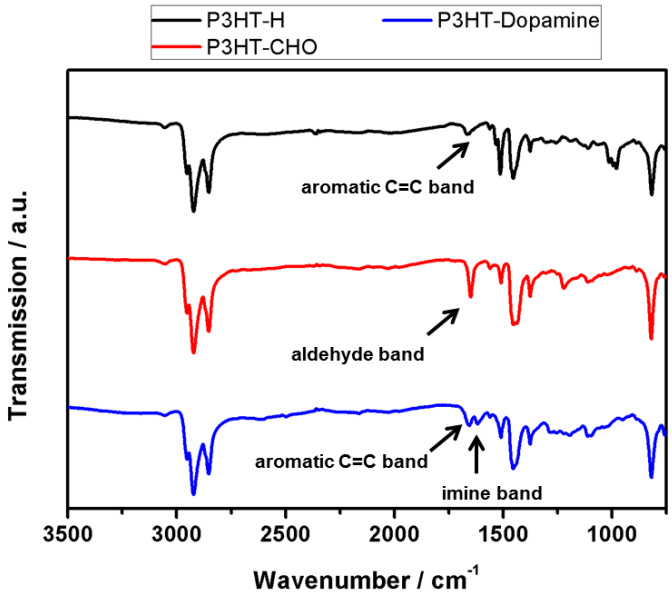

Figure 12: IR spectra of H terminated, aldehyde-terminated and dopamine terminated P3HT.

IR spectroscopy confirms the presence of an aldehyde end-group, as compared to the

hydrogen terminated P3HT, which shows a C=C stretching band at 1666 cm^{-1} and an additional band at 1650 cm^{-1} attributed to the carbonyl band can be observed (see Figure 12).

Finally, dopamine is introduced by the aminolysis of the carbonyl group yielding in an imine group. The formation of this imine group can be nicely followed in the IR spectrum, as the carbonyl bond observed for the aldehyde terminated P3HT disappears and a new band at 1616 cm^{-1} appears (see Figure 12). In the ^{1}H-NMR spectrum a new peak at 8.22 ppm can be observed matching an imine peak. Furthermore, additional peaks at 6.60 and 6.80 ppm can be observed due to the aromatic dopamine signals as shown in Figure 13. The conversion of the aldehyde to the imine does not occur to 100 %, as there is still a small amount of aldehyde left. This is as expected around 15 % as confirmed by NMR spectroscopy. However, the polymer without dopamine end-group can be removed at least after the functionalization of inorganic particles by centrifugation.

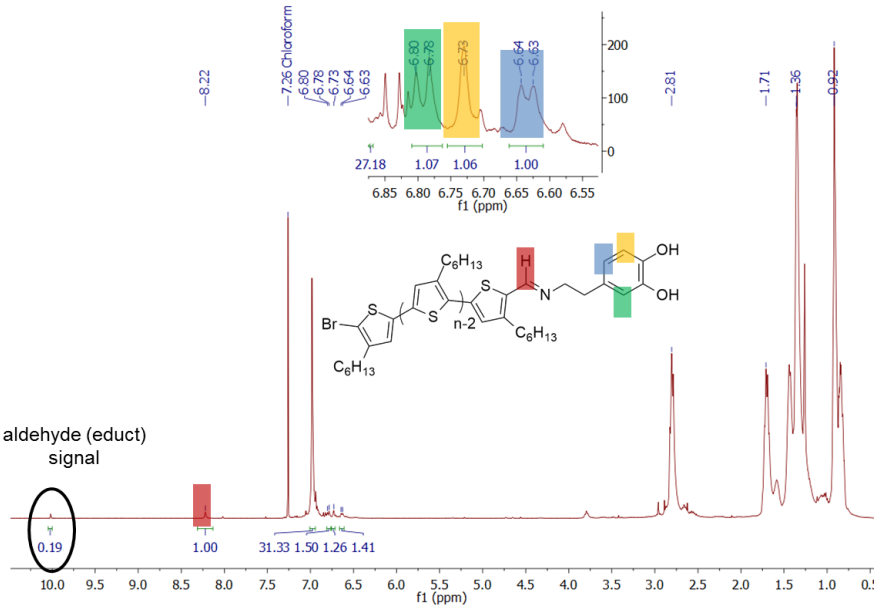

Figure 13: ^{1}H-NMR spectrum of dopamine terminated P3HT.

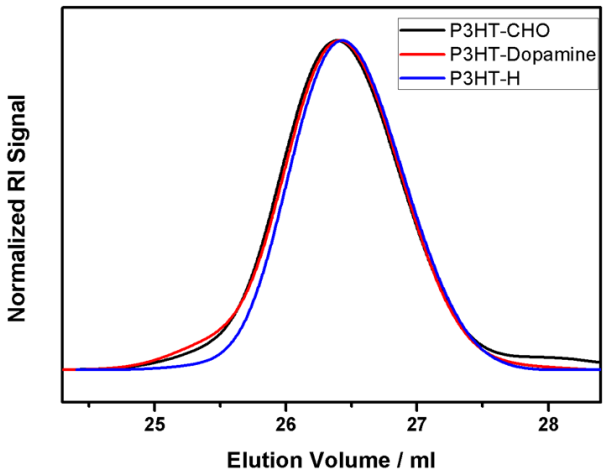

Figure 14: SEC elugram of hydrogen-, aldehyde- terminated and dopamine-terminated P3HT.

Figure 14 shows the SEC elugrams of the hydrogen-terminated, aldehyde-terminated and dopamine-terminated P3HT, whereby almost no shift and no broadening compared to the peak of the hydrogen-terminated polymer can be observed. This is also expected, since only the end-group is modified, which has a rather low impact on the elution volume.

The synthesized polymers were used to coat commercially available NMC particles by dispersing the particles in a solution of the polymers in chloroform. Unbound polymer could be removed by centrifugation. The amount of coordinated polymer could be determined by thermograviemtric analysis (TGA) and energy dispersive X-ray spectroscopy (EDX). As shown in Figure 15, pure NMC does not show a significant weight loss, whereas the coated particles lose weight. In the case of the block copolymer coating the weight loss is 5 wt.% and for the end-group functionalized polymer coating the weight loss is determined to be 7 wt.%. Thus, the end-group functionalized polymer binds more efficiently to the particle, probably due to steric effects.

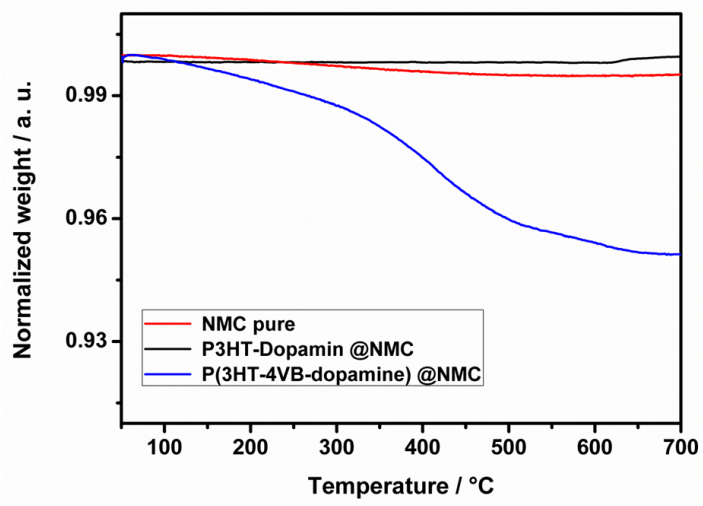

Figure 15: TGA data of pure NMC and polymer coated NMC.

Furthermore, SEM and EDX data conducted for the block copolymer bound to the particles confirms an increased organic content for the polymer coated sample compared to the pure NMC.

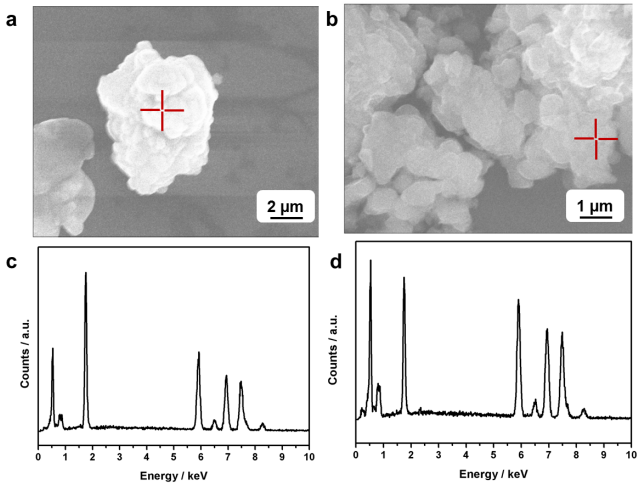

Figure 16: SEM images and EDX data of uncoated NMC (a and c) and polymer coated NMC (b and d).

The carbon content detected for the uncoated particles might either result from the

contaminated wafer or from organic solvent residues on the particle surface. Figure 16 shows SEM images and Table 1 contains the relative amount of the different elements. Compared to the TGA result, the carbon content observed in the EDX data is higher.

Table 1: Elemental composition according to EDX results.

element	**uncoated NMC**	**coated NMC**
C	5.6 wt.%	15.3 wt.%
O	48.9 wt.%	48.2 wt.%
Mn	14.8 wt.%	11.9 wt.%
Ni	15.9 wt.%	12.7 wt.%
Co	14.9 wt.%	11.9 wt.%

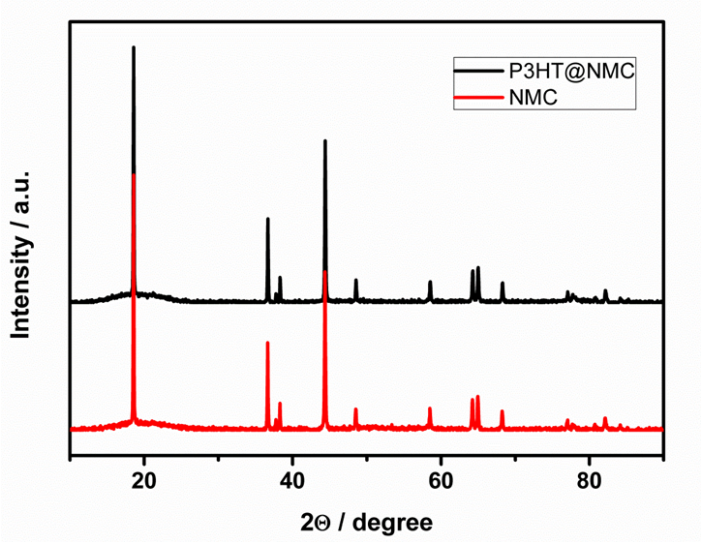

Figure 17: XRD data of coated and uncoated NMC.

Finally, X-ray spectroscopy proves the stability of the crystallinity during the coating process, as there are no changes observed after the coating (see Figure 17).

Electrochemical characterization

As the end-group modified P3HT binds more efficiently onto the NMC particles, the coating approach was up-scaled only for end-group modified P3HT and thus only NMC coated with end-group functionalized P3HT was investigated in lithium-ion batteries. The performance for coated particles was compared to the performance of uncoated particles and results of galvanostatic cycling are shown in Figure 18.

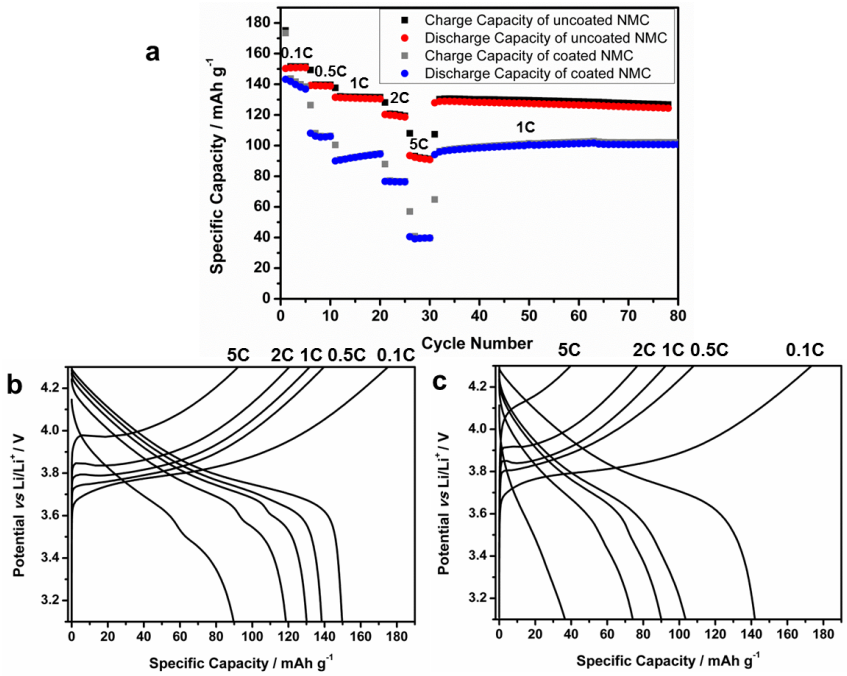

Figure 18: a) Galvanostatic cycling of coated and uncoated particles. Voltage profiles of uncoated (b) and coated particles (c).

A C-rate test was conducted with C-rates in the range of 0.1C to 5C, whereby 1C corresponds to 270 mA g^{-1}. As shown in Figure 18a the performance of uncoated particles is better for all applied C-rates compared to the particles coated with P3HT. Figure 18 b and c show the voltage profiles of coated and uncoated particles. The voltage plateaus at 3.8 V are more pronounced for all C-rates in case of the uncoated NMC compared to the coated NMC. Although it was expected that the electrode with

the conductive polymer coated particles features an increased electronic conductivity enhanced battery performance, this is not the case. Possible reasons, which might cause a worse battery performance for the sample with coating might be that the polymer coating hinders the diffusion of lithium ions. This might increase the resistivity with respect to ionic conductivity. Additionally, it could be possible that the increase of electronic conductivity due to the presence of P3HT contributes less to the overall battery performance than the possibly decreased lithium-ion conductivity.

4.3.3 Experimental

Synthesis of ethynyl and hydrogen end-group functionalized P3HT:
2,5-dibromo-3-hexlthiophene was synthesized as described in the previous chapter.[11] The ethynyl end-group functionalization was conducted as described in literature.[6] Therefore, 2,5-dibromo-3-hexlthiophene (1 eq., 3.0 g, 9.21 mmol) and a solution of tBuMgCl (0.95 eq., 8.75 mmol) were solved in a dried Schlenk flask in 20 ml of dry THF under argon and stirred over night. The solution was diluted with 45 ml of dried THF. Ni(dppp)Cl_2 was added and the reaction mixture was stirred for 11 min.

Ethynyl-terminated P3HT was obtained by the addition of an excess of ethynyl-MgCl (0.3 eq.) solution. The reaction mixture was stirred for further 5 min and then precipitated in methanol. As this product is reported to undergo cyclization reactions.[8] the product was not further purified at this stage. The yield of the product was 56 %.

^{1}H-NMR (chloroform-d1, 400 MHz): δ [ppm] = 6.98 (b, 28H, aromatic thiophene H); 3.53 (s, 1H, ethynyl-H); 2.80 (b, 56H, thiophene-CH_2); 1.22 (b, 56H, thiophene-CH_2-C**H**$_2$); 1.34-1.44 (b, 168H, C**H**$_2$-C**H**$_2$-C**H**$_2$-CH_3); 0.92 (b, 84H, CH_3).

SEC: M_n= 5174 g mol^{-1}, PDI= 1.26

Hydrogen terminated P3HT was obtained by quenching the reaction mixture in methanol/concentrated HCl solution (1:1). The raw product was further purified

by soxhlet extraction. First, the product was extracted with methanol, followed by extraction with hexane and chloroform. The product was isolated from the chloroform phase and was obtained in yields of about 48 %. ^{1}H-NMR (chloroform-d1, 400 MHz): δ [ppm] = 6.98 (b, aromatic thiophene H); 2.80 (b, thiophene-CH_2); 1.22 (b, thiophene-CH_2-C**H**$_2$); 1.34-1.44 (b, C**H**$_2$-C**H**$_2$-C**H**$_2$-CH_3); 0.92 (b, CH_3).

GPC: Mn: 5,367 g mol^{-1}, PDI=1.12

Synthesis of dopamine end-group functionalized P3HT

The formylation of hydrogen terminated P3HT (1eq., 120 mg) was conducted following a reported method by a Vilsmeier reaction.[12] Briefly, P3HT was solved in toluene (30 ml) under argon. DMF (183 eq., 0.36 ml) and $POCl_3$ (107 eq., 0.25 ml) was added. The reaction mixture was stirred for 50 h at 75 °C. After the completion of the reaction an aqueous saturated sodium acetated was added and stirred for further 30 min. Thereafter the reaction mixture was precipitated in methanol and dried under reduced pressure. The product was solved in chloroform and precipitated two more times in methanol. The yield was 87 %.

^{1}H-NMR (chloroform-d1, 400 MHz): δ [ppm] = 10,04 (s,1H, carbonyl-H), 6.98 (b, 28H, aromatic thiophene H), 2.80 (b, 56H, thiophene-CH_2), 1.22 (b, 56H, thiophene-CH_2-C**H**$_2$), 1.34-1.44 (b, 168H, C**H**$_2$-C**H**$_2$-C**H**$_2$-CH_3), 0.92 (b, 84H, CH_3).

IR (FTIR): ν = 2924 (w, CH), 1649 (s, C=O), 1443 (w, aromatic ring), 820 (w) cm^{-1}.

SEC: Mn: 5,236 g mol^{-1}, PDI=1.12

Dopamine was introduced by the aminolysis of the carbonyl group. Therefore, carbonyl terminated P3HT (1 eq., 8 mmol, 38 mg) was solved in dried THF (1 ml) and a solution of dopamine hydrochloride (15 eq., 120 mmol, 21.6 mg), triethylamine (15 eq., 120 mmol, 15 μl 1 ml) in DMF (1 ml) was added. The reaction mixture was stirred at 65 °C over night. The polymer was purified by precipitation in methanol. The yield was 76 %.

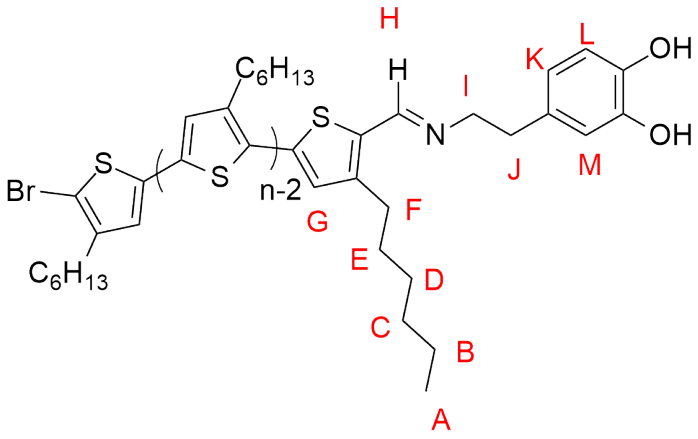

^{1}H-NMR (chloroform-d1, 400 MHz): δ [ppm] =8.22 (s, 1H, H); 6.98 (b,G); 6.80 (d, M, L); 6.64 (d,K); 2.90-2,70 (b,F,I,J); 1.22 (b,E); 1.34-1.44 (bm,B,C,D); 0.92 (b,A).
IR (FTIR): ν = 2924 (CH), 1654 (C=C), 1617 (C=N), 1453 (aromatic ring), 820 cm^{-1}.
SEC: M_n: 4,064 g mol−1, PDI=1.14

Synthesis of CTA terminated P3HT

2-Dodecylsulfanylthiocarbonylsulfanyl-2-methylpropionic acid 3-azidopropyl ester was synthesized according to literature.[13] 2-Dodecylsulfanylthiocarbonylsulfanyl-2-methyl-propionic acid (DMP, 1 eq., 49.3 mmol, 18.0 g), which was already synthesized for one of the pervious projects,[14] was solved in 500 ml dichloromethane under argon. The solution was cooled to 0 °C and oxalylchloride (3 eq. 148 mmol, 12,7 ml), solved in 100 ml of dichloromethane, was slowly added. The reaction mixture was stirred for 3 hours at room temperature. Afterwards, the solvent was removed under reduced pressure and the obtained acid chloride (DMP-Cl) was used without further purification.

A solution of 3-azidopropanol (1 eq., 39.4 mmol, 3.6 ml) and 75 ml of dichloromethane was cooled at 0 °C. A solution of triethylamine (2 eq., 78.8 mmol, 10.9 ml) in 75

ml dichloromethane was added within one hour. DMP-Cl (1 eq., 39.4 mmol, 15.1 g) solved in 95 ml dichloromethane was added within 30 min. The solution was stirred for 3 hours at room temperature. Afterwards the solvent was removed under reduced pressure and the residue was solved in 1 l of diethylether. The solution was washed with 300 ml of $NaHCO_3$-solution, water and brine. The organic phase was dried over $MgSO_4$ and diethylether was removed. The raw product was further purified by column chromatography (silicagel, eluent: cyclohexane(ethylacetate (40:1)). The yield of the product was 83 %.

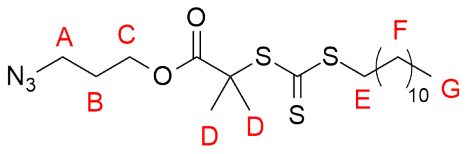

^{1}H-NMR (chloroform-d1, 400 MHz): δ [ppm] = 4.18 (t,2H,C); 3.36 (t,2H,A); 3.27 (t,2H,E); 1.89 (quint,2H,B); 1.69-1.62 (m,6H,D); 1.38-1.25 (m,20H,F); 0.88 (t,3H,G). The CTA was introduced into the P3HT by a Cu-catalyzed [3+2] cycloaddition of ethynyl-terminated P3HT and the azide-CTA following a modified procedure.[15] Therefore, ethynyl-terminated P3HT (1 eq., 0.0625 mmol, 250 mg), the azide modified CTA (20 eq., 1.25 mmol, 559.3 mg), and $[Cu(NCCH_3)_4][PF_6]$ (5 eq., 0.31 mmol, 115.5 mg) were solved in 50 ml chloroform and 2,6-lutidine (100 eq., 6.25 mmol, 725 μl) was added under argon. The solution was stirred for 64 hours at room temperature. The product was precipitated in methanol, centrifuged and dried under vacuum. For the further purification, the polymer was dissolved and precipitated two more times. The yield was about 84 %.

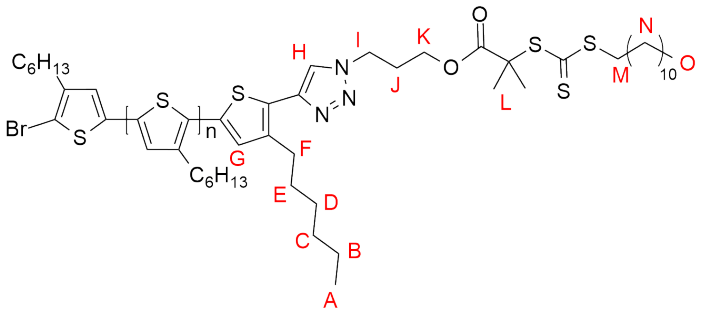

^{1}H-NMR (chloroform-d1, 400 MHz): δ [ppm] = 7.67 (s,1H,H); 6.98 (bm,G); 4.46 (t,2H,I); 4.19 (t,2H,K); 3.72(m,M); 2.80 (b,F); 2.05 (m,J); 1.5-1.0 (bm,B,C,D,E,L,N); 0.92-0.88 (b,A,O).

Synthesis of pentafluorophenyl-4-vinylbenzoate

The reactive ester monomer was synthesized as described previously.[16] 4-Vinylbenzoic acid (1 eq., 22.0 mmol, 3.28 g) and oxalyl chloride (2.2 eq., 48.0 mmol, 6.14 g) were solved in benzol under argon. The solution was refluxed for two hours. The solvent was removed under reduced pressure. The residue was used without further purification. Pentafluorophenol (2 eq., 44.0 mmol, 8.1 g) and triethylamine (2 eq., 44.0 mmol, 2 ml) were solved in 26 ml THF and cooled in an ice bath. 4-Vinylbenzoic acid chloride was solved in 20 ml THF and added slowly to the solution. The resulting reaction mixture was stirred for 12 h at room temperature. THF was removed under reduced pressure. The raw product was purified by column chromatography (silica, eluent: toluene/hexane (1:1)). The yield of the product was 78 %.

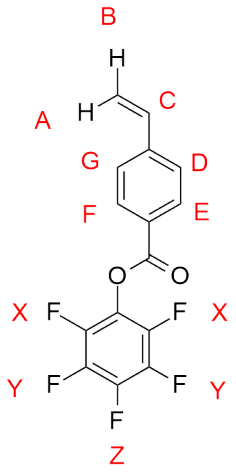

^{1}H-NMR (chloroform-d1, 400 MHz): δ [ppm] =8.16 (d,2H,E,F), 7.56 (d,2H,D,G), 6.80 (dd,1H,C), 5.94 (d,1H,A), 5.48 (d,1H,B). ^{19}F-NMR (chloroform-d1, 400MHz): δ [ppm] = 153,6 (d,2F,X), -159,2 (t,1F,Z), -163,5 (t,2F,Y).

Synthesis of P(3HT-b-PFP4VB)

PFP4VB (25 eq., 0.42 mmol, 231,4 mg), the macro-CTA (1 eq., 0.017 mmol, 75.0 mg), and AIBN (0.2 eq., 0.0017 mmol, 0.28 mg) were solved in 2 ml o-dichlorobenzene and air was exchanged by nitrogen by three freeze-pump-thaw cycles. The reaction mixture was stirred for 48 hours at 70 °C. The reaction was stopped by quenching in methanol and the product was further purified by solving and precipitating two more times.

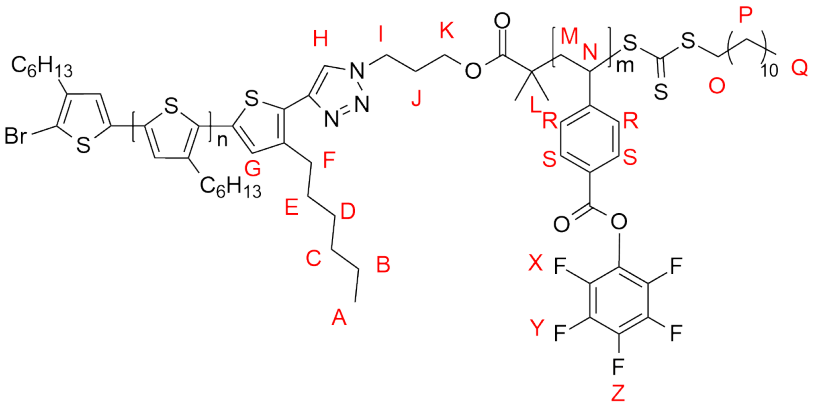

^{1}H-NMR (chloroform-d1, 400 MHz): δ [ppm] = 8.04 (bm,R); 7.67 (s,H); 7.28-

6.83 (bm,G,S); 4.46 (t,I); 4.19 (t,K); 3.72(b,O), 2.80 (b,F); 2.05 (m,J); 1.5-1.0 (bm,B,C,D,E,L,M,N,P); 0.92-0.88 (b,A,Q) ppm.

^{19}F-NMR (chloroform-d1, 400MHz): δ [ppm] = 153,6 (b,X); -159,2 (b,Z); -163,5 (b,Y) ppm.

IR (FTIR): ν = 2925 (CH), 1760 (C=O), 1519 (Ar-F), 1240, 1044 (aromatic band), 1013, 819cm^{-1}.

SEC: 6,193 g mol^{-1}, PDI: 1.31.

Synthesis of P(3HT-b-4VBDA)

P(3HT-b-PFP4VB) (1 eq., 0.0034 mmol, 27 mg) was solved in 1.4 ml THF and a solution of dopamine hydrochloride (20 eq., 0.068 mmol, 12.7 mg) in 0.6 ml DMF was added. Triethylamine (20 eq., 0.068 mmol, 2.4 ml) is added as well. The reaction mixture is stirred at room temperature over night.

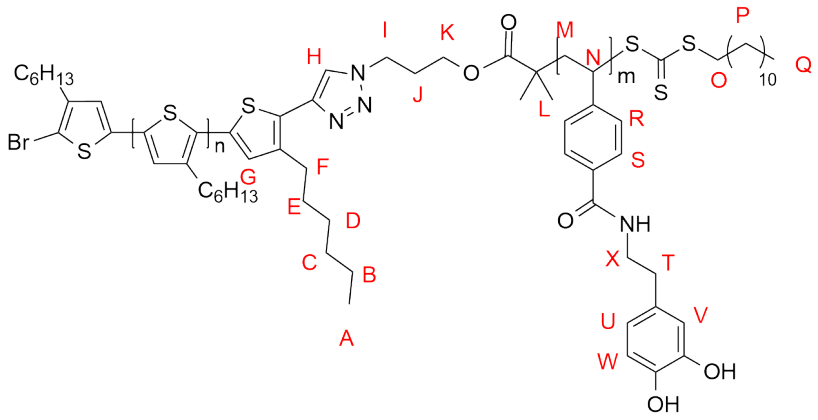

^{1}H-NMR (chloroform-d1, 400 MHz): δ [ppm] =8.04 (bm,R); 7.67 (s,H); 7.28-6.68 (bm,G,R,S,U,V,W); 4.46 (t,I); 4.19 (t,K); 3.72(b,N,X); 2.80 (b,F,T); 2.05 (m,J); 1.5-1.0 (bm,B,C,D,E,L,M,N,P); 0.92-0.88 (b,A,Q) ppm.

IR (FTIR): ν = 3248 (O-H), 1734 (C=O) cm^{-1}.

Coating of inorganic particles

930 mg of NMC particles were dispersed in 1 ml of a polymer solution (64 mg block copolymer or end-group functionalized polymer). The particles were centrifuged

and dried in vacuum.

Electrochemical characterization

Electrodes were prepared as follows: Sodium carboxymethyl cellulose (CMC) was dissolved in water. Then conductive carbon additive (Super C65, IMERYS, Switzerland) was added and stirred for 30 min. polymer coated particles were finally added and dispersed by stirring for additional 30 minutes. The final composition of active material: conductive material: CMC was 88:7:5. The resulting slurry was cast on aluminum foil with a wet film thickness of 150 μm. After drying over night at room temperature, disc electrodes were punched and further dried at 150 °C under vacuum. The active mass loading was in the range of 5.4-5.8 mg cm-2. Pouch cells were assembled under inert conditions in a glove box. Lithium foil was used as a counter electrode. Electrochemical experiments were conducted by means of MACCOR Battery Tester.

References

[1] P. Novák, K. Müller, K. S. V. Santhanam, O. Haas, Chem. Rev. 1997, 97, 207.

[2] M. D. Levi, Y. Gofer, D. Aurbach, Polym. Adv. Technol. 2002, 13, 697.

[3] J. Tang, L. Kong, J. Zhang, L. Zhan, H. Zhan, Y. Zhou, C. Zhan, Reactive and Functional Polymers 2008, 68, 1408.

[4] N. Loeffler, J. von Zamory, N. Laszczynski, I. Doberdo, G.-T. Kim, S. Passerini, Journal of Power Sources 2014, 248, 915.

[5] S. N. Patel, A. E. Javier, N. P. Balsara, ACS Nano 2013, 7, 6056.

[6] M. Jeffries-EL, G. Sauvé, R. D. McCullough, Macromolecules 2005, 38, 10346.

[7] K. Mizushima, P. Jones, P. Wiseman, J. Goodenough, Mater. Res. Bull. 1980, 15, 783.

[8] Z. Li, R. J. Ono, Z.-Q. Wu, C. W. Bielawski, Chem. Commun. 2010, 47, 197.

[9] M. Zorn, S. Meuer, M. N. Tahir, Y. Khalavka, C. Sönnichsen, W. Tremel, R. Zentel, J. Mater. Chem. 2008, 18, 3050.

[10] R. H. Lohwasser, M. Thelakkat, Macromolecules 2011, 44, 3388.

[11] Y. Nie, B. Zhao, P. Tang, P. Jiang, Z. Tian, P. Shen, S. Tan, J. Polym. Sci. A Polym. Chem. 2011, 49, 3604.

[12] M. Surin, O. Coulembier, K. Tran, J. de Winter, P. Leclère, P. Gerbaux, R. Lazzaroni, P. Dubois, Organic Electronics 2010, 11, 767.

[13] S. R. Gondi, A. P. Vogt, B. S. Sumerlin, Macromolecules 2007, 40, 474.

[14] B. Oschmann, D. Bresser, M. N. Tahir, K. Fischer, W. Tremel, S. Passerini, R. Zentel, Macromol. Rapid Commun. 2013, 34, 1693.

[15] W. Weymiens, F. Hartl, M. Lutz, J. C. Slootweg, A. W. Ehlers, J. R. Mulder, K. Lammertsma, Eur. J. Org. Chem. 2012, 2012, 6711.

[16] K. Nilles, P. Theato, European Polymer Journal 2007, 43, 2901.

[17] Y. Nyquist, Bachelorarbeit, Johannes Gutenberg-University, 2014.

[18] J. Kiehl, Bachelorarbeit, Johannes Gutenberg-University, 2014.

4.4 Copolymerization of Sulfur with a Semiconductive Polymer

As discussed in section 2.3.3, lithium-sulfur batteries are highly interesting battery systems due to the high natural abundance, non-toxicity and theoretically high specific capacity of sulfur. However, the electrically insulating property of sulfur and the solubility of the intermediately formed polysulfides are challenging issues and most approaches attempting to solve these problems reported in literature are based on the encapsulation of sulfur in carbonaceous material.

A very different approach termed as “inverse vulcanization” was recently developed by Prof. Char et al. It is based on the radical reaction between molten sulfur and an organic comonomer (1,3-diisopropenylbenzene, DIB) to obtain S-DIB copolymers as shown in the following Figure. The application of these copolymers results in an advanced battery performance compared to pure sulfur as it is proposed that this approach reduces the dissolution of polysulfides.

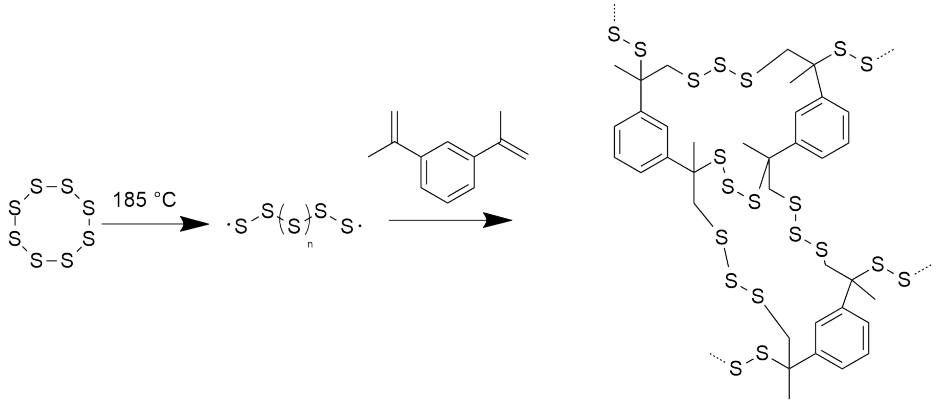

Figure 1: Synthesis of S-DIB copolymers according to Char et al.

However, also DIB is an insulating material and a reasonable battery performance is possible only by the addition of conductive carbon particles. In this chapter, Prof. Char’s idea of a radical copolymerization with molten sulfur is adopted and further developed to the application of a copolymerization approach of sulfur with a semiconductive polymer, in this case poly(3-hexylthiophene-2,5-diyl) (P3HT). This

is motivated by the idea to incorporate a semiconductive material into sulfur. For this purpose, P3HT is synthesized by Girgnard metathesis (GRIM) polymerization and an allyl double bond is incorporated as an end-group. This double bond end-group allows the radical reaction with sulfur, which enables the covalent linkage of sulfur and P3HT. The successful reaction between P3HT and sulfur can be proven by several methods including NMR and Raman spectroscopy, SEC and elemental analysis.

In cooperation with Jungjin Park from Prof. Yung-Eun Sung's group (Seoul National University, SNU, South Korea) this material was evaluated as a cathode material in lithium-sulfur batteries during a research stay at the SNU. In order to investigate the influence of the covalent linkage of P3HT to sulfur the battery performance of S-P3HT copolymers (mixed with conductive carbon particles) was compared to the performance of 2 reference systems, which consist of i) a mixture of sulfur and conductive carbon particles and ii) a physical mixture of P3HT (not covalently linked to sulfur), sulfur and carbon particles. The battery performance of the S-P3HT copolymer containing electrodes show the best performance with respect to C-rate capability and longterm cycling compared to the two reference systems. Electrochemical impedance spectroscopy was conducted for all three samples and proves a reduced charge transfer resistance for the S-P3HT copolymer containing sample. Thus, we can conclude that a covalent incorporation of P3HT into sulfur results in a rather homogeneous distribution of a semiconductive material, which increases the electrical conductivity within the electrode composite and enables an enhanced battery performance.

For this contribution the synthesis and synthetic characterization was conducted by myself, whereas the electrochemical characterization was conducted by Jungjin Park.

4.4.1 Submitted Manuscript

Copolymerization of Polythiophene and Sulfur to Improve Electrochemical Performance in Lithium-Sulfur Batteries

Bernd Oschmann, Jungjin Park, Chunjoong Kim, Kookheon Char, Yung-Eun Sung, and Rudolf Zentel

Abstract

We report on the copolymerization of sulfur and allyl-terminated poly(3-hexylthiophene-2,5-diyl) (P3HT) derived by Grignard metathesis polymerization. This copolymerization is enabled by the conversion of sulfur radicals formed by thermolytic cleavage of S_8 rings with the allyl end-group. The copolymer, especially the formation of the C-S bond, is characterized by a variety of methods, including NMR spectroscopy, size exclusion chromatography and near edge X-ray absorption fine spectroscopy. The S-P3HT copolymer is applied as a cathode material in lithium-sulfur batteries and compared to a simple mixture of sulfur and P3HT not covalently linked to each other. The S-P3HT copolymer exhibits an enhanced battery performance with respect to the cycling performance at 0.5C (799 mAh g^{-1} after 100 cycles for S-P3HT copolymer and only 544 mAh g^{-1} for the simple mixture) and with respect to the C-rate performance. This is related to the increased electrical conductivity (proven by electrochemical impedance spectroscopy) due to the homogeneous incorporation of P3HT into sulfur by covalently linking sulfur and P3HT.

Currently, Li-ion rechargeable batteries are considered promising energy storage devices to tackle problems related to the use of renewable energy instead of fossil fuels.[1] However, Li-ion batteries that commonly contain graphite as an anode and lithium cobalt oxide as a cathode material are limited with regard to the specific capacity and energy density. In addition, cobalt containing materials are neither economically nor environmentally friendly. To meet the extensively growing demand of high energy storage devices for electric vehicles, energy storage system (ESS), and artificially bio-medical equipment, the substitution of the currently used electrode materials will be necessary in a timely manner. The lithium sulfur battery with a theoretical specific energy more than six times higher than the current Li-ion battery is one of the most promising candidates to solve these issues, additionally, as sulfur is a very abundant, cheap and non-harmful material.[2–4]

However, lithium-sulfur batteries still suffer from several issues, including the insulating nature of sulfur, the volume expansion during cycling and the unique reaction processes (dissolution/precipitation of active material) during (de-)lithiation. This and the so called ”shuttle” mechanism[2,5,6] causes capacity decay by irreversible loss of reaction species and/or sites. So far, several approaches were tried to increase the electrical conductivity and prevent the loss of the soluble polysulfides. This includes the use of conductive polymer coating or the encapsulation of sulfur with various carbonaceous materials such as mesoporous carbon, hollow carbon particles, carbon nanotubes, and graphene based materials, which possibly interact with the polysulfides.[7–16] Recently, an experimentally simple approach based on the so-called inverse vulcanization has been introduced. It uses 1,3-diisopropenylbenzene (DIB) for a radical copolymerization with a molten sulfur radical species resulting in polymeric sulfur materials, which exhibited an improved battery performance compared to pure sulfur.[17,18] The extension of this approach to a tandem inverse vulcanization resulted in an electropolymerization derived polythiophene incorporated in a sulfur-DIB copolymer with a reduced charge transfer resistance.[19] However,

the detailed study about the structure and chain length of the resulting oligo- or polythiophenes is not yet reported. Furthermore, this composite material contains a relatively low sulfur loading (50 wt.% after inverse vulcanization), which limits its capacity.

Herein, we are firstly introducing the copolymerization of well-defined allyl-terminated poly(3-hexylthiophene-2,5-diyl) (P3HT) synthesized by Grignard metathesis polymerization with an excess of molten sulfur radicals resulting in the S-P3HT composite, where P3HT copolymers are embedded in a sulfur matrix. This S-P3HT allows the homogeneous incorporation of a well-defined semi-conductive material into sulfur as well as the formation of a stable framework. In this communication, the detailed structure of the S-P3HT composite was studied by various analytical tools, which confirmed the covalent linking between sulfur and P3HT in the composite. The covalent linkage led to the enhanced battery performance by effective stabilization of the electrodes during the battery operation. This work clearly demonstrates that a homogeneous composite of P3HT and sulfur can be synthesized and assembled into the electrodes for high performance Li-S batteries.

The synthetic approach to obtain the S-P3HT copolymers is shown in Figure 1. First, the conductive polymer used for the covalent incorporation into sulfur is synthesized by GRIM polymerization technique (see Figure 1a). This synthesis route allows the controlled synthesis of allyl-terminated P3HT. The monomer precursor 2,5-dibromo-3-hexlthiophene synthesized by bromination of the 3-hexylthiophene with N-bromosuccinimide[20] is first treated with tert butylmagnesium bromide (tBuMgCl) resulting in the Grignard metathesis products with the magnesium species mainly incorporated on position 5 of the thiophene.[21,22] The reactive monomer is polymerized by the addition of [1,3-bis(diphenylphosphino)propane]dichloronickel(II) (Ni(dppp)Cl_2) as a catalyst.[21] The polymer end-group functionalization is achieved by quenching the polymerization with a second Grignard reagent, in this case with a solution of allylmagnesiumbromide.[23,24]

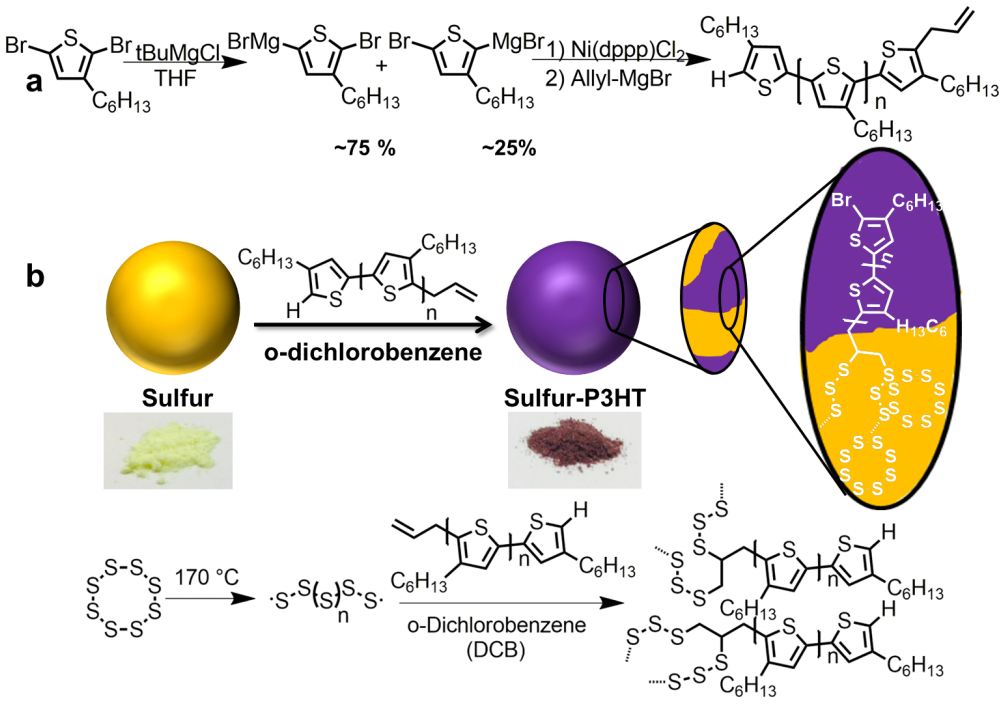

Figure 1: a) Synthesis of allyl-terminated P3HT applying GRIM polymerization. b) Copolymerization of allyl-terminated P3HT and sulfur.

In this case, the allyl group first coordinates to the nickel catalyst and finally terminates the polymer by a reductive elimination reaction.[24] Applying matrix assisted laser desorption/ionization time of flight mass spectroscopy (MALDI-TOF-MS) proves the successful incorporation of the allyl end-group, as the detected main peaks can be attributed to P3HT terminated with one H- and one allyl end-group as shown in Figure 2a. Besides the main peak a rather small peak can be identified as a Br/allyl terminated P3HT. ^{1}H-NMR spectroscopy further confirms the presence of the allyl end-group, as the typical allyl bands can be observed besides the typical broad peaks corresponding to the P3HT backbone and hexyl side-chains as demonstrated in Figure 2b.The integration of the end-group signals and comparison with the backbone signal of the polymer at 6.99 ppm allows a rough estimation of the polymer chain length and the average number of repeating units is determined to be

around 30 assuming that all polymers are terminated with one allyl end-group (see Figure S1).

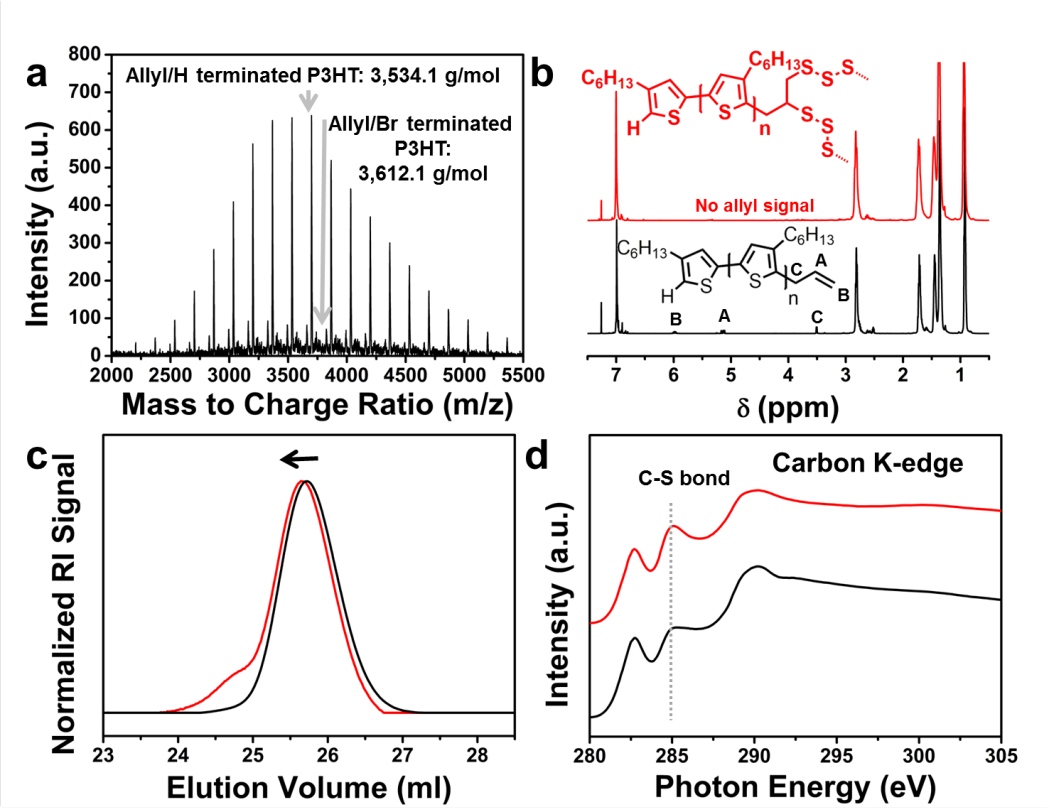

Figure 2: MALDI-TOF spectrum of allyl-terminated P3HT. NMR spectra (b), SEC elugram (c) and near edge X-ray absorption fine spectra (NEXAFS) (d) of allyl-terminated P3HT (black) and S-P3HT copolymer (red).

Heteronuclear single quantum coherence (HSQC) NMR spectroscopy was conducted for the allyl-terminated polymer. As shown in Figure S2 the C/H couplings of the allyl end-group can be clearly identified.

According to size exclusion chromatography (SEC, Figure 2c) the polymer is rather monodispersed with a polydispersity of 1.08. The molecular weight obtained by SEC is calculated to be of 9,450 g $mol^{-1}$and is significantly higher compared to the value calculated by NMR spectroscopy (5,022 g mol^{-1}). This is due to the stiff nature of

P3HT, which leads to an overestimation of the molecular weight compared to the flexible polystyrene used for calibration of the SEC system.

The allyl end-group of the P3HT enables the reaction with sulfur radicals formed at elevated temperatures, which allows the covalent linkage of P3HT and sulfur (see Figure 1b). As the modified P3HT possesses only one allyl group, this reaction creates linear (soluble) polymers in which either a sulfur cycle is linked to the P3HT or several P3HT units are linked by sulfur bridges. As P3HT is not soluble in molten sulfur, small amounts of o-dichlorobenzene are added as a solvent. The ratio between sulfur and P3HT was chosen to be S:P3HT of 9:1. The mixture was heated to 170 °C for the homolytic cleavage of the S_8 ring to produce the sulfur radical species to initiate the reaction.

After the completion of the reaction (1 hour), which was determined by ^{1}H-NMR spectroscopy due to the disappearance of the allyl double bond as shown in Figure 2b, the reaction mixture was quenched in methanol to precipitate the modified polymer whole composite. NMR spectroscopy further shows the presence of all previously observed aromatic backbone and aliphatic side chain signals of P3HT confirming that no (significant) side reaction with the aromatic thiophene rings or aliphatic side chain occurs. Furthermore, the observed coupling signals of the allyl end-group disappear in the HSQC spectrum in case of the S-P3HT copolymer and instead two new coupling signals can be observed at 2.30/33.0 ppm and at 2.03/27.2 ppm (Figure S3), which fit to newly formed RCH_2-S and RR'CH-S groups. The SEC data shown in Figure 2c of the S-P3HT copolymer shows a shift to a lower elution volume compared to the allyl-terminated P3HT. This shift can be explained with the covalent linking of sulfur to the polymer, which increases the hydrodynamic radius of the polymer and lowers the elution volume. A shoulder at lower elution volumes, i.e. at higher molecular weight, can be observed, which might be either attributed to the connection of longer sulfur chains to the polymer or to the connection of P3HT polymer chains by sulfur bridges. However, the polydispersity of 1.13 is still rather

low. To quantify the amount of incorporated sulfur within the S-P3HT copolymer, the excess sulfur was removed by preparative SEC. After the successful separation of the S-P3HT copolymer from the sulfur, elemental analysis was applied to allyl-terminated P3HT and compared to the S-P3HT copolymer. The copolymer has an increased sulfur content of about 5.3 wt.% compared to the allyl-terminated P3HT corresponding to the addition of eight sulfur atoms in average per polymer chain due to the occurring radical reaction between the double bond and sulfur radicals.
Soft X-ray absorption spectroscopy (XAS) was also studied since XAS is a powerful tool for probing chemical bonding in the materials. Figure 2d represents the carbon K-edge absorption spectra for both a S-P3HT copolymer containing electrode and for an electrode containing a mixture of P3HT and sulfur not covalently linked with each other. The absorption features around 283 eV and 290 eV are observed in the both samples. They are attributed to the π^* and σ^* state, respectively. Interestingly, the peak at 285 eV results from C-S bonding nature and is significantly enhanced in the S-P3HT copolymer sample. This indicates an enhanced chemical interaction between S and the carbon of P3HT, as during the copolymerization new C-S bonds are formed. Raman spectroscopy was also performed to identify the C-S bonds in S-P3HT composite. Raman spectrum shown in Figure S4 the typical bands of P3HT can be observed for the as-synthesized allyl-terminated P3HT. For S-P3HT, an additional band at 677 cm^{-1} can be observed, which can be attributed to the formation of new C-S bonds.
Thermogravimetric analysis (TGA) of the composite (containing both excess sulfur and the S-P3HT copolymer) was conducted under nitrogen atmosphere. The detected weight loss at 280 °C (see Figure S5) is attributed to the evaporation of sulfur and is in a good agreement with the amount of sulfur added for the synthesis, as it is 86 wt.%. Generally, it is also possible to vary the ratio between sulfur and P3HT during the copolymerization and exemplarily further ratios between S and P3HT were chosen, such as S:P3HT 9.5:0.5 and S:P3HT 8:2 (see foto in Figure S5). The weight

loss detected by TGA is in these cases 93 wt.% and 79 wt.% respectively (Figure S4). In order to investigate the effect of the covalent linkage of P3HT to sulfur on the battery performance, three different electrodes were applied as a cathode material: i) Sulfur, ii) sulfur and P3HT mixture (S/P3HT), and iii) S-P3HT were thoroughly mixed with carbon black to prepare the cathode electrode and each can be abbreviated as S/CB, S/P3HT/CB, and S-P3HT/CB, respectively. In all electrodes, the amount of the conductive material, i.e. the sum of carbon black and P3HT, was set to be 25 wt.%. As shown in Figure 3a, initial specific capacities of S/CB, S/P3HT/CB, and S-P3HT/CB are 1260 mAh g^{-1}, 1154 mAh g^{-1}, and 1212 mAh g-1 at 0.5C (1C is defined as 1675 mA g^{-1}), respectively. Slightly higher initial capacity of S/CB can be achieved due to the higher electrical conductivity of CB than P3HT. However, as cycles go on, S-P3HT/CB exhibits a superior cycling performance compared with S/CB and S/P3HT/CB. S/CB and S/P3HT/CB electrodes show a rapid drop of capacity within the first 20 cycles to 696 mAh g^{-1} and 754 mAh g^{-1}, respectively. In contrast, the capacity of S-P3HT/CB is 877 mA g^{-1} after 20 cycles and preserved with very little decay upon further cycling. The capacity of S-P3HT/CB is, however, still conserved after 100 cycles with 799 mAh g^{-1} compared to 482 mAh g^{-1} (S/CB) and 544.70 mAh g^{-1} (S/P3HT/CB).

In case of S-P3HT, P3HT is homogeneously incorporated into the sulfur particles as shown in scanning electron microscopy (SEM) images (see Figure S6), and XRD data (Figure S7). As sulfur and P3HT by themself are not miscible, we assume that P3HT decorated with sulfur chains acts as a polymeric surfactant, which forms nm sized phase separated structures of P3HT within the sulfur (as schematically shown in Figure 1 b). It seems that homogeneous incorporation of P3HT into sulfur and corresponding strong interaction between them can stabilize the electrode against irreversible loss of polysulfides during the repeated cycles. The capacity retention can be even slightly increased by increasing the amount of P3HT used during copolymerization as shown in Figure S10, where a capacity of 838 mAh g^{-1} can be obtained

for a sample synthesized with a weight ratio S:P3HT 8:2 after 100 cycles. Figure 3b displays the charge/discharge profiles after 10 cycles, which can provide information about the overpotential of each sample, whereby the overpotential can be obtained from the potential difference of the discharge and charge plateau (see indicated blue colored arrow compared to green and red colored arrow in Figure 3b).

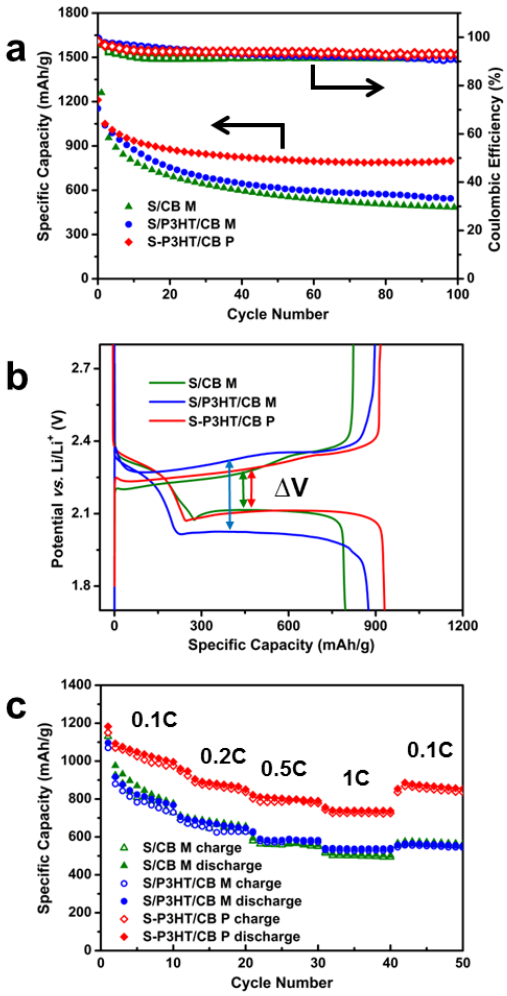

Figure 3: a) Cycling performance, b) potential profiles and C-rate performance of S/CB M (green), S/P3HT/CB M (blue) and S-P3HT/CB P (red).

While S/P3HT/CB exhibits serious increase of overpotential, the S-P3HT/CB electrode shows a similar overpotential to S/CB. The similar overpotential from S-P3HT/CB

and S/CB can be understood that lower conductivity of P3HT than CB can be compensated by easily accessible reaction sites as the homogeneous incorporation of P3HT was introduced into the S-P3HT composite at the nanoscale dimension. Electrochemical impedance spectroscopy (EIS) data also confirms the charge transfer kinetics among the electrodes as shown in Figure S6. The semicircle on the Z_{re} axis corresponding to the charge transfer resistance is the smallest for S/P3HT/CB, whereas the semicircle of S/P3HT/CB is significantly larger.

Furthermore, the S-P3HT/CB electrode exhibits an improved C-rate capability as shown in Figure 3c. Significantly higher specific capacities can be obtained for all applied currents in the case of S-P3HT/CB. 739.41 mAh g^{-1} at 1C was obtained in the S-P3HT/CB whereas S/P3HT/CB and S/CB electrodes revealed lower capacities of 527 mAh g^{-1} and 501 mAh g^{-1}, respectively. The structural integrity at the nanoscale of S-P3HT/CB accounts for the enhanced rate capability by shortened diffusion length of reactant.

In summary, we introduced the copolymerization of allyl-terminated P3HT with sulfur enabled by a radical reaction between the allyl end-group and a radical sulfur species. This approach allows the covalent linkage of sulfur and P3HT yielding in S-P3HT copolymer homogeneously distributed in a sulfur matrix. The homogeneous incorporation of this semiconducting polymer lowers the electrical resistance, thus, an improved battery performance can be observed for S-P3HT copolymer containing electrodes.

Supporting Information

Experimental

Reagents:

Tert. butylmagnesium bromide (tBuMgCl, 1.0 M in THF), allylmagnesium chloride (2.0 M in THF), [1,3-Bis(diphenylphosphino)propane]dichloronickel(II) (Ni(dppp)Cl_2), N-bromosuccinimide (NBS, 99 %), and o-dichlorobenzene (DCB, 99 %) were pur-

chased from Sigma Aldrich, 3-hexylthiophene was purchased from TCI. NBS was recrystallized from water. All solvents were dried before use.Polyvinylidene fluoride (PVDF) binder (Sigma Aldrich),Conductive carbon (Super C65, Timcal), Lithium bis(trifluoromethane)sulfonimide (Sigma Aldrich), Lithium nitrate (Sigma Aldrich), Polypropylene separator (Celgard), Lithium foil (FMC), 1,3-Dioxolane (Novolyte) and 1,2-Dimethoxy ethane (Novolyte) were used as received.

Synthesis of allyl-terminated P3HT:

The monomer 2,5-dibromo-3-hexlthiophene was synthesized according to literature.1 Briefly, NBS (18.25 g, 98,7 mmol) was solved in DMF and added to a solution of 3-hexylthiophene (8.00 g, 47.7 mmol) in chloroform. The reaction was stirred under argon over night at 60 °C. The reaction mixture was purified first by extracting with diethyl ether and then by column chromatography (petrolether; Rf of the product: 0.8). The yield of the colorless product was 71 %.

^{1}H NMR (400 MHz, $CDCl_3$, δ): 6.80 (s, 1H), 2.53 (t, J= 8.0 Hz, 2H), 1.57 (m, 1H), 1.34 (m, 6H), 0.92 (m, 3H) ppm.

The polymerization was conducted following a previous description.2 2,5-dibromo-3-hexlthiophene (600 mg, 1,84 mmol), 4.2 ml THF and tBuMgCl (1.75 mmol) were stirred under argon for 20 h at room temperature. Afterwards the reaction mixture was diluted with 9 ml of THF and 25.6 mg of Ni(dppp)Cl_2 (0.05 mmol) was added to start the polymerization, whereby the reaction mixture turns from slightly yellow to red. Allylmagnesium chloride (1.5 mmol) was added after 10 minutes and the reaction mixture was stirred for further 5 minutes. The polymer was precipitated in methanol. After centrifugation and drying, the polymer was purified by soxhlet extraction using first methanol, then hexane and finally chloroform. Typically, the yield is around 50 %.

^{1}H NMR (400 MHz, $CDCl_3$, δ): 7.01 (s, 31 H), 6.00 (m, 1H), 5.16 (m, 2H), 3.54 (d,J= 4.0 Hz 2H), 2.84 (bs, 62H), 1.74 (bs, 63H), 1.45-1.29 (bm, 192 H), 0.95 (bs,

96 H) ppm.

^{13}C NMR (400 MHz, $CDCl_3$, δ): 140.0, 133.8, 136.5 (end-group), 130.6, 128.7, 116.3 (end-group), 32.3 (end-group), 31.9, 30.7, 29.6, 29.4, 22.8, 14.2 ppm.

SEC: M_n(P3HT)= 9,450 g mol^{-1}, PDI: 1.08.

Elemental analysis: Calculated for allyl-terminated P3HT:C: 72.29, H: 9.43, S: 19.28; found: C: 71.86, H: 10.47, S: 17.67.

Synthesis of S-P3HT:

Allyl-terminated P3HT was dissolved in DCB and added to an excess of sulfur, whereby the weight ratio between S and P3HT was varied between S: P3HT of 9.5:0.5, 9:1, 8:2. The reaction mixture was stirred for 1 h at 170 °C. After the complete conversion as detected by NMR, the reaction mixture was quenched in methanol. After centrifugation the product was dried under reduced pressure. The product can be obtained almost quantitatively.

^{1}H NMR (400 MHz, $CDCl_3$, δ): 6.98 (s, 31 H), 3.2-3.8 (m), 2.80 (s, 62H), 1.74 (s, 63H), 1.45-1.20 (m, 192 H), 0.95 (s, 96H) ppm.

^{13}C NMR (400 MHz, $CDCl_3$, δ): 140.0, 133.8, 130.6, 128.7, 120.0 (end-group) 31.9, 30.7, 29.6, 29.4, 29.1 (end-group), 22.8, 14.2 ppm.

SEC: M_n(S-P3HT)= 10,300 g mol^{-1}, PDI: 1.13

Elemental analysis: Found: C: 67.59, H: 9.43, S: 22.98.

Electrochemical characterization:

S-P3HT copolymer containing compositions(S-P3HT/CB P) were mixed with the binder (polyethylene) and conductive carbon (Super P) so that the mixture ratio was fixed to S:(P3HT+conductive carbon):polyethylene=70:25:5. The S-P3HT mixtures were ball milled for 30 minutes to pulverize and homogenize particles and then mixed with binder and carbon. Chloroform (2 ml) was added as a solvent. The slurry was casted on aluminum foil by doctor blading method and dried underair.

The sulfur loading was commonly around 1 mg/cm^2. The reference electrodes containing S/P3HT/CB M and S/CB M respectively were prepared in the same way with the same composition (i.e. S:(P3HT+conductive carbon):polyethylene=70:25:5) and the sulfur loading was commonly around 1 mg/cm^2 as well. The prepared electrodes were used to assemble CR2032 coin cells in an argon filled glove box. The polypropylene separator was supported by SK innovation corp. The electrolyte composition was 1.0 M lithium bis(trifluoromethane)sulfonamide (LiTFSI), and 0.1 M lithium nitrate in a 1:1 (v/v) mixture of 1,3-dioxolane and 1,2-dimethoxy ethane (Panax Etec, Korea).

The evaluation of the electrochemical performance was conducted by the use of a WBCS3000 battery tester (Won-A Tech, Korea) in avoltage range from 1.7 to 2.8 V vs. Li^+/Li. Electrochemical impedance spectroscopy (EIS) measured at the charged state and the frequency range was fixed to 100 kHz to 10 mHz at the open circuit voltage (OCV). The AC amplitude was set to be 10 mV. Cyclic voltammetry wasconductedat various scan rates (from 41 μV to 2,080 μV) and for each scan rate 5 cycles were operated, whereby only the 5th cycles are shown in Figure 3.

Acknowledgements

B.O. would like to thank the graduate school MAINZ and is recipient of the fellowship through the Excellence Initiative (DFG/GSC 266). This work was supported by Project Code. (IBS-R006-G1) and the IRTG 1404 jointly funded by DFG and NRF. The authors want to thank Erik Kersten for synthetic preliminary work for this project.

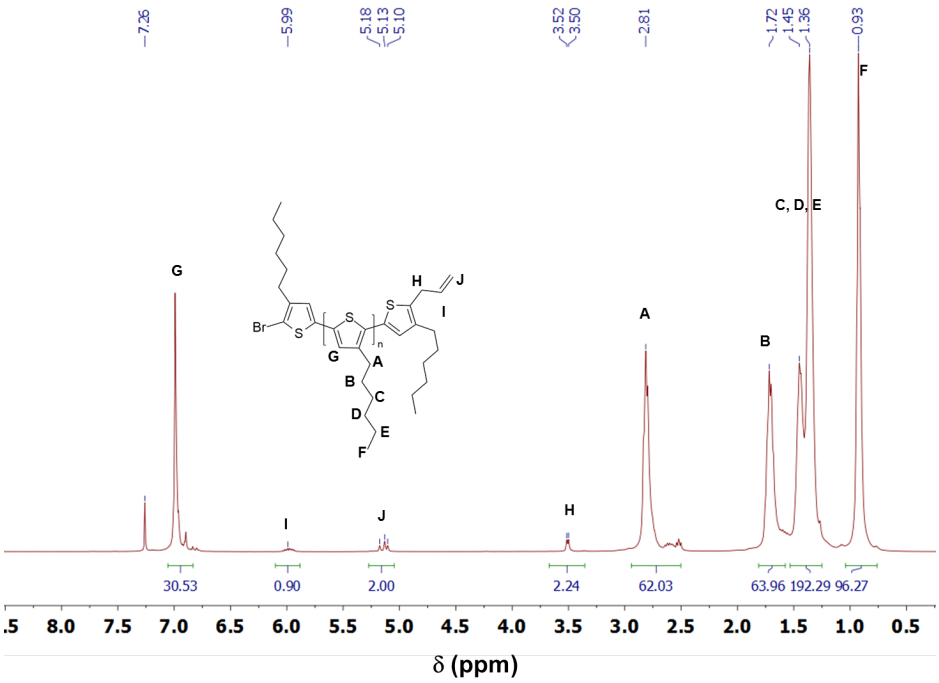

Figure S 1: ^{1}H-NMR spectrum of allyl-terminated P3HT.

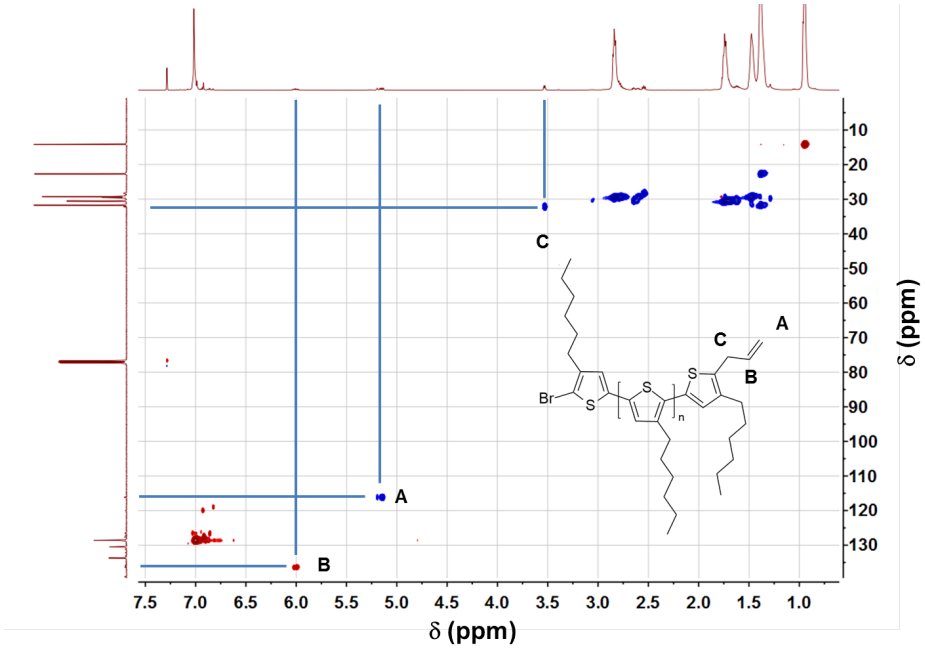

Figure S 2: Heteronuclear single quantum coherence (HSQC) spectrum of allyl-terminated P3HT.

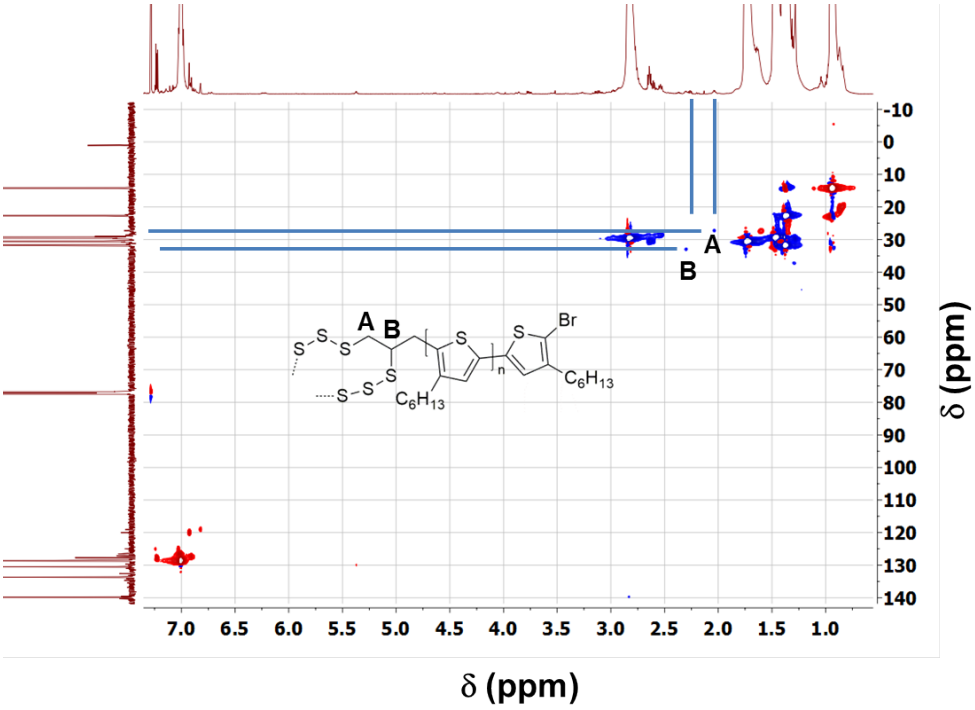

Figure S 3: Heteronuclear single quantum coherence (HSQC) spectrum of S-P3HT.

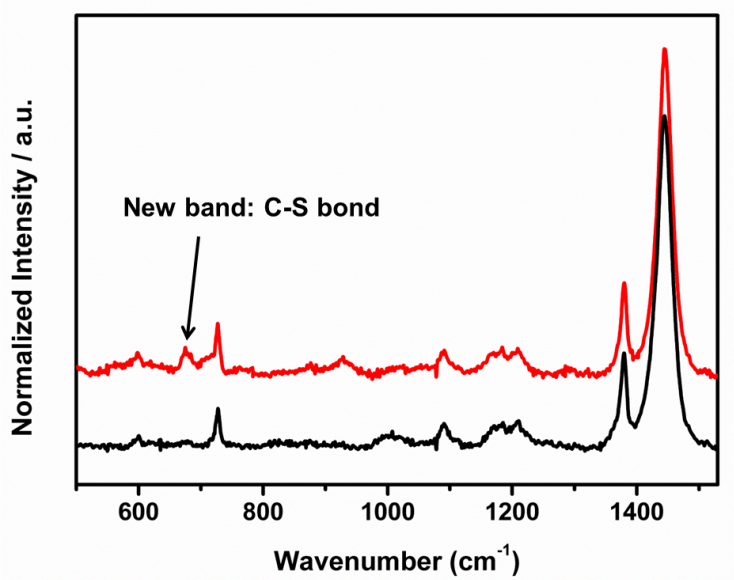

Figure S 4: Raman spectrum of S-P3HT copolymer (red) and allyl-terminated P3HT (black).

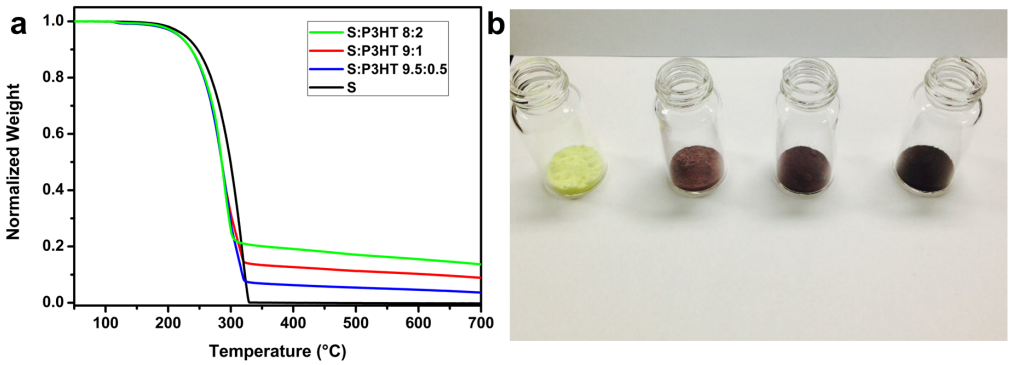

Figure S 5: a) Thermogravimetric analysis of S:P3HT 8:2 (green), S:P3HT 9:1 (red), S:P3HT 9.5:0.5 (blue) and pure sulfur (black). B) Foto of samples with different P3HT content: from left to right: S, S:P3HT 9.5:0.5, S:P3HT 9:1, S:P3HT 8:2.

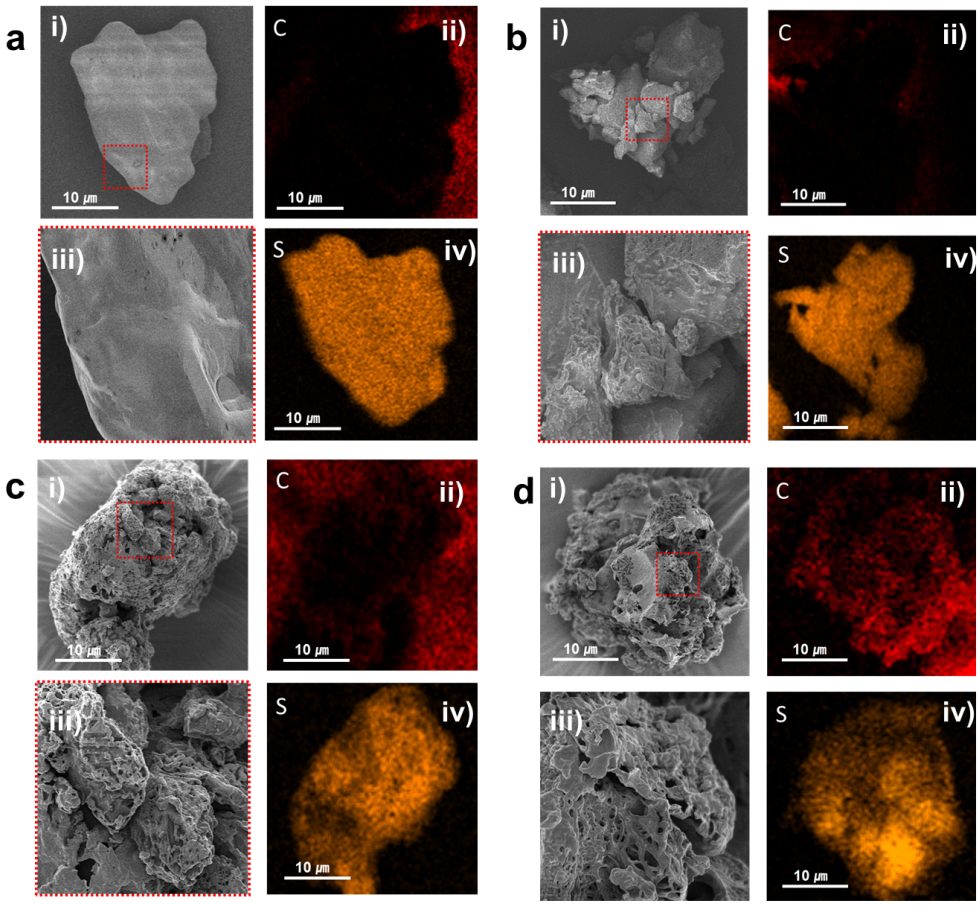

Figure S 6: Scanning electron micrsocopy image and energy dispersive X-ray spectroscopy analysis of sulfur (a), S-P3HT (9.5:0.5) (b), S-P3HT (9:1) (c), and S-P3HT (8:2) (d) showing SEM images with low(i) and high (iii) resolution and corresponding elemental mapping of S (ii) and C of SEM image in i) showing an increasing homogeneously C content and decreasing S content with an increasing P3HT content.

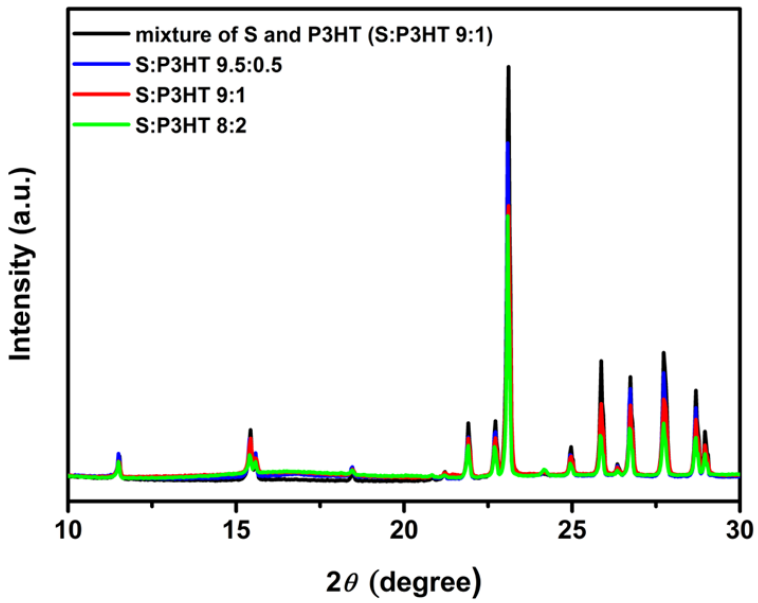

Figure S 7: XRD patterns for a mixture of S and P3HT as well as for composites containing different ratios of S and P3HT applied during synthesis proving an decreased intensity for incorporated P3HT with increasing P3HT content due to covalent linkage and homogeneous incorporation.

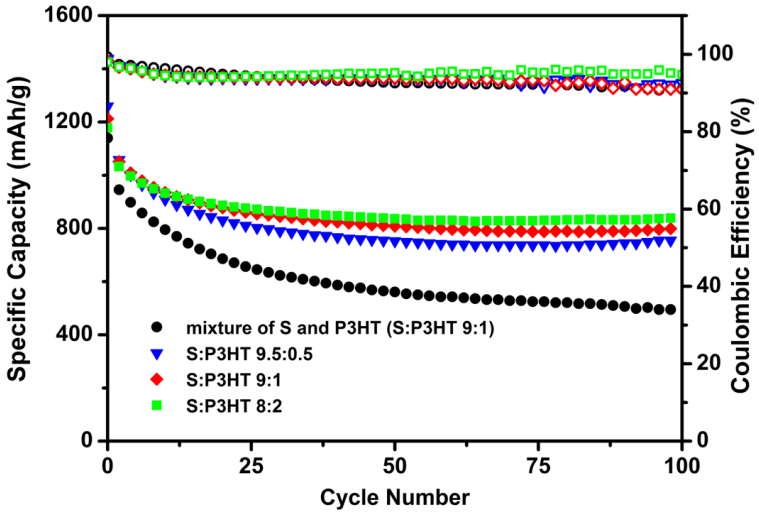

Figure S 8: Galvanostatic cycling of different S-P3HT copolymer containing compositions and comparison to physically mixed S and P3HT.

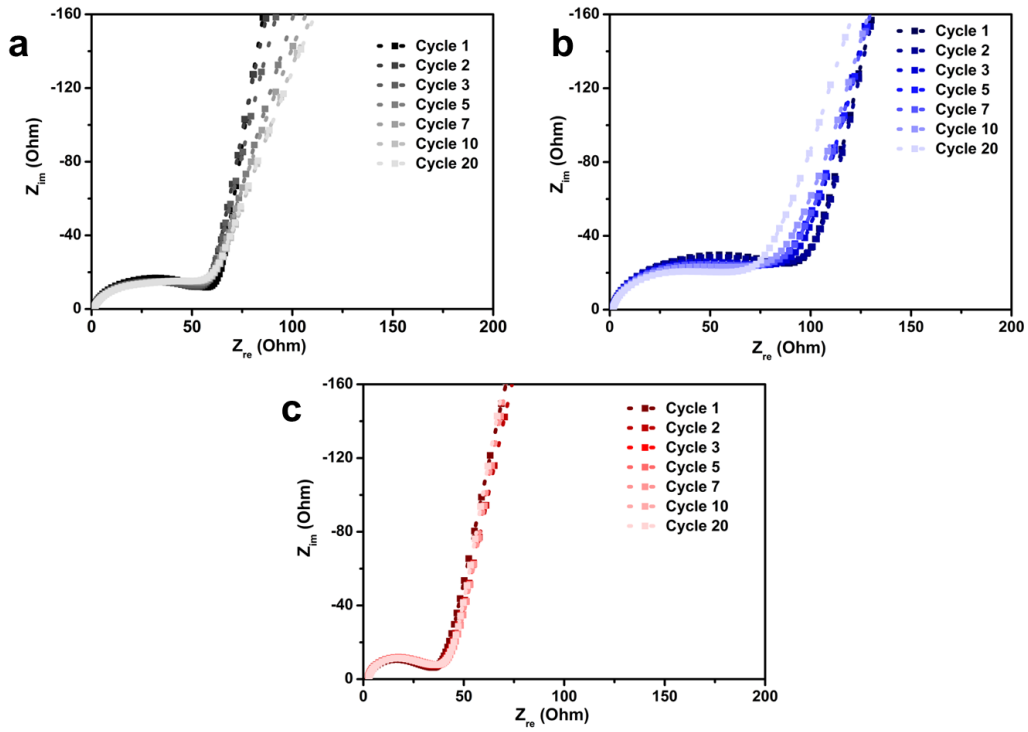

Figure S 9: Electrochemical impedance spectroscopy of selected cycles of S/P3HT/CB (a), of S/CB M based electrodes (b), and of S-P3HT/CB (c).

References

[1] M. Armand, J.-M. Tarascon, Nature 2008, 451, 652.

[2] D. Bresser, S. Passerini, B. Scrosati, Chem. Commun. 2013, 49, 10545.

[3] S. Evers, L. F. Nazar, Acc. Chem. Res. 2013, 46, 1135.

[4] P. G. Bruce, S. A. Freunberger, L. J. Hardwick, J.-M. Tarascon, Nat Mater 2011, 11, 19.

[5] Y. V. Mikhaylik, J. R. Akridge, J. Electrochem. Soc. 2004, 151, 1969.

[6] A. Manthiram, Y. Fu, Y.-S. Su, Acc. Chem. Res. 2013, 46, 1125.

[7] Y. Yang, G. Yu, J. J. Cha, H. Wu, M. Vosgueritchian, Y. Yao, Z. Bao, Y. Cui, ACS Nano 2011, 5, 9187.

[8] J. Wang, J. Yang, J. Xie, N. Xu, Adv. Mater. 2002, 14, 963.

[9] F. Wu, J. Chen, R. Chen, S. Wu, L. Li, S. Chen, T. Zhao, J. Phys. Chem. C 2011, 115, 6057.

[10] G. He, X. Ji, L. Nazar, Energy Environ. Sci. 2011, 4, 2878.

[11] X. Ji, K. T. Lee, L. F. Nazar, Nat Mater 2009, 8, 500.

[12] G. Zheng, Y. Yang, J. J. Cha, S. S. Hong, Y. Cui, Nano Lett. 2011, 11, 4462.

[13] Y. Cao, X. Li, I. A. Aksay, J. Lemmon, Z. Nie, Z. Yang, J. Liu, Phys. Chem. Chem. Phys. 2011, 13, 7660.

[14] S. Evers, L. F. Nazar, Chem. Commun. 2012, 48, 1233.

[15] J.-Z. Wang, L. Lu, M. Choucair, J. A. Stride, X. Xu, H.-K. Liu, J. Power Sources 2011, 196, 7030.

[16] L. Ma, H. Zhuang, Y. Lu, S. S. Moganty, R. G. Hennig, L. A. Archer, Adv. Energy Mater. 2014.

[17] W. J. Chung, J. J. Griebel, E. T. Kim, H. Yoon, A. G. Simmonds, H. J. Ji, P. T. Dirlam, R. S. Glass, J. J. Wie, N. A.

Nguyen, B. W. Guralnick, J. Park, Á. Somogyi, P. Theato, M. E. Mackay, Y.-E. Sung, K. Char, J. Pyun, Nature Chem 2013, 5, 518.

[18] A. G. Simmonds, J. J. Griebel, J. Park, K. R. Kim, W. J. Chung, V. P. Oleshko, J.

Kim, E. T. Kim, R. S. Glass, C. L. Soles, Y.-E. Sung, K. Char, J. Pyun, ACS Macro Lett. 2014.

[19] P. T. Dirlam, A. G. Simmonds, R. C. Shallcross, K. J. Arrington, W. J. Chung, J. J. Griebel, L. J. Hill, R. S. Glass, K. Char, J. Pyun, ACS Macro Lett. 2015.

[20] Y. Nie, B. Zhao, P. Tang, P. Jiang, Z. Tian, P. Shen, S. Tan, J. Polym. Sci. A Polym. Chem. 2011, 49, 3604.

[21] R. S. Loewe, S. M. Khersonsky, R. D. McCullough, Adv. Mater. 1999, 11, 250.

[22] R. S. Loewe, P. C. Ewbank, J. Liu, L. Zhai, R. D. McCullough, Macromolecules 2001, 34, 4324.

[23] M. Jeffries-EL, G. Sauvé, R. D. McCullough, Adv. Mater. 2004, 16, 1017.

[24] M. Jeffries-EL, G. Sauvé, R. D. McCullough, Macromolecules 2005, 38, 10346.

5 Summary

In this dissertation, approaches were developed to increase the conductivity in alternative inorganic electrode materials for lithium-ion batteries by hybridizing organic material with inorganic material. The work includes different aspects from inorganic side, i.e. a broad variety of different inorganic materials ranging from oxides, sulfides to pure sulfur in advanced morphologies (tubes, multipods, sponges) and different aspects from organic side, namely the reasonable adjustment of the organic counterpart for the hybridization for the corresponding inorganic material. The third aspect is the electrochemical characterization of alternative active material (anode and cathode) with different electrochemical reaction behavior (insertion material, conversion-alloying material, conversion material). In order to overcome the issues of inorganic active materials (low electrical conductivity and volume changes during cycling) four different hybridization approaches were developed and adjusted to different inorganic materials.

For the first approach, block copolymers and statistical copolymers were synthesized by RAFT polymerization and coated onto a variety of inorganic nanoparticles with advanced morphologies. The copolymers consist of anchoring units and well-graphitizable repeating units, in this case polyacrylonitrile. The anchoring unit could be adjusted to several inorganic nanoparticles with different coordination chemistry. Thus, dopamine, thiol and hydroxamic acid were used as anchors for oxides (TiO_2 in different morphologies, Au@ZnO multipods, SnO_x sponge-like structures) and polyethyleneglycol, polyvinylpyrrolidone and sulfonates were used as anchors for sulfide materials (Li_2S and FeS_2). The introduction of anchoring groups was achieved by either reactive ester units (pentafluorophenyl or N-acryloxysuccinimide) followed by the aminolysis of the reactive ester using different amines or by block copolymerizing anchoring monomers (vinylpyrrolidone, styrenesulfonate). Subse-

quent thermal annealing of the polymer/inorganic nanoparticle hybrid material converted the polymer shell around the particles to a homogeneous carbon coating as confirmed by high resolution TEM and EELS or EDX spectroscopy. As proven by conductivity measurements, this carbon coating enhances the conductivity within the active material compared to uncoated particles. Carbon coated materials were applied as electrode materials in lithium- and sodium-ion batteries. The comparison of uncoated particles with coated particles proves the positive influence of the carbon coating. Enhanced cycling performance, improved C-rate capability as well as the ability to protect the inorganic material from degradation are the key features of the herein introduced carbon coating. However, during the extension of this project the borders of this approach became obvious, as this approach is applicable to thermally stable materials only.

In order to overcome this issue of incompatibility with thermally unstable inorganic materials, a different approach was developed based on the use of functionalized reduced graphene oxide. Therefore, graphene oxide was reduced and functionalized with sulfated groups, which can coordinate onto transition metal oxide or sulfide particle surfaces. Examplarily, this approach was applied to Ni@Fe_2O_3 superparticles. The successful wrapping could be proven by SEM and high resolution TEM. Wrapped particles were applied as anodes in lithium-ion batteries and high capacities exceeding 1000 mAh g^{-1} could be achieved, which is more than 2.5 times as much as the specific capacity of currently used anode material, graphite. Compared to unwrapped particles, the battery performance could be strongly enhanced with respect to C-rate capability and longterm cycling.

A further approach to increase conductivity by a non-thermal route is presented using semiconductive polymers. In this case poly(3-hexylthiophene-2,5-diyl) (P3HT), a prominent candidate often used in photovoltaics application, was synthesized by

GRIM polymerization. Systematic end-group functionalization of the polymer enabled the introduction of i) an anchoring end-group and of ii) an anchoring block, which was attached by subsequent RAFT polymerization and polymer analogous reaction. The attachment of P3HT to $LiNi_{0.3}Mn_{0.3}Co_{0.3}O_2$ was possible, but could not improve the battery performance properly, which might be attributed to a decreased lithium-ion diffusibility through the P3HT coating.

Finally, a new cathode material based on sulfur was synthesized. For this purpose, allyl-terminated P3HT synthesized by GRIM polymerization was copolymerized with molten sulfur. The double bond end-group reacts with radicalic sulfur species forming a S-P3HT copolymer. This copolymer is homogeneously incorporated into ssulfur. Electrochemical impedance spectroscopy reveals an increased conductivity for a composite material containing S-P3HT copolymers compared to a simple mixture of S and P3HT. Additionally, the composite material was applied as an cathode material in lithium-sulfur batteries. An improved battery performance is observed for the copolymer containing composite material, which might be related to the increased conductivity.

In summary, this work presents the synthesis of polymeric materials, which are used for the hybridization with inorganic material in order to increase the electrical conductivity. The electrochemical performance of the hybridized material is evaluated and underlines the importance of coating approaches to enhance the battery performance of alternative electrode materials to enable a possible commerzialization.

6 Abbreviations

AFM	atomic force microscope
AIBN	azobisisobutyronitrile
AN	acrylonitrile
ATRP	atom transfer radical polymerization
ATR	attenuated total reflection
CTA	chain transfer agent
CV	cyclic voltammetry
DAAM	dopamine acrylamide
δ	chemical shift
DMF	*N,N*-Dimethylformamid
DMP	2-dodecylsulfanylthiocarbonylsulfanyl-2-methyl-propionsäure
DMSO	dimethylsulfoxide
DOSY	diffusion ordered spectroscopy
EIS	electrochemical impedance spectroscopy
EDX	energy dispersive x-ray spectroscopy
EELS	electron energy loss spectroscopy
eq.	equivalent
GO	graphene oide
GPC	gel permeation chromatographi
GRIM	Grignard metathesis
HA	hydroxamic acid
HEV	hybrid vlectronic Vehicle
HRTEM	high resolution transmission electron microscope
HSQC	heteronuclear single quantum coherence
IR	infra red

nBA	n-butylacrylate
MALDI tof	matrix-assisted laser desorption/ionization time of flight
M_n	number average of molecular weight
M_w	weight average of molecular weight
NAS	N-acryloxysuccinimide
NMP	nitroxide mediated polymerization
NMP	N-methylpyrrolidone
NMR	nuclear magnetic resonance
P3HT	poly(3-hexylthiophene -2,5-diyl)
PAN	polyacrylnitrile
PFPA	pentafluorophenylacrylate
RAFT	reversible addition fragmentation chain transfer
RI	refractive index
rpm	rounds per minute
SEC	size exclusion chromatography
SEI	solid electrolyte interface
SEM	scanning electron microscope
srGO	sulfated and reduced graphene oxide
TEM	transmission electron microscopy
TGA	thermogravimetric analysis
THF	tetrahydrofuran
XPS	x-ray photoelectron spectroscopy
XRD	x-ray diffraction

7 Danksagung - Acknowledgement

Zunächst möchte ich mich bei meinem Betreuer XXX bedanken. Ich hätte mir kaum einen besseren Betreuer ausdenken können. Für Ihre fürsorgliche und gleichzeitig fachlich sehr hochwertige Betreuung, sowie für Ihr Vertrauen und Ihre Unterstützung bin ich sehr dankbar. Unter Ihrer Anleitung hatte ich die Möglichkeit, eigene Forschungsideen sowie Forschungsaufenthalte in Korea und Ulm, aber auch Konferenzbesuche zu verwirklichen, was nicht bei jedem Betreuer möglich gewesen wäre. Auch dafür bin ich Ihnen sehr dankbar.

Als nächstes möchte ich mich bei meiner Familie bedanken, die mich im Laufe meines Lebens in allen Situationen unterstützt. Insbesondere möchte ich an dieser Stelle für die Unterstützung während meiner Promotion bedanken: Einerseits für aufbauende Worte, wenn es im Labor mal nicht so lief, aber andererseits auch für die Unterstützung im privaten Bereich.

Dem gesamten AK Zentel möchte ich danken für eine sehr angenehme Zusammenarbeit, aber auch für die vielen schönen Aktionen im privaten Bereich.

Speziell möchte ich mich an dieser Stelle auch bei XXX ganz herzlich für unsere Freundschaft und auch für die Zusammenarbeit im gemeinsamen ausgelagerten Labor bedanken. Unsere gemeinsamen Stunden im Labor mit diversen Diskussionen im chemischen, aber auch privaten Bereich werde ich nicht vergessen. XXX möchte ich für die vielen gemeinsamen Jogging Runden in Wald und Feld danken. Auch XXX möchte ich für die Freundschaft danken und dafür, dass durch sie ein Hauch Koreas in unserem Labor weht :)

XXX möchte ich auch bedanken für einerseits die Bereitstellung des Graphens, aber

auch für seine immer hilfsbereite Art sowie für diverse Aktivitäten im privaten Bereich.

Meinen Kooperationspartnern in Mainz möchte ich mich auch ganz herzlich bedanken: XXX für die Bereitstellung von anorganischem Material, das ich weiterverarbeiten durfte. XXX und XXX möchte ich für die Nutzung des TEMs sowie für die durchgeführte Service-TEM und-SEM Messungen danken.

Bedanken möchte ich mich weiterhin ganz herzlich bei meinen Kooperationspartnern XXX, für die Möglichkeit, in seinen Laboratorien arbeiten zu dürfen, für seine Unterstützung und Co-Betreuung, XXX aus Münster bzw. Ulm für die Einführung in die Thematik der unterschiedlichen Batterietypen sowie für die Einführung in das praktische Arbeiten in den Batterielaboratorien.

Weiterhin möchte ich bei meinen koreanische Kooperationspartnern bedanken: Bei XXX und XXX für die Möglichkeit, für 6 Wochen deren Laboratorien nutzen zu dürfen. Bei XXX möchte ich mich bedanken für die nette Zusammenarbeit am Thema der P3HT-Schwefel Copolymere. Außerdem möchte ich der gesamten PEEL-Forschungsgruppe danken für eine schöne Zeit, die ich in deren Gruppe verbringen durfte.

Den „International Research and Training Group“ (IRTG) Mitgliedern (sowohl den deutschen als auch den koreanischen) möchte ich auch sehr danken für den super Zusammenhalt, viele schöne Erlebnisse bei Konferenz- und Workshop-Besuchen, aber auch für diverse Freizeitaktivitäten. Hier möchte ich mich auch bei XXX bedanken, der mir im Lauf der Promotion sehr ans Herz gewachsen ist und mit dem ich neben diversen an Wochenenden einen unvergesslichen Urlaub erlebt habe.

Bei meinen Kommolitoninnen und Kommolitonen, die mich seit dem ersten Semester begleitet haben, möchte ich mich auch ganz herzlich bedanken: Vielen Dank an XXX für eine schöne Zeit an der Uni in Mainz (und teilweise auch in Korea).

Bei diversen helfenden Händen im Labor, die aus verschiedenen Anlässen (Modularbeit, Bachelorarbeit, Hilfswissenschaftliche Stelle, Ausbildung, Lehramtsstudiumsabschlussarbeit) mich im Labor unterstützt haben, möchte ich auch danken. Dazu gehören XXX. Bedanken möchte ich mich auch bei XXX, die ich während ihrer Diplomarbeit co-betreuen durfte, für die gute Zusammenarbeit.

Ich möchte mich bei diversen Institutionen danken, die mich während der Promotion finanziell unterstütz haben: Dazu zählen der Verband der Chemischen Industrie, das IRTG sowie die „Graduate School of Excellence – Material Science in Mainz (MAINZ)“: Bedanken möchte ich mich hierbei auch besonders für die Mittel zum Bereisen diverser Konferenzen, Workshops, Social Skill Kurse Studentenseminaren und Forschungsaufenthalten. In diesem Zusammenhang möchte ich auch den weiteren MAINZ Mitgliedern für eine schöne Zeit bei den Studentenseminaren Danken.

Bei XXX sowie beim MAINZ office möchte ich mich für die nette administrative Zusammenarbeit danken.
Schließlich möchte ich mich bei XXX von der BASF bedanken, der mich während der Promotion als Mentor betreut hat, was mir unterstützend durch MAINZ ermöglicht wurde. Dabei danke ich auch für die Anregung, nach der Promotion eine PostDoc Stelle anzunehmen. Auch dies war ausschlaggebend für meinen nächsten Schritt, einen PostDoc Stelle in Santa Barbara, CA anzunehmen.